THM ANALYSIS OF ARGILLACEOUS ROCKS WITH APPLICATION TO NUCLEAR WASTE UNDERGROUND STORAGE

Saeed Tourchi

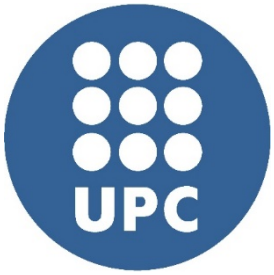

Supervisors:

Antonio Gens Sole

Jean Vaunat

Submitted in partial fulfilment of the requirements for the degree of Doctor of Philosophy

Department of Civil and Environmental Engineering Section of Geotechnical Engineering and Geosciences Technical University of Catalonia BARCELONATECH

2020

Saeed Tourchi: *THM analysis of argillaceous rocks with application to nuclear waste underground storage, October 2020.*

To *my wife*

Abstract

Argillaceous rocks (Stiff sedimentary clays) provide the geological background to many civil engineering projects. In recent years, interest in these types of material has increased, because they are being considered as potential host geological media for underground repositories of high-level radioactive waste (HLW). The possible use of these types of clay as geological hosts for radioactive waste has prompted the construction of several underground laboratories. Among the very different topics addressed in the Underground Research Laboratories (URLs), the thermo-hydro-mechanical (THM) behaviour of the host rock is the one that most concerns the present research. In situ observations have revealed a considerable number of coupled THM processes in the operation of an HLW repository.

In this context, the main objective of the present study is to describes the performance, observations and interpretation of the full-scale in situ heating test conducted on Callovo-Oxfordian (COx) claystone in the Meuse / Haute-Marne URL simulating a heat-emitting, high-level radioactive waste disposal concept. The test is fully instrumented, and attention is focused on the near-field region's the THM behaviour consisting of the sleeve surrounding the heater and the host rock. The interpretation of the test is assisted by the performance of a coupled numerical analysis based on a coupled formulation incorporating the relevant THM phenomena. The calculations have used a reference isothermal constitutive model especially developed for this type of material. The reference model later has been extended to non-isothermal condition by incorporating thermal dependency of strength parameters and stiffness. The thermomechanical model has been successfully used in the simulation of triaxial tests on COx claystone. The numerical analysis performed has proved able to represent the progress of the experiment very satisfactorily. The performance and analysis of the in-situ test has significantly enhanced the understanding of a complex THM problem and have proved the capability of the numerical formulation and non-isothermal constitutive model to provide adequate predictive capacity.

Keywords: in situ testing; numerical modelling; radioactive waste disposal; temperature effects.

Acknowledgements

First and foremost, praises and thanks to God, the Almighty, for His showers of blessings throughout my research work to complete the research successfully.

I would like to express my deep and sincere gratitude to my thesis supervisor, Prof. Antonio Gens for giving me the opportunity to do research and providing invaluable guidance throughout this research. His dynamism, vision, sincerity and motivation have deeply inspired me. It was a great privilege and honour to work and study under his guidance. I am extremely grateful for what he has offered me. I would also like to thank him for his friendship and empathy.

I would like to say a very big thank you to my co-supervisor Dr. Jean Vaunat for all the support and encouragement he gave me, during my PhD. Without his guidance and constant feedback this PhD would not have been achievable.

I gratefully acknowledge the funding received towards my PhD from the French national radioactive waste management agency (Andra).

Thanks to Dr. Alessio Ferrari, for hosting me at EPFL-Swiss Federal Institute of Technology Lausanne and allowed me to participate in the academic activities of the Soil Mechanics Laboratory (LMS) during my study-visit. Also, to all the wonderful people that I met in Lausanne, especially Prof. Laloui.

I am also very grateful to Prof. Sebastian Olivella whose support were advantageous during my PhD studies. His office door was always open whenever I ran into a trouble spot or had a question about my research.

I would like to express my deepest gratitude to my wife and my parents. This accomplishment would not have been possible without them. Thank you.

Contents

List of Publications

This is a list of all the work published, submitted or to be submitted, related to this PhD.

Journal Papers

Tourchi S, Gens A. Thermomechanical model for argillaceous rocks. (in preparation)

Tourchi S, Vaunat J, Gens A., et al. A full-scale in situ heating test in Callovo-Oxfordian claystone: observations, analysis and interpretation. Computers and Geotechnics (in review)

Bumbieler F, Plúa C, Tourchi S, et al. Feasibility of constructing a full-scale radioactive high-level waste disposal cell and characterization of its thermo-hydro-mechanical behavior. Int J Rock Mech Min Sci (in review)

Tourchi S, Ferrari A, Gens A. Thermal pressurization effect on the shaft bearing capacity of energy piles. (in preparation)

Conference abstracts and proceedings

Tourchi, S., Vaunat, J., Gens, A., M.N, V., and Bumbieler, F. (2019). "Coupled THM analysis of long-term anisotropic convergence in the full-scale micro tunnel excavated in the callovo-oxfordian argillite." *VIII International Conference on Computational Methods for Coupled Problems in Science and Engineering*, Barcelona, 292–299.

Tourchi, S., Vaunat, J., Gens, A., Vu, N., and Bumbieler, F. (2019). "Thermo-Hydro-Mechanical simulation of a full-scale steel-lined micro-tunnel excavated in the Callovo-Oxfordian Argillite." *XIV International Conference on Computational Plasticity. Fundamentals and Applications COMPLAS 2019*, Barcelona, 544–552.

Tourchi, S., Vaunat, J., Gens, A., Vu, M. N., and Bumbieler, F. (2020). "3D numerical modelling THM behaviour of a full-scale in situ heating test for high-level radioactive waste disposal: observations, analysis and interpretation." *8th International Clay Conference 2020*, Paris, 341–350.

Reports

Tourchi, S., Vaunat, J., and Gens, A. (2017). *THM modelling of the ALC1604 experiment. 2nd preliminary report.* Barcelona.

Tourchi, S., Vaunat, J., and Gens, A. (2019). *THM modelling of the ALC1604 experiment. Final report.* Barcelona.

Workshops proceedings

Tourchi, S., Vaunat, J., and Gens, A. (2017). *Thermo-Hydro-Mechanical modelling of full-scale in situ heating test in the callovo-oxfordian argillite.* 9th Workshop of CODE_BRIGHT USERS. Barcelona, Spain.

List of Figures

List of Tables

Chapter 1: Introduction

1.1 BACKGROUND

In the middle of the increasing concern regarding carbon emissions and global warming, non-fossil fuel alternatives are gaining increased attention, in particular to nuclear power. With an increasing interest in nuclear energy, radioactive waste will grow simultaneously. Three main strategies were developed for the management of spent nuclear fuel: reprocessing, storage and direct disposal. Nowadays, deep geological disposal is accepted internationally as the safe and most feasible disposal method of high-level radioactive waste (HLW) (IAEA, 2003). The principle of geological disposal of radioactive waste is to place carefully prepared and packaged waste in excavated tunnels in geological formations such as salt, hard rock, or clay (Kim et al., 2011).

Several countries, including France, the United States, Germany, Sweden, Finland and Canada, have built underground research laboratories (URLs) to carry out related research of geological disposal. The need to study the problem of high-level nuclear waste disposal under conditions similar to those that will prevail in the real disposal facilities has made underground research laboratories (URLs) an essential feature of research in this field (NEA, 2001). The study of geotechnical aspects, obviously, is a very significant part of the work carried out in those facilities. They are excavated in rock types considered to be suitable for repository construction and, typically, they are located a few hundred meters below the surface. URLs are a crucial tool to integrate the various hydrologic, thermal, mechanical, chemical and biological phenomena and coupled processes in a realistic geological setting (Gens, 2003).

Repository construction foresees the excavation of a network of tunnels in a suitable rock formation located within a few hundred meters below the ground level (Gens et al., 2009). The host rock (natural barrier) has to provide mechanical stability to the excavated galleries and be a medium of very low permeability to prevent or retard any possible leakage from the isolation system.

The concept relies on a series of natural barriers and an Engineered Barrier System (EBS), called a multi-barrier, to contain the waste for a long time and to minimise the amount of radioactive material that may eventually escape from a

repository and reach the human environment. The presence of multi-barrier systems serves a complimentary safety function in that it increases confidence in the HLW repository (Kim et al., 2011). These natural and engineered barriers will be subjected to simultaneous thermal, hydraulic and mechanical (THM) phenomena resulting from the heat-emitting nature of the high-level radioactive waste (HLW) and the highly confined isolation system conditions.

The THM processes will control the evolution and long-term response of the whole isolation system; therefore, a good understanding of the main THM phenomena is required to achieve a safe design of HLW repositories. To assess the hydro-mechanical effects of the thermal transient on the host material in a deep repository, various in situ heating tests have been performed at several underground laboratories (Gens et al., 2011). The CACTUS, ATLAS, and CERBERUS tests (Picard et al., 1994; Bernier and Neerdael, 1996; De Bruyn and Labat, 2002; François et al., 2009) were performed in the Boom clay at the HADES underground research facility in Mol, Belgium. The HE-D test was carried out in the Mont Terri laboratory in Northern Switzerland, which was constructed in Opalinus clay. And the TER and TED heating tests were performed in Bure at the Meuse-Haute Marne laboratory located in Eastern France (Garitte et al., 2014), which was constructed in the Callovo–Oxfordian mudstone.

High-level waste (HLW) produces heat. Therefore, the thermo-hydro-mechanical (THM) behaviour of COx claystone is essential in the rational design of an underground nuclear waste disposal facility. This thesis presents the programme launched at the MHM URL to study the THM effects of the thermal transient on the host clay and the strategy implemented in this new programme to demonstrate and optimise actual repository components. However, significant outcomes are highlighted.

In 2000 the French national radioactive waste management agency (Andra) started the construction of the Meuse-Haute-Marne (MHM) underground research laboratory (URL) at Bure, in the Callovo-Oxfordian argillaceous formation, in order to demonstrate the feasibility of this geological unit to host a nuclear waste repository. Insight was given regarding the work performed on understanding THM behaviour, and on testing and optimising techniques for the construction of HLW disposal vaults (steel-lined micro-tunnel about 0.8 m in diameter) at the MHM URL (Armand et al., 2017). In parallel, Andra has also conducted theoretical work and characterisation on samples through collaborative work with academia. This part of the work is discussed in this thesis.

1.2 OBJECTIVES AND METHODOLOGY

The general objective of this research is a THM modelling of the full-scale HA-ALC1604 in situ heating test carried out on Callovo-Oxfordian (COx) claystone in the Meuse/Haute-Marne underground research laboratory (MHM-URL). The main aims of ALC full-scale emplacement experiment performed within the context of in the EU project LUCOEX (WP3) and consisted in demonstrating the construction feasibility of a High-Level Waste (HLW) cell representative of the 2009 benchmark concept and in order to determine the impact of thermal loading on the total cell's behaviour.

The experiment has also been used to acquire new data on the THM behaviour of the surrounding rock and to compare it with that of previous small-scale heating experiments. Interpretation of the test has been assisted by the performance of a series of analyses simulating the experiment reported in this document. Coupled 3D-THM numerical analyses have been carried out to provide a structured framework for interpretation, and to enhance understanding of THM behaviour of Callovo-Oxfordian claystone. By performing the 3D numerical analysis, it has been possible to incorporate anisotropy of material parameters and of in situ stresses. The performance and analysis of the in-situ tests have significantly enhanced the understanding of a complex THM problem and have proved the capability of the numerical formulation to provide adequate predictive capacity.

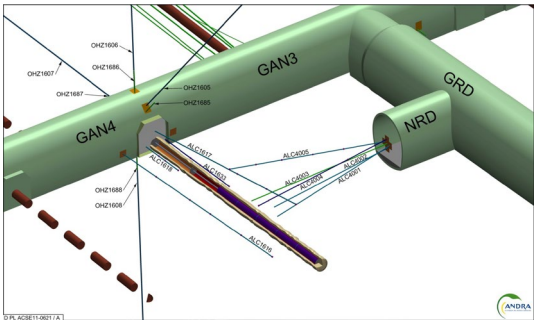

Figure 1.1: HA-ALC1604 test in a three-dimensional view (Andra, 2013).

The HA-ALC1604 experiment has yielded valuable data on the in-situ behaviour of the Callovo-Oxfordian claystone subjected to heating and cooling around an HA disposal cell as well as on the response of the steel lining. Interpretation, based on thermal and coupled THM analyses, has proved satisfactory showing that the processes involved are well understood and adequately incorporated in the formulation and associated computer code. It is worth noting

that the numerical works performed in this project have converged to a unique final three-dimensional model accounting for most experiment elements (rock, steel lining, insert, gap, the thermos-hydraulic effect of surrounding galleries), based on THM parameters consistent with those used in other tests, and reproducing well all measurements.

1.3 THESIS LAYOUT

This thesis consists of six chapters. If the pdf version of the document is being used, please note that all references, sections, equations, figures, tables, and appendices are hyper-referenced to facilitate navigation through the document. If a link has been used, the reader can return to the previous position using Alt+Left in most of the softwares used to read pdf files.

Chapter 2 presents an overview of thermo-hydro-mechanical behaviour of argillaceous rocks. The chapter is organized as follows: the mechanical behaviour is examined first. Hydraulic behaviour and hydromechanical coupling are considered next. Afterwards, the thermal behaviour is reviewed in order to examine more closely the behaviour of argillaceous rocks under thermal loading. Finally, an overview of some important in-situ heating tests discusses the outstanding research issues in disposal from the aspect of geotechnical engineering, such as brittleness and progressive failure, the response of argillaceous weak rocks to deep underground excavations and coupled thermo-hydro- mechanical (THM) response of argillaceous rocks.

In chapter 3 explanation of thermo-hydro-mechanical processes in the in-situ heating test as well as general information about THM processes occurring in the nuclear fuel repository is reviewed more on that a theoretical basis and equations used to simulate THM processes, as well as general information about mechanical models, are presented. Time-dependent elastoplastic is considered for Callovo-Oxfordian (COx) claystone. Elastic model for liner; and bi-linear elastic model for gap element with two branches for considering the gap open and closed. Description of the ALC1604 in situ test is presented in Chapter 4.

Chapter 5 deals with the interpretation of the temperature field obtained during the heating experiment and the determination of the optimum thermal parameters. In this regard, purely thermal analysis was performed to find the value of thermal conductivity that achieves the closest agreement with measured temperatures. In Chapter 6, the THM modelling of the HA-ALC1604 experiment is presented. It corresponds to the final 3D model carried out of the work, which includes most of

experiment geometrical features including the thermo-hydraulic influence of the surrounding GAN and GRD gallery, as well as all experiment phases since the excavation of the alveolus. And finally, in chapter 6 the general conclusions of the thesis are presented.

Chapter 7 is centred on the enhancement of an existing isothermal elastoplastic model for argillaceous rocks to enhance its predictive capability with respect to temperature changes, in the light of new experimental evidence. The thermomechanical constitutive model developed is then applied, via a suitable coupled THM formulation, to the coupled THM analysis of an in-situ heating test performed in the Meuse/Haute-Marne Underground Research Laboratory.

In appendix A temperature results from the thermal analysis are given. Appendix B presents pore pressure results from the reference 3D THM analysis. And finally, appendix C deals with the THM modelling of energy piles which has been performed during the academic stay in EPFL.

Chapter 2:

On the THM behaviour of Argillaceous rocks

2.1 BACKGROUND

This chapter focuses on the thermo-hydro-mechanical (THM) behaviour of argillaceous rocks, i.e. geological materials where fine-grained particles predominate (see Hawkins and Pinches, 1992, Hallsworth and Knox, 1999 and Hawkins 2000 for more details). They have been widely distributed in nature and are estimated to represent up to 50% (Pettijohn, 1957) in the world's sedimentary rock mass and to surface in about one-third (Franklin and Gruspier, 1983). Although there are certainly argillaceous hard soils, this work focuses mainly on argillaceous weak rocks, though no specific limits have ever been universally established for material ranging from hard soils to weak rocks. Thus Hawkins (Hawkins, 2000) suggests a lower threshold for undrained shear strength of very stiff soils of 160 kPa and upper unconfined compression strength for weak rocks of 10 MPa. There have also been many other attempts for the definition of hard soils-weak rock not only with respect to strength but, also, in terms of porosity and compressibility (see Clayton, 1997 for more detiles).

Specifically, three argillaceous geomaterials receive special attention, Boom clay, Opalinus clay and Callovo-Oxfordian (COx) claystone in this chapter as they correspond to the materials being investigated in three underground laboratories in the context of deep geological disposal of high-level radioactive waste. The laboratories are the HADES Underground Research Facility (Mol, Belgium) in Boom clay (Bastiaens and Bernier, 2006), the Mont Terri underground laboratory (St. Ursanne, Switzerland) in Opalinus clay (Thury and Bossart, 1999) and he Meuse-Haute Marne underground laboratory (Bure, France) in Callovo-Oxfordian claystone (Delay et al., 2007). These argillaceous materials are investigated at both the small and large scale through laboratory and in situ experiments.

The tremendous interest in these materials lies in the fact that hard argillaceous soils and rocks are very desirable as potential host media for high-level radioactive waste. They provide advantageous features such as low permeability, a degree of self-healing capability when damaged, substantial retardation properties for solute

transport, and no unpredictable economic value. The probable need to support the excavated openings, and exposure to chemical behaviour and desaturation caused by ventilation are possible shortcomings (Gens et al. 2007b). High-level radioactive waste is strongly heat emitting; so thermal properties assessment is one of the priorities of those investigations (Gens et al., (2009; Gens, 2010).

Table 2.1 presents some general properties for three materials, Boom clay, Opalinus clay and Callovo-Oxfordian (COx) claystone. They should be viewed only as reference values; the variability and anisotropy of the materials cannot be fully collected in the Table and parameter values outside the ranges given certainly occur. Opalinus clay and COx claystone are obviously part of the indurated mudrock class that tends towards the rock end of hard soils–the weak spectrum of rocks. On the other hand, Boom clay is considerably weaker and is closer to the range soil area. Thus, the materials emphasized cover a large proportion of the geological span considered, providing information on a useful range of geotechnical characteristics and behaviour. Nonetheless, very low permeability is prominent to all of them.

Table 2.1: Some reference properties for the host materials of the three underground laboratories (modified from Gens, 2013).

	COx claystone	Opalinus clay	Boom clay
Dry density (g/cm3)	2.21-2.33	2.22-2.33	1.61-1.78
Calcite content (%)	23 - 42	6 - 22	0 - 3
Porosity (%)	11-16	11-14	35-40
Water content (%)	<6.5	4 - 8	20-30
Clay content (%)	50-65	45-55	40-70
Liquid limit (%)	21-25	21-25	55-80
Plasticity index (%)	11-19	13-17	32-51
Young's modulus (GPa)	3.6-8.5	4-10	0.2-0.4
UCS (MPa)	10-16	8-22	2-2.8
Permeability (m/s)	$0.7\text{-}5\times10^{-13}$	$0.5\text{-}5\times10^{-13}$	$2\text{-}5\times10^{-12}$
Geological stage	Callovo-Oxfordian	Aalenian	Rupelian
(millions of years)	156-164	171-176	28.4-33.9

The chapter is organized as follows: the behaviour under compressive loading is examined first in the context of behaviour frameworks developed for this type of materials. A discussion on some additional aspects of mechanical behaviour like brittleness and progressive failure and material anisotropy follows. Hydraulic behaviour and hydromechanical coupling are considered next. Afterwards, the thermal behaviour is reviewed in order to examine more closely the behaviour of

argillaceous rocks under thermal loading. Finally, an overview of in situ heating tests based on Belgian, Swiss, and French disposal programs, discusses the outstanding research issues in disposal from the aspect of geotechnical engineering, such as brittleness and progressive failure, the response of argillaceous weak rocks to deep underground excavations and coupled thermo-hydro- mechanical (THM) response of this sedimentary clays.

2.2 ON MECHANICAL BEHAVIOUR

From a general point of view, the mechanical behaviour of argillaceous materials results from the combination of the different effects of sedimentation, gravitational compaction, uplift/unloading and cementation/bonding (Gens, 2013). The effects of the complex processes outlined above on behaviour calls in situ testing, fabric studies, routine index experiments and advanced laboratory testing as advocated in (Jardine, 2011). In this section, some of the most important mechanical properties of these materials are discussed.

2.2.1 Gravitational compaction and structure development

By constructing general behaviour frameworks of argillaceous materials, the overall behaviour can be perceived in an integrated and structured manner, underlining common behaviours patterns that can be identified in inexplicably quite different materials. The usual starting point in these developments is the paper by Skempton (Skempton 1969) on the consolidation of clays by gravitational compaction in which he plotted a series of in situ consolidation curves for a wide range of argillaceous materials and accordingly a dependency of the sedimentation consolidation curves (SCCs) slope with the plasticity of the material was identified. Later Burland (1990) normalized the same type of data for normally consolidated soils using void ratio rather than water content and they observed that data plots very close to a single line, the sedimentation compression line (SCL), which lies above the intrinsic consolidation line (ICL).

A soil structure, which is a characteristic of most natural materials, is the ability of natural clays to lie right to the possible stress states of the reconstituted material (Gens 2013). It is worth noting that both fabric and antepartum bonding are the product of the soil structure. The framework was extended to include materials with different sensitivities by Cotecchia and Chandler (2000); higher sensitivity corresponded with more cemented materials.

The impact of natural soil and rock structure was considered by Leroueil and Vaughan with a unified approach later in 1991. They also identified a

structured soil's ability to lie on a stress state outside the space allowed for the unstructured reconstituted soil, and drew attention to the effects of structural degradation when a natural soil is stressed beyond the yield point. Those factors can be outlined in the Figure 2.1 where the oedometer consolidation lines for a structured and a destructured soil are given.

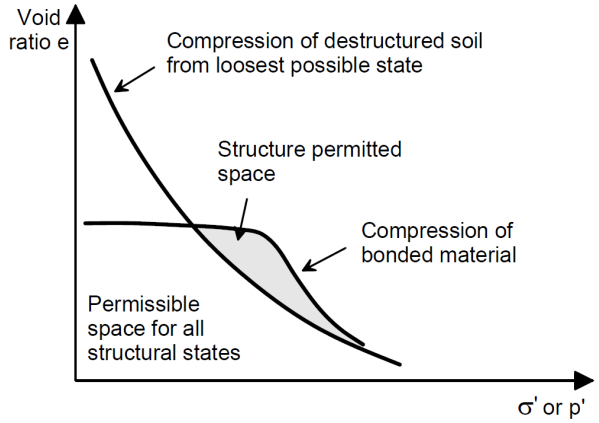

Figure 2.1: The comparison of structured and destructured compression in the oedometer test (Lemueil and Vaughan, 1990).

The outcomes of a one-dimensional Boom clay compression test provide a good example for this type of behaviour. Figure 2.2 shows one-dimensional compression test results on Boom clay sample. The intrinsic compression line (ICL) corresponds to the reconstituted material, whereas the sedimentation compression line (SCL) is obtained as the best-fit regression line of the field $e-\log\left(\sigma_v'\right)$ relationship for several argillaceous materials (see Burland, 1990, for more details). The yield point lies beyond the ICL, and in situ vertical stress as shown in the figure. However, when loaded after yielding, the compression curve tends to converge to the ICL as the load is increased.

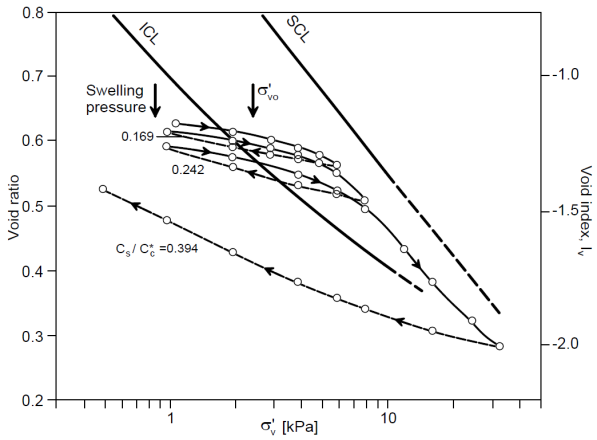

Figure 2.2: One dimensional compression behaviour of Boom clay (Burland, 1990; Horseman et al., 1987).

After loading beyond the yield point, the structures can also be degraded due to compression from the slope of the swelling line. Figure 2.3 provides a remarkable example of experimental results achieved in a high-pressure oedometer test on the Panama Canal's Culebra shale. The Degradation (line with black symbols) takes place during compression. Then the material (line with white symbols) is unloaded and experiences enormous swelling, which ends in a void proportion higher than the original.

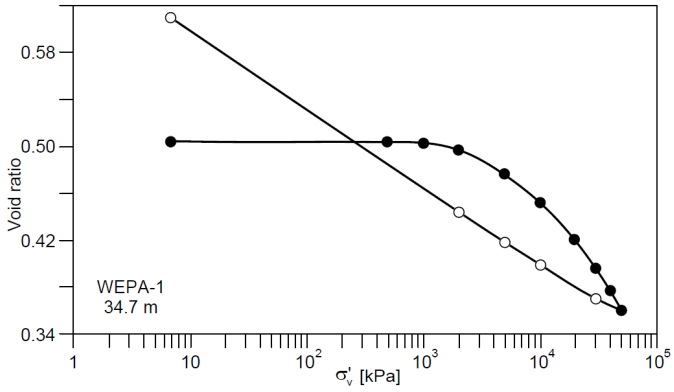

Figure 2.3: High-pressure oedometer test on Culebra shale (Banks et al., 1975 referenced in Gens, 2013).

Interestingly, there are very few cases of consolidation lines going beyond sedimentation compression lines of natural clays (SCC). Test results on samples of clays from France extracted from large depths are shown in Figure 2.4. As Figure 2.4 shows, the consolidation curves go beyond the intrinsic consolidation curve but,

again, they do not cross the corresponding sedimentation consolidation curves. Therefore, it seems either the development of post-sedimentary structures is rare or that the swelling / weathering and/or sample removal effects have been overcome by such additional structures.

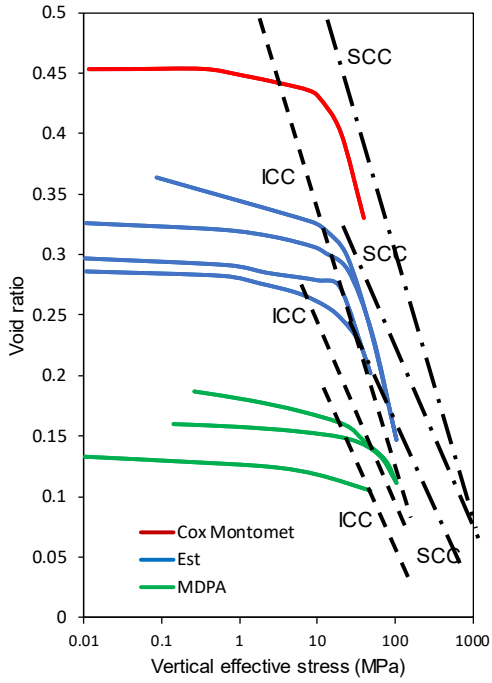

Figure 2.4: Oedometer compression curves for three argillaceous rocks from France (modified from Heitz and Hicher, 2002).

Another important observation is that, after loading, some materials do not converge onto the intrinsic consolidation line because there is a stable structure configuration that allows stable void ratios above the intrinsic consolidation line. The behaviours of Vallericca clay, shown in Figure 23, is an example. Coop and Cotecchia, (1995) have obtained a similar result by testing normally consolidated clays from Sibari, Italy.

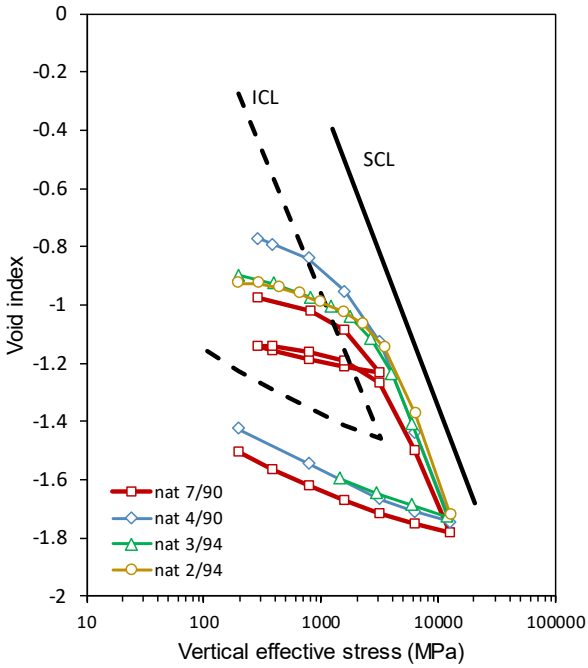

Figure 2.5: One-dimensional compression data for Vallericca clay (modified from Amorosi and Rampello, 2007).

To summarize, the observation of compression lines of natural materials and their relationship with the ICL provides a unifying framework, on the basis of the work described in (Burland, 1990; Cotecchia and Chandler, 2000; Leroueil and Vaughan, 1991), for a readily measurable assessment of the effects of gravitational compaction and structure (fabric and bonding).

2.2.2 Brittleness and progressive failure

Argillaceous rocks generally fail quasi-brittle under deviatoric loading. Ductile behaviours are also possible to observe if the samples are tested at very high effective confining stresses (e.g. Ohtsuki et al. 1981), but brittle failure predominates in conventional geotechnical situations. Skempton (1964) put forward one of the first descriptions of this kind of behaviour on the basis of slow drained tests carried out on a stiff clayey material in the direct shear box apparatus (Figure 2.6). He identified a first stage, characterized by resistance increases to a maximum value, defined the peak strength.

After this point a strain softening process begins to develop. It consists of a decrease in strength until a limit state reaches, where the strength will no longer

decrease during further displacement application. This lowest-bound constant strength is known as residual strength and was early identified using the ring shear apparatus by Tiedemann (1937) and Hvorslev (1937). As shown in Figure 2.6, the intercept of cohesion vanishes, and the friction angle decreases slightly as the force envelope moves from peak to residual. The reduction of the friction angle may vary from 1° or 2° to 10°, depending on the materials. It should be noted that, during the process, water content increases, evidencing the material's tendency to dilate during shearing.

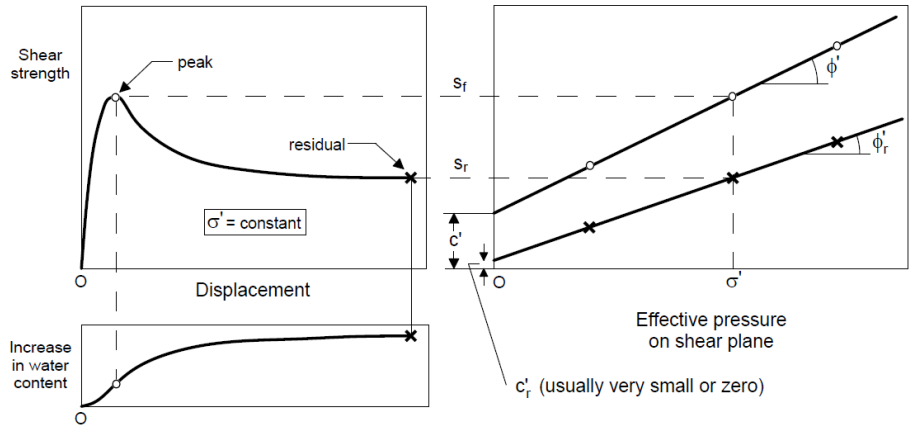

Figure 2.6: Shear characteristics of stiff clayey materials (Skempton, 1964).

Later, these phenomenological features were used to distinguish the softening process between two different stages (Figure 2.7). The first stage occurs just after the peak, characterized by a high rate of strength loss associated with interparticle bond degradation and breakage (Burland, 1990; Simpson, 1979). The second stage follows the first and is characterized by a gentler reduction in strength until the residual value, generally attributed to a gradual realignment of clay particles along the failure plane (Gens, 2013). Fully softened strength is often known as the strength between both stages ((Terzaghi et al., 1996; Mesri and Shahien 2003; Skempton, 1970) or post-rupture strength (Burland, 1990).

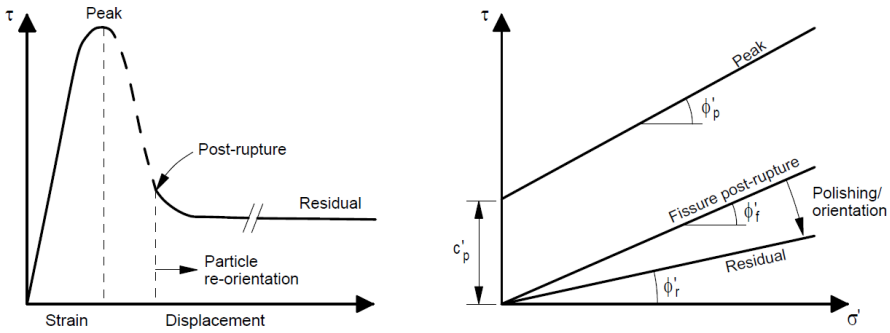

Figure 2.7: Conceptual scheme for the strength of argillaceous hard soils and weak rocks (Jardine et al. 2004a).

Argillaceous rocks are not an exception regarding this type of behaviour. As an example, Figure 2.8 and Figure 2.9 show typical stress-strain curves of Kimmeridge Bay Shale and COx claystone under triaxial loading presented by Nygård et al. (2006) and Belmokhtar et al., (2018) respectively. In Figure 2.8, the peak, fully softened, and residual strengths can be clearly identified in curves M2 and M3. It seems moreover that strain reachable in triaxial tests are not large enough to reach the residual strength for high confining pressures (M4 and M5), while post-peak curve could not be experimentally followed at low confining pressures (curve M1), probably because the large dilatancy experienced by the sample at this level of stress leads to the loss of control of the test.

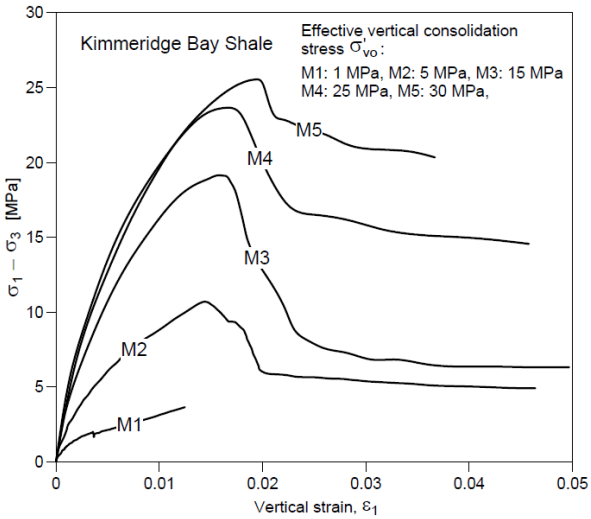

Figure 2.8: Stress-strain behaviour of Kimmeridge Bay Shale under triaxial loading (Nygård et al., 2006).

Figure 2.9a presents stress–strain curves in drained triaxial compression tests with different confining stresses performed by Hu et al. (2014) on COx claystone sample. The loading procedure was conventional and composed of two stages: setup of confining stress and application of deviatoric stress under drained condition. Six values of confining stress are used such as 2, 5, 10, 15, 20 and 40 MPa. As shown in this figure, the mechanical response of claystone is strongly dependent upon confining stress.

Under low confining stress, there exists some nonlinear phase at the beginning of deviatoric loading. This nonlinear phase is attributed to the progressive closure of initial bedding planes and microcracks in the axial direction. With the increase in confining stress, such a nonlinear phase disappears because the initial microcracks are almost closed during the application of confining stress. Also, under low confining stress, the sample failure is marked by sharp peak stress, due to the coalescence of cracks leading to splitting of sample. Under higher confining stress, this peak stress state is much less pronounced and even disappears (confining stress of 40 MPa). The failure of sample is generally associated with the onset of shear enhanced compaction bands. There is a clear transition from brittle to ductile behaviour with confining stress increase. However, for all confining stress, after a more and less marked linear stress strain phase, we observe nonlinear responses of material before and after peak stress. These nonlinear inelastic strains are directly related to the nucleation and growth of microcracks and mainly generated by frictional sliding along cracks surfaces.

There is a clear transition from volumetric compressibility to dilatancy for almost all the confining stress considered (Hu et al. 2014; Belmokhtar et al., 2018) However, this transition occurs much earlier under low confining stress than higher one. Physically, this volumetric dilatancy in brittle rocks under compressive stresses may be related to the normal opening of microcracks generated by frictional sliding along rough crack surfaces. This is similar to the published experimental data on dilatant effects on clayey rocks (Naumann et al., 2007; Zhu and Wong, 1997).

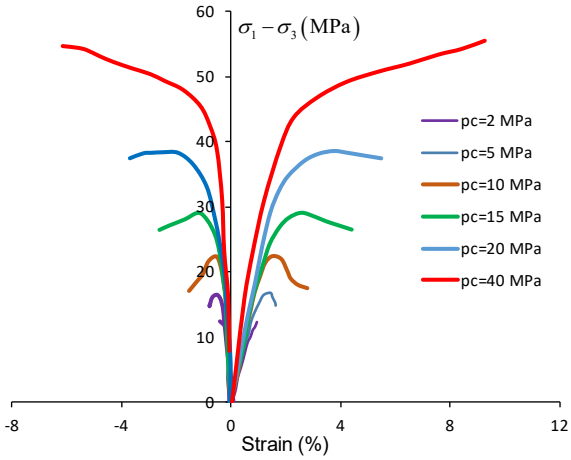

Figure 2.9: Stress–strain curves in drained triaxial compression tests with different confining stresses (Hu et al. 2014).

The post-peak response is governed by the creation of a shear plane with an inclination of about 65° with respect to horizontal, as shown in Figure 2.10. These results are comparable to other ones obtained in claystones by Naumann et al. (2007), Zhang et al. (2007), Hu et al. (2014) and Menaceur et al. (2015).

Figure 2.10: Sheared specimen (EST51338b), with shear plane inclined at an angle of 65° from horizontal (Belmokhtar et al., 2018).

The values of shear strength are plotted together in a q – p′ diagram together with the results of Hu et al., (2014) on small specimens and Menaceur et al. (2015) in the hollow cylinder apparatus (Figure 2.11). One observes a good overall comparability of the drained shear strength data obtained on various devices, with parallel curves that provide the same value of friction angle of 21°. Shear strength values are also well related with respect to the specimen's porosities, with the largest

strength at lower porosity of 13% (Hu et al. 2014; Menaceur et al. 2015) and smallest one at the highest porosity of 17% (Menaceur et al. 2015).

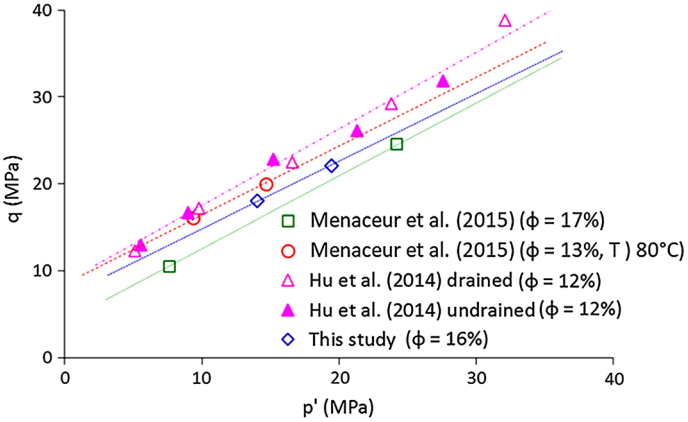

Figure 2.11: Comparison of the shear envelopes with data of shear tests determined with different devices on saturated specimens of the Callovo-Oxfordian claystone(Belmokhtar et al. 2018).

2.2.3 Material Anisotropy

It has long been recognised that geomaterials may exhibit anisotropic behaviour (Donath, 1964; Ladd and Varallyay, 1965; McLamore and Gray, 1967), whose origin has been related to different sources such as deposition processes (Oda and Nakayama, 1989), tectonic processes (Amadei, 1996), loading history (Li and Yu, 2009) and fabric (Anandarajah, 2000), among others. In argillaceous rocks, it is essentially related to the process of sedimentation and compaction, which results in an oriented structure controlled by bedding planes and fissility. As a consequence, two main directions of anisotropy (parallel and orthogonal to the bedding plane) are generally identified and modelled in the framework of transverse isotropy (or cross- anisotropy). The degree of anisotropy has been often related to the compaction process, due to both porosity reduction and smectite-to-illite transformation with diagenesis (Vernik and Liu, 1997), although micro-cracks and kerogen content may also play a role (Carcione, 2000; Vernik and Liu, 1997).

It has been well described in Mánica (2018) that anisotropy can be generally observed in properties such as stiffness, strength or permeability. Stiffness anisotropy in argillaceous rocks has been usually assessed indirectly through its seismic velocity anisotropy (Vernik and Liu, 1997). Anisotropy can be inferred from field seismic measurements by considering the non-hyperbolic moveout of wave reflection (Alkhalifah, 1997), or in laboratory through multi- (Hornby, 1998) or single-core methods (Wang 2002a,b). Direct stiffness measurements have also

been reported (Niandou et al., 1997; Valès et al., 2004). In general, measurements indicate a marked tendency for higher stiffness (or wave velocities) in the direction parallel to the bedding planes than perpendicular thereto. In Figure 2.12, Sayers (2013) collected data of various shales from the literature where the relationship between the Young's moduli perpendicular and parallel to bedding is shown, and where the mentioned tendency is clearly identified.

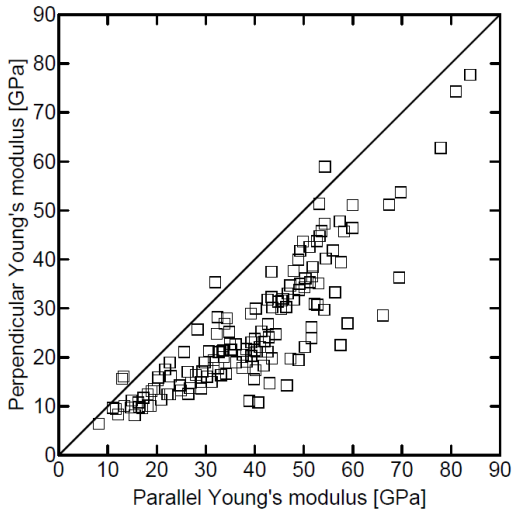

Figure 2.12: Perpendicular versus parallel Young's modulus of various shales (modified from Sayers, 2013).

Data on the strength anisotropy of argillaceous rocks are scarce, although this issue is currently gaining increasing attention, especially in relation with hydraulic fracturing issues. Anisotropy is usually assessed by conventional methods for strength determination (e.g. uniaxial compression or triaxial compression test) on samples trimmed with different bedding orientations (Cho et al. 2012; Niandou et al. 1997; Valès et al. 2004). Figure 2.13 shows typical strength distributions in shale rocks, where the minimum strength is generally obtained for intermediate orientations between the loading and the bedding planes.

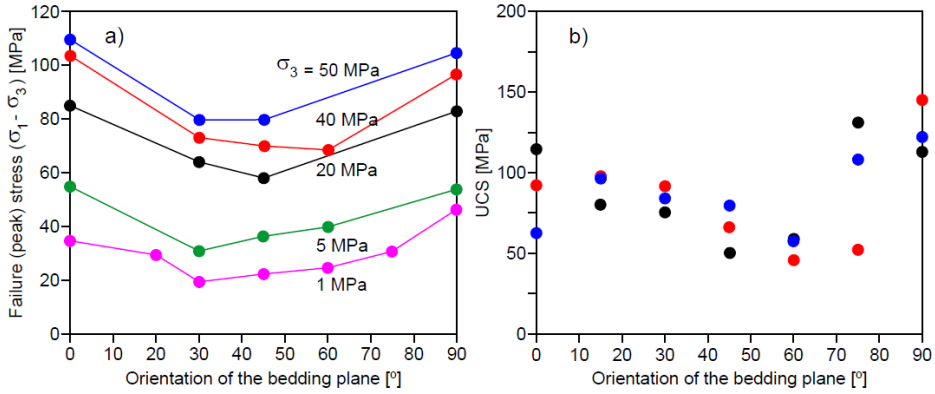

Figure 2.13: Strength variations (a) under triaxial loading of Tournemire shale (Niandou et al., 1997) and (b) under uniaxial loading of Boryeong shale (Cho et al., 2012).

2.3 ON HYDRAULIC BEHAVIOUR

2.3.1 Permeability

Very low permeability of argillaceous materials implies that the precise determination of permeability is often difficult and requires the use of transient methods (Figure 2.14).

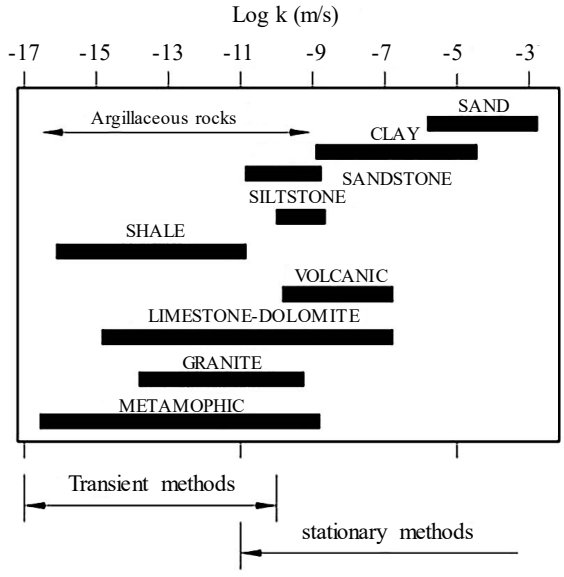

Figure 2.14: Range of permeabilities measured under a confining pressure of 10 MPa indicating the type of determination method (Brace, 1980).

Permeability ranges for argillaceous materials as a function of porosity are given in Figure 2.15. Looking at the figure, permeabilities lie well within the same range and the plot extends to very low porosity values. However, what is most evident in Figure 2.15 is not the predicted reduction of permeability with porosity, but the broad range of values for a given porosity (Gens 2013), this implies that the permeability predicted by using the porosity is a rough estimation and what matters is pore size (more precisely the largest interconnected pore entry magnitude that is related to pore (and grain) size distribution). It is also perhaps worth mentioning due to the possible effect of the presence of thin more granular layers values is bound to be higher in the case of field measurements.

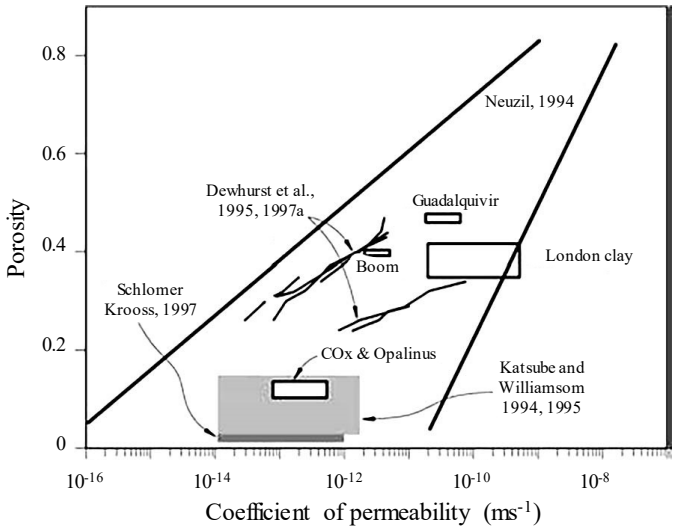

Figure 2.15: Range of porosity-permeability data for argillaceous materials (modified from (Neuzil, 1994).

The microstructural features of sedimentary materials may also result in anisotropy of permeability. In general, observations show that the permeability measured parallel to bedding is higher than the one measured perpendicular thereto (Bhandari et al., 2015; Kwon et al., 2004). An example is shown in Figure 2.16 where tests on COx claystone specimens cut parallel and perpendicular to bedding exhibit about one order of magnitude difference in permeability (Zhang and Rothfuchs 2004a). Bonding may affect permeability contrastingly. On the one hand, bonding tends to reduce porosity, thus reducing permeability. Strong bonding, on the other hand, can keep fissures open even during swelling, increasing bulk permeability.

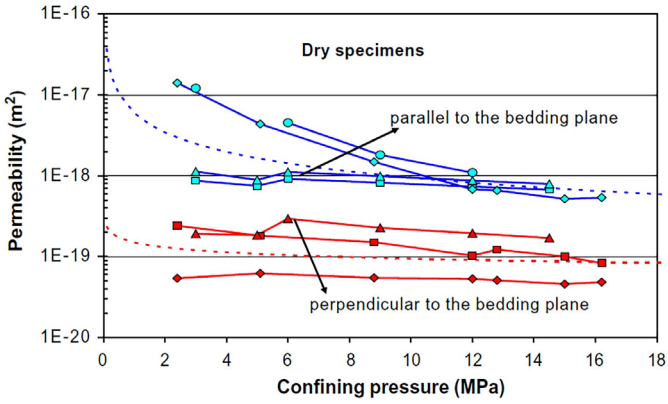

Figure 2.16: Dependence of intrinsic gas permeability on confining pressure for COx claystone specimens cut parallel and perpendicular to the bedding planes (Zhang and Rothfuchs 2004a).

Figure 2.17 shows the reduction of transmissivity (directly related to permeability) in Opalinus clay measured in a saturated zone damaged by an excavation in the Mont Terri laboratory. This transmissivity reduction implies a quite significant capacity for self-sealing even in strongly bonded materials such as Opalinus clay.

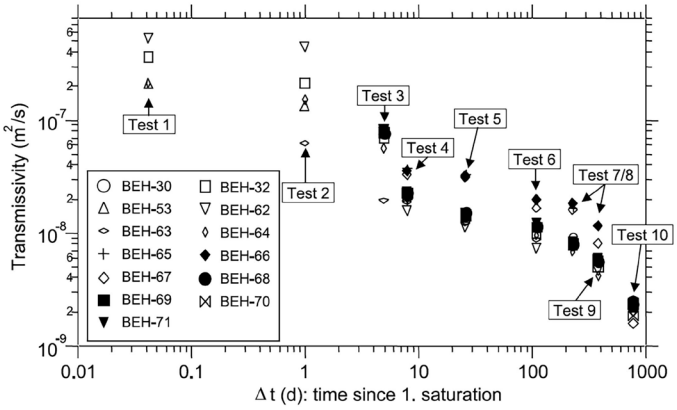

Figure 2.17: Time evolution of transmissivity measured in a saturated excavation damaged zone in Opalinus clay (Bossart et al. 2004).

2.3.2 Hydromechanical coupling: Biot's coefficient

Due to low porosity of argillaceous materials Terzaghi's principle of effective stress is not assured (Jardine et al. 2004). Biot's poromechanical theory could be convenient framework considering cases (Biot and Willis, 1957; Coussy, 2004). In the simple case of poroelasticity, effective stress becomes:

$$\sigma'_{ij} = \sigma_{ij} - bu\delta_{ij} \qquad b = 1 - K_d / K_s \tag{1.1}$$

Where σ'_{ij} are the effective stresses, σ_{ij} the total stresses, u the pore pressure, δ_{ij} Kronecker's delta, K_d the drained volumetric modulus of the skeleton , K_s the volumetric modulus of the solid phase and b Biot's coefficient which is a key property for the porous medium in the context of poroelastic theory.

There has been a sustained effort to determine Biot's coefficient of the COx claystone by a number of researchers using both oedometer and isotropic triaxial tests as summarised by Mohajerani (2011) (Figure 2.18). A large proportion of the range of results obtained arises may arises from testing procedures and difficulties and more research is needed in this area.

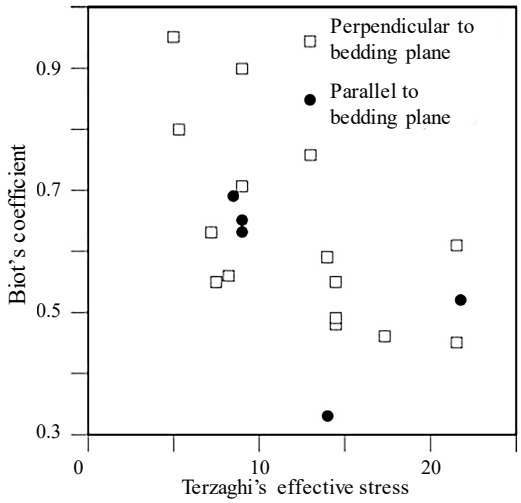

Figure 2.18: Measured Biot's coefficient for COx claystone as a function of stress level (Salager, 2008).

2.4 ON THERMAL BEHAVIOUR

2.4.1 Elastic response

Early attempts to describe the elastic behaviour of argillaceous rocks at elevated temperatures assumed that the elastic properties of these material are temperature independent. Menaceur et al., (2015) performed a series of triaxial tests have been conducted on COx claystone specimens along various thermo-hydro-mechanical paths in fully saturated and drained conditions by using the hollow cylinder device. All the values obtained at 25°C and 80°C are plotted together in Figure 2.19 that

clearly shows that there is no effect of temperature on the elastic properties determined here (Young's modulus E_1 and Poisson coefficient ν_{12}). Similar comparison has been drawn in Mohajerani et al., (2014) from isotropic compression tests, showing no effect of temperature (80°C) on the elastic compression parameters.

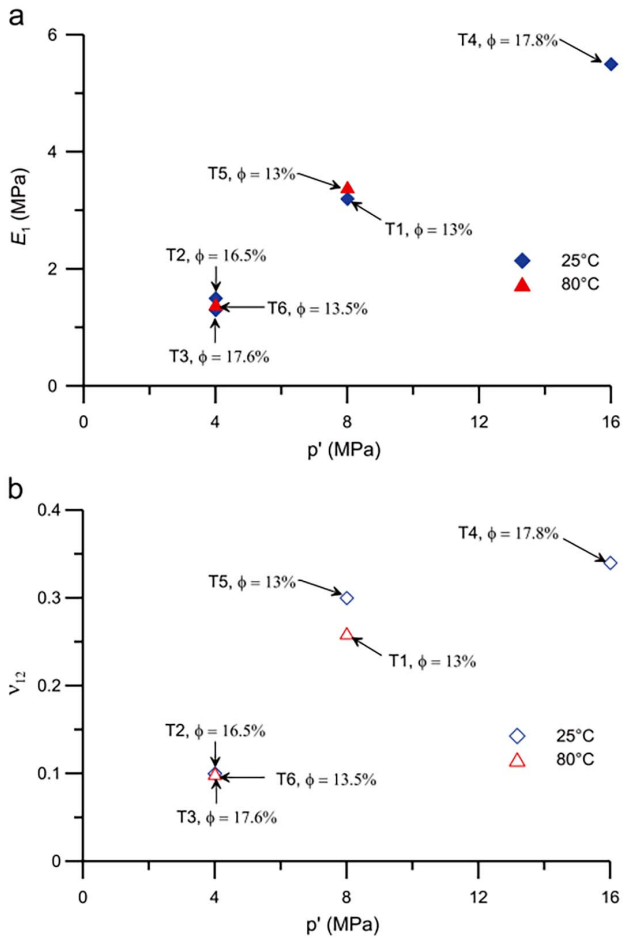

Figure 2.19: Elastic parameters, (a) Young's modulus, (b) Poisson coefficient (Menaceur et al., 2015).

Considering that lateral decompression tests (LD) correspond more closely to the stress paths in the surrounding rocks of an underground cavity during excavation than the conventional triaxial compression tests (CTC), Liu et al., (2019) were investigated elastic properties of the claystone by conducting unloading–reloading cycles during the LD tests under five different values of temperature from 20 to 90 °C which are the representative temperature range for the host claystone specified

in the French radioactive waste disposal project for the investigation of thermal effects. Four unloading–reloading cycles have been performed during the differential stress phase in each LD test. The four elastic moduli, such as defined in Eq. (1.2), are calculated from the stress–strain curves in each loading-reloading cycle.

$$M_{11} = \frac{\Delta\sigma_1}{\Delta\varepsilon_1},\ M_{31} = \frac{\Delta\sigma_3}{\Delta\varepsilon_1},\ M_{13} = \frac{\Delta\sigma_1}{\Delta\varepsilon_3},\ M_{33} = \frac{\Delta\sigma_3}{\Delta\varepsilon_3} \qquad (1.2)$$

The variations of these moduli as functions of the relative normalized axial strain are plotted in Figure 2.20a–d. From Figure 2.20a, the modulus M_{11} varies in the range of [3,6] GPa depending on the values of temperature and axial strain. It seems that the temperature has no significant effect on the values of the modulus M11 except that there is an important degradation at T = 90 ◦C . The values of the modulus M_{31} are presented in Figure 2.20b and evolve within the range of [− 3.3, − 1.5] GPa, which are about a half of the values of the corresponding modulus M_{11} (absolute values). The variation characteristics of M_{31} are practically the same as those of M_{11}. One can see that the two moduli related to the axial strain (M_{11} and M_{31}) show a significant degradation when the normalized axial strain is higher than 0.6. The thermal effect on these moduli becomes significant only when the temperature reaches 90 °C.

In Figure 2.20c, the values of the modulus M_{13} are given and included in the range of [− 17, − 10] GPa. For the two axial moduli related to the axial strain, the thermal effect is negligible except for the case of T = 90 ◦C for which an obvious degradation of the modulus is observed and amplified by the applied axial strain. As a difference with the modulus M_{11}, the modulus M_{13} exhibits a continuous decrease during nearly the whole loading process. The decrease is enhanced when the normalized axial strain is higher than 0.6. The values of the modulus M_{33} presented in Figure 2.20d vary within the range of [5, 7.5] GPa, which are also about a half of the values of the corresponding M_{13} (in absolute values). The variations of M_{33} with the axial strain are similar to those of M_{13}.

As a conclusion, the two moduli related to the lateral strain (M_{13} and M_{33}) exhibit an earlier and larger degradation (mechanical damage) induced by the shear

stress loading than the moduli related to the axial strain (M_{11} and M_{31}), but the thermal degradation effect is also evident only when the temperature reaches 90°C. The difference of mechanical damage rate between the axial and lateral directions suggests that the COx claystone can exhibit an induced anisotropy by mechanical loading.

The effect of temperature increase on the elastic properties of the COx claystone is not yet clearly demonstrated. Further tests are needed to verify the existence of a potential critical temperature from which there is a significant decrease of elastic modulus for the COx claystone.

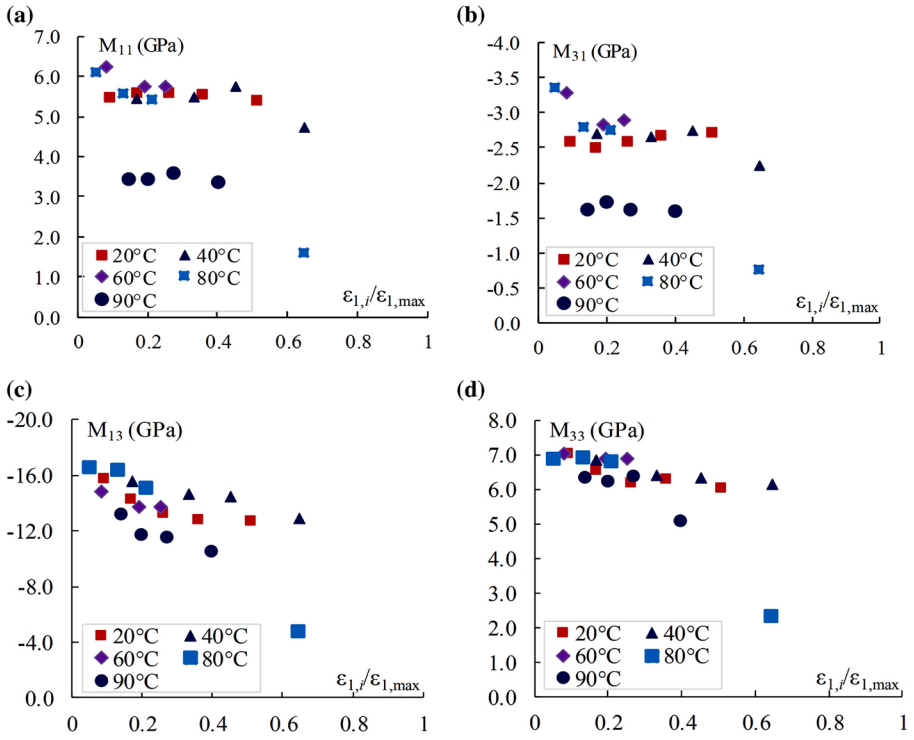

Figure 2.20: Unloading moduli variation during LD tests under different temperatures (Liu et al., 2019).

2.4.2 Volume change behaviour

Comprehensive experimental data on the thermal effects on volume change behaviour of argillaceous hard soils-weak rocks is scarce in the scientific literature (Campanella and Mitchell, 1968; Plum and Esrig, 1969; Habibagahi, 1976; Demars and Charles, 1982; Houston et al., 1985; Eriksson, 1989; Hueckel and

Borsetto, 1990; Towhata et al., 1993; Boudali et al., 1994; Tanaka, 1995; Crilly, 1996; Fox and Edil, 1996; Delage et al., 2000; Graham et al., 2001). Campanella and Mitchell (1968) performed a series of isotropic consolidation tests on a saturated remoulded illite at different temperatures using triaxial equipment. The experimental results revealed that the compressibility index was independent of temperature, but the preconsolidation pressure reduced with increasing temperature. The variation of the compressibility index with temperature was also investigated by Plum and Esrig (1969). They carried out one-dimensional consolidation tests on illite and Newfield clay and showed that the compressibility index of the material varied with temperature. This was in contrast with the observations of Campanella and Mitchell (1968). Nevertheless, the changes in the compressibility indices with temperature were insignificant at high stresses. Later, Eriksson (1989) and Boudali et al., (1994) repeated Plum and Esrig (1969) tests and showed that temperature had no effect on the compressibility indices. Similar results were also reported by Graham et al (2001) for isotropic consolidation. The decrease in the preconsolidation pressure by temperature, which was first observed by Campanella and Mitchell (1968), was further investigated and confirmed by Habibagahi (1973), Eriksson (1989), Boudali et al (1994), and Graham et al (2001). This effect causes the entire compression curve to move towards smaller effective stresses with increasing temperature. Some investigators have also shown that with an increasing temperature, the soil becomes more compressible in unloading-reloading regions (e.g. Eriksson, 1989; Tanaka, 1995). However, results to the contrary have been reported by Campanella and Mitchell (1968) and Crilly (1996).

The pioneering work of Hueckel and Borsetto (1990) on Boom Clay samples demonstrated that the volume changes of natural clays under constant isotropic effective stress depended on the overconsolidation ratio (OCR), independently of the applied stress. A thermo-plastic contraction is observed in normally consolidated clays and an elasto (expansion) plastic (contraction) response is observed in overconsolidated clays, depending on the OCR. This has been confirmed in Boom Clay by Sultan et al., (2002) as shown in Figure 2.21 that presents the results of drained thermal tests run on samples at various OCRs in which the temperature elevation was very slowly applied (1 ◦C/h) to ensure fully drained conditions. In the overconsolidated regime, Figure 2.21 also shows that the temperature of the expansion-contraction transition increases with the OCR as accounted for in the thermomechanical model of Cui et al., (2000).

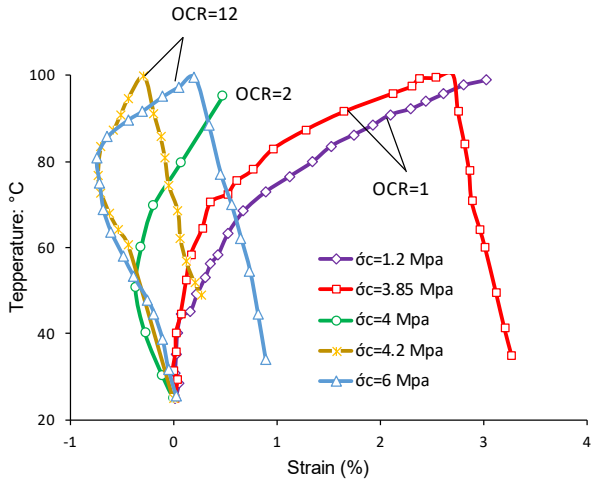

Figure 2.21: Thermoelastoplastic response of Boom Clay (modified after Sultan et al., 2002).

Whereas the thermoelastic expansion can be easily interpreted in terms of thermal dilation of the solid phase (see thermal dilation coefficients in Table 2.2), the plastic contraction is more difficult to interpret. It seems that the role of water adsorbed along the clay particles plays an important role. There would be two modes of separating the adsorbed water from the (plastic) clay particles along which they are bonded: either by compression and squeezing out (effect of preconsolidation) or by heating, given that in general temperature reduces the physico-chemical interactions between molecules (consider for instance the effects of temperature on the Brownian movement and the changes in properties of gases when submitted to temperature elevation)(Delage, 2013).

Table 2.2: Thermal expansion and compressibility coefficients of some typical minerals present in clays and claystones.

Mineral	Thermal expansion coefficient ($°C^{-1}$), α_s	Reference	Solid compressibility (GPa^{-1}), c_s	Reference
Clay	3.4×10^{-5}	McTigue (1986)	0.02	Skempton (1954); McTigue (1986)
Quartz	3.34×10^{-5}	Palciauskas and Domenico (1982)	0.0265	Bass (1995)
Calcite	1.38×10^{-5}	Fei (1995)	0.0136	Bass (1995)
Felspar	1.11×10^{-5}	Fei (1995)	0.0145	Bass (1995)
Water	27 × 10–5	Spang (2002)	0.447	Spang (2002)

The response of a specimen of Opalinus clay to a drained thermal cycle between 25°C and 80°C under in situ mean stress conditions is presented in Figure 2.22. The figure shows that the first temperature elevation phase is characterized by a linear thermo-elastic expansion that is typical of overconsolidated samples between 25°C and 65°C, followed by a plastic contraction between 65°C and the maximum temperature applied, i.e. 83°C. The subsequent cooling phase is characterized by a thermo-elastic contraction with a slope approximately parallel to that of the first heating phase, confirming the reversible nature of the response. The thermal irreversible contraction observed during the first heating phase is comparable to that observed in normally consolidated plastic clays (e.g. Baldi et al., 1988 and Delage et al., 2000). In fine grained soils, this phenomenon is understood as a thermal consolidation of the sample which corresponds to the rearrangement of the grains after a critical temperature.

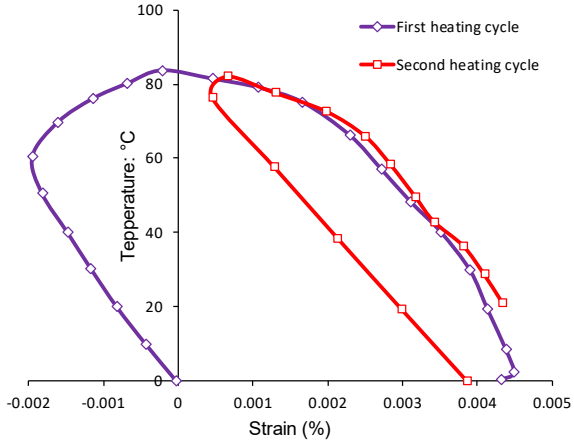

Figure 2.22: Drained thermal volume changes of Opalinus clay under in situ mean stress conditions (modified after Monfared et al., 2012).

It is interesting to relate this first temperature threshold to the maximum temperature previously experienced by the Opalinus clay. From geological arguments the maximum burial depth of the Opalinus clay at Mont Terri is 1350 m. Assuming a geothermal gradient of about 0.03 °C/m, the value of 65°C appears as a plausible maximum temperature experienced by the material before our test. The observed behaviour is typical of thermal hardening, with an elastic thermal expansion observed below the maximum supported temperature, followed by a plastic contraction at yielding once the maximum temperature is attained.

In the COx claystone, a contracting behaviour has been observed when heating the sample under in situ stress, comparable to the response of normally consolidated clays (Mohajerani et al., 2014). It seems that the claystone has kept the memory of its maximum supported temperature like overconsolidated soils conserve the memory of the maximum supported load. Thermal volumetric behaviour of COx claystone characterized by the strong post-sedimentation diagenetic bonds which has an important role as compared to plastic clays like Boom and Opalinus. Indeed, most numerical predictions of the behaviour of claystones around waste disposal systems consider a thermo-elastic response (Gens et al., 2007). Actually, this trend is not in agreement with the in-situ measurements of thermally induced pore pressure that appeared to be correctly modelled under a thermoelastic (dilating) hypothesis.

The contracting behaviour of the COx claystone by temperature, which was already evidenced by Mohajerani et al., (2014), was further investigated and confirmed by Menaceur et al., (2015). They were performed two drained heating tests to investigate the thermal volumetric response of the COx claystone. They confirmed the contracting behaviour already evidenced Mohajerani et al., (2014), but with smaller contraction coefficient. A possible reason of the significantly smaller contraction observed here could come from the differences in origin and in porosity between the specimens. More porous samples have larger clay content and clay content is the driving force of thermal contraction, given that the grains of quartz and calcite contained in the clay matrix simultaneously expand, probably resulting in some thermal damage at the interface between the grains and the clay matrix.

Later, Zhang et al., (2016) was determined thermal expansion behaviour of the claystones by heating and cooling the samples under different isostatic stresses and undrained conditions which was consistent with the in situ observations during heating experiments. Figure 2.23 shows the strain evolution measured on a COx claystone sample during a heating/cooling cycle under sequentially lowered confining stress. The sample with a high initial saturation degree was heated by stepwise increasing temperature from 23°C to 68°C and then cooled down to the ambient temperature. The data show that (a) each temperature increases generated expansion in all directions; (b) the expansion did not change much with time at each constant temperature below 47°C and then a gradual contraction reversely occurred at higher temperatures; and (c) cooling down yielded contraction and then was followed by a swelling process as shown in Figure 2.23.

The sedimentary clay rocks commonly exhibit thermal anisotropy with bedding structure. Figure 2.24 illustrates the thermal expansion anisotropy of an

Opalinus sample without confining load. The expansion coefficient of $\alpha_{\perp}$ =1.6×10^{-6}°C^{-1} measured in direction perpendicular to the bedding planes is about one order of magnitude higher than that of $\alpha_{\square}$ = 1.5×10^{-6}°C^{-1} parallel to the bedding planes. The thermal anisotropy observed may not be so significant when the claystone is subjected to confining stress such as the lithostatic stress in the rock mass, which hinders opening of microfissures lying in the bedding planes.

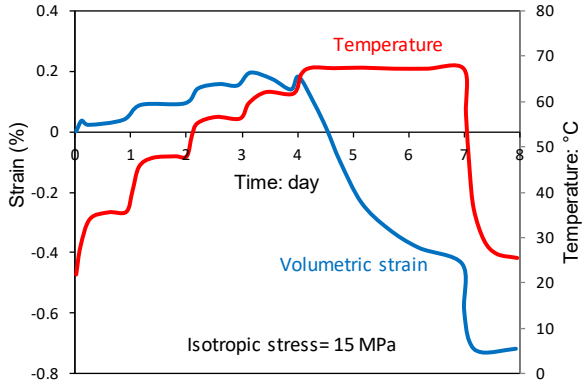

Figure 2.23: Thermal expansion and contraction of a COx claystone sample during heating and cooling under different isostatic stresses (modified after Zhang et al., 2016).

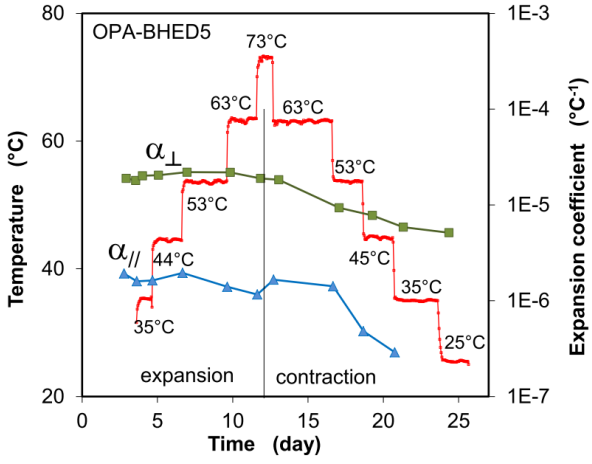

Figure 2.24: Anisotropy of thermal expansion of an Opalinus sample without confining load (Zhang et al., 2016).

2.4.3 Temperature influence on the strength

Effect of temperature on the preconsolidation pressure

The key thermal effects in argillaceous materials are those that lead to irreversible changes, particularly irreversible deformation. To address the irreversible strain in thermal conditions, the classical notion of the elasticity domain in the elasto-plastic context must be revised. The main new feature is the strong sensitivity of the plastic limit to temperature. However, other prominent thermomechanical characteristics of soils like a substantial thermoplastic contraction in normally and slightly overconsolidated soils, as opposed to the thermoelastic expansion of heavily overconsolidated these geomaterials need to be considered in this context. Several authors have studied the effect of temperature on the preconsolidation stress (e.g. Tidfors and Sällfors 1989; Eriksson, 1989; Belanteur et al., 1997; Bouladi et al. 1994; Akagi and Komiya, 1995; Sultan et al., 2002) (Figure 2.25). The results of these studies confirm a decrease in preconsolidation stress with the increase in temperature.

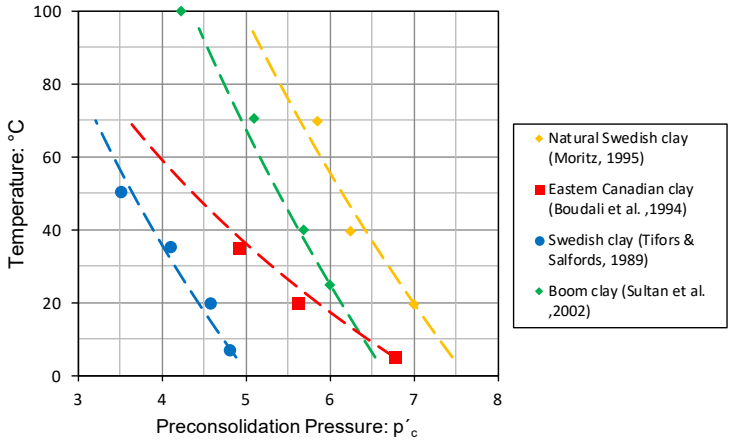

Figure 2.25: Decrease in the preconsolidation of Boom clay with temperature.

Effect of temperature on the compression index and swelling index

Campanella and Mitchell (1968) presented the first works on the effect of temperature on the compression index and swelling index of clays. They carried out isotropic compression tests on three illite samples at three different temperatures (24.7-37.7-51.4°C). Their results show that these indices are not affected by temperature, Figure 2.26. According to Cui et al., (2004) this conclusion seems correct when the stress level is relatively low (less than 1 MPa);

on the other hand, with stronger constraints, Sultan (1997) have shown that the compression index at different temperatures converges to a value when the total stress increases, which has also been shown by Tanaka (1995).

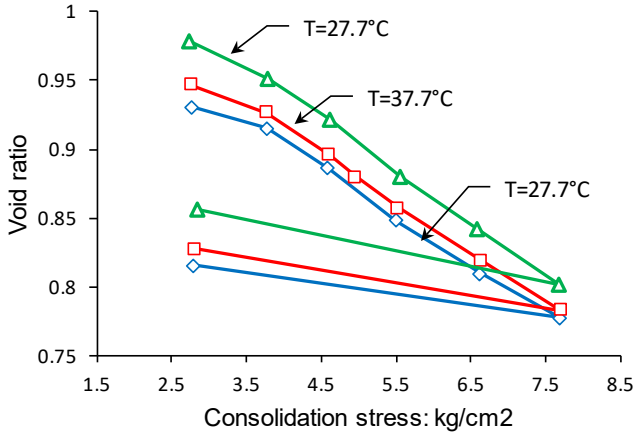

Figure 2.26: Isotropic compression of three samples of illites at three temperature levels, according to (Modified after Campanella and Mitchell, 1968)

Effect of temperature on shear strength

A conflicting report of temperature, causing strength increases or decreases were reported in literature. Hueckel et al. (2009) have concluded that there is no unique a priori answer to the question, at least in the temperature range 4°C<T<120°C. Nevertheless, it has also been shown that the strength dependency on temperature is material-specific and the evolution of both the yield and failure behaviour is critically dependent on the history of thermomechanical loading, in particular the stress and drainage state in which the heating is done, which was suggested earlier by Kuntiwattanakul et al. (1995) as well.

Experimental studies of the triaxial strength of argillaceous materials show that remoulded kaolin clay and natural Boom Clay exhibit temperature dependence of their internal friction, whereas this is not the case for largely smectitic or illitic clays (Hueckel and Borsetto, 1990; Hueckel and Baldi, 1991; Cekerevac and Laloui, 2004). Interestingly, the effects of the thermal variation of internal friction depend heavily on the history of heating and loading. In particular, the state of stress at which heating is performed, including the soil overconsolidation ratio, impacts on the ensuing variation of strength (Hueckel et al., 2009). Figure 2.24 shows the friction angle evolution with temperature for different argillaceous materials. For a

material such as kaolin, the effect of temperature is significant. Despax (1976) and Robinet et al. (1996) observed a significant decrease in the friction angle for kaolin while the results of Cekerevac and Laloui (2004) on this material show an increase in the friction angle.

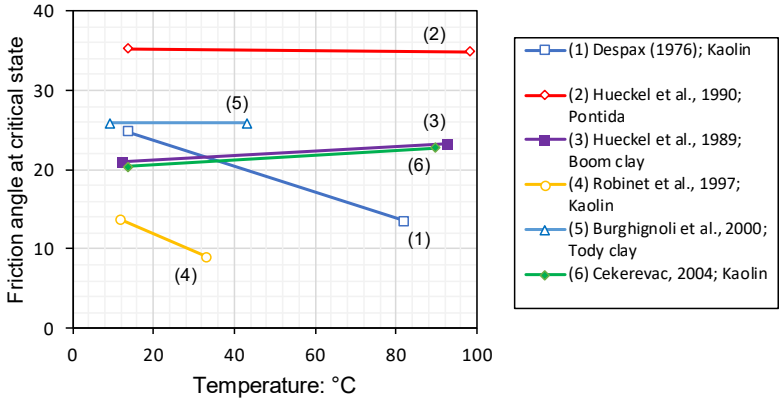

Figure 2.27: Effect of temperature on the friction angle of argillaceous materials.

In 1999, De Bruyn performed several series of CIU triaxial tests at different temperatures on Boom clay samples taken around the CERBERUS in situ experiment. Considering that these samples were submitted for the excavation of the Test Drift and for the drilling of the experiment itself, it is observed that heating to about 90°C has led to a significant loss (30%) of cohesion (in five years) and eventually lead to decrease in shear strength. This strength reduction was later confirmed by Hueckel et al. (2009) which is discussed above.

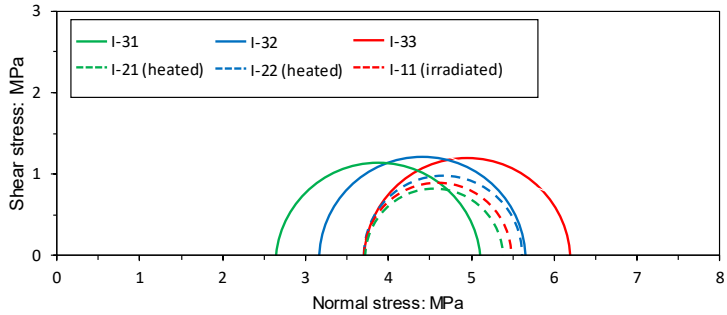

Figure 2.28: CIU tests on samples taken around CERBERUS in situ experiment (modified from Bruyn, 1999).

Undrained triaxial shearing tests under constant 3 MPa confining stress on Opalinus clay specimens with bedding planes inclined of 30–40° were run at various

temperatures from 20 to 115°C by Zhang et al. (2007). The specimens had an initial degree of saturation of 88%. They observed in such conditions a more ductile behaviour at elevated temperature with a clear decrease in strength due to temperature elevation. Figure 2.29 shows the undrained short-term compression behaviour of the saturated Opalinus clays at temperatures between 20°C and 116°C and at lateral stresses around 3MPa. The axial load was parallel to the bedding planes. It is obvious that the Opalinus clays became more plastic at the elevated temperatures. The weakness is probably caused by thermally-induced pore pressure increase and the corresponding decrease in effective confining stress on one hand and by thermally-induced reduction of the inherent cohesion and friction resistance of the bound pore water between solid particles on the other hand. Correspondingly, the effective confining stress must reduce down to zero. Therefore, the strengths obtained at high temperatures of 70°C-116°C are lower than that at 20°C, as compared in Figure 2.30 with the average strength envelope for the direction parallel to the bedding planes (Bock, 2001). The strength at 116°C is as low as the uniaxial strength at 20°C.

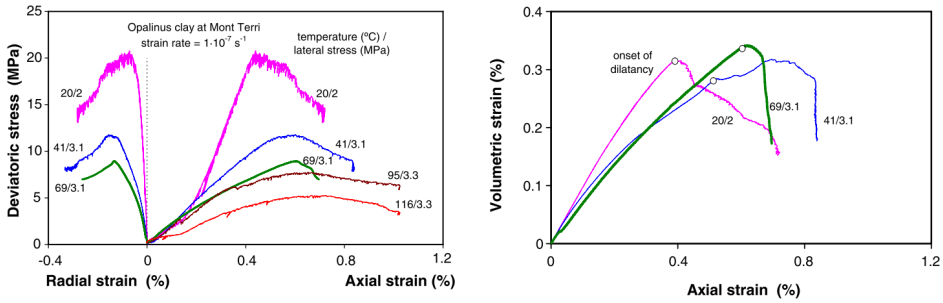

Figure 2.29: Compression behaviour of the Opalinus clay at elevated temperatures and under undrained conditions (Zhang et al. 2007a).

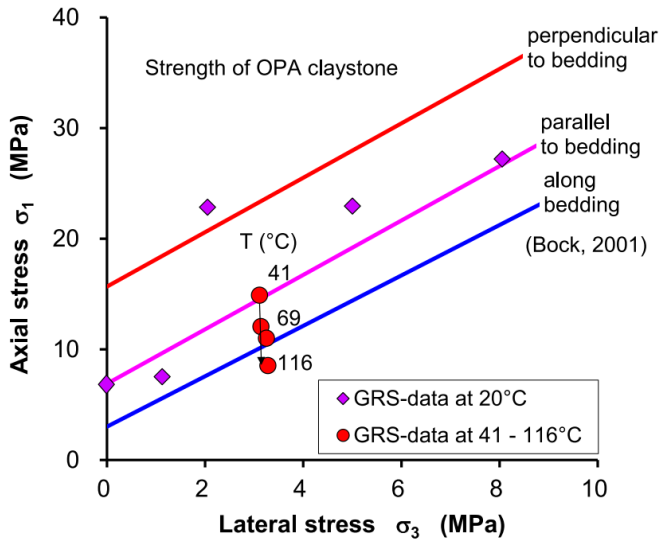

Figure 2.30: Comparison of the strengths obtained at high and ambient temperatures for the Opalinus clay (Zhang et al., 2017).

More recently, Zhang et al. (2014), conducted triaxial micro-compression tests on unsaturated triaxial specimens submitted to a relative humidity of around 74%. They observed little sensitivity with respect to temperature in the stress-strain curves obtained between 20°C and 95°C under a confining stress of 15 MPa (around twice the in-situ effective stress), whereas a decrease in peak stress (with small sensitivity in the elastic regime) was observed under a confining stress of 5 MPa (smaller than the in-situ stress).

Masri et al. (2014) conducted a series of what they called "pseudo-drained" triaxial shear tests on Tournemire claystone at temperatures between 20°C and 250°C under three confining pressures (5, 10 and 20 MPa). Their observations are comparable to that made by Zhang et al. (2007) on Opalinus clay, with significantly more ductile behaviour observed at elevated temperature and peak stress decreasing from 90 MPa at 20°C down to 40 MPa at 250°C.

While substantial progress has been made in understanding the principal effects of elevated temperature in Boom clay and Opalinus clay, the failure conditions of COx claystone at elevated temperatures remain less well understood. In fact, there is a somewhat confusing view of the experimental evidence concerning the thermal dependence of shear strength in COx claystone.

Bauer et al. (1997) and later Andra (2005) were reported that the temperature influence on the strength of the COx claystone is not so significant in undrained

condition. Moreover, in contrast to the undrained thermal tests heating a claystone in drained condition, increasing the inner friction resistance between solid particles against shearing and hence strengthening the rock. As shown in Figure 2.31 strength envelopes at different temperatures are close to each other, indicating an insignificant influence of temperature on the strength. Nevertheless, the strength reached by the drained heating tests at T = 90ºC-150 ºC (upper part in Figure 2.31) are much higher than the undrained thermal strength.

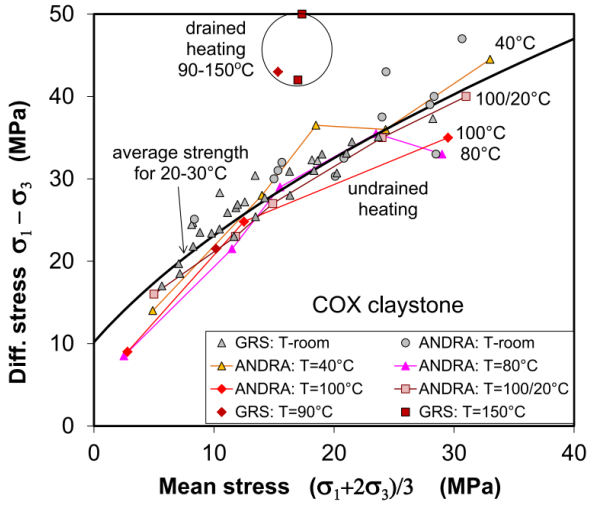

Figure 2.31: Comparison of drained and undrained thermal strengths of the COx claystone (Zhang, 2018).

Previous works indicate that there is a *suspicion* of shear strength change in COx claystone with elevated temperature representing a contrast behaviour with the Boom clay and Opalinus clay strength evolution with temperature.

However, due to obvious experimental difficulties, these results are based on tests that have not been conducted under fully saturated and drained conditions. In this regard, and to overcome this shortcoming, Menaceur et al. (2015) were performed two drained heating tests under fully saturated conditions with well adapted devices and procedures. The preliminary results evidenced a more ductile response and slightly smaller shear strengths of the COx claystone at elevated temperature, in agreement with the available published data on argillaceous material like the Boom clay and Opalinus clay.

Figure 2.32 shows the values of peak strength as a function of effective mean stress for all of the tests carried out here, together with the data obtained in Hu et al. (2014) at 25°C under fully saturated conditions. All tests at 25°C are aligned along

parallel lines that define a friction angle of 21° equal to that proposed in Hu et al. (2014). As shown in the figure there is a decrease in cohesion that makes the more porous specimen weaker with the cohesion of 1.94 MPa at 17% compared to 4.2 MPa at 13%. The two points obtained at a porosity of 13% at a temperature of 80°C are located slightly below the points at the same porosity and 25°C, indicating a slight reduction in shear strength due to temperature. The slight difference observed is actually in the range of the dispersion observed when testing COx specimens.

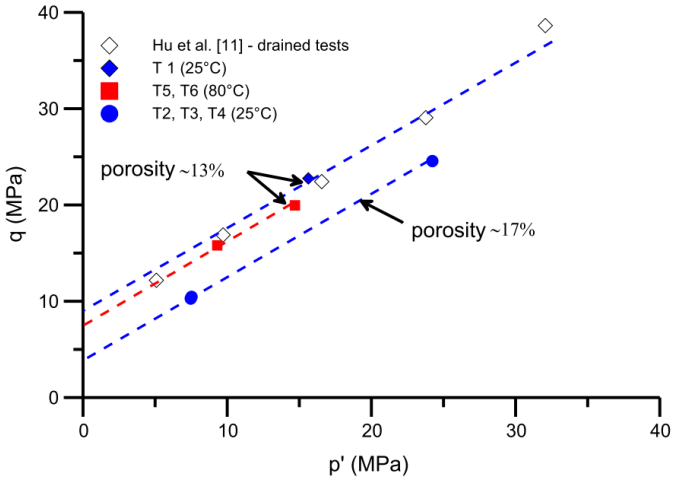

Figure 2.32: Shear strength of all tests carried out in the plan q–p' (Menaceur et al., 2015).

The decrease in the COx claystone strength by temperature, which was first observed by Menaceur et al. (2015), was further investigated and confirmed by Liu et al. (2019). They were designed and performed a series of lateral decompression (LD) tests, based on a theoretical analysis of stress evolution in surrounding rocks of an underground cavity during excavation, to investigate the thermomechanical behaviour of the COx claystone. A number of unloading–reloading cycles were included in each LD test. Furthermore, to evaluate the effect of temperature on mechanical strength and elastic properties of the COx claystone, the LD tests are performed under five different values of temperature from 20 to 90°C. The shear strength as well as failure pattern in the LD tests were analysed. The COx claystone showed a shear failure in the LD tests, and the failure was characterized by the creation of a localized macro-crack and of a damaged zone with many micro-cracks around the macro-crack.

The temperature increase induced a degradation of the shear strength of the COx claystone. An obvious mechanical damage of elastic properties was observed

in the COx claystone during the shear stress loading in the LD tests. This damage was more important in the lateral direction than the axial one, leading to an induced anisotropy of the material. As shown in Figure 2.33, with the increase of temperature, the irreversible strain during the nonlinear phase before the peak stress is significantly enhanced. Therefore, it seems that the temperature increase induces a more ductile behaviour in the COx claystone.

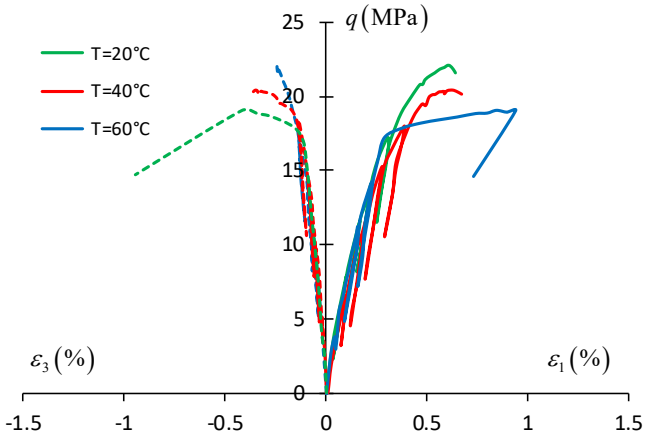

Figure 2.33: Experimental results of LD test under T = 20, 40 and 60°C (modified after Liu et al., 2019).

Moreover, the values of differential stress, radial stress, and axial and lateral strain at the peak state are calculated and presented in Figure 2.34 for the LD tests under the different values of temperature. It is observed that the peak differential stress decreases with the increase of temperature.

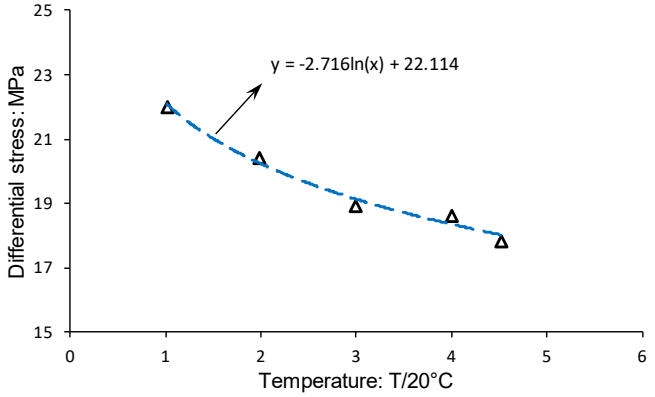

Figure 2.34: Thermal effect on peak stress in LD tests: Differential stresses at peak strength (modified after Liu et al., 2019).

2.4.4 Thermal pressurization

In argillaceous rocks, the main hydraulic phenomenon associated with thermal effects is the generation of pore pressure due to changes of temperature. When argillaceous rocks are subjected to a temperature increase, the pore pressure will also increase due to the fact that the thermal expansion of the water is larger than that of the porous skeleton itself. However, the low permeability of argillaceous rocks ensures that the resulting excess pore pressure does not dissipate rapidly. By looking at Table 2.2, it can be observed that the water expansion coefficient is almost one order of magnitude higher than that of the minerals, and that the coefficient of quartz and clay are comparable and larger than that of calcite or feldspar. Given that the structure of claystones is generally characterized by a clay matrix containing grains (of quartz, calcite and feldspar), one can suspect some significant differential expansions in the solid phase at clay-calcite interfaces (the most frequent) and also at clay- feldspar interfaces. Ghabezloo and Sulem (2010) gathered some values of the thermal pressurization coefficient ($\Lambda = \Delta p / \Delta t$; MPa/ºC) measured in various soils and rocks and presented in Table 2.3. The table has been completed by their own values on the Rothbach sandstone, by a value on Boom Clay recently obtained by Lima et al. (2010) and by a value on the Opalinus claystone deduced from the data of Muñoz et al. (2009).

Table 2.3: Thermal expansion coefficients of various soils and rocks.

Mineral	Thermal expansion coefficient (MPa/ºC $^{-1}$)	Reference
Clay	0.01	Campanella and Mitchell (1968)
Boom Clay	0.06	Vardoulakis (2002)
	0.019	Lima et al. (2010)
Opalinus claystone	0.1	Muñoz et al. (2009)
Sandstone	0.05	Campanella and Mitchell (1968)
Kayenta sandstone	0.59	Palciauskas and Domenico (1982)
Rothbach sandstone	From 0.25 to 0.025	Ghabezloo and Sulem (2010)
Clayey fault gouge	0.1	Sulem et al. (2004, 2007)
Intact rock at great depth	1.5	Lachenbruch (1980)
Mature fault at 7000 m depth	Intact fault wall: 0.92; Damaged fault wall: 0.31	Rice (2006)

Some large values have been obtained in rocks, but the values in clays are between 0.01 MPa/ºC and 0.1 MPa/ºC. Quite different values are given for clays, in

particular in Boom Clay, comparing the data of Vardoulakis (2002) that were obtained from experimental data of Sultan (1997) and of Lima et al. (2010).

Later Delage (2013) showed that the thermally induced pore pressure did not depend only on the mineral composition and porosity of the rock, but on the stress state, the range of temperature variation and the previously induced damage. The pressure dependency of the compressibility of both rock and water and the temperature dependency of the pore water compressibility appeared to play an important role, as shown by Ghabezloo and Sulem (2010) who provided values between 0.25 MPa/°C and 0.025 MPa/°C at temperatures between 20°C and 70°C for the Rothbach sandstone.

Figure 2.35 shows the thermally induced excess pore water pressures observed on COx during heating and cooling in a temperature range of 30°C - 120°C. The slightly desaturated samples were firstly resaturated at the temperature of 30°C for about 10d. The subsequent undrained load generated high pore pressures of 11-12 MPa at sample. The following undrained heating from 30°C to 60°C resulted in a large increase in pore pressure from 1 MPa to 12 MPa at COx sample. The thermally induced excess pore water pressures remained over time, except for P_{out} at COx sample. However, as unexpected, further heating up to 80°C, 100°C and 120°C did not produce higher pore pressures. This might result from the possible escape of the thermally mobilized pore water through the insolation boundary, which might not resist such high temperatures. The release of the pore water and the resulting dissipation of the pore pressure led to gradual compaction of the porous medium.

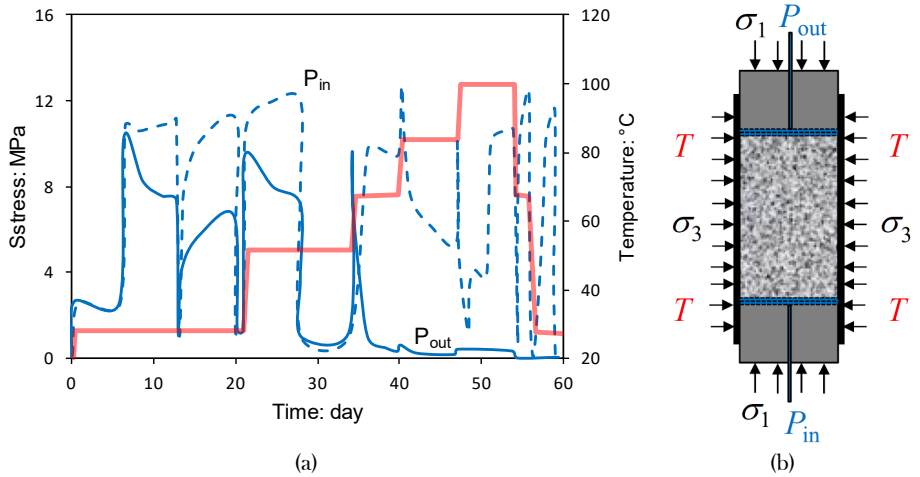

Figure 2.35: (a) Thermally induced excess pore water pressures of COx claystone (b) THM load conditions of thermal experiments on normal-sized samples. σ_1 is external axial stress; σ_3 is external radial stress; P_{in} is water back pressure at inlet; P_{out} is water back-pressure at outlet. (modified after Zhang et al., 2017).

The data shown in Figure 2.36 show the response in pore pressure obtained in a COx sample along a ramp of stepwise progressive temperature elevation between 25°C and 70°C. Compared with thermal response of dummy metal sample, the first peak of temperature corresponds to the instantaneous response of the water contained in the permeable porous elements in COx sample. Afterwards some time has to be waited to get equilibrium between the pore water and that present in the porous elements, leading to the drainage of pore water from the specimen to the porous elements.

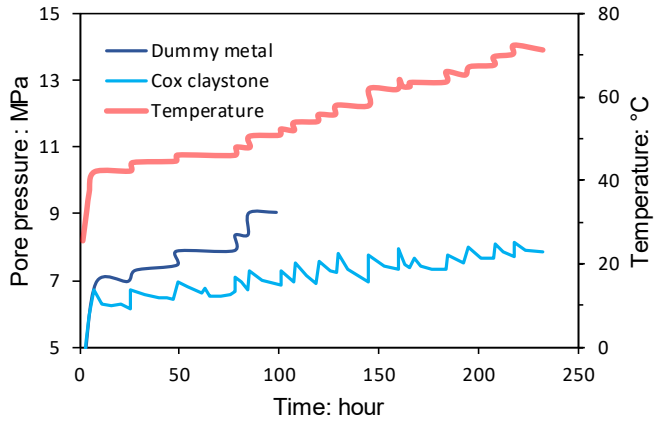

Figure 2.36: Comparison between thermally induced excess pore water pressures with a COx claystone and a dummy metal sample (Modified after Mohajerani et al., 2012).

2.4.5 Effect of temperature on permeability

The effect of temperature on the permeability of argillaceous materials has been studied by different authors. Among others, Habibagahi (1976) studied this effect on a mixture of illite (70%) and chlorite (20%). He showed that the hydraulic conductivity of material increases with temperature, Figure 2.37a. This increase in hydraulic conductivity can be explained by the decrease in the viscosity of water with temperature. If we reinterpret Habibagahi's data in terms of intrinsic permeability and void index (Figure 2.37b) we observe that permeability is almost insensitive to temperature change. The same trend is observed by Morin and Silva (1984), Towhata et al. (1993), Khemissa (1998) on different clays.

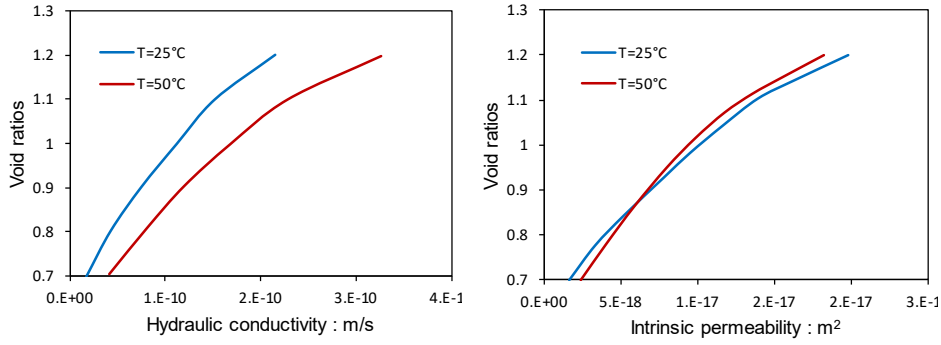

Figure 2.37: Effect of temperature on the permeability of an illite clay chlorite mixture (a) Hydraulic conductivity (b) Intrinsic permeability (modified from Habibagahi 1976).

Later in 2000, Delage studied the effect of temperature on the permeability of Boom clay (Delage et al., 2000). They found a linear relationship between porosity and permeability which is independent of temperature, as shown in Figure 2.38.

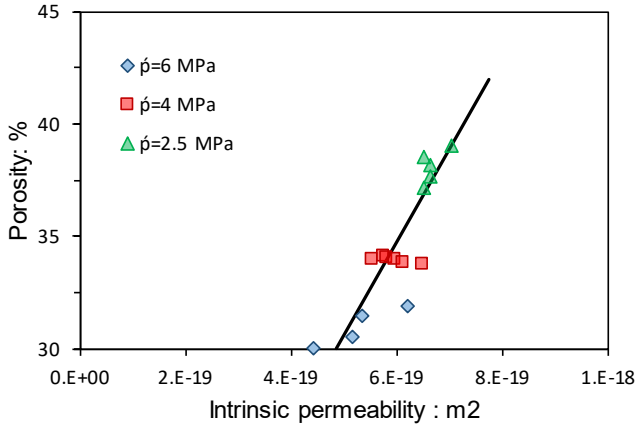

Figure 2.38: Insensitivity of the permeability-porosity relationship of Boom clay with temperature (modified after Delage et al., 2000).

Recently Menaceur et al. (2015) were performed steady-state radial permeability tests on the COx claystone. They have reported that the permeability is not totally independent of temperature, unlike what was previously observed on the Boom clay (Delage et al., 2000), with here a slight increase with temperature. Note that these tests also showed an enhancement of swelling with temperature, with around twice more swelling at 80°C compared to 25°C under the same stress conditions.

2.4.6 Self-sealing and temperature effects

Thermal impact on the self-sealing capacity of damaged claystone is one of the most concerns in the assessment of the long- term safety of HLW repositories. This was examined by measuring water permeability of fractured claystones in various thermal conditions.

Thermal effects on the self-sealing behaviour of argillaceous materials have been investigated within the TIMODAZ project (Yu et al., 2014). Within the framework of this project Monfared et al. (2012) performed series of hollow cylinder triaxial tests to investigate the effect of the temperature increase on the hydro-mechanical properties of sheared Boom clay samples. One of the main interests of the hollow cylinder test is that it allows performing permeability tests that do account for the shear plane network affecting a sheared sample. The system was then applied to the investigation of the combined effects of shear discontinuities and temperature on the permeability of a Boom Clay specimen. They observed excellent self-sealing properties of the Boom Clay, faster diffusion at elevated temperature and a very minor impact of temperature on intrinsic permeability.

Figure 2.39 shows pore pressure dissipation obtained in various conditions (after sample resaturation under in situ stress conditions, after shearing, after heating the sheared sample and after cooling). The slower diffusion observed after shearing compared to the initial state confirms the excellent self-sealing properties of the Boom Clay as shown in Figure 2.39. However, they have reported slight decrease in intrinsic permeability which is due to a decrease in porosity that results from the increase in mean effective pressure occurring during shearing. The faster diffusion observed at elevated temperature (Figure 2.39) in the sheared sample is due to the decrease in viscosity of water with temperature. Indeed, the permeability values obtained from the experiment, show that the intrinsic permeability is not significantly affected.

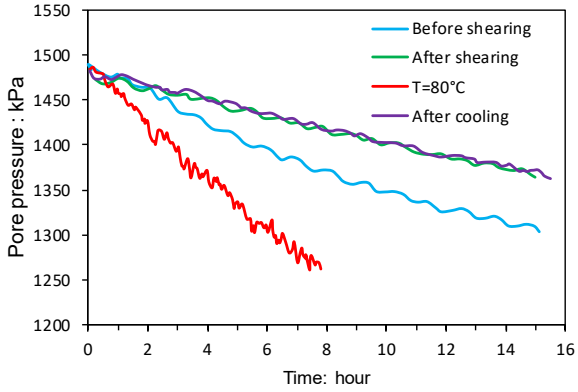

Figure 2.39: Experimental data and model results for pore pressure dissipation, external wall transducer (modified after Monfared et al., 2012).

These data, along with other data obtained in the Opalinus clay (conducted by Monfared et al., 2012), show that the self-sealing properties of both the Boom Clay and the Opalinus clay are not affected by temperature elevation. This important result obtained within the TIMODAZ project is quite important in terms of performance assessment (Yu et al., 2014).

Thermal impact on the sealing of fractures was also investigated by heating cracked COx and Opalinus samples under constant confining stress and water injection pressure by Zhang (2011). A test was performed on an axially-cracked COx claystone sample under an axial stress of 2.5 MPa and a radial stress of 2.0 MPa. The synthetic water was introduced into the fractured sample at inlet pressure of 0.5 MPa while the outlet was kept atmospheric. The sample was heated stepwise from 27°C to 40, 60, 75, 90°C and then cooled down to 60°C and 30°C, whereby radial strain normal to the fracture planes and water permeability in axial direction parallel to the fractures were measured. Figure 2.40 shows the evolution of the normal strain and the water permeability. Each rapid temperature rise caused a fast expansion of the fractured sample. After a short-term compaction and water injection at 27°C, the fractured sample expanded gradually with time but the intrinsic permeability decreased due to the effect of swelling and slaking of clay matrix between fractures as mentioned before. At elevated temperature of 40°C, the dilation continued while the permeability increased slightly. Over 60°C, the swelling disappeared and the permeability varied slightly. In contrast to the heating effects, cooling down to 60°C and 30°C led to a compaction of the fractures and a drop-in permeability down.

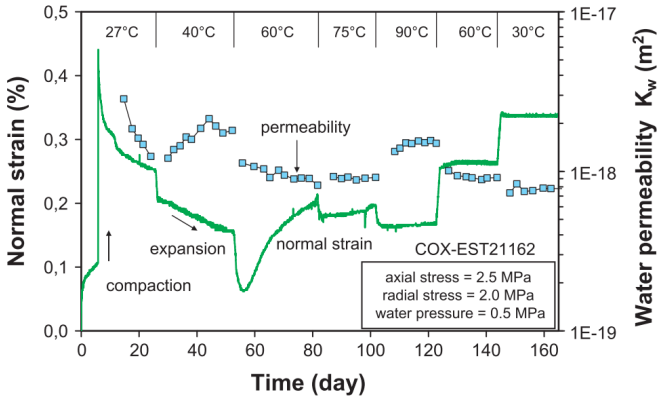

Figure 2.40: Evolution of normal strain and permeability parallel to fractures during water flowing under different temperatures (Zhang 2011).

Long-term measurements of water permeability were performed on cracked COx and Opalinus samples at temperatures between 20°C and 90°C.

The synthetic water was injected into the fractured. The results are summarized in Figure 2.41. Again, the water-induced effect on the hydraulic sealing of fractures is evident during the first stage at 20°C. The permeability decreased at Opalinus and COx sample. Subsequently, the rates of permeability reduction, however, are less affected by the temperature increase up to 60°C. Further heating up to 90°C and cooling down to 60°C had no effect on the permeability which had been obtained. The second cooling-down phase to 20°C, however, induced a slight decrease in permeability for the Opalinus and COx samples.

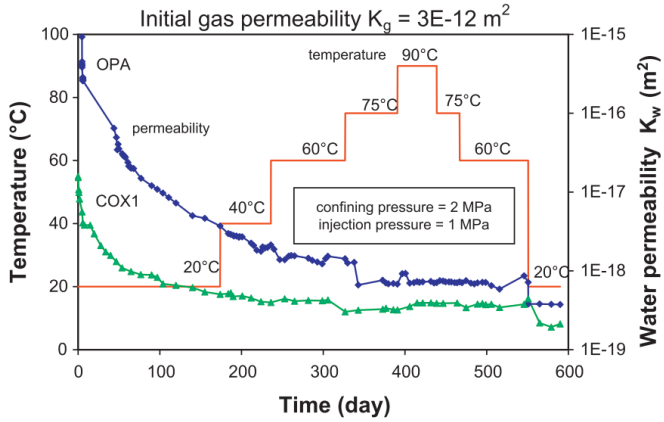

Figure 2.41: Long-term measurements of water permeability on fractured COx and Opalinus samples at different temperatures (Zhang 2011).

Figure 2.42 depicts the last data of water permeability within each phase as function of applied temperature. It is obvious that the water permeability of the fractured claystones decreases more or less with increasing temperature and drops down further after cooling. So, an important conclusion can be drawn: thermal loading up to the maximum temperature of 90°C designed for repositories in clay rocks has no negative effects on the sealing process of fractures in the EDZ. However, because the hydraulic conductivity depends both on the structure of fractures and pores in the material and the thermally induced changes in viscosity and density of the pore water, the relatively constant intrinsic permeability suggests an enhanced hydraulic conductivity during heating due to the decrease of water viscosity.

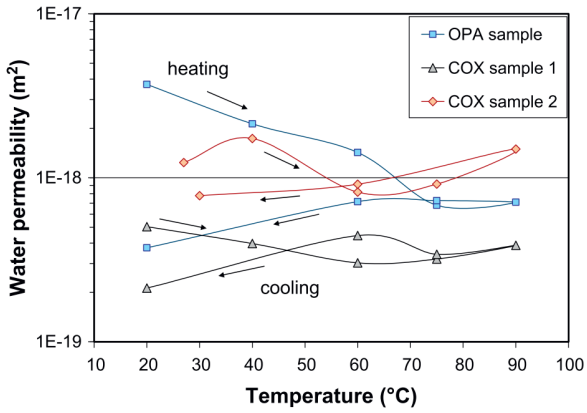

Figure 2.42: Dependency of water permeability of fractured claystone on temperature (Zhang 2011).

Various laboratory sealing experiments were carried out on strongly cracked samples of different sizes and shapes from the Callovo-Oxfordian claystone and the Opalinus clay under relevant repository conditions. The sealing behaviour of the fractures was detected by deformation, permeability, and wave velocity measurements, and are summarised as follows, based on the experimental work cited above.

a) The fracture aperture decreases exponentially with increasing normal confining stress.

b) Wetting by water flow through fractures induces swelling and slaking of the clay matrix, filling and clogging of the interstices, and a drastic decrease in permeability.

c) Heating from 20°C to 90°C has no remarkable impact on the water permeability of fractures, while cooling down again decreases the permeability slightly.

d) The thermally induced changes in hydraulic conductivity are mainly attributed to the variations of water viscosity and density.

e) Under the applied THM conditions, the intrinsic permeability of the fractured claystones decreases significantly to the very low levels, which corresponds to intact claystone.

2.4.7 Long-term deformation at high temperatures

Long-term deformation of a clay host rock is of high importance for assessment of the safety of a repository with regard to the support of the openings, compaction of the EDZ as well as the backfill/seal, and progressive closure of the repository to permanent isolation of the waste in the host rock. This important issue has been intensively investigated on the COx and Opalinus claystones during the last decade. Both claystones exhibit creep capability or time-dependent deformability under various THM conditions (Gasc-Barbier et al., 2004; Zhang and Rothfuchs 2004; Zhang et al. 2007; Gräsle 2009; Zhang 2015).

The long-term deformation of the claystones is influenced by temperature, which was observed in creep tests under various thermal loads to high temperatures up to 90°C-110°C (Zhang et al. 2017). Indeed, larger creep strains appear at elevated temperature (Belmokhtar et al. 2017a).

As a typical example, Figure 2.43 shows two creep tests on COx samples during a heating/cooling cycle in the temperature range of 28°C-110°C and 30°C-60°C and under stresses of σ_1/σ_3 =15 MPa/0.5 MPa and 15 MPa/3 MPa, respectively. The samples were highly saturated with water in degrees of 94%-99%. The strain-time curves obtained on each sample show that:

a) each temperature increase led to a radial expansion shortly but a slight compression in axial direction.

b) the axial, radial, and volumetric strains increased quite linearly with time at each elevated temperature below 90°C, suggesting no or less thermal transient creep.

c) at higher temperatures above 90°C, the creep slowed down.

d) cooling down resulted in a radial contraction shortly but negligible axial strain, and almost no further creep continued at the lowered temperatures.

The acceleration of creep at temperatures up to 90°C is probably contributed by the reduction of viscosity and friction resistance of bound water-films between solid particles.

At higher temperatures above 90°C, the undrained conditions could not sustain, allowing the thermally mobilized pore water release to an amount of □ 2% after testing. As a consequence, the pore structure was consolidated, increasing the friction resistance between particles and hence decelerating the creep at the high temperatures.

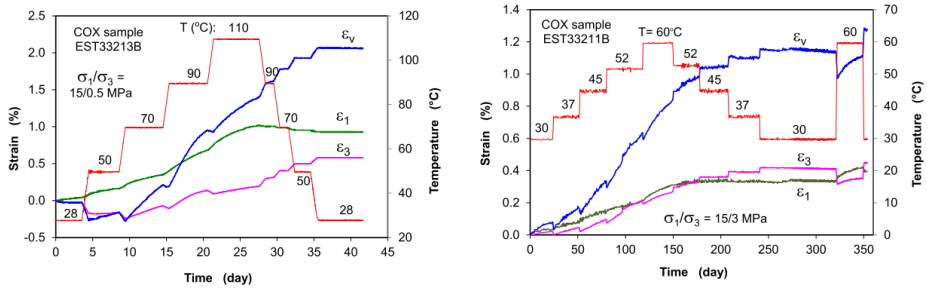

(a) (b)

Figure 2.43: Creep of COx samples during heating/cooling cycle at different temperatures (Zhang et al. 2017).

The creep rates obtained for the Opalinus claystone are relatively higher due to the high content of clay minerals, compared to those of the COx claystone. As mentioned earlier, the creep under low stresses of $\Delta\sigma < 10$ MPa varies almost linearly with stress, which is probably controlled by diffusion in bound water-films between solid particles. Beyond that the creep is additionally contributed by microcracking (Figure 2.44).

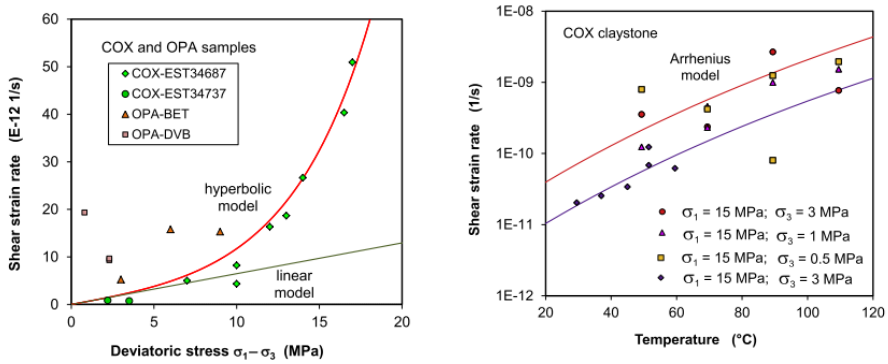

(a) (b)

Figure 2.44: Stationary shear creep rate of the water-saturated COx claystone as function of deviatoric stress (a) and temperature (b) (Zhang et al. 2017).

An observed time dependent anisotropic compaction under two different temperatures 25°C and 80°C is shown in Figure 2.45. The figure shows a volumetric creep response under constant isotropic stress, with axial creep strain larger than radial one. Larger creep strains appear at elevated temperature as shown in Figure 2.45. However, at times larger than 10 days creep rates do not differ too much, with an axial strain rate of $4.8\times10^{-10}s^{-1}$ at 25°C compared to $3.5\times10^{-10}s^{-1}$ at 80°C and a radial one of $1.5\times10^{-10}s^{-1}$ at 25°C compared to $0.9\times10^{-10}s^{-1}$ at 80°C.

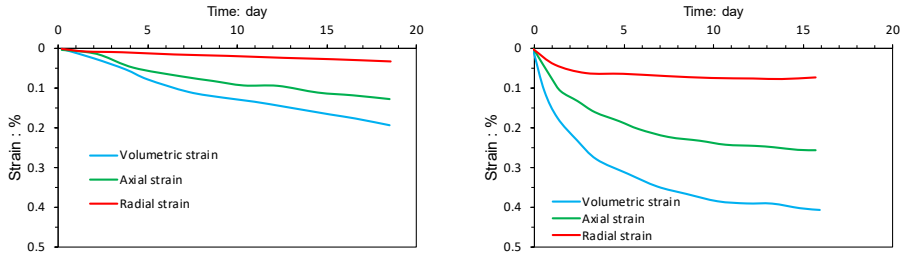

(a) (b)

Figure 2.45: Creep strains: (a) 25°C, (b) 80°C (modified after Belmokhtar et al. 2017).

2.5 IN-SITU THM CHARACTERISATION

In this section some key features of the response of argillaceous materials to in-situ heating test in three underground laboratories are reviewed. The aim in this section is to use the observations obtained in in-situ heating tests to enhance our understanding of the THM behaviour of argillaceous geomaterials under field conditions. Considering the fact that these materials provide the geological background to many civil engineering projects, interest in these types of material

has increased, because they are being considered as potential host geological media for underground repositories of high-level radioactive waste, in recent years (Gens, 2003). As discussed above, they exhibit favourable characteristics, such as low permeability, a degree of self-healing capacity when fractured, significant retardation properties for solute transport, and no foreseeable economic value.

Another significant issue is heat-emitting nature of High-level radioactive waste. Therefore, the use of Argillaceous materials in this type of application brings to the fore the thermal response of this type of material and, especially, the interaction of thermal phenomena with hydraulic and mechanical behaviour. The possible use of these types of clay as geological hosts for radioactive waste has prompted the construction of several underground laboratories. They include: the Hades laboratory in Mol (Belgium), excavated in Boom clay; and the Mont Terri laboratory of northern Switzerland, constructed in Opalinus clay and the Meuse/Haute Marne laboratory of Eastern France, sited in a thick stratum of Callovo-Oxfordian claystone. Underground laboratories allow, by the performance of appropriate in situ tests, observation of the clay response in complex situations that mimic some of the conditions likely to be encountered in a deep geological repository. To assess the hydro-mechanical effects of the thermal transient on the host clay in a deep repository, various in situ heating tests have been performed at several underground laboratories (Gens et al., 2007).

The CACTUS, ATLAS, and CERBERUS tests (Picard et al., 1994; Bernier and Neerdael, 1996; De Bruyn and Labat, 2002; François et al., 2009) were performed in the Boom clay at the HADES underground research facility in Mol, Belgium. The HE-B, HE-D and HE-E tests were carried out in the Mont Terri laboratory in Northern Switzerland, which was constructed in Opalinus clay (Gens et al., 2007). The TER and TED heating test is was carried out in Bure at the Meuse/Haute Marne laboratory located in Eastern France (Gens et al., 2011; Conil and Armand 2012), which was constructed in the Callovo-Oxfordian mudstone. Finally, HA-ALC1604 in situ heating test which is currently under way in Bure at the Meuse/Haute Marne laboratory which is constructed in the Callovo-Oxfordian claystone. Observations, interpretation and THM modelling of this test will be given in the later chapters. This section concentrates on the response of Boom clay, Opalinus clay and Callovo-Oxfordian claystone, to thermal loading in the context of the insitu heating tests performed in the different underground laboratory stated above.

2.5.1 HADES underground research facility

General

The HADES underground research facility is located in Mol, Belgium (Bastiaens and Bernier, 2006). It consists of two access shafts and a main gallery with some secondary drifts and shafts (Figure 2.46). The main gallery has a length of about 200m with an average internal diameter of 4 and is situated at a depth of 223 m. The laboratory has been excavated in Boom clay, a Tertiary plastic clay of modest cementation and relatively low strength. At the underground facility location, the Boom clay lies between 190 m and 290 m below the surface. The Boom clay layer is nearly horizontal, dipping about 1-2% towards the north-east. It is bound on the upper and lower part by pervious materials. A regional geological profile is sketched in Figure 2.47.

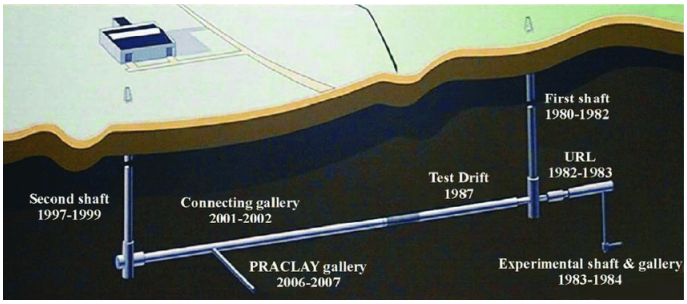

Figure 2.46: Layout of the HADES underground research facility (Gens, 2013).

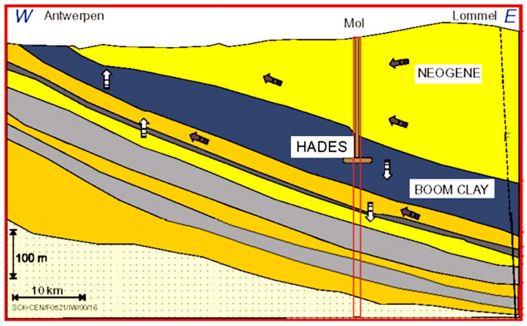

Figure 2.47: Geological profile showing the location of the HADES laboratory (very distorted scales) (Gens, 2013).

Response to underground excavation

The response of Boom clay to deep excavation has been explicitly studied in the CLIPEX experiment (Li et al. 2006). It involved the close observation of the excavation of the 85m-long 4.8m diameter connecting gallery using a comprehensive monitoring system installed prior to the start of the excavation. Open face excavation was adopted using a road header protected by a 2.3 m-long shield. The shield was equipped with a cutting head to achieve a smooth excavation profile. Lining was provided by 40-cm thick unreinforced concrete segments. Excavation rate was of the order of 3 m/day. At the excavation level, vertical stress is 4.5 MPa and the pore water pressure undisturbed by excavation is 2.2 MPa. A value of K_o=0.9 is usually accepted, consistent with the best estimate of overconsolidation ratio of about 2.4 (Horseman et al., 1987). In this case, therefore, initial stress anisotropy is unlikely to be large. Perhaps the most interesting observations involved the measurements of pore water pressure that exhibited a very characteristic behaviour (Figure 2.48). Pore pressure increases as the excavation approaches due to the transfer of stress to the ground away from the excavation. At some point, pore pressure drops due to excavation unloading becoming even negative (suction). Pore pressure finally goes to atmospheric when connection is established with the already excavated area. It was also noteworthy that effects of excavation on displacements and pore pressures were felt at very large distances, of the order of 60 m, i.e. more than 12 diameters.

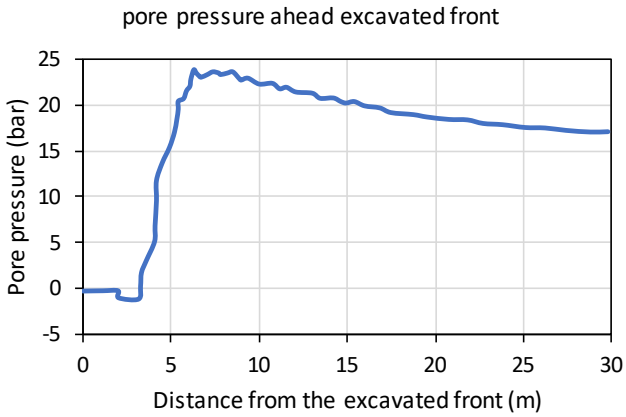

Figure 2.48: Evolution of pore pressure as a function of the distance to the excavation front (Bernier et al., 2007).

Development of fractures was observed during the excavation. Excavation disturbance is generally reflected in an increase of permeability. This is illustrated

in Figure 2.49 that shows the measured values of permeability against distance to the tunnel wall in two different directions. It can be observed that the increased permeability extends about one diameter. The effect is certainly larger in the vertical direction. Measurements were made one year apart but little change in permeability was recorded. A modest permeability anisotropy is also observed, permeability along bedding is, as expected, the larger one.

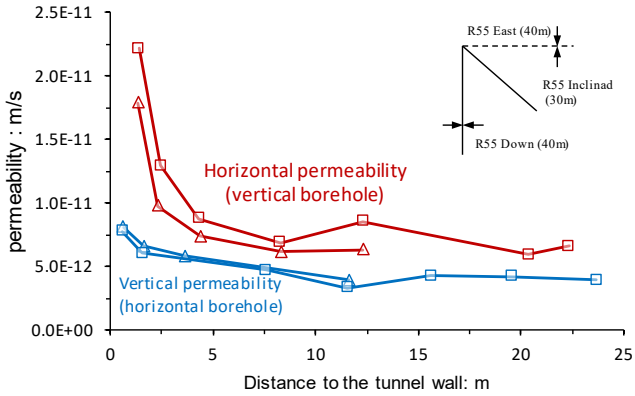

Figure 2.49: Permeability around the connecting gallery measured in a horizontal and a vertical borehole (Bastiaens et al., 2006).

ATLAS III in situ heating test in boom clay

The original test set-up for ATLAS was performed in 1992 by SCK.CEN within the framework of the European project Interclay II (1990–1994) (Knowles et al., 1996). During the first phase of the heating test programme, later named *ATLAS I*, a constant heat source of 900W was used from July 1993 to June 1996. During the second phase (*ATLAS II*), the power was increased to 1800W and maintained from June 1996 to May 1997. This was followed by shutdown and natural cooling starting from June 1997 on (De Bruyn and Labat, 2002; François et al., 2009). After the set-up had been extended in 2006, the heater was switched on again from April 2007 to April 2008 with a stepwise power increase, followed by an instantaneous shutdown. This phase is called ATLAS III (Figure 2.50).

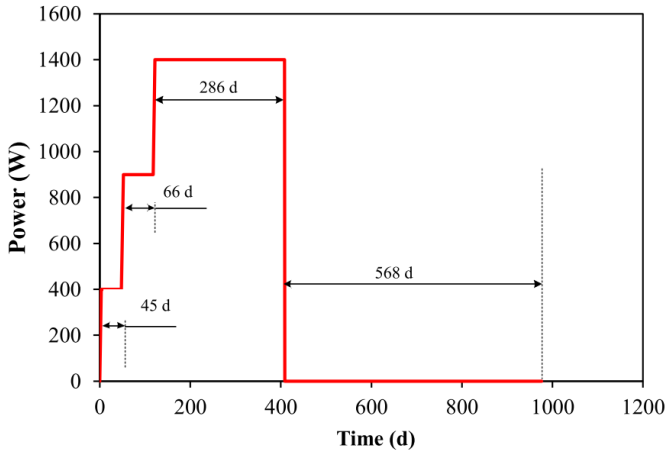

Figure 2.50: Heating procedure of ATLAS III in situ heating test.

The objectives of ATLAS III were to obtain a more accurate picture of the temperature and pore water pressure by drilling two additional instrumented boreholes, to broaden the THM characterization of the Boom clay at a larger scale and at different temperature levels, to serve as preparation for the Praclay Heater test, to provide a reference for up-scaling the Praclay Heater test and finally to provide data for a modelling benchmark study in the European project TIMODAZ (2006–2010) (TIMODAZ, 2007).

The test set-up consists of a central heater borehole and four instrumented observation boreholes. The central heater borehole (AT89E) and three observation boreholes (AT85E, AT93E, and AT98E) are in the same horizontal plane while the fourth observation borehole (AT97E) is slightly inclined towards the heater borehole. The inclination is about 10° down and 10° towards the heater borehole. Figure 2.51 illustrates the plan view of the ATLAS III test.

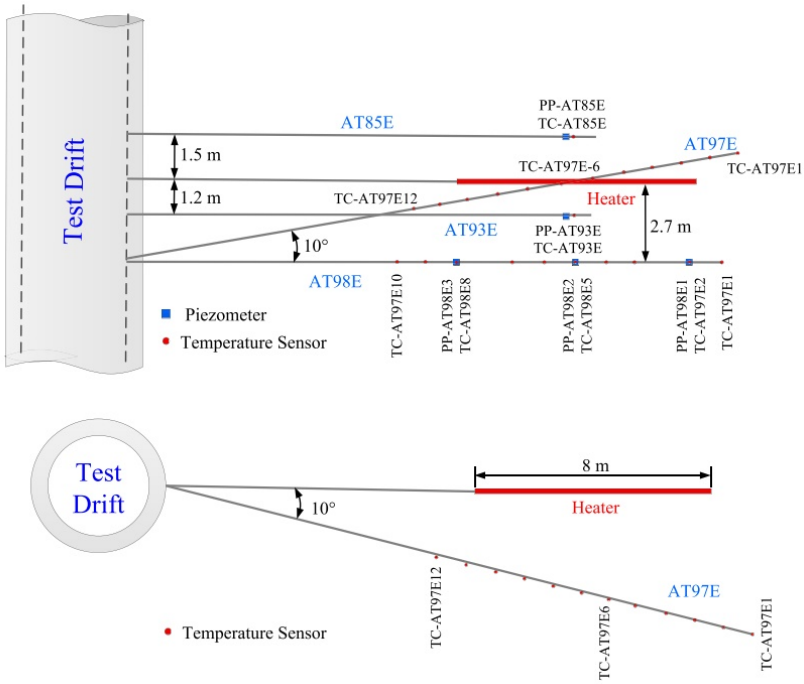

Figure 2.51: Schematic view with instrumentation of the ATLAS III in situ test (Chen et al., 2017).

Thermal results

The average temperature increases in the boreholes AT85E and AT93E is shown in Figure 2.52. The temperature increase is larger at AT93E than that at AT85E due to the shorter distance of AT93E to the heater tube (see Figure 2.51). Maximum temperature increases of 24°C and 22°C are observed by the sensors at AT93E and at AT85E, respectively. The successive heating steps are well visible. A decrease in temperature is only visible 2 days after switching off the heater.

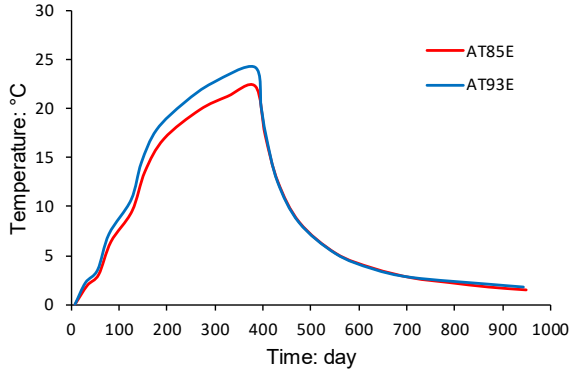

Figure 2.52: Evolution of temperature change measured in boreholes AT85E and AT93E (modified after Chen et al., 2011).

Pore pressures

Figure 2.53 shows the evolution of the por pressure evolution at five piezometer filters located in boreholes AT85E, AT93E and AT98E. The maximum por pressure increases range between 0.5 MPa and 1.0 MPa. Due to the slow drainage towards the underground laboratory, initial pore water pressures range from 1.2 MPa to 1.75 MPa depending on the distance to the Test Drift. At the end of March 2008, a sudden drop of pore pressure was imposed on the piezometer PP-AT85E in order to determine the permeability of the clay host rock near this sensor. It is interesting to observe that at the start of each heating phase, a temporary decrease of the pore pressure occurs in all the piezometers. The opposite phenomenon is observed when switching off the heater.

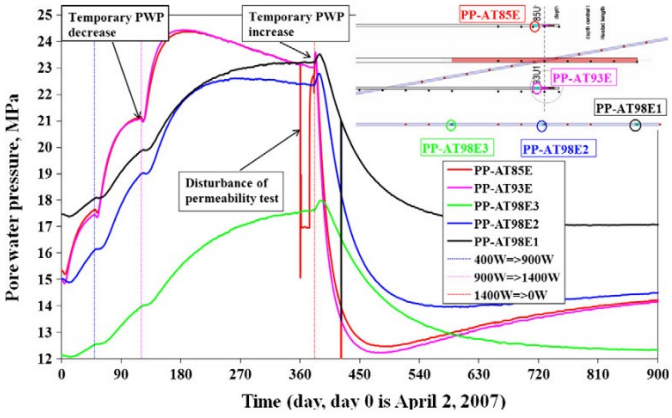

Figure 2.53: Evolution of pore pressure at five piezometer filters located in boreholes AT85E, AT93E and AT98E (Chen et al., 2011).

THM coupling

Figure 2.54 present the increases of temperature, pore pressure and average total stress measured in boreholes AT85E and AT93E respectively, and for groups of sensors that are very close to each other. As shown in the Figures, After the power is increased, pore pressure decreases immediately, then they start to increase only when the local temperature reacts to the increased power. After the power is switched off, pore pressure increases immediately and then decrease when the local temperatures start to decrease due to the switching off of the power. However, changes of both pore pressure and average total stress measured in AT85E (and AT93E) show similar trends of evolution and magnitude.

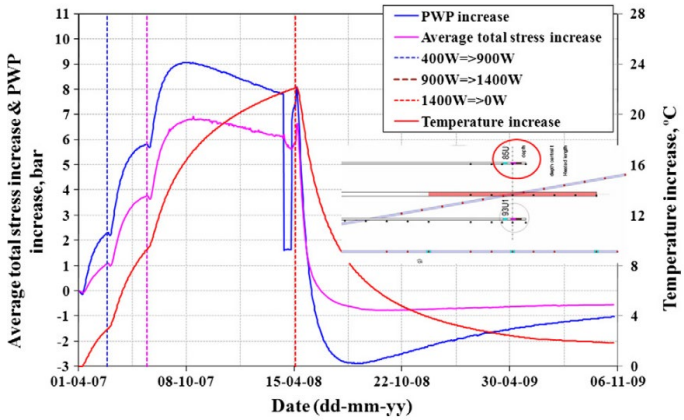

Figure 2.54: Summary of the increases of average total stress, pore water pressure, and temperature in borehole AT85E, measured close to the mid-plane of the heater (Chen et al., 2011).

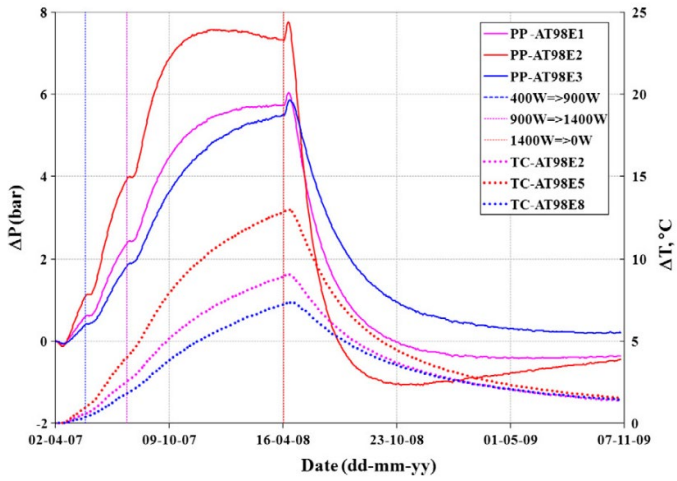

Figure 2.55: Summary of the increase of pore water pressure and temperature in borehole AT98E (Chen et al., 2011).

Thermal anisotropy

Borehole AT98E lies in the same horizontal plane as the heater, while borehole AT97E is inclined and passes below the heater. Close to the symmetry plane perpendicular to the heater axis, sensor AT98E5 lies at a horizontal distance of 2.68 m from the centre of the heater while sensor AT97E6 is located 2.75 m from the heater in the vertical direction, so they are located in different directions and with almost the same distance to the heater. Figure 2.56 shows a maximum temperature difference of 6°C between both sensors. The temperature increase in AT98E5 is about twice the increase observed in AT97E6. Such a difference is a clear evidence of the anisotropic thermal conductivity in the Boom clay.

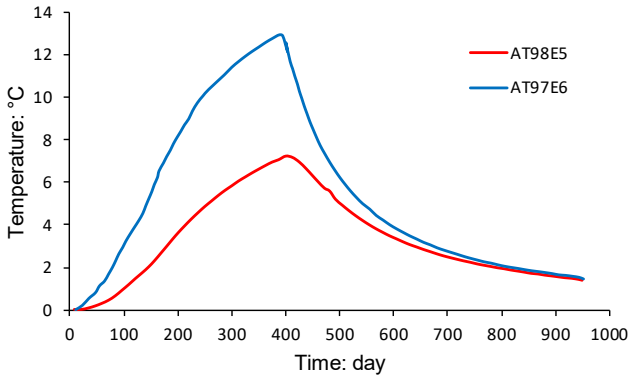

Figure 2.56: Both measured and computed temperature increase at locations TC-AT98E5 and TC-AT97E6 (modified after Chen et al., 2011).

The ATLAS III small scale in situ test has been developed to assess the hydro-mechanical effects on the Boom clay of a significant temperature gradient. The test was provided a large set of good quality and well documented data on temperature, pore pressure and total stress, and many interesting observations have been made. The extended measurements of the temperature field provide clear evidence of thermal anisotropy. The test had a simple geometry, depends essentially on a single material (Boom clay), and has well defined boundary conditions, which facilitates the comparison between measurement and numerical modelling.

2.5.2 Mont Terri rock laboratory

General

The Mont Terri rock laboratory (Thury and Bossart, 1999) is located in Northwestern Switzerland near the town of St. Ursanne and has been excavated from an existing reconnaissance/evacuation gallery of a motorway tunnel. The laboratory is situated in an asymmetrical anticline formed during the folding of the Jura mountains as shown in the geological cross- section of Figure 2.57. It is excavated in Opalinus clay a strongly bedded claystone. Because of tectonic activity, the rock strata dip at an angle of 45° to the southeast. Intense bedding is observed throughout, bedding thickness is generally on the centimetre scale. Opalinus clay at the laboratory site has an overall thickness of around 160 m and the present overburden is 250 m approximately. Three facies are distinguished in the Opalinus clay layer: shaly, sandy and carbonate-rich; most of the laboratory is contained in the shaly facies, the most clayey one.

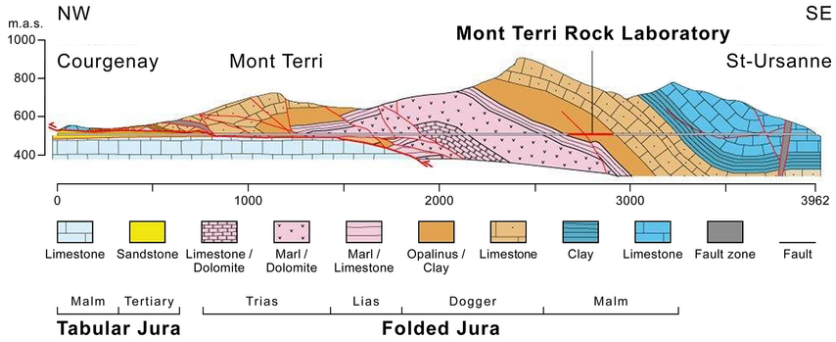

Figure 2.57: Geological cross-section of the Mont Terri rock laboratory (Freivogel and Huggenberger, 2003).

Response to underground excavations

A mine-by test (ED-B test) was carried out in the Mont Terri rock laboratory (Corkum and Martin, 2007) taking advantage of the completion of the central part of the New Gallery (Figure 2.58). The drift is circular, 3.6 m-diameter and the test section is 35 m long at a depth of approximately 270 m. The tunnel was excavated full face with a road header progressing from the NW to towards the SE. A 200 mm-thick steel fibre-reinforced shotcrete, installed about 7m behind the front, was used as support. Most of the instrumentation was installed before the start of the exaction from Niches OP and BF excavated in the reconnaissance gallery. The distance between the two galleries is 24 m approximately.

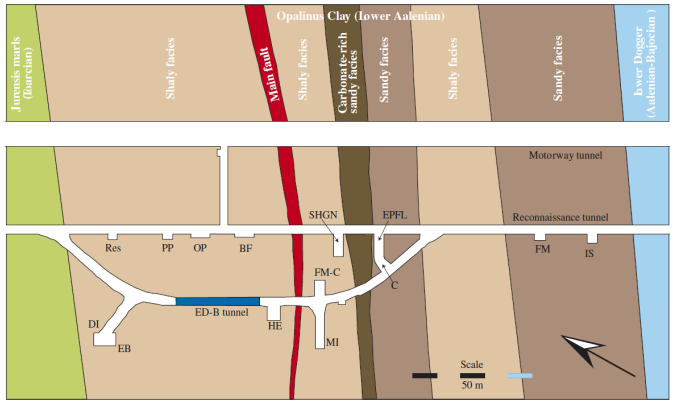

Figure 2.58: Location of the mine-by test ED-B (Corkum and Martin, 2007).

Again, the most relevant information obtained in the mine-by test refers to the development of pore pressures. Figure 2.59 shows the evolution of pore pressure during the excavation of the New Gallery. A familiar pattern emerges. Long before the arrival of the excavation front, pore pressures rise steadily as excavation proceeds. When the excavation front crosses the measuring section, there is a sharp increase due to the anisotropy of in situ stresses and material stiffness. Afterwards the pore pressure reduces; in the case of the sensor located 50 cm from the tunnel wall, atmospheric pore pressure is measured suggesting a direct connection with the tunnel opening.

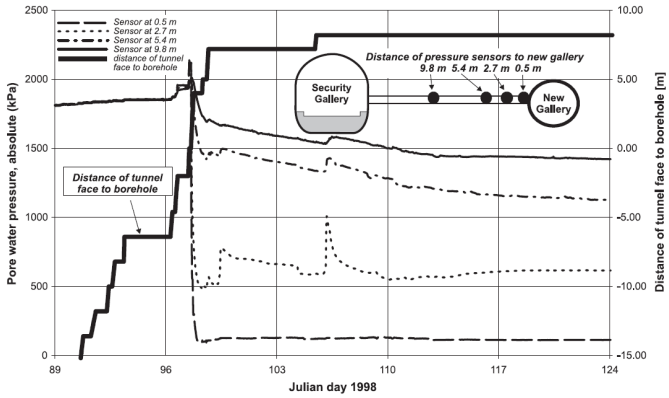

Figure 2.59: Pore pressure evolution during the excavation of the New Gallery measured in sensors at different distances from the tunnel wall (Bossart et al., 2004).

The pattern of fractures generated in the excavations in the Mont Terri laboratory is quite specific and it is summarised in Figure 2.60. Laterally, a series of extensional fractures roughly parallel to the tunnel wall generally appear. In

contrast, fractures in roof and floor are more related to the deformation of the bedding that is especially intense in this material. Indeed, failure mechanisms clearly controlled by the deformation, detachment and buckling of bedding layers have been observed a number of times. In fact, the same fracture and failure patterns have been found in hollow cylinder tests performed in the laboratory.

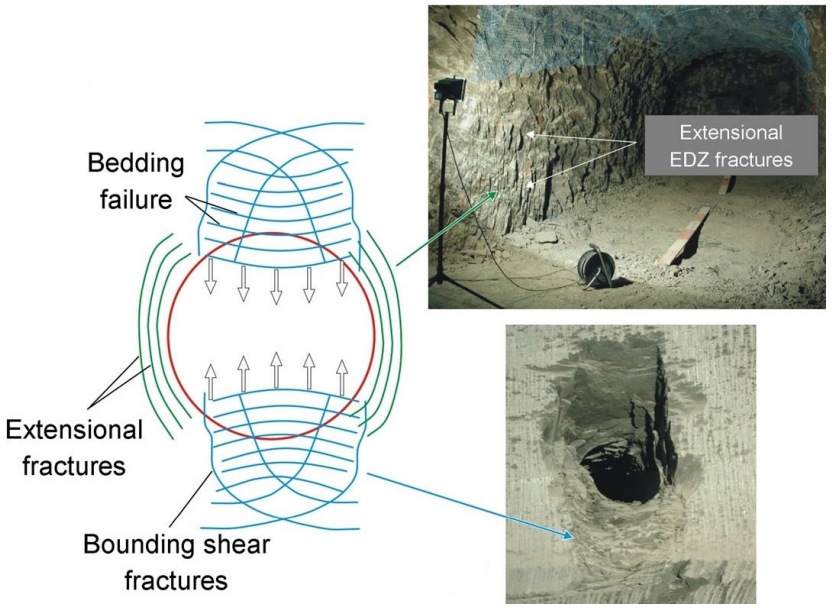

Figure 2.60: Fracture patterns as observed in the Mont Terri rock laboratory (Blümling et al., 2007).

The extent and characteristics of the fractured zone in stable openings away from failure has been studied intensively (Bossart et al., 2004; Bossart et al., 2002). A variety of observation methods have been used. The conceptual model shown in Figure 2.61 has been derived. The excavation damaged zone comprises two subzones, the inner one where factures are interconnected and an outer one in which fractures are isolated and less frequent. In the inner zone oxidation phenomena are observed and the hydraulic conductivity may increase up to 2-4 orders of magnitude. However, much of this loss of tightness is subsequently recovered as Opalinus clay has a significant capacity for self-sealing once it becomes saturated (Bossart et al., 2004).

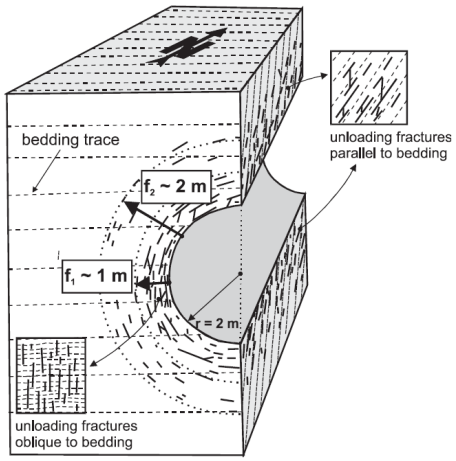

Figure 2.61: Conceptual model of the excavation damaged zone. f1 indicates the extent of the inner zone and f2 the boundary of the outer zone (Bossart et al., 2004).

HE-D insitu heating test in Opalinus Clay

The three Mont Terri rock laboratory in situ heating tests considered are: HE-B, HE-D and HE-E. They encompass a variety of features concerning the geometrical setting, presence and type of backfill, maximum temperature and heating duration. Figure 2.62 shows their location in the Mont Terri rock laboratory. Opalinus Clay is intensively bedded; the closely-spaced bedding planes dip at an angle of approximately 45° at the laboratory location. All tests have been performed in the shaly facies of Opalinus Clay.

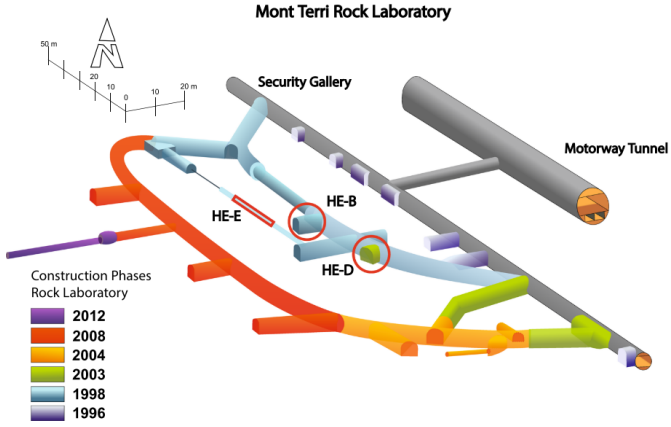

Figure 2.62: Location of the main heating tests performed in the Mont Terri rock laboratory (Gens et al., 2017).

Figure 2.63 shows a top view of the HE-D test area. A horizontal test layout was chosen in order to have a largely uniform lithology. Temperatures were measured along two boreholes drilled (D1 and D2) from the niche HE-D. However, perhaps the most relevant observations were those combining measurements of temperatures and pore pressures at the same point in order to relate directly the two variables. This was achieved in borehole D3 and in a series of small diameter boreholes (D7 to D17) drilled from the MI niche. The pore pressure measurements of sensors located below the main borehole were quite successful but the pore pressure probes located above the main borehole exhibited a rather slow response attributed to difficulties encountered in de-airing the sensor area. Finally, sliding micrometre tubing was installed in boreholes D4 and D5 to measure incremental deformations at 1 m intervals.

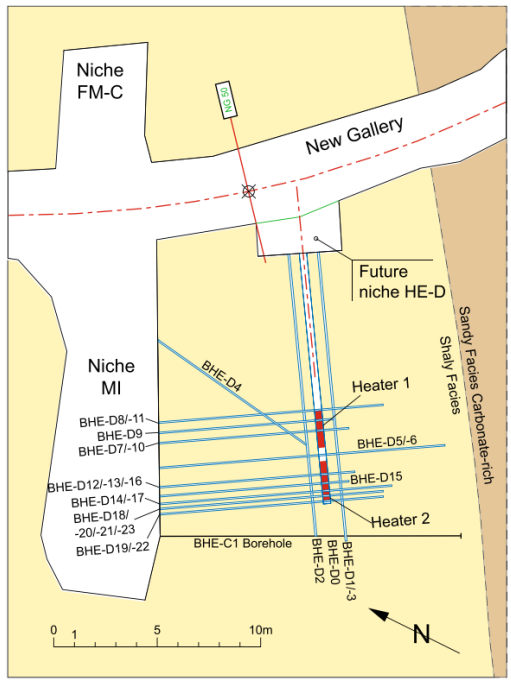

Figure 2.63: Schematic layout of the in situ test HE-D (Gens et al., 2017).

Approximately 1 month after installation and pressurization, the heaters were switched on with a total power of 650 W (325 W per heater). The heaters were then left under constant power during 90 days. Afterwards the power was increased threefold, to 1950 W (975 W per heater) and maintained at that level for 248 days more. The heating period lasted form March 2004 to February 2005. At the end of the second heating stage, the heaters were switched off and the clay was allowed to

cool down. Temperatures, pore pressures and deformations were measured throughout.

Thermal results

Examples of the observations obtained are shown in Figure 2.64 in terms of evolution of at different distances from the heaters.

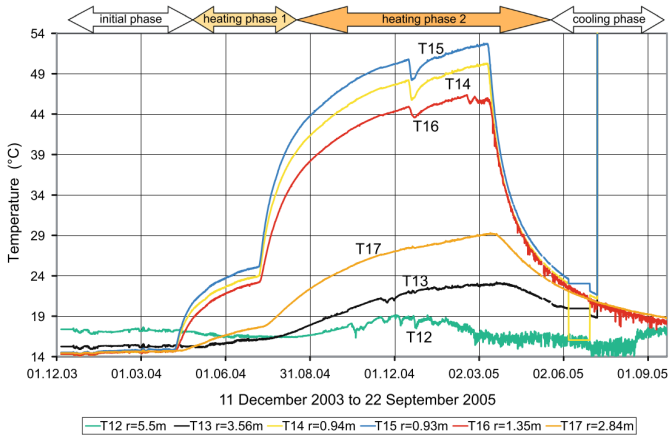

Figure 2.64: Evolution of temperature at different distances of the heater axis. Experiment HE-D (Gens et al., 2017).

pore pressures

In Opalinus Clay, the main hydraulic phenomenon associated with thermal effects is the generation of pore pressure due to changes of temperature. When Opalinus Clay (and other argillaceous rocks) is subjected to a temperature increase, the pore pressure will also increase due to the fact that the thermal expansion of the water is larger than that of the porous skeleton itself. The low permeability of Opalinus Clay ensures that the resulting excess pore pressure does not dissipate rapidly.

Interesting insights can be obtained examining a typical evolution of temperature and pore pressure as presented in Fig. 16. It was recorded in borehole D3 (Figure 2.65) with the sensors located 1.1 m away from the axis of the heater in the direction of the bedding planes. It can be observed that pore pressures react immediately to heating, exhibiting a very strong response. Increments of 2.25 MPa are measured at this particular location; this is a magnitude similar to the estimated minor principal stress in the area. It is also interesting to note that the evolutions of temperature and pore pressures do not coincide. Pore pressure reaches a maximum at a particular time and then it decreases in spite of the fact that temperature continues to rise. This is the result of the interplay between the generation of pore

pressures due to thermal action and the dissipation of pore pressures due to consolidation. At this particular location, dissipation by liquid-flow overcomes the temperature increase effects in the later stages of the experiment.

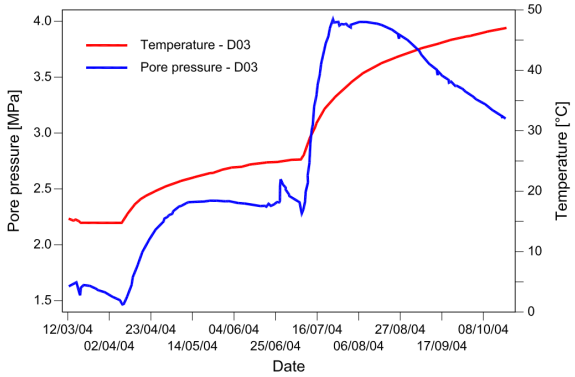

Figure 2.65: Evolution of temperature and pore pressure in borehole D3 during the HE-D test (Gens et al., 2017).

Thermally induced mechanical effects

Mechanical effects result from the joint action of temperature changes and pore pressure generation and dissipation. They can be perceived from the measurements of relative displacements in boreholes D4 and D5 performed using a sliding micrometer (Figure 2.66). Borehole D5 was drilled at a direction approximately normal to the main borehole containing the heaters; the deformations measured at various times are plotted in Fig. 21. It can be observed that in the region around the heaters, extension deformations occur, but they become compressive strains at locations further away from the heater. The volume increases of the clay close to the heater, driven by thermal expansion, produces compression in the outer zones.

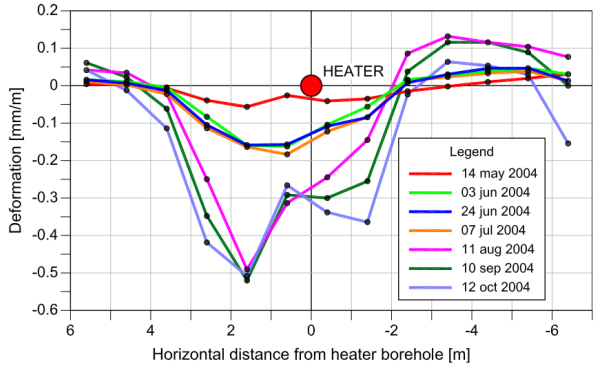

Figure 2.66 Distributions of deformation measured at different times in borehole D5, drilled approximately perpendicular to the main borehole. HE-D test (Gens et al., 2017).

2.5.3 Meuse/Haute-Marne underground research laboratory

General

The Meuse/Haute-Marne underground research laboratory is located in Eastern France near the town of Bure (Delay et al. 2007). It consists of surface facilities, two shafts (an access shaft and a ventilation shaft) and a network of drifts, constructed at a depth of 490m, in which the scientific experiments are carried out. It has been excavated in the Callovo-Oxfordian (COx) claystone, an indurated hard clay that forms part of the Jurassic formation of the Parisian Basin. A geological profile is shown in Figure 2.67. The target horizon is 130 m thick, between elevations 420 and 550 below the surface. Very little tectonic activity has taken place since the mudstone deposition and the bedding planes are practically horizontal throughout.

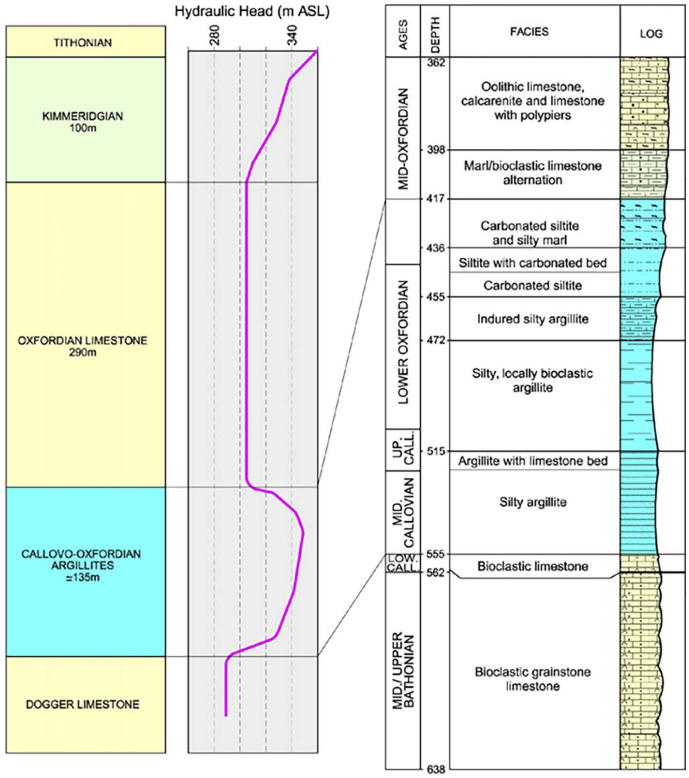

Figure 2.67: Geological profile at the Meuse/Haute-Marne underground research laboratory (Delay et al. 2007).

Shaft excavation

A mine-by test experiment (REP) was performed during the sinking of the main shaft of the Meuse/Haute-Marne underground laboratory (Figure 2.68). The shaft had an average diameter of 6.1 m and was excavated by drill-and-blast method. Prior to reaching the test section, excavation was stopped (at elevation -445 m from the surface) and a 40-m long observation niche was constructed. From this niche a series of instrumentation boreholes were drilled. Once observations had stabilized, shaft excavation was resumed. The experiment section was located between elevations -460 and -476 with special attention to the central zone. As discussed earlier, the clay fabric is likely to be isotropic on the horizontal planes. However, the horizontal in situ stresses are not isotropic; there is a major horizontal principal stress (σ_H) oriented in the NW-SE direction estimated to be around 15 MPa. The minor horizontal principal stress (σ_h) is oriented in the NE-SW direction and has a value of 12 MPa, approximately similar to overburden. Initial pore pressure is about 4.2 MPa but it is affected somewhat by drainage towards the shaft and the niche.

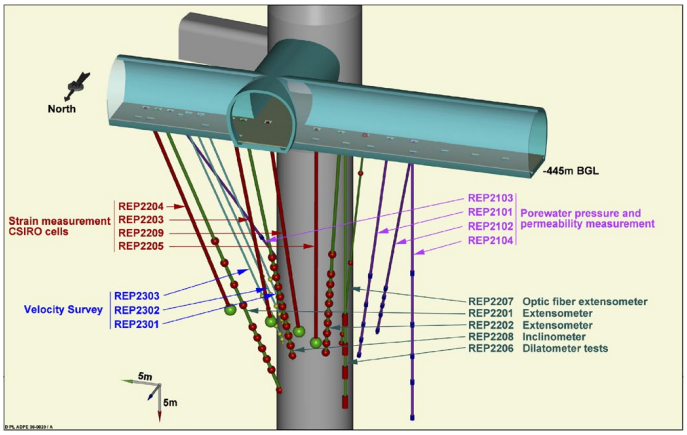

Figure 2.68: Layout of the REP experiment showing the main shaft, the observation niche and the instrumentation boreholes.

Figure 2.69 shows the axial displacements in borehole 2202, located in the zone of the major principal horizontal stress, σ_H. It can observe that compression is measured ahead of the excavation but when the excavation front passes a particular measurement location, displacements change to extension. In any case, movements are small, less than 3 mm. In a similar borehole, located in the area of the minor principal horizontal stress, displacements are even smaller.

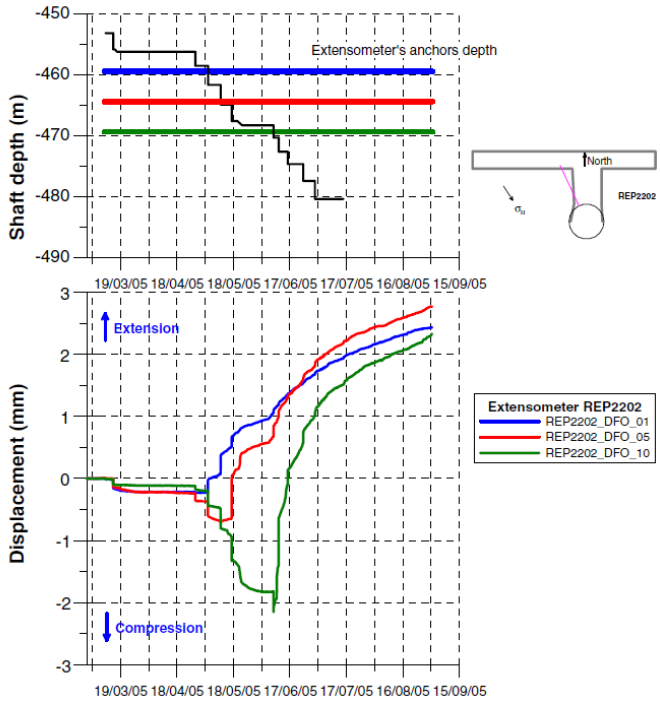

Figure 2.69: Axial displacements in borehole 2202 (Delay et al. 2007).

More interesting is the evolution of pore pressures as excavation progresses. In Figure 2.70a, the pore pressures measured in a borehole placed in the zone of the major principal horizontal stress are shown. It can be observed that there is a reduction of pore pressures even before the excavation reaches the measuring point; the reduction becomes much larger as excavation progresses past due to unloading. In contrast, the pore water measured in the zone of the minor principal stresses (Figure 2.70b) exhibits an increase prior to the arrival of the excavation front. The different behaviour of the pore pressures in the two zones corresponds precisely with what is predicted if the anisotropy of principal stresses is considered. As the material is presumed basically isotropic in a horizontal plane, this contrast in rock response can be safely attributed to the anisotropy of in-situ stresses. Naturally, once the excavation has progressed beyond the measuring points the two boreholes behave similarly, showing a large reduction in pressures. However, the final pore pressure values still show some differences for points located at similar distances from the shaft wall, measurements in the minor principal stress zone giving larger values.

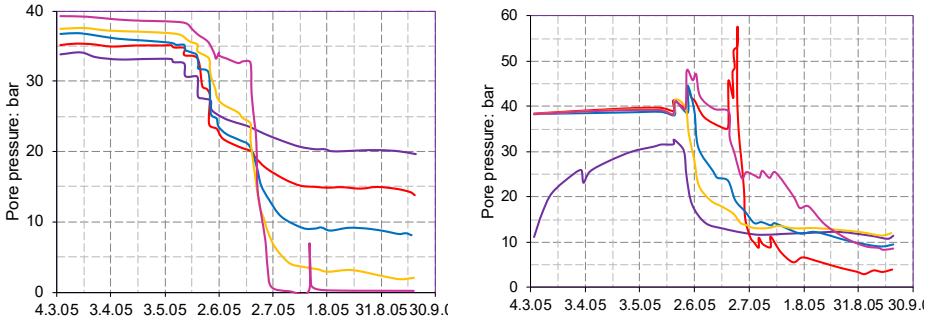

(a) (b)

Figure 2.70: Pore water pressure measured in (a) borehole 2101 located in the zone of the major principal stress (b) borehole 2102 located in the zone of the minor principal stress (modified from Armand et al., 2005).

Rock permeabilities were measured before and after excavation. Before excavation, permeability ranged from 9×10^{-14} m/s to 7×10^{-13} m/s. It was found that close to the shaft wall permeability had increased up to an order of magnitude in spite of the small displacements observed. Figure 2.71 shows the distribution of permeability increase with distance to the shaft wall, the zone extends to 4-5 m, less than one shaft diameter. Measurements continued for 2.5 years after the end of excavation but permeability remained largely unchanged over this period.

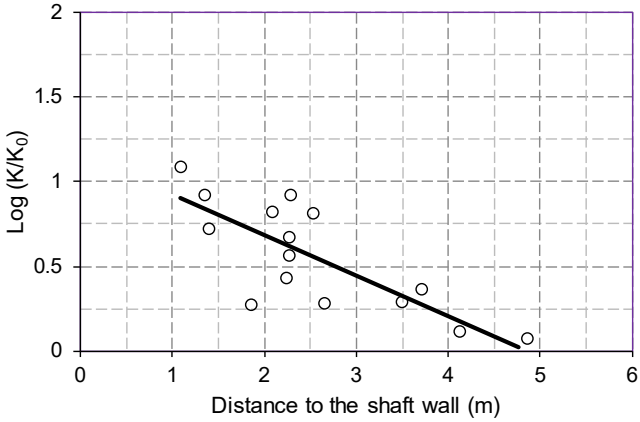

Figure 2.71: Distribution of permeability after excavation compared to the permeability values before excavation (modified from Armand et al., 2005).

Excavations of horizontal drifts

Field observations of the effects of the excavation of the horizontal drifts forming the main body of the laboratory have also yielded significant information. Again,

only a very limited selection of results is presented here. The tunnels network is located at the main level of the laboratory (depth: 490 m). It can be noted that, on purpose, the drifts are aligned with the principal stress directions. The tunnels have a horseshoe shape and a section of 17m² and have been normally excavated with pneumatic hammer. The support generally consists of steel sets, 2.4 m-long rock bolts (about 1 bolt / m2) and shotcrete. Convergence sections have been installed very close to the excavation face.

Figure 2.72 shows vertical and horizontal convergences measured in a drift with the same orientation as the minor horizontal principal stress whereas Figure 2.73 presents the same type of data for a drift aligned with the major horizontal principal stress. At this depth, deformations due to excavation are significantly larger than at the level of the REP experiment indicating a weaker, less stiff material. The observations also demonstrate very clearly the effect of the insitu stresses. In the case of drifts aligned with the minor principal stress (Figure 2.72), the stress state is anisotropic and the vertical convergence is significantly larger than the horizontal one. When the drift is aligned with the major principal stress, vertical and horizontal convergences are very similar, consistent with a nearly isotropic stress state, as the minor horizontal principal stress and the vertical overburden stress have very similar magnitudes.

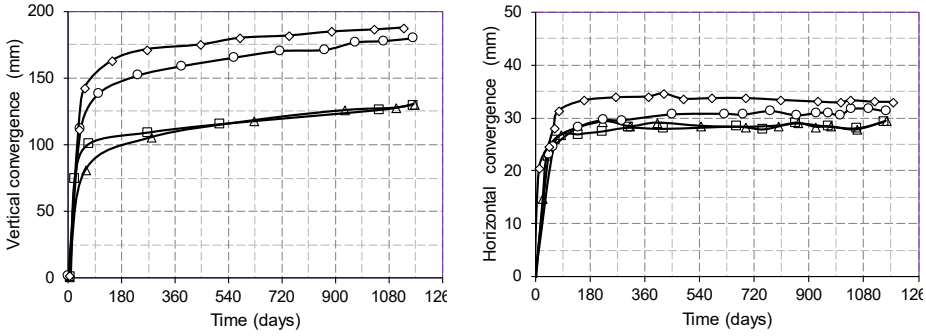

(a) (b)

Figure 2.72: Observed horizontal and vertical convergence in a drift aligned with the minor horizontal principal stress (modified from Armand et al., 2005).

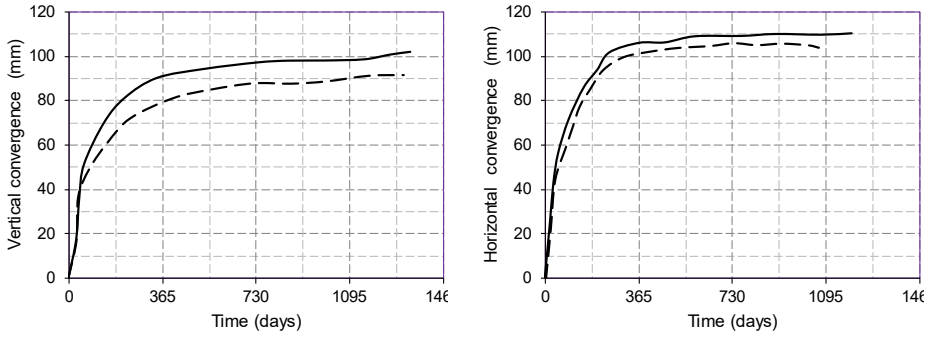

Figure 2.73: Observed horizontal and vertical convergence in a drift aligned with the major horizontal principal stress (modified from Armand et al., 2005).

Moreover, convergences have been measured over a period of over three years to characterize the evolution of tunnel deformations over time (Armand et al., 2005). Observations revealed that there may be behaviour differences in the short term after excavation but, for longer periods, time-dependent deformations settle down to a logarithmic relationship with time. Similar creep rates are observed in the two cases. It may be recalled that a logarithmic long-term development of deformations was also observed in tunnel excavated in Boom clay; a similar behaviour for quite different materials.

Indeed, a number of fracture systems were observed during the excavation of the tunnels. The most characteristic one is the herringbone fractures that form about 1 diameter (4 m) ahead of the excavation front (Figure 2.74). The system of fractures follows the same herringbone pattern as observed in the horizontal drifts at the HADES underground laboratory in Mol in spite of the very large differences in the type of host material; in one case it is a weak plastic soil-like clay and in the other case it is a strong indurated argillite. It is therefore interesting to note that materials sitting at opposite ends of the spectrum of hard soils-weak rocks exhibit the same pattern of fracturing. In the Meuse/Haute-Marne laboratory, this system of fractures is generally somewhat more pronounced in the drifts aligned with the major horizontal principal stress direction.

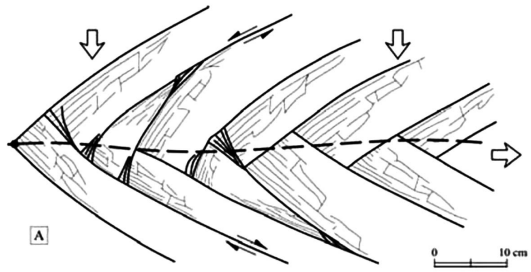

Figure 2.74: Scheme of the herringbone fractures caused by drift excavation (Armand et al., 2005)

In addition, vertical and oblique fractures are created after the herringbone fractures. The final size of the fractured zone depends on the orientation of the drift as illustrated in Figure 2.75. As indicated above, the presence of the fracture zones influences very strongly the pattern and distribution of displacements; indeed, a large proportion of the displacements is localised in the fractured zone.

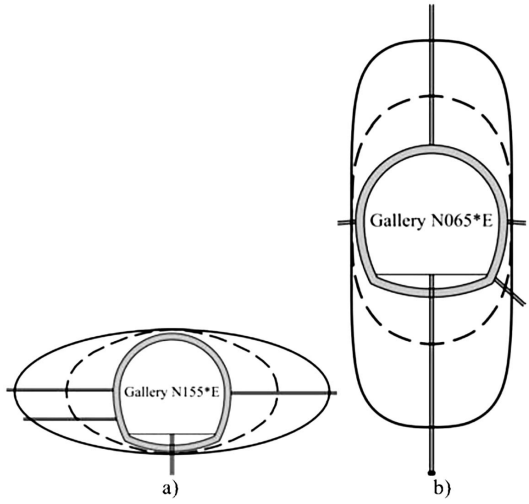

Figure 2.75: Extension of the fractured zone (Armand et al., 2005). a) Drifts parallel to the major principal horizontal stress, b) Drifts parallel to the minor principal horizontal stress.

TER in situ heating test in COx claystone

The TER experiment has been dedicated to observe and investigate the response of the Callovo-Oxfordian claystone subjected to heating and cooling and to characterize thermal and THM properties of the rock. It consists of heating the clay rock during a long enough period of time in order that a significant change can occur and be measured by different sensors. The TER experiment has been

conducted in the Callovo-oxfordian claystone at a depth of 490 m in the M/HM underground research laboratory. It consists of a heater borehole (TER1101) and nine observation boreholes (Figure 2.76). The heater borehole is drilled horizontally form the TER "Carrure" to the depth of 10 m in the direction of maximum horizontal stress rH (in the direction of N65°E). In addition, TER1101 is equipped with a heating element and temperature sensors in order to control the homogeneity of temperature field within the probe (Figure 2.77). To monitor the impact of heating cycles on the rock, about 50 sensors are implanted in the surrounding observation boreholes.

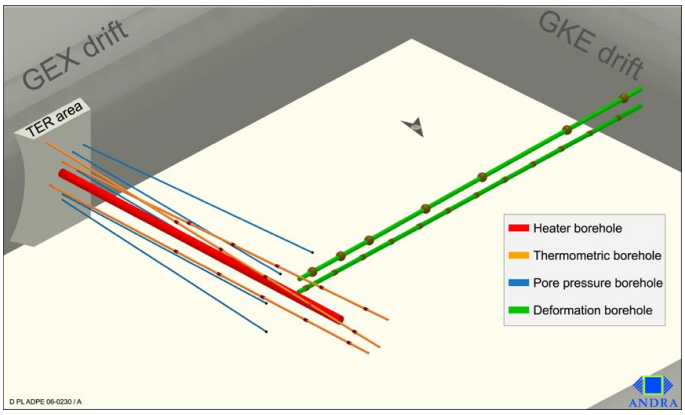

Figure 2.76: View of the TER experiment in the Meuse Haute Marne underground research laboratory (Bian et al., 2012).

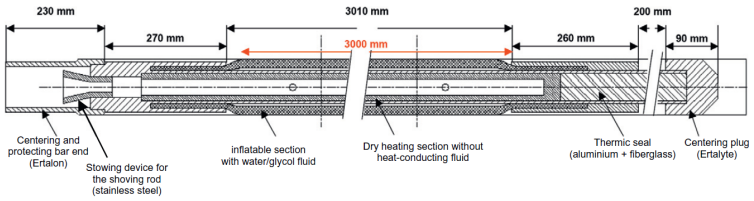

Figure 2.77: Detailed layout of TER hater device (Bian et al., 2012).

Thermal results

Figure 2.78 illustrates the measurement results of different sensors located on the heater surface during heating phases and cooling phase. The so-called "cooling phase" is relative to the period when the injected power is switched off. At the beginning of each heating phase, a rapid increase of temperature is observed. Then the temperature stabilizes progressively with the applied constant heater power. Finally, during the cooling phase, due to the switch off of heating power, the temperature drops sharply and tends to recover its initial value. Furthermore, it is

noted that at the end of first heating phase, an increase of temperature up to 24°Cis obtained in the heater while a greater variation of 58°C is observed during the second heating phase. This difference is relative to the fact that a greater heating power is applied during the second heating phase.

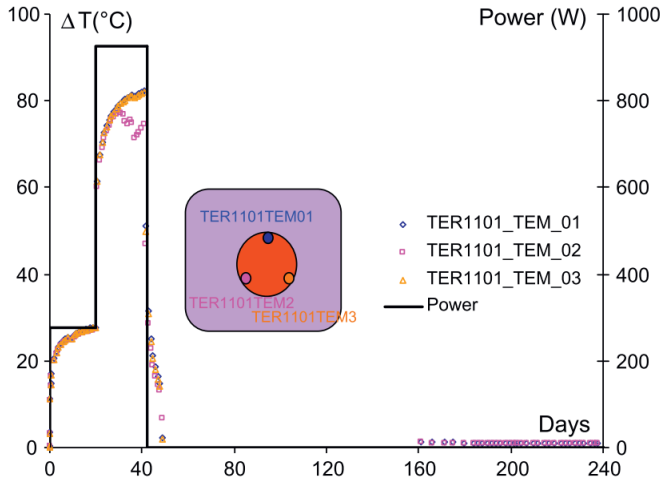

Figure 2.78: Variation of temperature at the surface of heating borehole TER1101 (Bian et al., 2012).

The comparison of measurement data shows that the temperature evolution depends strongly on the sensor location: distance from the heater and location direction. Two captures (TER1401TEM01 and TER1402TEM01), located in the same direction with respect to the bedding plan, are compared first. It is noted that the bigger temperature is obtained at TER1401TEM01which is close to the heater element with respect to TER1402TEM01 (Figure 2.79).

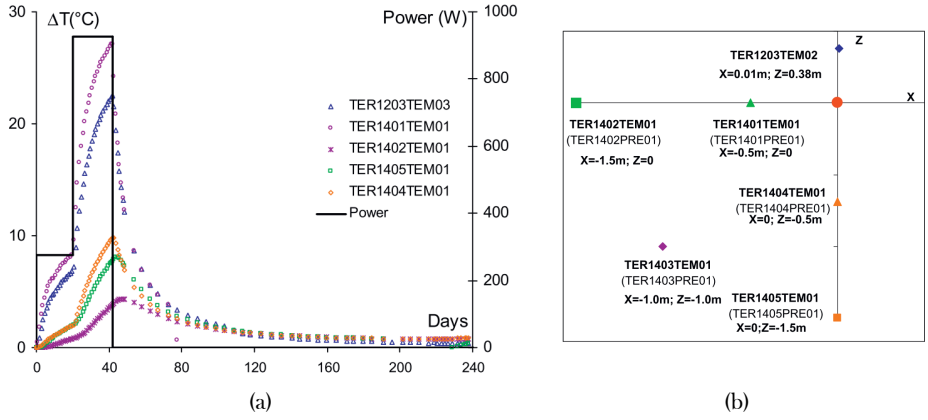

(a) (b)

Figure 2.79: Variation of temperature in the observation boreholes (Bian et al., 2012).

In conclusion, the maximum temperature and the temperature's increase speed decreases with the distance from the heater. Furthermore, it's interesting to note that, during two heating phases, the temperature increases more strongly in the bedding plan direction (TER1402TEM01). On the other hand, after switching off the heating power, at the measured points located far from the heater, the temperature continues to rise during 5 days in the direction perpendicular to the bedding (TER1405TEM01) while in the direction parallel to the bedding (TER1402TEM01), a short period (≈ 3 days) of temperature increase is observed. However, these experimental results confirm the anisotropy of thermal properties.

pore pressures

The evolution of water pore pressure at different measured points is illustrated in Figure 2.80 the nearest measure point TER1401PRE01 to the heater is studied (Figure 2.80). The first heating period creates an important pressure increase up to 1 MPa. The second heating phase induces a rapid augmentation of water pore pressure up to 3 MPa. This overpressure is essentially relative to the difference of thermal expansion between solid matrix and water. Moreover, the very low permeability of claystones cannot provide adequate drainage to dissipate this pressure. After that, with the stabilization of temperature, the generated overpressure is dissipated by advection of water according to the Darcy's law. Consequently, after reaching the maximum level, the pore pressure drops down slowly even when the temperature still increases. In the cooling phase, the contrary phenomenon is observed when the heater power stops working: a sudden drop of pressure is perceived due to the condensation and contraction of pore water. At some measured points (TER1401/1404PRE01), the pressure is significantly lower than its initial value. The under pressure may be relative to the following phenomena: thermal consolidation, microcrack network and permeability. However, hydraulic equilibrium process is very slow due to low permeability of studied material. As the duration of TER experiment is very short, one cannot see the recovery of initial pressure at the end of the experiment.

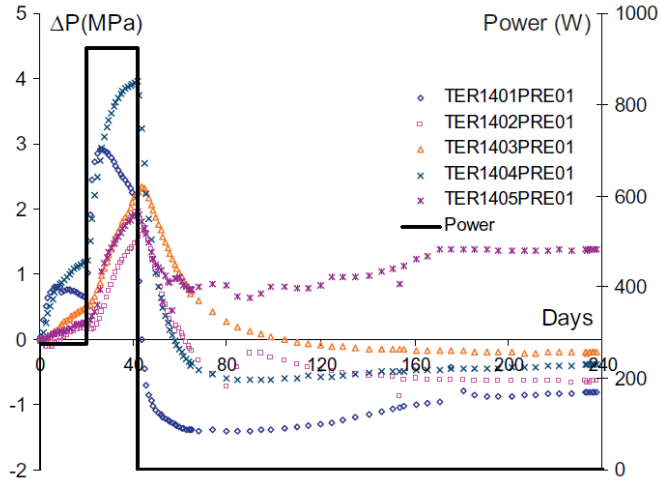

Figure 2.80 Variation of pore pressure in the observation boreholes (Bian et al., 2012).

Displacement

The displacement is measured in borehole TER1301 which is perpendicular to the heating borehole TER1101. Figure 2.81 presents the radial deformation evolution at different points in borehole TER1302. The location of these points is illustrated in Figure 2.82. For all sensors, an important expansion is observed. This phenomenon can be detected clearly at the sensors in the near-field. Due to the start of heating, the sensors are subjected to a phase of dilation and the intervals between the sensors adjoins exhibit an evident expansion of interval due to the expansion of the rock close to the heater. A further rapid increase of deformation can be recognized at the beginning of the second heating phase. During the cooling phase, the rocks contacts gradually and recover progressively the nature state of rock. However, in the far-field, the claystone formation works essentially in compression due to the increasing rock pressure created by the expansion of rock near the heater. Generally, the duration of phase and value of maximum dilation are location dependent.

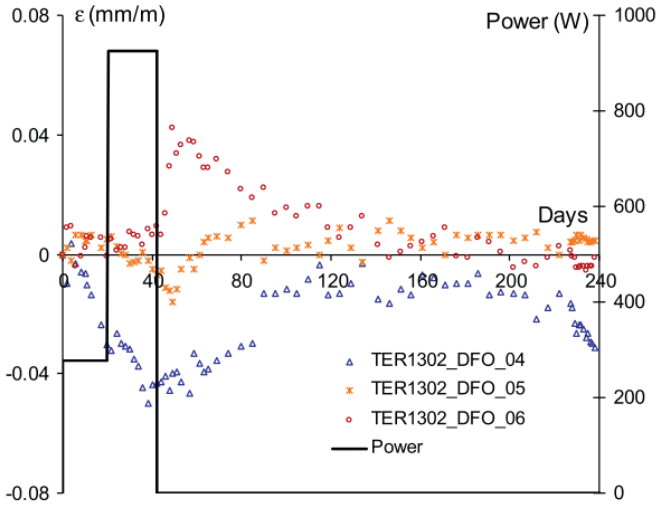

Figure 2.81: Variation of strain in the observation TER1302 (Bian et al., 2012).

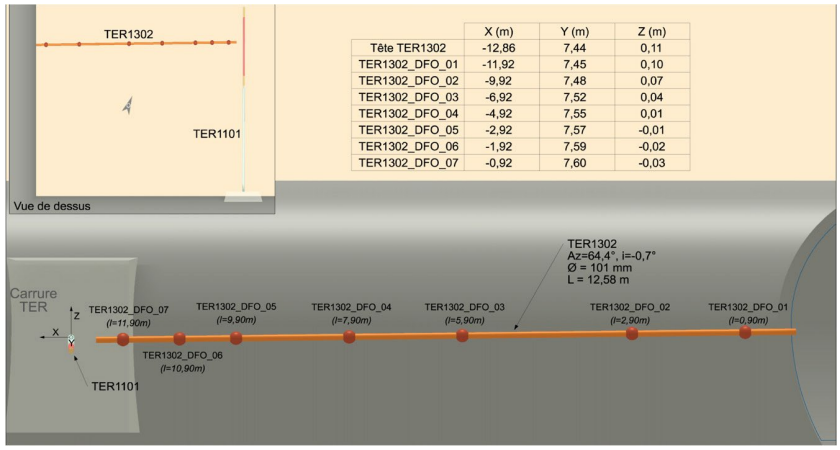

Figure 2.82: Position of strain sensors in the observation borehole TER1302 (Bian et al., 2012).

2.5.4 Summary of In-situ THM characterisation

The observations of the response of argillaceous rocks to deep underground excavations and in-situ heating tests in three different laboratories have provided important information concerning the thermo-hydro-mechanical behaviour of these materials.

Thus, it has been observed that the short-term hydromechanical response is strongly affected by stiffness and in situ stress anisotropy. It has also been noted that the hydromechanical response is detected at large distances from the excavation

front and that the displacements close to the tunnel are mainly controlled by fractures. Indeed, development of very systematic fracture systems has been observed even for quite different materials and depths. Fracturing is mainly governed by stress redistribution and material strength, the method of excavation and support has only limited influence. In some cases (such as in the Opalinus clay at Mont Terri), fracturing is fully controlled by the presence of strong structural features. Finally, very long-term observations indicate that the delayed development of displacements (under contained conditions) follows closely a semi-log relationship with time.

The understanding of the behaviour of Opalinus Clay, Boom clay and COx claystone under thermal loading has been much advanced by the performance and study of a number of in situ heating tests: ATLAS III, HE-D and TER experiments. Those tests cover a wide range of test layouts and conditions. In spite of this, the observed behaviour of those materials is quite similar in the three cases. Although the temperatures applied by the heaters are rather high, the temperature increases in the materials have been generally moderate because of the rapid thermal attenuation with distance. In spite of those modest increases, the generation of pore pressures has been very significant in all cases. The mechanism underlying the generation of pore pressures is well understood; it arises from the combination of the effects of differential rock/water thermal dilation and of pore pressure dissipation, controlled by rock permeability.

There is less information on thermal effects on mechanical variables. However, insitu tests indicated that deformations and displacements are small but more modest effects result from the coupling of hydraulic phenomena to mechanical behaviour. The dissipation of pore pressures induces additional displacements and strains that, due to the high argillaceous rock's stiffness, are smaller than thermally-induced deformations. In principle, mechanical damage could impact the hydraulic observations if a zone of higher permeability develops due to material damage. However, no such thermally induced damaged zone has been observed; in fact, hydraulic measurements carried out in a different test, revealed that heating might be beneficial with respect to rock damage as the intrinsic permeability reduced significantly after an increase of temperature.

And finally, there is no perceptible coupling from hydraulic and mechanical phenomena to thermal behaviour. Practically all heat transport is by conduction and the thermal conductivity of the material does not change as deformations are small the material remains saturated throughout. In addition, mechanical energy dissipation is negligible in a non-isothermal case.

2.6 CONCLUDING REMARKS

In spite of the large variability of composition, grading and geological history of argillaceous rocks, there exists a common core of geological processes and framework interpretations that provides a unified scheme for the understanding of the thermo-hydro-mechanical behaviour of these materials. Naturally, there are a number of exceptions to the general trends that require appropriate modifications of the conceptual frameworks. Indeed, a proper understanding of non-standard behaviour benefits from the existence of an established framework that can be used as benchmark.

A number of factors and features of hydromechanical behaviour have been reviewed including response under compressive loading, brittleness and progressive failure, anisotropy, permeability and hydromechanical coupling. It has been argued that anisotropy is a basic feature in these materials that must be considered in order to achieve a proper understanding of their engineering response in geotechnical problems. Permeability is always low in argillaceous materials and requires especial techniques for their determination. Permeability values are more closely related to pore size distribution than to overall porosity. The role, value and determination of Biot's coefficient in indurated materials still require considerable further research.

Brittleness is a widespread feature of the strength of these materials in conventional geotechnical situations. Strength loss usually occurs in two stages corresponding basically to two mechanisms: loss of bonding and particle realignment. Brittleness leads to the occurrence of progressive failure and to difficulties in determining the operational strength in engineering problems. It is unlikely that a general rule to estimate operational strength can be found and, at present, numerical analysis appears as an increasingly effective way to tackle this type of problems.

Moreover, a number of factors and features of thermal behaviour have been reviewed including elastic response, volume change behaviour, strength, thermal pressurization, effect of temperature on permeability, self-sealing and long-term deformation at high temperatures. The effect of temperature increase on the elastic properties of the COx claystone is not yet clearly demonstrated. Further tests are needed to verify the existence of a potential critical temperature from which there is a significant decrease of elastic modulus for the COx claystone.

A thermo-plastic contraction is observed in normally consolidated clays and an elasto (expansion) plastic (contraction) response is observed in overconsolidated clays, depending on the OCR in Boom clay. Opalinus clay characterized by a linear

thermo-elastic expansion that is typical of overconsolidated samples (Boom clay), followed by a plastic contraction. The peculiarities of the mechanical response of COx claystone to heating established in early experiments consist in a thermoplastic contraction, as opposed to the thermoelastic expansion of heavily overconsolidated Boon clay and Opalinus clay. Since these initial developments, an additional experimental evidence has been added later, which have determined thermal expansion behaviour of the claystones by heating which was consistent with the in-situ observations during heating experiments.

In spite of conflicting report of thermal dependency of strength in argillaceous materials, experimental studies on Opalinus Clay, Boom clay and COx claystone evidence a more ductile response and smaller shear strengths at elevated temperatures. Thermal pressurization was investigated in details, showing a decrease in thermal pressurization coefficient with increased temperature. Undrained heating tests indeed appeared as quite complex with the combined effect of thermal pore pressure build- up with the corresponding effective stress decrease that mobilises some changes in compression-swelling coefficients with both temperature and stress changes. Good understanding of thermal pressurization is necessary to better assess the stability of galleries during the thermal phase.

Early experiments have revealed that hydraulic conductivity of argillaceous rocks increases with temperature. Later has been found a linear relationship between porosity and permeability which is independent of temperature. More recently, investigations showed that the permeability is not totally independent of temperature and slightly increases with temperature. Excellent self-sealing properties of the argillaceous materials have been reported in the literature. Experimental data showed that the self-sealing properties of the Boom Clay, the Opalinus clay and COx claystone are not affected by temperature elevation. The long-term deformation of the claystones is influenced by temperature, which was observed in creep tests under various thermal loads to high temperatures up to 90°C-110°C. Indeed, larger creep strains appear at elevated temperature. Carefully monitored response to deep underground excavations and in situ heating test have provided useful insights into the behaviour of these materials under field conditions concerning their coupled thermo-hydro-mechanical response and long-term behaviour.

Chapter 3: Theoretical Basis

In the field of a deep geological repository for high-level nuclear waste, engineering problems generally involve a variety transport phenomenon that takes place in porous multiphase argillaceous materials. Coupled phenomena are a very characteristic feature of these problems because of the interaction between the phases. In the theory of effective stress of saturated soils where the mechanical problem (represented by tension) and the hydraulic problem (represented by pore pressure) interact, the most straightforward and most well-known coupling is implied. The number of possible couplings multiplies when the number of phases increases. Besides, the engineered clay barrier and adjacent host rock (usually called the 'near field') are subject to nuclear waste heating effect and as well, varying associated hydraulic and mechanical physical processes interact in a complex manner.

In fact, it is usually of interest not only to find the final situation for a particular problem but also to track the processes' progress over time. Also, early events will monitor the final status of the system under review. Transient analyses are, therefore, a typical feature of this field. This chapter will only discuss the THM aspects of the engineered barrier systems (EBS), concentrating on heat and mass transport phenomena so contaminant transport will not be discussed here.

A review of the physical processes and mechanisms thought to take place during the heating of a low permeability stiff porous medium are first summarised. Then the theoretical formulation of the coupled thermohydromechanical (THM) processes that take place during the heating in a porous medium using a multi-phase, multi-species approach (Olivella et al., 1994) are reviewed. Afterwards, a coupled THM formulation is discussed in some detail to address the problem in a more systematic way. The formulation provides a logical basis for proper evaluation of the various THM phenomena and their interactions.

3.1 THM PROCESSES

A considerable number of coupled THM processes are expected to occur in the operation of the high-level nuclear waste (HLW) repository (Gens et al. 2002). For reference, the key features of these THM processes should be qualitatively anticipated in order to identify the main characteristics of the required theoretical

formulation. The behaviour of the argillaceous rocks, such as COx claystone, under thermal loading, has to be considered in the framework of thermohydromechanical (THM) couplings as the various THM phenomena interact. Olivella and Gens have developed conceptual and mathematical models for coupled THM processes since the early 1990s.

Beginning with thermal phenomena, it may be claimed that heat conduction is in most instances, the primary mechanism for heat transport. The heat conduction reacts to temperature gradients, T. Nevertheless, due to the movement of the three phases: solid, liquid and gas, additional heat transfer will also be undertaken by advection. The endogenous residual heat from phase changes can also have serious thermal effects.

As for hydraulic phenomena, two of the main ones are, of course, liquid and gas advective fluxes. The term hydraulic is used in a generic way here, including both the flow of liquid and gas. In the absence of gravitational or osmotic potential gradients, liquid and gas pressures regulate advective flows in a unique way. Consider that the pressures of liquid and gas are now used instead of water and air. This is in line with the assumption that more than one species may be present at each phase Advective flows are subject to phases.

Non-advective (diffusion) flows are potentially significant, as more than one species may be present in the fluid phases. The most important of these is the diffusion of water vapor in the gas phase, especially in nonisothermal conditions. The conventional conceptual interpretation of this phenomenon is the binary diffusion one. There is another mol of air (considered as a single species) diffusing in the opposite direction for each mol of water vapour diffusing in one direction. Consequently, the total contribution to advective flow is zero. Vapor diffusion is controlled by concentration (or partial pressure) of vapour gradients. Essentially the same considerations can be made for the dissolved air diffusion in the liquid phase, although it is usually much less relevant in practice.

Eventually, in addition to the usual stress/strain relationship, the mechanical behaviour of unsaturated porous media will be associated with additional contributions from changes in suction (matric and sometimes osmotic) and temperature changes. Most of the above-mentioned phenomena are in fact strongly coupled, and they must be perceived as parts of a single integrated system.

Following Gens et al. (2017), coupled processes in geological media could be illustrated by the interaction diagram shown in Figure 3.1.

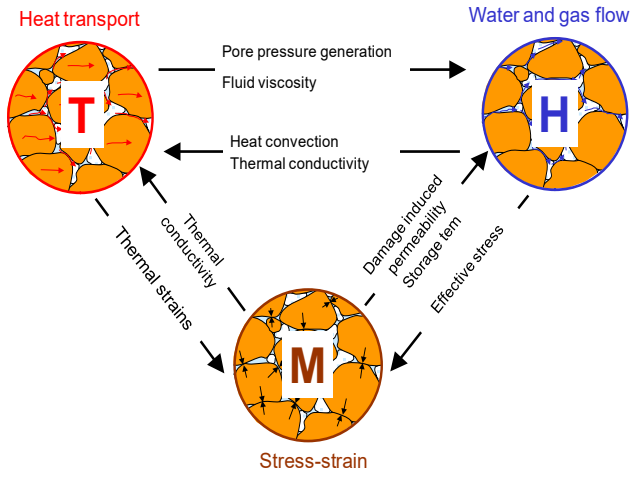

Figure 3.1: Coupled thermo-hydromechanical (THM) phenomena (Gens et al., 2017).

Referring to Figure 3.1 as follows, let us look at the different vectors of interaction:

- **T→ M**: A change in temperature induces the soil skeleton's thermal expansion and contraction, leading to thermal stress if deformations are constrained.
- **T→ H**: An increase in temperature induces thermal expansion of the pore fluids, resulting in an increase in pore fluid pressure if drainage away from the source of heat is impeded.
- **H→T**: The flow of pore fluids is responsible for the transfer of heat by convection. In very low permeability formations, heat convection can usually be neglected. Resaturation from infiltrating water can increase the bulk of thermal conductivity and thermal capacity in mediums partially saturated with water.
- **H→ M**: When external loads are applied to the porous medium, a new state of stress will develop. This total stress will be distributed between the solid skeleton and the pore fluids. The Classical Effective Stress Principle (Terzaghi, 1923; Biot, 1941; Bishop and Blight, 1963) was used and adapted to take this distribution into account, as detailed later in the thesis.
- **M→ H**: Deformation of the solid skeleton will change the pore volume, which may be irreversible depending on the stress level, and will, therefore, affect the permeability of the medium.

The key feature of the described THM behaviour is that all these phenomena are strongly coupled and complexly interact with each other. The THM formula should, therefore, include the following phenomena to provide the above-mentioned processes:

a) heat transport
    i. heat conduction
    ii. heat advection (liquid water)
    iii. heat advection (water vapour)
    iv. heat advection (gaseous air)
    v. phase changes
b) water flow
    i. liquid advection
    ii. water vapour diffusion
c) air flow
    i. gas advection
    ii. dissolved air diffusion
d) mechanical behaviour

the behaviour of porous materials dependent on stresses, suction and temperature.

3.1.1 Thermal process

Regarding the French concept of disposal for HLW, a maximum temperature of up to 90°C is expected at the interface between the steel liner and the host rock. Heat output from the heaters will dissipate into first air gap (which is partially filled by rock materials) and then into the surrounding host rock which is COx claystone. Under such a high temperature, complex THM processes can be generated in the host rock, liner and annular air-filled gap formed by the liners and the COx claystone. As an overarching point, the magnitude of applied heating power will govern the temperature level of system. In the present work, this is a given input that will not be altered throughout this study (Chapter 4, Analysis of the thermal response).

The thermal problem will be considered by global and local processes. As for the global scale, the cell wall temperature will be controlled by the adjacent galleries. The gallery GAN has influence on the near field temperature evolution at certain distance from the gallery wall (5 meters inside the mass rock), liner and gap formed by host rock and steel liner. The local scale processes determine the temperature differences between the heaters and different points in the system. At the local scale, the state of the annular air-filled gap (i.e. open/closed gap and degree of

saturation) and the host rock adjacent to the steel liner is expected to be an important factor controlling the maximum temperature of near field. Heat transport takes place mainly by conduction. Heat dispersion is considered negligible as the fluid fluxes are small due to the low hydraulic conductivity of the host rock (COx claystone).

The advective/convective heat transport is relatively low because the amount of mass moving through the rock is small (due to quit low hydraulic conductivity). The radiation heat transport take place in the gap between the host rock and liner and is active only during the time that the gap remains open. Moreover, given that the heated zone in the deposition cell is not isolated, there is a heat transfer mechanism through the air zone of the cell (This mechanism will be explained in detail in chapter 4).

An important process from thermal point of view is the annular air-filled gap closure. When the gap is open and dry, it has the maximum insulation capacity and therefore, the heater will increase its temperature as compared with other situations. Then host rock temperature in contact with liner is higher when the gap is close than if it is open because its thermal conductivity is lower when the gap is open than when the gap is closed. This fact also indicated in the model result (chapter 3) where three-dimensional view of computed contours of equal temperature in the steel liner shows higher temperature at the bottom of the heated zone due to the geometry of the gap (annular shape formed by steel liner supported on the bottom of the excavated cell). However, closure of the gap is relatively fast (400 days after cell excavation) which is evidenced from insitu observation. So, considering the gap closes before the temperature in heater reaches the maximum, then two main heat transfer mechanism are dominated in the annular air-filled gap, radiation and conduction. The first one is achieved before the closure and the second mechanism take place after the closure.

Heat capacity and thermal conductivity of host rock (COx clay stone) is of great importance near field heat dissipation. On the other hand, due to the fact that thermal conductivity of the host material does not change throughout the whole experiment, and the changes of porosity are minimal, a purely thermal analysis can be performed to find the value of thermal conductivity that achieves the closest agreement with insitu temperature observations. It should be noted that both parameters are dependent on the composition of the porous materials (porosity, mineralogy of solid phase and pore fluids).

3.1.2 Hydraulic process

Thermally induced excess pore fluid pressures (or thermal pressurization) is the major action affecting COx claystone. In fact, when the thermal load is applied to the saturated porous material, hydraulic and mechanical effects occur. In general, the increase in pore pressure will result from an increase in temperature due to the differential rate of expansion of the skeleton of the argillaceous material, the solid phase and the water. Indeed, in stiff materials, the increase in pore pressure may be very large and approach or even reach hydraulic fracture conditions.

Figure 3.2 shows, in a schematic way, some of the thermohydraulic processes occurring in the ALC1604 in situ heating test. At the inner boundary, steel liner receives a very strong heat flux from the heaters. A temperature gradient will, therefore, develop from air gap into the near field, and heat dissipation will basically be controlled by the thermal conductivity of the host rock, liner and annular air-filled gap.

In the inner zone of the host rock, the heat supplied by the heater results in a large temperature increase and in strong water evaporation, which induces host rock drying. The degree of saturation and water pressure will reduce significantly in this region. Vapour arising from the drying of the COx claystone will move outwards until it finds a colder region, where it will condense, causing a local increase in water saturation. Vapour diffusion is a significant mechanism of water transfer, and it contributes, but to a much lesser extent, to heat transport.

During the early evolution of the experiment, the hydraulic gradients induced by the open excavations and the thermal gradients due to the heating are the main drivers for the transient flow and deformation phenomena. Infact, owing to the high suction initially present in the annular air-filled gap, hydration will occur, with water moving from the host rock towards the gap and eventually hydration should lead to saturation of the air-filled gap. However great temperature increase supplied by the heater results in water evaporation so that drying a few years after the beginning of the heating phase.

It should also be noted that a few thousand years after the start of repository operations, anthropogenic gradients would vanish but not natural gradients. The surface topography and hydrogeological zones will continue to generate geothermal gradients and regional hydraulic gradients. Natural gradients, though slow, cause changes afterwards. It is expected that the entire repository will be completely saturated, but some of it will become saturated early, depending on local conditions.

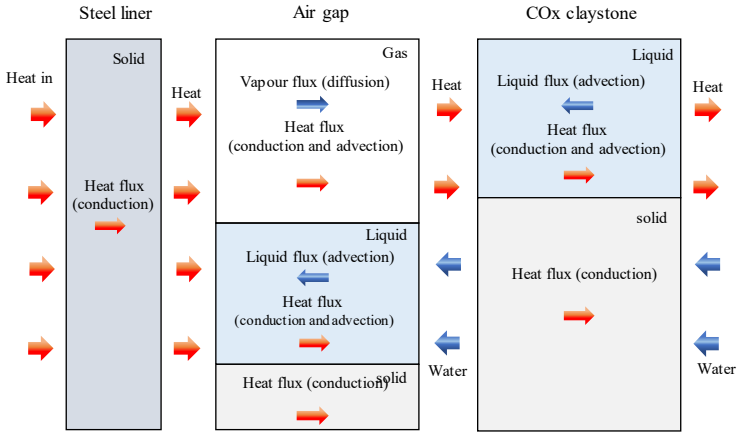

Figure 3.2: Scheme of thermo-hydraulic processes in the near field.

3.1.3 Mechanical process

There are important mechanical phenomena, in addition to the thermohydraulic behaviour. The temperatures and pore pressure evolution will lead to material stresses and strains variations. Inversely, volume changes will affect the hydraulic regime via the consolidation process. Coupling towards the thermal problem also occurs via energy transport by water convection (hydraulic), and by energy loss associated with deformation processes (mechanical). Naturally, the strength and significance of each coupling relationship vary widely (Bai and Abousleiman, 1997 and Zimmerman, 2000).

Insitu observations have revealed that excavation operations induce damage and fracturing around the ALC1604 cell, creating an excavation damaged zone (EDZ), in which the mechanical and hydraulic properties are modified. The tunnel excavation damaged zone extends further in the horizontal direction, suggesting strong anisotropic characteristics of the rock mass. Its configuration is achieved by plotting contours of the cumulative plastic multiplier in a 3D coupled THM model that will be presented in chapter 5.

The tunnel excavation process is expected to induce stress redistribution within a perturbed zone around the openings which leads to trigger the damage propagation. The damage can either be diffuse or localised and can lead to significant changes in the material properties. The excavation process creates the so-called excavation damaged zone (EDZ) in which the mechanical and hydraulic properties are modified. The EDZ geometry can also significantly impact suction distribution, thereby changing thermal conductivity through water saturation.

Moreover, the increase in EDZ hydraulic conductivity could also be inhomogeneous and anisotropic. Besides the change in hydraulic permeability, other properties of COx claystone could change, for instance, thermal conductivity or strength that could be significant when tunnels of large diameters are excavated or excavation is under unfavourable conditions. The thermoplastic behaviour (shrinkage) under a high-temperature load could lead to changes in the mechanism of temperature transport and also increase the permeability in host rock. Also, while the resaturation process, the swelling behaviour could also seal the local fissures.

As mentioned above the effect of anisotropy in tunnelling works has been recently demonstrated in the MHM URL that were excavated in the COx claystone formation (Armand et al. 2013). Mechanical behaviour of steel liner is linked with geometry of EDZ as well, which is more pronounced horizontally and generates rock convergence mainly in the lateral plane as a result. To incorporate the stated anisotropy, a cross-anisotropic formulation which is based on a non-uniform scaling of the stress tensor has been used. Using the material symmetries characteristic of cross-anisotropy, only two scaling factors were considered, one for normal stress components and one for shear stress components. When heating began, the liner diameter variations accelerated until fully taking up the vertical air gap thus resulting in it becoming oval .

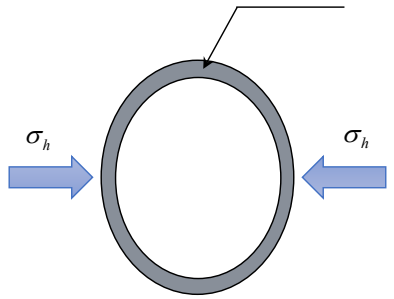

Figure 3.3: Schematic representation of the loading process.

3.2 BASIS OF THE FORMULATION

Processes occurring in a heating experiment in argillaceous rocks can be described in terms of mass and heat transport phenomena in deformable porous media. The fluids in rock, more generally, are pore water and air. Temperature and pressure gradients cause all three phases to flow simultaneously. Each phase may consist of several components and the dispersive and diffusive effects of components within each phase account for transport. Changes in pressure and temperature are further

accompanied by deformation of the porous medium. Mass balance equations can, therefore, be established to determine the spatial and temporal variations of each of the components, within each of the phases present. An energy balance equation determines the temperature variations.

A number of coupled THM formulations have been proposed (e.g. (Gawin et al., 1995; Thomas and He, 1995). The one used in this thesis has been described previously (Olivella et al. 1994; Gens et al. 1998; Gens and Olivella, 2000; Gens et al., 2011) and it will only be outlined herein. It is based on a multi-phase, multi-species approach. The porous medium should consist of three species: mineral (-), water (w) and air (a), distributed in three phases: solid (s), liquid (l) and gas (g). In the particular form presented here, the mineral phase and the solid phase coincide. However, the liquid phase may contain dissolved air, and the gas phase is a mixture of water vapour and dry air. Local equilibrium is assumed throughout. To construct a well-posed mathematical system for the description of the stress, pore pressure, flux and deformation in the porous medium, equations based on mass and momentum conservation principles need to be introduced. Together with the constitutive laws and equilibrium restrictions, these equations constitute the governing equations.

3.3 BALANCE EQUATIONS

Balance or conservation principles express fundamental physical observations concerning the interaction of a continuum medium and the environment. They reflect the balance of the essential physical measures for the body of interest.

A general balance equation contains three terms: the change concerning the time of a property of the porous material, the divergence of the flux of this property and the rate of production/decay of the property, given by:

$$\frac{\partial}{\partial t}\left(\theta_{\psi}\cdot\rho\right)+\nabla\cdot\left(j_{\psi}\right)-f^{\psi}=0 \qquad (3.3)$$

where $\theta_{\psi}$is the mass content of ψ per unit volume, j_{ψ} is the total mass flux of ψ and f^{ψ} is the rate of production/decay of ψ per unit volume. Using a compositional approach, the volumetric mass of a species in a phase θ_{ψ} is the product of the mass fraction of that species, ω_{ψ}, and the bulk density of the phase,ρ. The total mass flux of a species in a phase,j_{ψ}, can be decomposed into an advective flux caused by fluid motion and non-advective flux, and advective flux caused by solid motion, to simplify the equations.

3.3.1 Mass balance of water

This balance equation introduces the state variableP_l, liquid pressure, which is linked with the Darcy flux $\boldsymbol{q}_l$. As water is present in liquid and gas phases, the total mass balance of water is expressed as:

$$\frac{\partial}{\partial t}\left(\theta_l^w S_l \phi + \theta_g^w S_g \phi\right) + \nabla\cdot\left(\mathbf{j}_l^w + \mathbf{j}_g^w\right) = f^w \tag{3.4}$$

where θ_l^w and $\theta_g^w$are the mass content of water per unit volume of liquid and gas, respectively.$S_l$and S_g is the degree of saturation of liquid and gaseous phases, respectively and ϕ is the porosity. $\boldsymbol{j}_l^w$ and $\boldsymbol{j}_g^w$ are the total water mass fluxes in the liquid and gas phases concerning a fixed reference system and f^w is an external supply of water per unit volume of the medium.

The definition of the material derivative:

$$\frac{D_s}{Dt}(\psi) = \frac{\partial_s}{\partial t} + \frac{d\mathbf{u}}{dt}\cdot\nabla(\psi) \tag{3.5}$$

leads to the following expression of the water mass balance:

$$\begin{aligned}&\phi\frac{D_s}{Dt}\left(\theta_l^w S_l + \theta_g^w S_g\right) + \left(\theta_l^w S_l + \theta_g^w S_g\right)\frac{D_s\phi}{Dt} + \\ &\left(\left(\theta_l^w S_l + \theta_g^w S_g\right)\phi\right)\nabla\cdot\frac{d\mathbf{u}}{dt} + \nabla\cdot\left(\mathbf{j}_l^w + \mathbf{j}_g^w\right) = f^w\end{aligned} \tag{3.6}$$

In saturated materials, the water mass balance can be reduced to the following expression:

$$\frac{\partial}{\partial t}\left(\rho_l\phi\right) + \nabla\cdot\left(\mathbf{j}_l\right) = f^w \tag{3.7}$$

3.3.2 Mass balance of solid

The mass balance of solid in the medium can be written in terms of porosity:

$$\frac{\partial}{\partial t}\left(\theta_s\left(1-\phi\right)\right) + \nabla\cdot\mathbf{j}_s = 0 \tag{3.8}$$

where θ_s refers to the grain content per unit volume of soil and $\boldsymbol{j}_s$ is the mass flux of solid.

3.3.3 Energy balance for the whole medium

The equation for internal energy balance for the porous medium is established, considering the specific internal energy per unit mass of each phase(E_s, E_l):

$$\frac{\partial}{\partial t}\left(E_s\rho_s\left(1-\phi\right)+E_l\rho_l\phi\right)+\nabla\cdot\left(\mathbf{i}_c+\mathbf{j}_{E_s}+\mathbf{j}_{E_l}\right)=f^Q \tag{3.9}$$

where $\boldsymbol{i_c}$ is the energy flux due to conduction through the porous medium, $\boldsymbol{j_{E_s}}$ and $\boldsymbol{j_{E_l}}$ are advective fluxes of energy caused by mass motions and f^Q is an internal or external energy supply.

3.3.4 Balance of momentum (equilibrium)

If inertial terms are neglected, the balance of momentum for the porous medium reduces to the equilibrium equation for total macroscopic stresses:

$$\nabla\cdot\boldsymbol{\sigma}+\mathbf{b}=\mathbf{0} \tag{3.10}$$

where $\boldsymbol{\sigma}$ is the stress tensor, and $\boldsymbol{b}$ is the vector of body forces.

The main unknowns of the equations are the state variables: solid displacements, $\boldsymbol{u}$ (three spatial directions); liquid pressure P_l; gas pressure P_g; and temperature T.

3.3.5 Thermally induced excess fluid pore pressures

The main thermal related hydraulic phenomenon in COx claystone is the generation of pore pressure due to temperature changes. The temperature increases in COx claystone (and other argillaceous rocks), due to the fact that the thermal expansion of the water is greater than that of the porous skeleton itself, also increases the polar pressure. The low permeability of COx claystone prevents excess pore pressure from disappearing rapidly. In fact, a significant number of interactions merely reflect this phenomenon of pore pressure generation; the water mass balance equation is best considered:

$$\phi\frac{D_s\rho_w}{Dt}+\frac{\rho_w}{\rho_s}\left(1-\phi\right)\frac{D_s\rho_s}{Dt}+\rho_w\nabla\frac{d\mathbf{u}}{dt}+\nabla\left(\rho_w q_l\right)=0 \tag{3.11}$$

where ϕ is the porosity, ρ_w and ρ_s are the water and solid densities respectively, t is time, $\mathbf{u}$ are displacements and q_l is Darcy's liquid velocity. D_s denotes material derivative.

Equation 3.9 can be further developed considering the variation of the liquid and solid densities that, with some simplifications, are assumed to be given by:

$$\beta_w = \beta_{w0} \exp\left[\beta_w \left(p_l - p_{l0}\right) + b_w T\right] \tag{3.12}$$

$$\beta_s = \beta_{s0} \exp\left[\beta_s \left(p_s - p_{s0}\right) + 3b_s \left(T - T_{ref}\right)\right] \tag{3.13}$$

where β_w and β_s are the water and solid compressibility's respectively, and b_w and b_s are the volumetric and linear thermal expansion coefficients for water and the solid grain respectively. p_l is the liquid pressure, p_s is the solid pressure, and T is temperature.

Then Eq. (3.9) becomes:

$$\left[\phi b_w + (1-\phi) 3b_s\right] \frac{D_s T}{Dt} + \phi \beta_w \frac{D_s P_w}{Dt} + (1-\phi) \beta_s \frac{D_s P_s}{Dt} + \frac{d\mathbf{u}}{dt} + \frac{\nabla(\rho_w q_l)}{\rho_w} = 0 \tag{3.14}$$

The generation and dissipation of pore pressure in clay due to changes in temperature can be more easily understood by examining Eq. (3.2). The first term is derived from the differential thermal expansion of the solid and liquid phases. The second and third terms are the changes in the volume of water and the solid phase associated with the change in pore pressure and solid pressure; the fourth term is the change in the volume of the material skeleton (including stress, pore pressure and temperature) and the fifth term corresponds to the flow of water into or out of the clay element considered. The interplay of all these phenomena results in the generation of pore pressure and its evolution over time.

3.4 CONSTITUTIVE EQUATIONS AND EQUILIBRIUM RESTRICTIONS

Besides the state variables, the thermohydromechanical problem is affected by many more. Consequently, closure of the formulation requires further equations to be incorporated in the form of constitutive laws and equilibrium restrictions. The fundamental constitutive laws in the thermal, hydraulic and mechanical form are presented. Although the three basic components of the problem are distinguished, the constitutive equation actually links the various phenomena considered in the formulation together.

The phase changes are assumed to be fast regards to the typical times for these problems. Thus, they can be taken into account in local equilibrium, creating a set of equilibrium restrictions which must be satisfied at all times. This assumption has

the added benefit of not explicitly changing the phase and thus reducing the number of equations.

The constitutive equations and equilibrium restrictions adopted are summarised in

Table 3.1. The following points should be noted:

a) The balances of momentum for fluid phases and dissolved species are reduced to constitutive laws: Darcy's law and Fick's law.

b) Fourier's law: thermal conductivity depends on the porosity and state of hydration of the material through a geometric mean expression.

c) Darcy's law: hydraulic conductivity depends on porosity, on the degree of saturation and, via water viscosity, on temperature.

d) Fick's law is adopted for vapour diffusion. A tortuosity coefficient, , is included to take into account the effect of a porous medium on the diffusion coefficient.

e) The mechanical constitutive law explicitly considers the

f) effects of strains, suction and temperature changes.

Table 3.1: Summary of constitutive laws and equilibrium restrictions.

Equation	Variable name	Equation	Parameter relationships
Constitutive equations			
Darcy's law	Liquid and gas advective flux	$\mathbf{q}_l = -\frac{\mathbf{k}k_{ra}}{\mu_a}\left(\nabla P_a - \rho_a g\right)$ $a = \text{l, g}$	$k = k_0 \frac{\phi^3}{\left(1-\phi\right)^2}\frac{\left(1-\phi_0\right)^2}{\phi_0^{\ 3}}$ $k_{rl} = S_{el}^{1/2}\left[1-\left(1-S_{el}^{1/\beta}\right)^{\beta}\right]^2 \quad k_{rg} = 1-k_{rl}$
Fick's law	Vapour non-advective flux	$i_g^w = -D_g^w \nabla \omega_g^w$ $= -\left(\phi\rho_g S_g \tau D_m^w \mathbf{I}\right)\nabla\omega_g^w$	$D_m^w\left(m^2/s\right) = 5.9\times10^{-12}\frac{\left(273.15+T\right)^{2.3}}{P_g}$
Fourier's law	Conductive heat flux	$\mathbf{i}_c = -\lambda\nabla T$	$\lambda_0 = \lambda_s^{1-\phi}\cdot\lambda_w^{\phi\cdot S_r}\cdot\lambda_a^{\phi\cdot(1-S_r)}$ $\lambda = \begin{bmatrix}\lambda_{\square} & 0 & 0\\ 0 & \lambda_{\square} & 0\\ 0 & 0 & \lambda_{\perp}\end{bmatrix}$
Retention curve	Liquid phase degree of saturation	$S_{el} = \left[1+\left(\frac{s}{P_0}\right)^{\frac{1}{1-\lambda_0}}\right]^{\lambda_0} f_d$	$S_{el} = \frac{S_l - S_{lr}}{S_{ls} - S_{lr}}$ $S_g = 1 - S_L$ $f_d = \left(1-\frac{s}{P_d}\right)^{\lambda_d}$
Phase density	Liquid density	$\rho_l = \rho_{l0}e^{\beta\left(P_l - P_{l0}\right)}$	
	Gas density	$\rho_g = \text{ideal gas law}$	
Phase viscosity	Liquid viscosity	$\mu_l\left(MPa.s\right) = 2.1\times10^{-12}e^{\left(\frac{1808.5}{273.15+T}\right)}$	
	Gas viscosity	$\mu_g\left(MPa.s\right) = \frac{1.48\times10^{-12}\sqrt{273+T}}{\left(1+\frac{119.4}{273+T}\right)}$	
Mechanical constitutive model	Stress tensor	$d\boldsymbol{\sigma} = \boldsymbol{D}d\varepsilon + \boldsymbol{h}ds + \boldsymbol{\beta}dT$	
Equilibrium restrictions			
Henry's law	Air dissolved mass fraction	$\omega_l^a = \frac{P_a}{H}\frac{M_w}{M_a}$	
Psychrometric law	Vapour mass fraction (vapour pressure)	$p_v = p_v^0 e^{\frac{\varphi M_w}{R(273+T)\rho_l}}$	$p_v\left(\text{MPa}\right) = 136075e^{\frac{-5239.7}{273+T}}$

3.5 A TIME-DEPENDENT ANISOTROPIC MODEL FOR ARGILLACEOUS ROCKS

In this section, a constitutive model is described aimed to reproduce the main features of hydromechanical behaviour of the COx claystone, as stated in chapter 2. In particular, it incorporates anisotropy of strength and stiffness, nonlinear isotropic hardening to compensate for plastic deformation prior to peak strength, softening behaviour after the peak, a non-associated flow rule time-dependent deformation and permeability dependency on irreversible strains.

The model is an enhanced version of the elastoplastic model for partially saturated argillaceous rocks first proposed by Mánica (2018), which consists of an elasticity law, plastic flow rule, hardening law, and yield condition. A core of the mechanical part of the model is taken from the Mohr-Coulomb criterion.

3.5.1 Elasticity

The elastic part of the mechanical constitutive law is based on transverse isotropic elasticity, given by the following constitutive matrix:

$$\begin{bmatrix}\sigma_{xx}\\ \sigma_{yy}\\ \sigma_{zz}\\ \tau_{xy}\\ \tau_{xz}\\ \tau_{yz}\end{bmatrix} = \begin{pmatrix} \Delta\left(\frac{E_H}{E_V}-\nu_{HV}^2\right) & \Delta\left(\frac{E_H}{E_V}\nu_H+\nu_{HV}^2\right) & \Delta\nu_{HV}\left(1+\nu_H\right) & 0 & 0 & 0 \\ \Delta\left(\frac{E_H}{E_V}\nu_{HV}+\nu_{HV}^2\right) & \Delta\left(\frac{E_H}{E_V}-\nu_{HV}^2\right) & \Delta\nu_{HV}\left(1+\nu_H\right) & 0 & 0 & 0 \\ \Delta\nu_{HV}\left(1+\nu_H\right) & \Delta\nu_{HV}\left(1+\nu_H\right) & \Delta\left(1-\nu_H^2\right) & 0 & 0 & 0 \\ 0 & 0 & 0 & G_V & 0 & 0 \\ 0 & 0 & 0 & 0 & G_V & 0 \\ 0 & 0 & 0 & 0 & 0 & \frac{E_H}{2\left(1+\nu_H\right)} \end{pmatrix} \begin{bmatrix}\varepsilon_x\\ \varepsilon_y\\ \varepsilon_z\\ \gamma_{x}\\ \gamma_{x}\\ \gamma_{y}\end{bmatrix} \tag{3.15}$$

$$\Delta = \frac{E_H}{\left(1+\nu_{HV}\right)\left[\frac{E_H}{E_V}\left(1-\nu_{HV}\right)-2\nu_{HV}^2\right]} \tag{3.16}$$

where H and V directions correspond, for the case of Callovo-Oxfordian, respectively to the direction in bedding plane (P in Figure 3.4a) and orthogonal to it (S in Figure 3.4b).

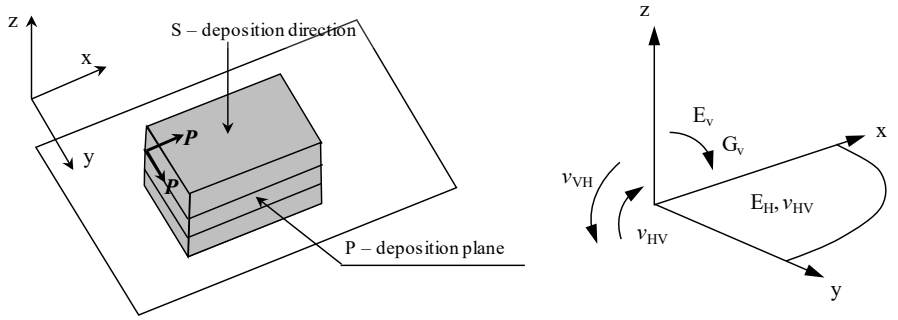

Figure 3.4: Axes orientation for considering transverse isotropy. The z-axis is in the direction of sediment deposition, S, while x and y axes are in the plane of deposition, P (modified after Potts and Zdravkovic, 1999).

The model comprises two main deformation mechanisms: an instantaneous response related to stress changes and a time-dependent response occurring under constant stress. However, the hydro-mechanical coupling will give rise to consolidation, and in this case, both mechanisms will be time-dependent. A generalised effective stress expression has been adopted here:

$$\sigma' = \sigma + p_l B \mathbf{I} \tag{3.17}$$

where σ' is the effective stress tensor, σ is the total stress tensor, S_e is the equivalent degree of saturation (defined below), s is suction, B is Biot's coefficient, and $\mathbf{I}$ is the identity tensor. In the following, the term "stress" always denotes effective stress.

3.5.2 Plasticity

The instantaneous response is described within the framework of elastoplasticity. Under low deviatoric stresses, the response is linear elastic but characterised through a transverse isotropic form of the Hook's law. For higher deviatoric stresses, plastic deformations can take place. An initial, a peak and a residual yield limits are considered. The first one defines a surface in the stress space that separates the elastic and plastic regions, but the material can sustain further loading. On the other hand, the peak limit represents the maximum strength of the material and states beyond this boundary are not allowed. From this point, strength is gradually reduced to its residual value modelled through softening plasticity. The Mohr-Coulomb criterion is used for the initial, peak and residual limits, which in terms of commonly employed stress invariants reads:

$$f = \left(\cos\theta + \frac{1}{\sqrt{3}} \sin\theta \sin\varphi \right) J - \sin\varphi \left(c \cot\phi + p \right) = 0 \tag{3.18}$$

where $p J \theta$ are stress invariants, $\varphi$is the friction angle and c is the cohesion. The initial, peak and residual limits are obtained with Equation 3.16, by using the corresponding strength parameters (ϕ and c). The evolution of the yield surface within these limits is considered through non-linear isotropic hardening/softening, driven by the evolution of the strength parameters. A scalar measure of the plastic strains has been chosen as the state variable controlling this evolution.

$$\varepsilon_{eq}^{p} = \left(\frac{2}{3} \varepsilon^{p} : \varepsilon^{p} \right)^{1/2} \tag{3.19}$$

The friction angle varies in a piecewise manner, as shown in Figure 3.5; the evolution laws corresponding to each zone are given in Table 3.2. Cohesion evolves in parallel with the friction angle according to:

$$c_{mov} = c_{peak} \cot\varphi_{ini} \tan\varphi_{mov} \tag{3.20}$$

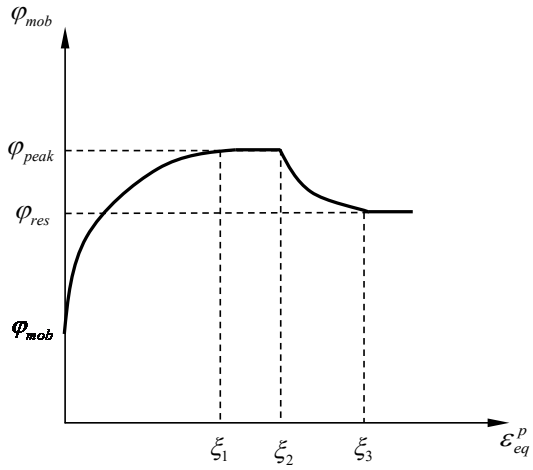

Figure 3.5: Friction angle evolution in hardening and softening regimes (Mánica, 2018).

Table 3.2: Evolution laws for the mobilized friction angle (Mánica, 2018).

Zone 1	$\varphi_{mob} = \varphi_{ini} + \dfrac{\varepsilon_{eq}^{p}}{a_{hard} + \left(\varepsilon_{eq}^{p} / \Delta\varphi_{hard}\right)}$, $\Delta\varphi_{hard} = \dfrac{\xi_1}{\left[\xi_1 / \left(\varphi_{peak} - \varphi_{ini}\right)\right] - a_{hard}}$
Zone 2	$\varphi_{mob} = \varphi_{peak}$
Zone 3	$\varphi_{mob} = \varphi_{peak} + \dfrac{\varepsilon_{eq}^{p} - \xi_2}{a_{soft} + \left[\left(\varepsilon_{eq}^{p} - \xi_2\right) / \Delta\varphi_{soft}\right]}$, $\Delta\varphi_{soft} = \dfrac{\xi_3 - \xi_2}{\left[\left(\xi_3 - \xi_2\right) / \left(\varphi_{peak} - \varphi_{ini}\right)\right] - a_{soft}}$
Zone 4	$\varphi_{mob} = \varphi_{res}$

φ_{mob} = mobilized friction angle, φ_{res} = residual friction angle, ξ_1 = equivalent plastic strain at which the maximum strength is reached, ξ_2 = equivalent plastic strain at which softening begins, ξ_3 = equivalent plastic strain at which the residual strength is reached, a_{hard} = constant that controls the curvature of the function in the hardening branch, a_{soft} = constant that controls the curvature of the function in the softening branch.

A non-associated flow rule is adopted in the model. Rather than deriving a specific function for the plastic potential, the flow rule is directly obtained from the yield criterion in the following way:

$$\frac{\partial g}{\partial \sigma'} = \omega \frac{\partial f}{\partial p}\frac{\partial p}{\partial \sigma'} + \frac{\partial f}{\partial J}\frac{\partial J}{\partial \sigma'} + \frac{\partial f}{\partial \theta}\frac{\partial \theta}{\partial \sigma'} \tag{3.21}$$

where g is the plastic potential and ω is a constant that controls the volumetric component of plastic deformations. The model has been extended to consider strength cross-anisotropy through a non-uniform scaling of the stress tensor. This extension is obtained by replacing $pJ\theta$ in Eq. 3.19 by $p_{ani}, J_{ani}, \theta_{ani}$ respectively. These variables are invariants with its usual definition but calculated from the anisotropic stress tensor (σ_{ani}). For the definition of this tensor, we consider an additional local coordinate system oriented with respect to the anisotropic characteristics of the material (Figure 3.6).

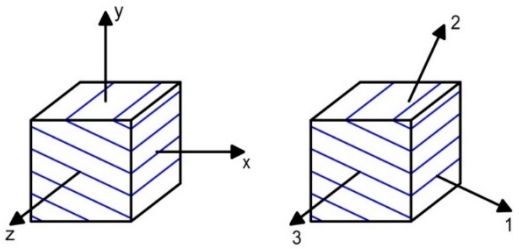

Figure 3.6: (a) Global and (b) local coordinate systems (Mánica, 2018).

Stresses with respect to the local system (σ_r) are evaluated by applying the usual rotation of axes. σ_{ani} is then obtained through the non-uniform scaling of σ_r.

Considering the restrictions imposed by the assumption of cross-anisotropy, the following form is proposed for σ_{ani}:

$$\mathrm{a} = \begin{bmatrix} \dfrac{\sigma_{11}^{loc}}{c_N} & c_s\sigma_{12}^{loc} & \sigma_{13}^{loc} \\ c_s\sigma_{12}^{loc} & c_N\sigma_{22}^{loc} & c_s\sigma_{23}^{loc} \\ \sigma_{13}^{loc} & c_s\sigma_{23}^{loc} & \dfrac{\sigma_{33}^{loc}}{c_N} \end{bmatrix} \tag{3.22}$$

where c_N and c_S are the normal and shear scaling factors, respectively.

3.5.3 Time-dependent response

An additional mechanism is considered for the time-dependent response, characterized by a modified form of the Lemaitre's law. The total strain increment is decomposed as the sum of the two mechanisms:

$$d\varepsilon = d\varepsilon^{ep} + d\varepsilon^{vp} = d\varepsilon^{ep} + \Delta t\left(\dot{\varepsilon}^{vp}\right) \tag{3.23}$$

where $d\varepsilon$ is the total strain increment, $d\varepsilon^{ep}$ is the elastoplastic strain increment, $d\varepsilon^{vp}$ is the visco-plastic strain increment (time-dependent response), dt is the time increment and $\dot{\varepsilon}^{vp}$ is the visco-plastic strain rate tensor. It is assumed that visco-plastic deformations are mainly caused by deviatoric stresses, with strain rates given by:

$$\dot{\varepsilon}^{vp} = \frac{2}{3}\frac{\dot{\varepsilon}^{vp}}{q}s \tag{3.24}$$

$$q = \left(\frac{3}{2}\mathrm{s} : \mathrm{s}\right)^{1/2} \tag{3.25}$$

$$\dot{\varepsilon}^{vp} = \gamma\left(q - \sigma_s\right)^n\left(1 - \varepsilon_{eq}^{vp}\right)^m \tag{3.26}$$

where γ is a viscosity parameter, σ_s is a threshold from which viscoplastic strain is activated, n and m are material constants and ε_{eq}^{vp} is the state variable of the time-dependent response given by:

$$\varepsilon_{eq}^{vp} = \int_0^t \left(\frac{2}{3}\dot{\varepsilon}^{vp} : \varepsilon^{vp}\right)^{1/2} dt \tag{3.27}$$

3.5.4 Hydraulic model enhancement

In the framework of argillaceous materials, the substantial increase in permeability that occurs when the rock is damaged must be considered. To reproduce this phenomenon, permeability cannot be constant but should evolve with growth in damage. This feature is incorporated into the proposed elastoplastic model by including an intrinsic permeability dependence on the plastic multiplier. An exponential function has been adopted:

$$k = k_0 e^{\eta\left(\lambda^p - \lambda_0^p\right)} \tag{3.28}$$

where k_0 is the intrinsic permeability of the intact rock, η is a constant that controls the rate of change, λ^p is the plastic multiplier. As indicated in Eq. 3.26, constant η controls the permeability change rate in excavation damage zone (EDZ) as well as beyond the EDZs, excavation influence zone (EIZ) that involves only elastic change.

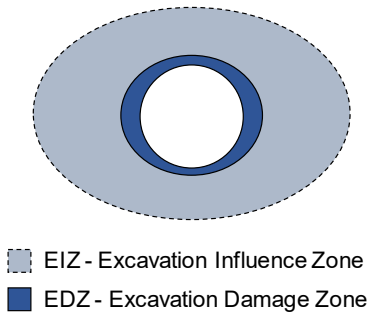

Figure 3.7: Schematic view of the excavation damage zones (EDZ and EIZ).

Based on the observed pore pressure evolution around the tunnel wall, increases of intrinsic permeability is negligible in EIZ. Therefore, The Eq. 3.28 should be modified so that the parameter η is only applied in EDZ. The threshold value for plastic multiplayer has been defined towards this effect. The following equation is suggested and implemented in the code to be used for numerical analysis based on what we discussed above:

$$k = \begin{cases} k = k_0 e^{\eta\left(\lambda^p - \lambda_0^p\right)} & \text{if} \quad \lambda^p > \lambda_{tr}^p \\ k_0 & \text{if} \quad \lambda^p < \lambda_{tr}^p \end{cases} \tag{3.29}$$

where λ_{tr}^p is the threshold value for Plastic multiplayer.

3.6 COMPUTER CODE

All the numerical analyses presented in this thesis have been performed using the computer code, named Code_Bright (Olivella et al., 1996), that is a finite-element code (with some finite volume features) developed in UPC capable of performing coupled THM analyses involving both saturated and unsaturated media.

From state variables, dependent variables are calculated using the constitutive equations or the equilibrium restrictions. The code has been used in many research projects in the context of radioactive waste disposal, and it is very well known in the scientific and technical community dealing with this kind of application. It incorporates a wide range of multi-physics processes and an extensive library of constitutive laws for geomaterial.

The numerical approach to solve the resulting system of partial differential equations can be viewed as divided into two parts: spatial and temporal discretization. Finite-element method is used for the spatial discretization, whereas finite difference method is used for the temporal discretization. The discretization in time is linear and the implicit scheme uses two intermediate points, $t^{k+\varepsilon}$ and $t^{k+\theta}$ between the initial t^k and final t^{k+1} time. Finally, as the problems are nonlinear, the Newton–Raphson method has been adopted to find an iterative scheme.

Chapter 4: The ALC1604 in situ test

4.1 BACKGROUND

The French National Radioactive Waste Management Agency (Andra) began a Callovo-Oxfordian (COx) claystone study as a possible host rock for radioactive waste disposal in the 1990s. A geological investigation covering more than one hundred square kilometres, involving geophysical survey and drilling of boreholes near Bure village, in the eastern part of the Paris Basin, was conducted. In 2000, Andra began building the so-called Meuse / Haute-Marne Underground Research Laboratory (MHM URL) to conduct experiments designed to establish and demonstrate the feasibility of building and operating a COx claystone radioactive waste disposal facility (Figure 4.1).

Experiments in URLs devoted to nuclear waste disposal address two sets of needs: THM characterisation and construction (and operation), which both type of the work performed in URLs have evolved over the years. At the beginning (about 25-30 years ago) the primary purpose was to define and develop methods for managing key scientific and technical issues. All the URLs have turned towards demonstrator development since the early 2000s and even more recently. Demonstration experiments are designed to represent, test and optimize actual potential disposal systems and repository components. The MHM URL also follows this pattern, with the first phase of research until 2006, in which the main objectives were to characterize the confining properties[1] of claystone and to demonstrate that the construction and operation of the geological repository would not lead to pathways for radionuclide migration (Delay et al., 2007).

In 2007, following the 2006 Waste Act[2], Andra began work on the preparation of a license application for the construction of a deep geological disposal facility. In this regard, due to heat-emitting nature of the nuclear waste, the THM behaviour of COx claystone was significant in the design of an underground nuclear waste disposal facility. Therefore, ALC1604 full scale emplacement experiment was launched at the MHM URL to demonstrate the construction feasibility of a High-

[1] Through in situ hydro-geological tests, chemical measurements and diffusion experiments.
[2] Adopted by the French parliament.

Level Waste (HLW) cell and to determine the impact of a thermal loading on the overall behaviour of the cell. The experiment has also been used to acquire new data on the THM behaviour of the surrounding rock and to compare them with those acquired in previous small scale heating experiments (TER and TED insitu heating tests reported in Gens et al., 2013; Garitte et al., 2014).

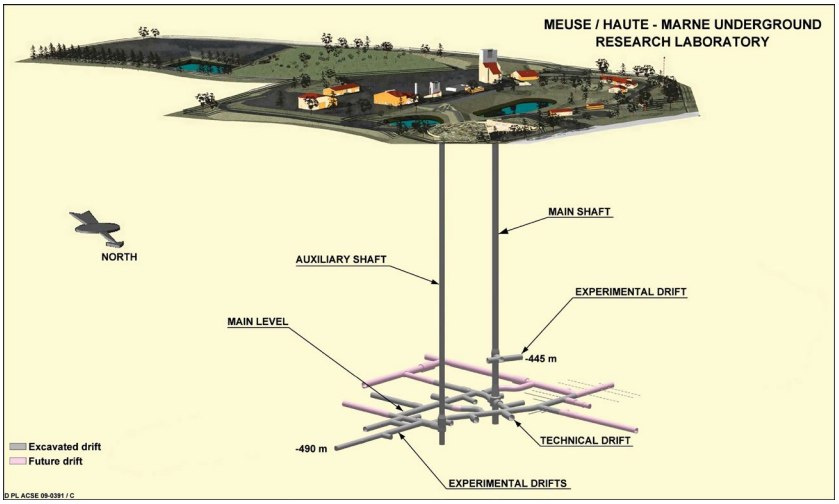

Figure 4.1: Meuse / Haute-Marne Underground Research Laboratory (MHM URL) layout (Andra, 2012).

4.2 HLW CELL CONCEPT

The HLW cell is a microtunnel approximately 40 m long and 0.7 m in diameter, according to Andra's 2009 benchmark concept (Figure 4.2). It comprises a *useful part*, approximately 30 m long, for package disposal and a 10 metre long cell head. They are to be favourably aligned with respect to the natural mechanical stress field. The useful part of the disposal cell, where the packages are placed, has a non-alloy steel casing. The cell base is closed off by a *base plate*, also made of non-alloy steel. A metal radiation-protection plug separates the cell head from the useful part. The cell head has a metal sleeve1 (called the *insert*). The insert is partly backfilled with a swelling-clay plug and then sealed with a concrete plug to provide additional safety. This final configuration corresponds to the period after cell operation and sealing.

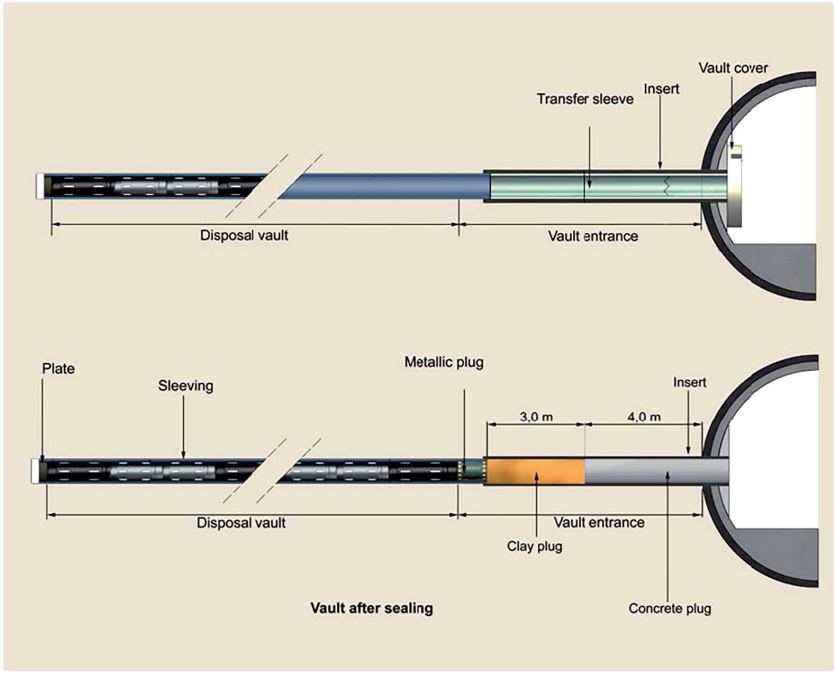

Figure 4.2: General scheme of French repository concept for HLW (Andra, 2013).

4.3 ALC1604 TEST CHARACTERISTICS

A general view of the experiment is shown in Figure 4.3. The characteristics of the ALC1604 cell are as follows:

- total length 25 m, including a *cell head* 6m in length and *cell body* 19 m in length, with an overlap zone 1m in width between the *liner* and *insert*;
- the excavated cell head 0.79 m in diameter, with the installation of an insert 0.76 m in external diameter (i.e. an annular air-filled gap 12mm wide at the radius) and 21 mm in thickness;
- the excavated useful part 0.75 m in diameter, with the installation of a liner 0.7 m in external diameter (i.e. an annular air-filled gap 12 mm wide at the radius) and 20 mm in thickness;
- a base plate, a liner head plate and an insert head plate;
- thermal loading is applied over a length of 15 m at between 10 m and 25 m in depth.

All these characteristics (except for the length) meet the requirements for proving the 2009 concept.

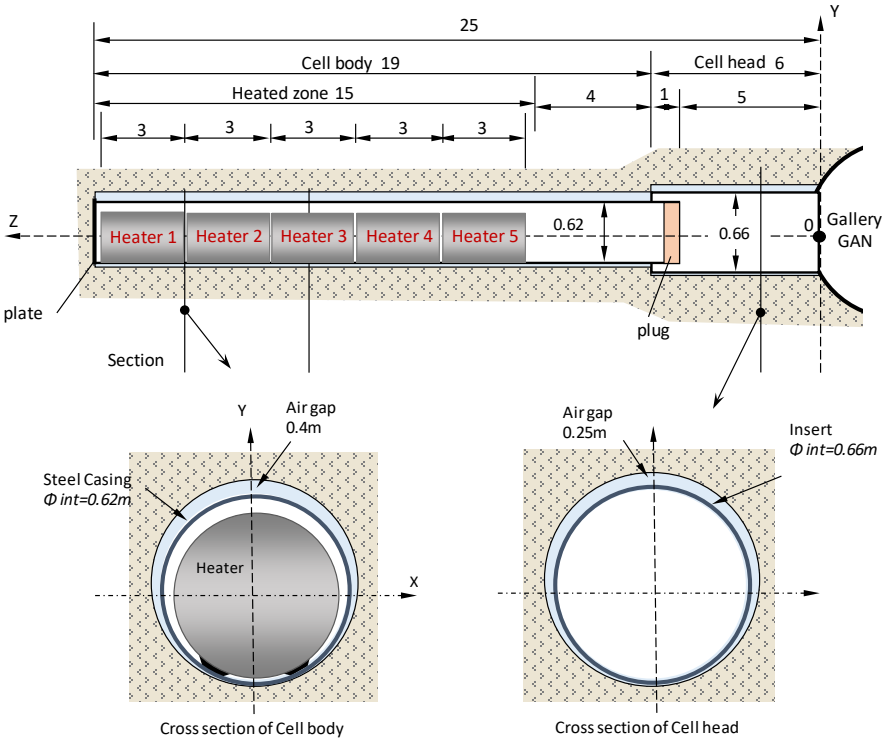

Figure 4.3: HA-ALC1604 in situ test.

4.4 CELL INSTRUMENTATION

The HA-ALC1604 cell has been heavily instrumented from the gallery GAN and the niche NRD as was shown in Figure 4.4. The THM behaviour of the COx claystone has been studied through 9 boreholes that contain 28 temperature sensors, 18 piezometers and one extensometer with 20 points of measurements. The temperature and convergence of the gallery GAN are also instrumented.

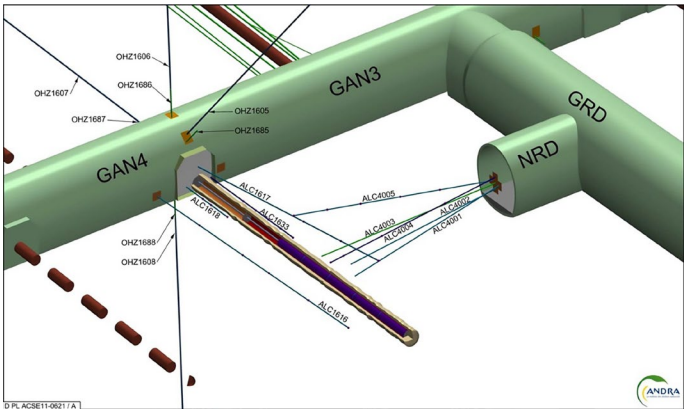

Figure 4.4: General view of the HA-ALC1604 cell in a three-dimensional view (Andra, 2013).

4.4.1 Measurements of the THM behaviour of COx claystone

The instrumentation of the THM behaviour of the COx claystone in the ALC1604 experiment comprises (Figure 4.5):

- Six boreholes with one (ALC4001 and ALC 4002), three (ALC1617 and ALC1618) and five (ALC4005 and ALC 1616) piezometer chambers associated with temperature sensors to measure the pressure gradient from the gallery into the rock mass and the pressure evolution near to the heated zone. These boreholes are backfilled with resin to ensure permeability and low compressibility.
- Two boreholes with five temperature measurements (ALC4003 and ALC1633) installed from the gallery niche NRD and gallery GAN, respectively. The boreholes are backfilled with a mix of bentonite and grout in order to reproduce the characteristics of the rock, mainly its permeability.
- The strain measurement borehole (ALC4004) equipped with 20 extensometers. These boreholes are located perpendicular to the heaters, and it is installed from the NRD niche.

Unlike previous tests (TER and TED experiments), HA-ALC1604 test does not focus only on a specific plane. Figure 4.5 shows a horizontal cross-section that coincides with the bedding plane. It shows all the borehole lines (ALC1916, ALC1617, ALC1618, ALC1633, ALC4001, ALC4002, ALC4003, ALC4004 and ALC4005) as well as all the vertical cross-sections where sensors measurements are available (Z = 3, 4, 4.5, 5, 10, 13 13.6, 14.5, 17.5 and 22 m).

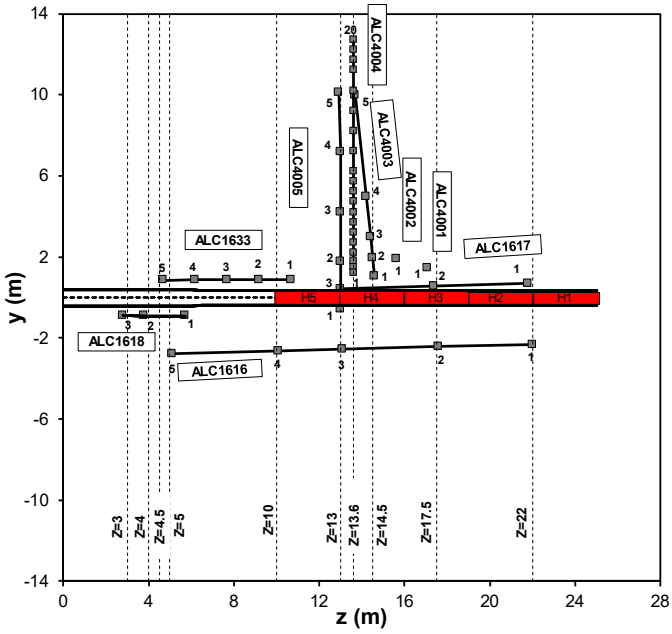

Figure 4.5. Horizontal cross-section of the instrumentation and alveolus arrangement.

4.4.2 Instrumentation on the steel liner and insert

Specific instrumentation is also installed to measure responses of the liner and the contacts with the rock (Figure 4.6). The temperature on steel casing is monitored in 13 sections along the cell. Vertical and horizontal convergence of the casing is measured in six sections in the heated zone and three sections in the non-heated zone. Relative humidity and gap aperture are monitored in the gap between the steel lining and the host rock.

Figure 4.7 shows the location of the liner sections (S1-S4) and insert sections (S11 and S12) equipped with sensors in the cell. Each liner section equipped with sensors contains the following (Figure 4.8):

- six strain gauge sectors at the liner intrados, with an axial gauge and a circumferential gauge for each sector;
- three rock/liner clearance measurement sensor sectors, one at each side and one in the vault;
- a relative humidity/temperature sensor taking a measurement in the annular space 15° below the horizontal axis (Figure 4.9);

- For section 9 (Figure 4.7), two convergence sensors for measuring the horizontal and vertical convergence of the liner.

In addition to these sections equipped with sensors, two temperature profiles are measured (one measurement point per section, 15° from the vertical axis and 15° above the horizontal axis) (Figure 4.10).

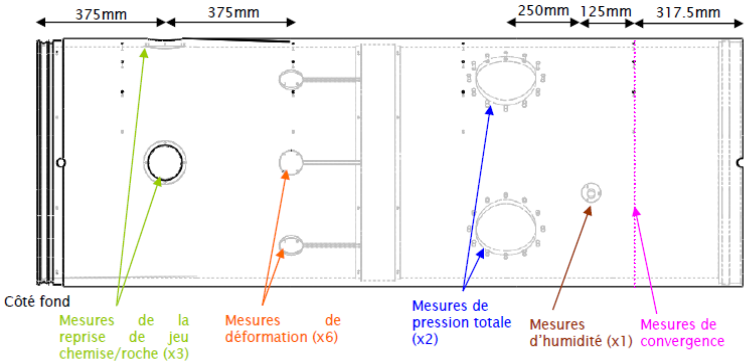

Figure 6 - Détails de l'instrumentation d'une chemise (vue 1)

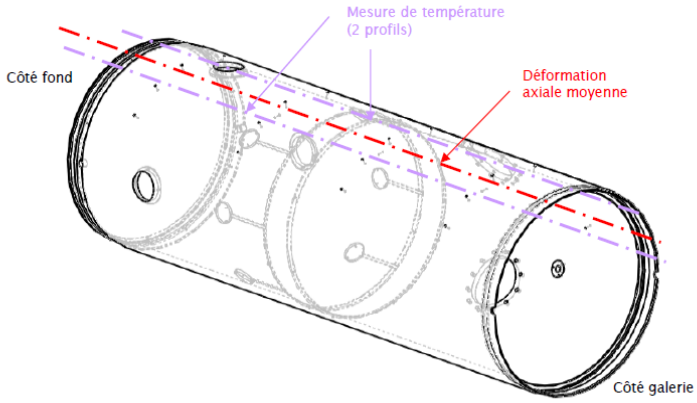

Figure 4.6. Location of the instrumentation on the steel liner.

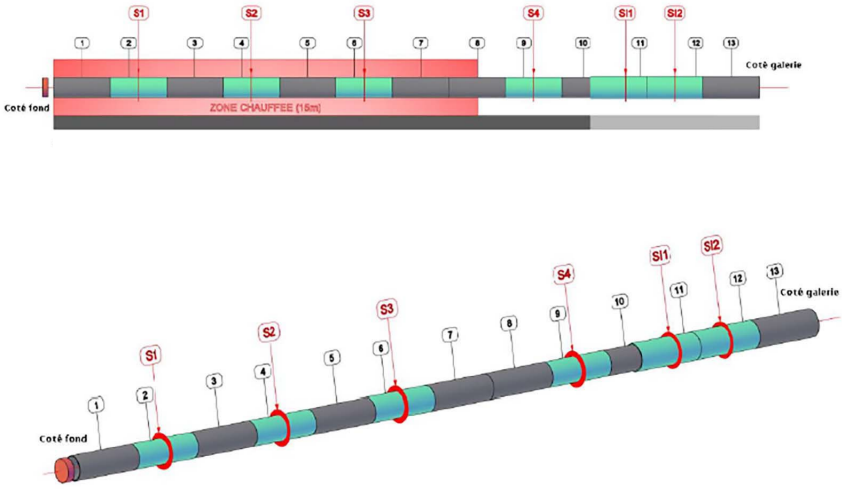

Figure 4.7: Location of the sleeve sections and insert sections equipped with sensors.

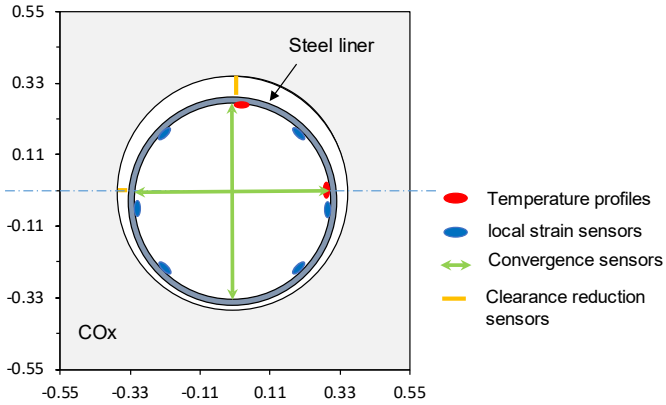

Figure 4.8: Summary of the measurements on each of the three sections of the cell body that are fitted with instrumentation.

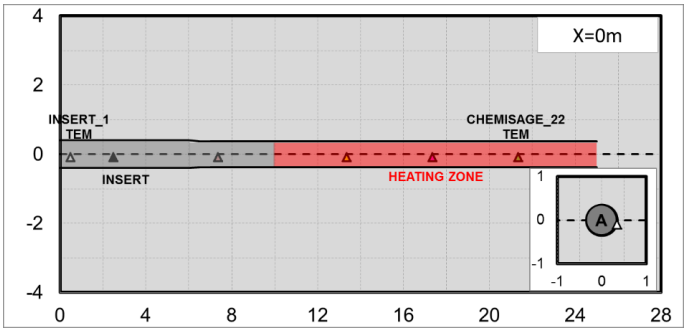

Figure 4.9: Vertical cross-section of the ALC1604 cell (perpendicular to bedding plane) indicating the location of relative humidity measurements at the annular air-filled gap.

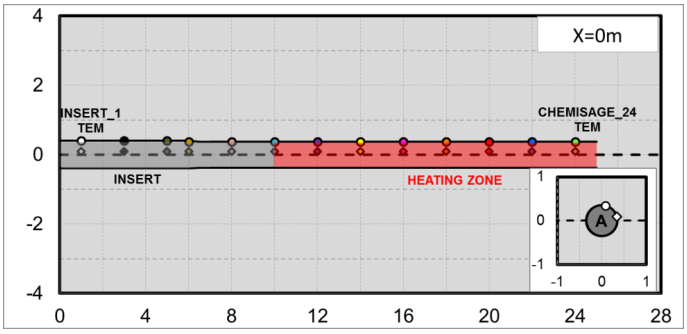

Figure 4.10: Vertical cross-section of the alveolus (perpendicular to bedding plane) indicating the location of temperature measurements.

The two *insert* sections equipped with sensors each contain the following (Figure 4.11):

- six strain gauge sectors on the insert intrados;
- a relative humidity/temperature sensor taking a measurement in the insert 15° below the horizontal axis;
- two convergence sensors for measuring the horizontal and vertical convergence of the insert (Figure 4.12).

Lastly, three displacement sensors fixed to the insert intrados and resting on the useful part's head plate measure the relative displacement of the liner in the insert.

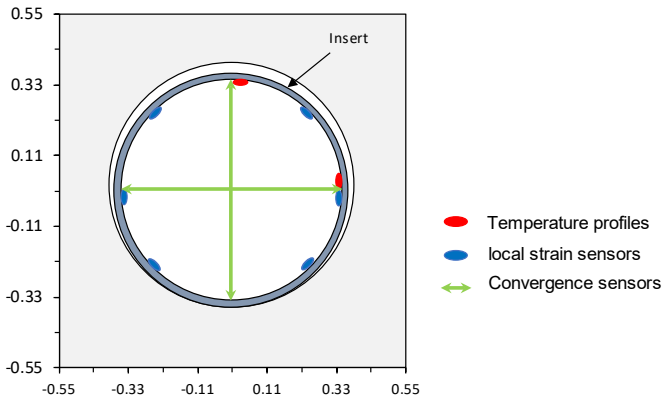

Figure 4.11: Summary of the measurements to be made on each of the three sections of the insert that are fitted with instrumentation.

Figure 4.12: convergence sensors installed on the insert.

4.5 CELL EXCAVATION

The ALC1604 experiment is excavated from the GAN gallery, at the main level (490 m deep, see Figure 4.13). The excavation of the GAN Gallery started in September 2010 followed by the drilling of the ALC1604 cell on 23 October 2012 during seven days. The excavation of the boreholes for the instrumentation sensors started on 31 October 2012. As indicated the Figure 4.13, the cell was excavated on the direction of the major horizontal stress. This fact has important implications for the hydro-mechanical response of the rock around the excavations. Different phases of cell excavation is shown in Figure 4.14.

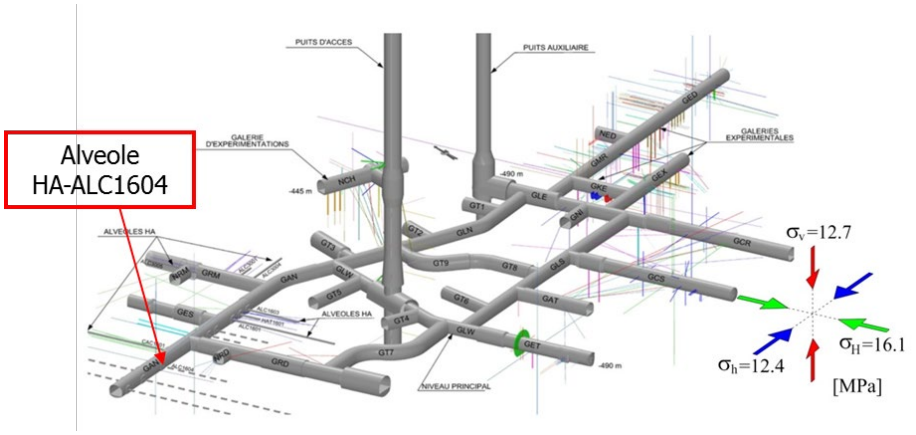

Figure 4.13: Location of the HA-ALC1604 alveolus in a three-dimensional view of MHM URL. The main galleries, as well as the boreholes (Andra, 2012).

(a)

(b)

(c)

(d)

Figure 4.14: phases of cell excavation (a) Drilling station in gallery (b) Drill head in position (c) View of the inserts with guide rails (d) Fixation of the insert at the cell head.

4.6 HEATING PHASE CHARACTERISTICS

Five heaters (H1 to H5), each 3 m long and 0.5 m diameter, are installed in the cell body, contiguously (was indicated in Figure 4.3). Each element is fitted with six transfer skids constructed in highly resistant plastic embedded in metal parts that are themselves welded to the heat source (Figure 4.15).

These skids, which are equipped with small wheels, enabled the heater elements to be easily put into place by rolling them along pre-installed rails. The position of the heater elements is very slightly off-centred downwards by 2 mm.

(a) (b)

Figure 4.15: (a) View of a heater element when it is installed (b) View of a heater/sleeve distance variation sensor section.

After performing a short low-powered heating test (33 W/m) between 30 January and 15 February 2013, the main heating phase began on 18 April 2013 with a constant 220 W/m power supply for the 15 m occupied by the heater elements, at a depth of between 10 and 25 m in the cell. This power was calculated so that a temperature of 90°C would be reached at the liner wall after two years. Heating has been applied in two stages; A cooling stage (also applied in steps) completes the experiment. The test has been completed by the schedule envisaged. During the heating stage of the experiment, the input power will be maintained long enough to achieve a quasi-permanent state, in order to separate the transitory and the steady-state (Table 4.1).

Table 4.1: Stages of HA-ALC1604 experiment.

Step	Phase	Date	Duration
1	Galleries GAN-GRD Excavation	September 9, 2010 → October 23, 2012	775 days
2	Alveoli Excavation	October 23, 2012 → October 31, 2012	56h
3	Boreholes/Instrumentation	October 31, 2012 → January 30, 2013	94 days
4	Heating Test (30W/m)	January 30, 2013 → February 15, 2013	16 days
5	Cooling	February 15, 2013 → April 18, 2013	61 days
6	Heating Stage (220W/m)	April 18, 2013 → February 6, 2019	~6 years
7	First cooling phase (85W/m)	February 6, 2019 → April 8, 2019	61 days
8	Second cooling phase (35W/m)	April 8, 2019 → June 11, 2019	64 days
9	Final cooling phase	June 11, 2019 → August 4, 2025	~6 years

Some punctual power cut-offs episodes have occurred during the experiment; however, they have had a negligible influence on the temperature evolution in the COx and punctual effects on the temperature evolution of the steel casing temperature (Figure 4.16).

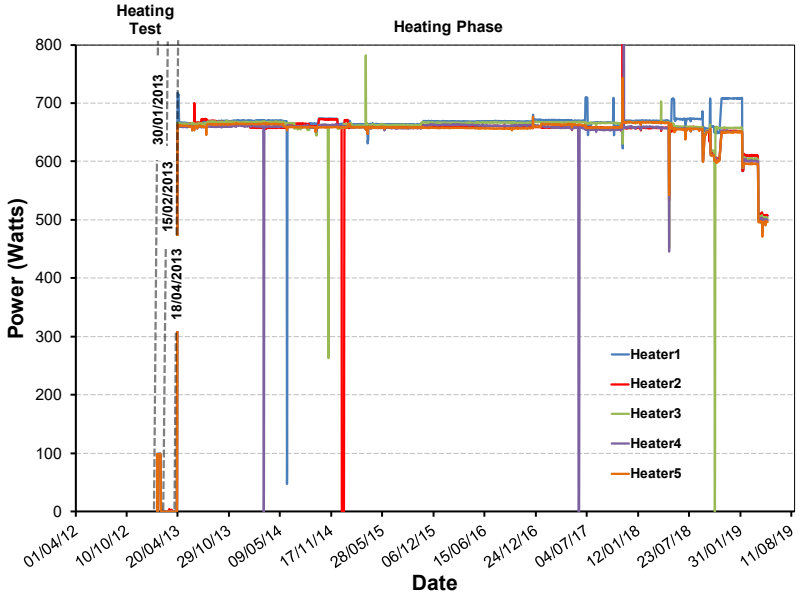

Figure 4.16: Timeline of the ALC1604 experiment with the different heating stages applied until the moment.

Chapter 5: Analysis of thermal response

Appropriate coupled thermohydraulic analysis requires good thermal field representation throughout the domain. On the other hand, given that conduction is the primary relevant heat transfer mechanism in COx claystone, the thermal field is therefore basically controlled by the value of thermal conductivity; the coefficient which, according to Fourier's law, links the conductive flux to the temperature gradient. To this end, the thermal conductivity value of the COx claystone must be determined as accurately as possible. Because the thermal problem is mainly independent of the hydromechanical one, considering the fact that thermal conductivity of the host rock does not change throughout the experiment, it remains saturated, and the changes of porosity are minimal, performing a purely thermal analysis suffices. In this regard, a purely thermal analysis can be performed to find the value of thermal conductivity that achieves the closest agreement with measured temperatures. The aim of this thermal analysis is, therefore, the interpretation of the temperature field obtained during the heating experiment and the determination of the optimum thermal parameters.

5.1 THERMAL PARAMETERS

The main mechanism for heat transfer, as mentioned above, is the conduction. Two parameters are directly related to the thermal conduction problem, *specific heat* and *thermal conductivity*. Both parameters are dependent on the composition of the porous materials: porosity, mineralogy of solid phase and pore fluids.

Specific heat is the amount of heat required to raise the temperature of the unit mass of the material by a given amount (usually one degree). Because of the storage nature of this parameter, a volumetric average considering the different constituents may be applied:

$$\rho \cdot C = \rho_s \cdot (1-\phi) \cdot C_s + \rho_w \cdot \phi \cdot S_r \cdot C_w + \rho_a \cdot \phi \cdot (1-S_r) \cdot C_a \qquad (5.30)$$

Where the "*s*", "*w*", and "*a*" are subscripts stand for solid, water and air, respectively, ϕ is the porosity and S_r is the degree of saturation. The specific heat of the solid phase of the rock measured in laboratory experiments was 800 J/kg/K (Andra, 2005), resulting in values for the saturated porous materials of about 1000 J/kg/K for the COx Claystone (Conil et al., 2010). Because of the lower uncertainty

associated with the specific heat that depends exclusively on the medium composition and not on grain arrangement, these values were assumed to be satisfactory estimates.

Conversely, thermal conductivity, the property of a material that indicates its ability to conduct heat, is not only influenced by the material composition but also by the arrangement of the different constituents. In argillaceous rocks, there is a specific arrangement of the clay particles because of their sedimentary nature. However, as a first approximation, the equation proposed by Farouki (1981) for the isotropic thermal conductivity of a random mixture of several materials can be applied to a porous medium as:

$$\lambda_0 = \lambda_s^{1-\phi} \cdot \lambda_w^{\phi \cdot S_r} \cdot \lambda_a^{\phi \cdot (1-S_r)} \tag{5.31}$$

Significant variations of carbonates or quartz, which are relatively high conductive minerals, are also known to occur in argillaceous rocks as a function of the sediment level and should be considered. The average composition of COx Claystone is 55% of clay, 28% of calcite, 17% of quartz and 15% of porosity. Considering the mineralogy and accounting for a thermal conductivity of the clay component of 1.1 W/m/K, of 0.7 W/m/K for the water and 3.75 and 8 W/m/K for calcite and quartz crystals respectively, a first-order approximation of the saturated thermal conductivity of the COx Claystone of 1.8 W/m/K can be obtained.

From the different laboratory experiment campaigns carried out on saturated COx claystone samples, it is well established that thermal conductivity of COx Claystone is anisotropic, exhibiting different values in the directions normal and parallel to bedding. With the coordinates aligned adequately, Fourier's law becomes:

$$i_c = \begin{bmatrix} \lambda_{par} & 0 & 0 \\ 0 & \lambda_{par} & 0 \\ 0 & 0 & \lambda_{per} \end{bmatrix} \tag{5.32}$$

where λ_{par} and λ_{per} are the thermal conductivity values in the bedding plane and the perpendicular direction, respectively.

A sufficient number of temperature measurements on COx Claystone samples were indicated average values of 2 W/m/K and 1.3 W/m/K for the parallel and the perpendicular thermal conductivity values respectively (Andra, 2005), therefore, it is in principle possible to estimate the thermal conductivity values form a back

analysis of an in situ heating test as the thermal problem is mainly independent of the hydromechanical one.

Taking these values as a departure, a three-dimensional sensitivity analysis has been performed to back-analyse the value of thermal conductivity that achieves the closest agreement with measured temperatures of the experiment. A slight variation of 2.5% has been found with respect to the reference values in both directions: 2.05 W/m/K along bedding planes and 1.33 W/m/K orthogonal to it.

5.2 EVOLUTION OF APPLIED POWER

After a short low-powered heating test (33 W/m), the main heating phase started with a constant 220 W/m power supply for the 15 m occupied by the heater elements (the nominal power of 660 W was reached in each heater). This power was calculated so that a temperature of 90°C would be reached at the liner wall after two years. Conversely, to past THM experimental tests, the nominal power was imposed in one single step; a cooling stage (applied in steps) completes the experiment.

The power applied during the different phases of heating and cooling for the ALC1604 experiment is given in Figure 5.1. As shown in the figure, during the heating stage, the input power has been maintained long enough to achieve a quasi-permanent state, in order to separate the transitory and the steady-state. Some punctual power cut-offs episodes have occurred during the experiment; however, they have had a negligible influence on the temperature evolution in the COx claystone and punctual effects on the temperature evolution of the steel casing temperature. The consequences of these successive faults, caused by the failure of the control cabinet fans, was reduced by the fact that the other four heater elements were operating normally. The liner temperature evolution also is added, to show the temperature response to the power input Figure 5.2.

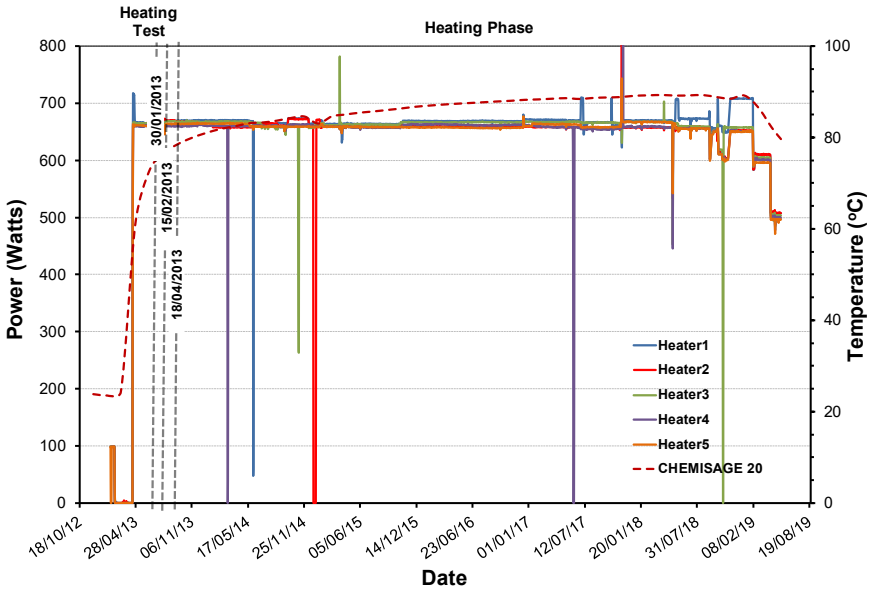

Figure 5.1: Evolution of the power applied in ALC1604 cell insitu test.

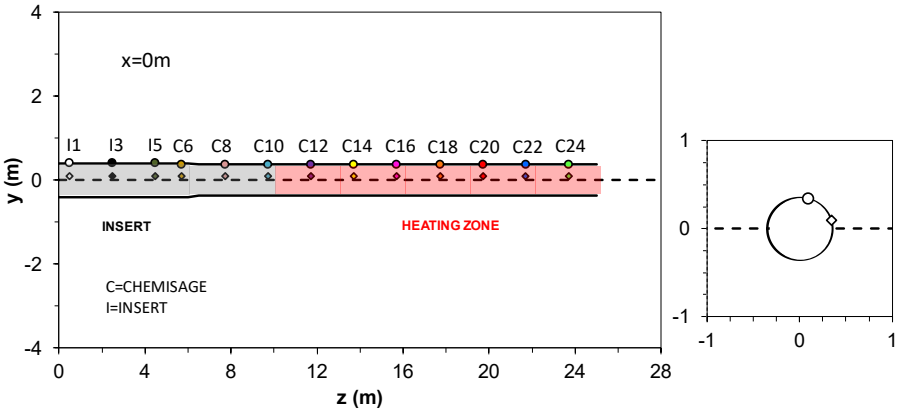

Figure 5.2: Vertical cross-section of the ALC1604 cell (perpendicular to bedding plane) indicating the location of temperature measurement sensor CHEISAGE_20 on the liner.

The gallery GAN influences the COx claystone temperature evolution at a certain distance from the gallery wall. Until 5 meter inside the mass rock, the evolution of temperature is the combination of the periodic temperature changes in the gallery GAN and the input power in the heated zone, which is shown in Figure 5.3 together with the temperature measured in the gallery GAN, to show the influence of the gallery.

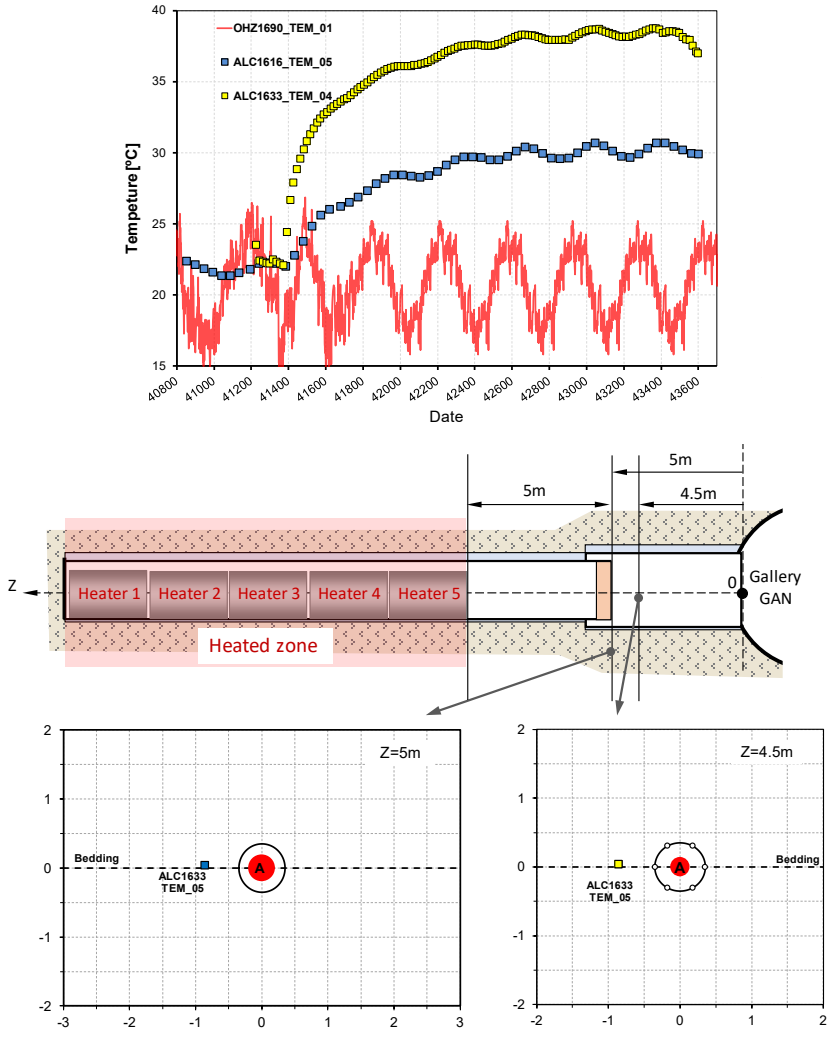

Figure 5.3: Layout of ALC1604 in situ test indicating instrumented sections a) Z=4.5m b) Z=5m. Evolution of temperature at 5 m from the gallery wall.

This influence of the temperature fluctuation in the gallery GAN is also registered at some meters inside of the casings and the gap between the COx claystone and the casings (Figure 5.4, Figure 5.5 and Figure 5.6). The overall evolution of the casing temperature was therefore little affected by above mentioned heater faults. For the main heat output of 220 W/m, the heaters lead to maximum temperature increases of about 90°C for the liner at the centre of the heated zone

after two years, and about 80°C at the gap between the steel casing and the host rock.

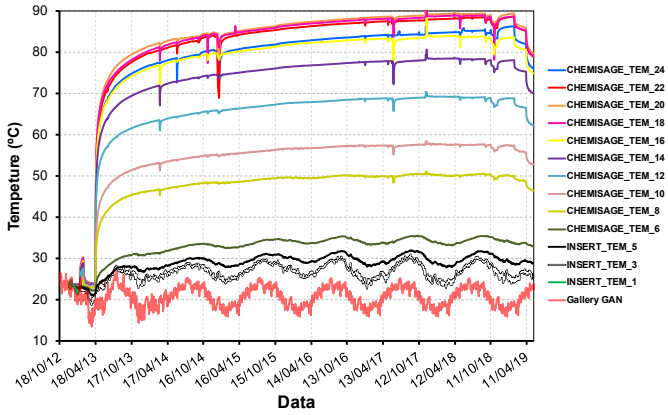

(a)

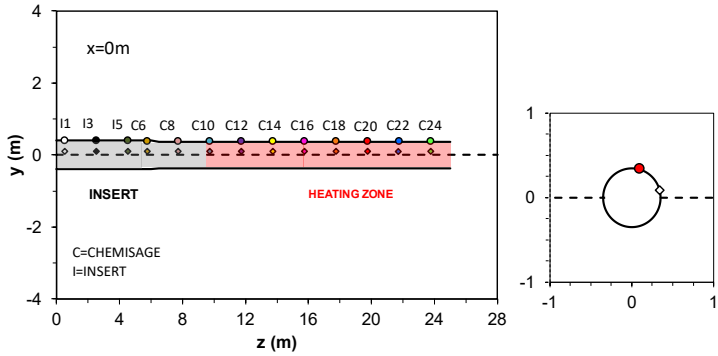

(b)

Figure 5.4: (a) Evolution of temperature in the casing at vertical measurement sensor; together with gallery GAN temperature evolution (b) location of observation points on the casing.

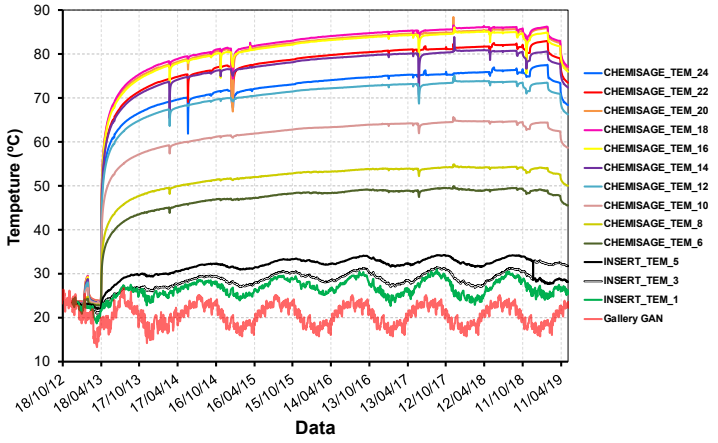

(a)

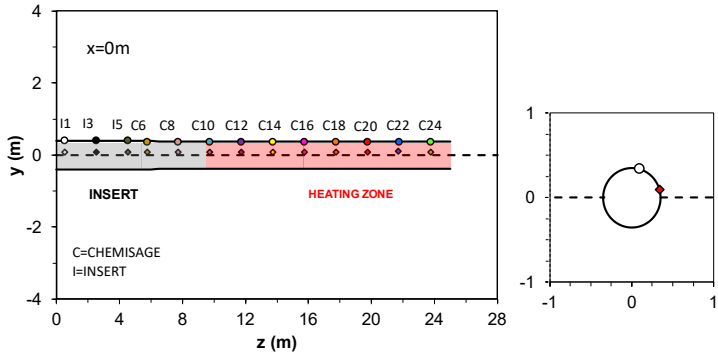

(b)

Figure 5.5: (a) Evolution of temperature in the casing at horizontal measurement sensor; together with gallery GAN temperature evolution (b) location of observation points on the casing.

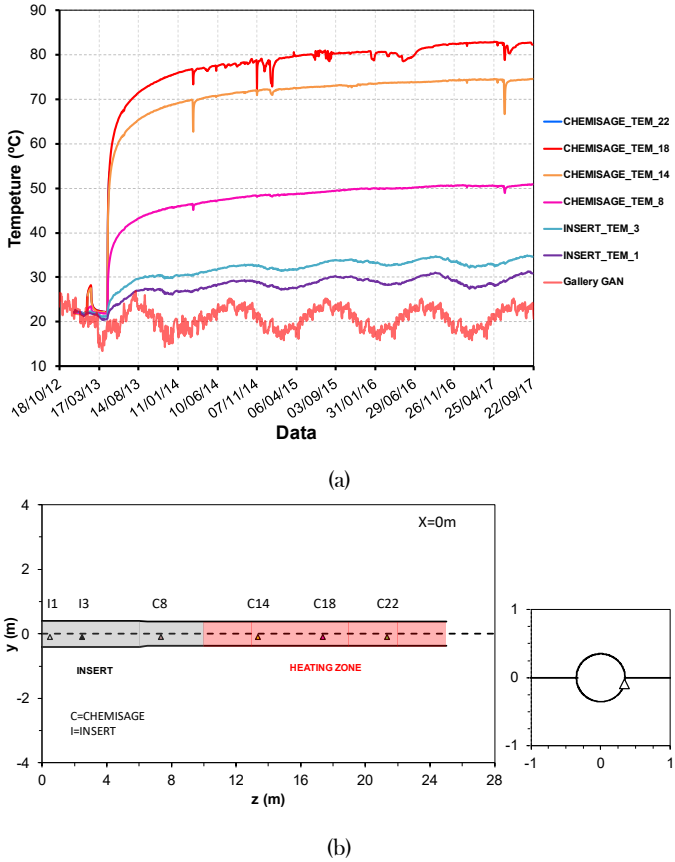

Figure 5.6. Evolution of temperature in the gap between the steel casing and the host rock; together with gallery GAN temperature evolution (b) location of observation points on the casing.

Figure 5.7 shows a comparison between two sensors located near (ALC4003_TEM_01) and far away (ALC4003_TEM_01) from the heaters. Both sensors indicate a marked increase in temperature when the input power started suggesting that the existence of heat flow from the open part of the alveolus. This mechanism will be explored in detail during the numerical modelling.

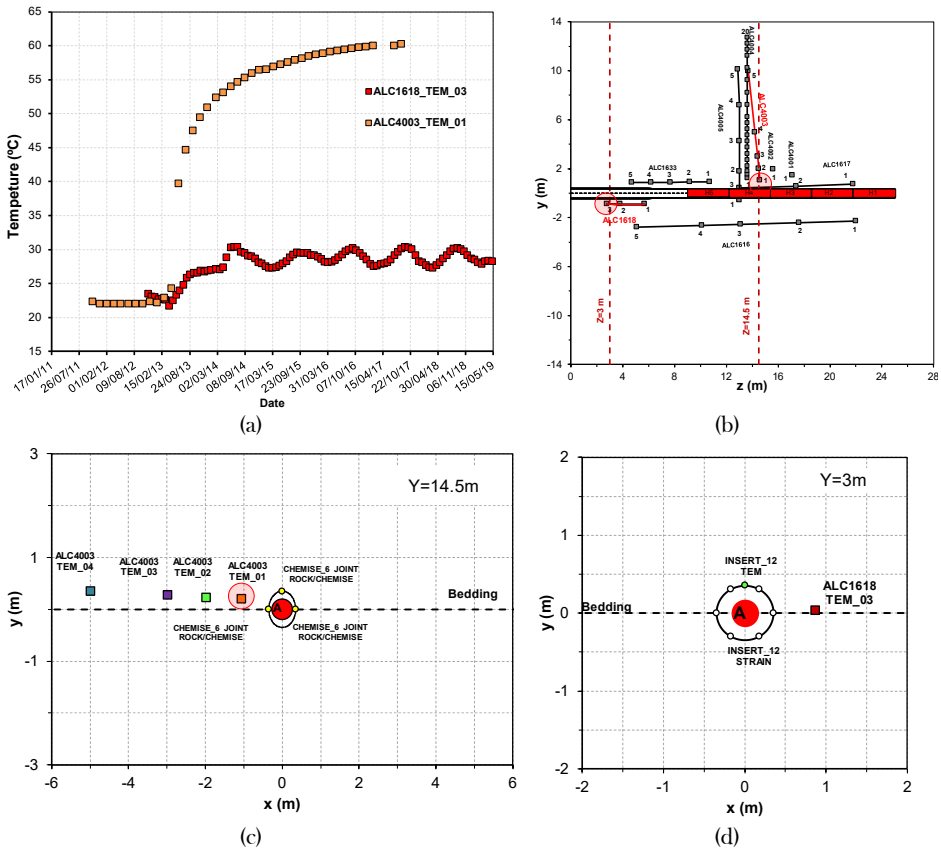

Figure 5.7: Evolution of temperature in the sensors ALC1618_TEM_03 and ALC4003_TEM_01.

The influence of the input power of the heaters covers a large area around the cell. Figure 5.8 depicts the evolution of temperature at sensor ALC4003_TEM_05 located at 10 meters from the heaters in a section at 13.6 m from the gallery wall. It experiences an increase of 4°C since the input power activation. This observation will be used to define the size of the computational domain and put the boundary conditions at a distance where it is expected not to influence the temperature field during the whole test duration. Temperature evolution also shows some small temporal variations generated by the influence of the niche NRD from which the borehole was drilled.

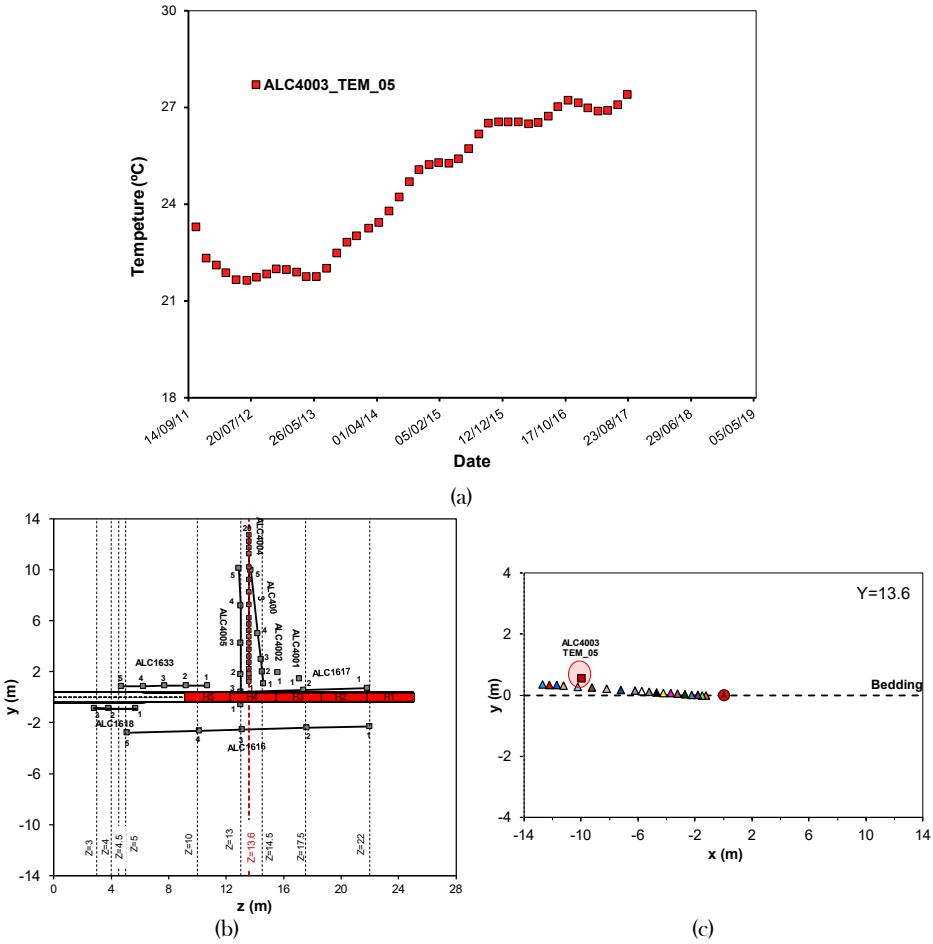

Figure 5.8. Evolution of temperature in the sensor ALC4003_TEM_05.

Conversely to TED experiment, instrumentation was not designed to monitor a specific cross-section of ALC1604 experiment but to provide temperature measurements all around the test. A corollary of that is the difficulty to compare measurements at the same distance from the heaters and in different directions with respect to the bedding plane. In fact, only two sensors in the section located at 13 meters from the gallery wall (ALC1617_TEM_03 and ALC1616_TEM_03) obey to this criterion. Unfortunately, sensor ALC1617_TEM_03 became damaged and did not provide temperature evolution at the corresponding point (Figure 5.9). As a consequence, evidence of anisotropic thermal field can be only obtained by analysing the temperature output by numerical simulations that match the measurements.

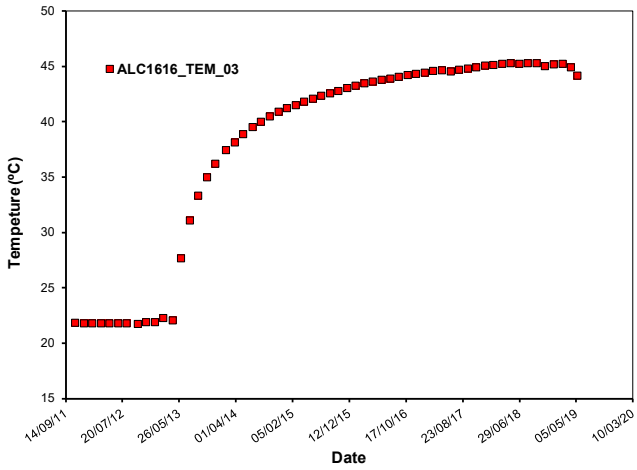

(a)

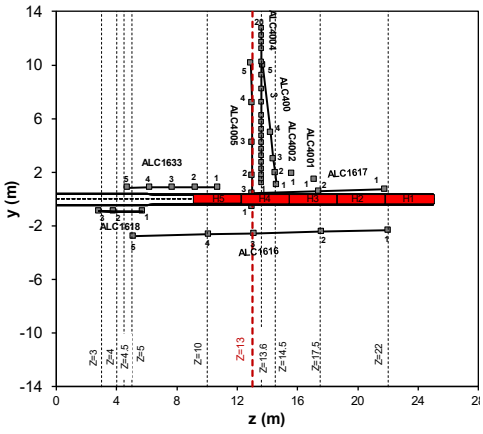

(b)

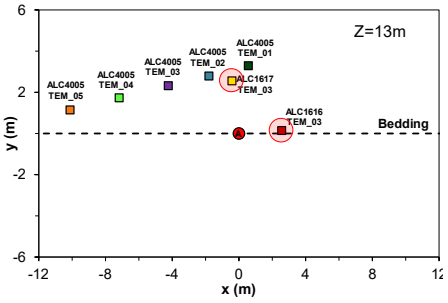

(c)

Figure 5.9: Evolution of temperature in the sensor ALC4003_TEM_05.

5.3 THERMAL MODELLING

Although the finite element code *Code_Bright* allows for the performance of coupled THM analysis, only the energy balance equation is solved at this stage of the work. Thermal calculations have been performed from the thermal parameters determined in the TED experiment to determine the thermal parameters that better match the simulation and measurements.

5.3.1 Domain discretisation

The insitu heating experiment has been numerically simulated by use of a 3D model in order to reproduce the characteristic anisotropic features of the rock mass. The mesh used in this computation contains about 122 000 hexahedral elements and 129 000 nodes. The domain and the finite element mesh used are depicted in Figure 5.10.

The reference axis system corresponds to the local system defined for the ALC1604 experiment (Andra, 2013): x-axis follows the centreline of the cell, y corresponds to the vertical axis, and z is perpendicular to both. Origin is located at the alveolus section intersecting the GAN gallery. The computational domain has been divided into several parts that compose the cell, including the five sections that represent the heaters (H1 to H5). Finally, a section with the same length of the cell is considered in order to evaluate the heated zone in the host rock. The mesh has been refined near the gallery and near the alveolus, in order to be able to cope with the high temperature (and subsequently pore pressure) gradients in this zone.

The model includes the host rock domain, insert, lining and the gaps between the insert and the COx claystone, the inset and the lining and the lining and the COx claystone (Figure 5.11). The gap will be addressed as a continuous medium for computational purposes. The discontinuous behaviour of this "material" at time of gap closure is modelled through a bi-linear elastic constitutive law. According to the experiment layout, the lining lies on the rock at the bottom of the alveolus. Thus, both insert, lining and gaps are eccentric concerning the centreline of the alveolus.

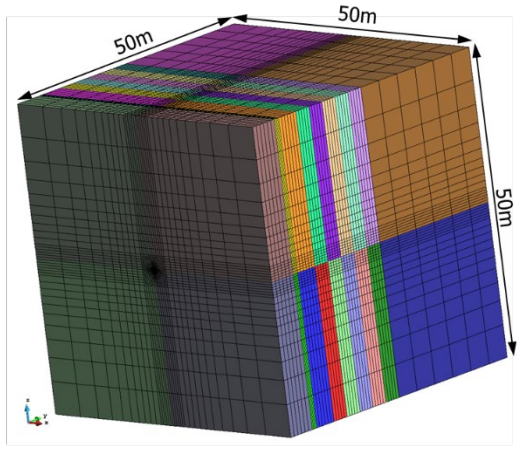

(a)

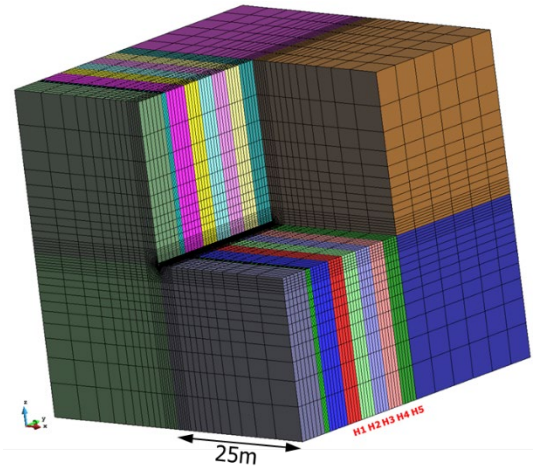

(b)

Figure 5.10: The geometry of the 3D mesh used for the thermal simulation.

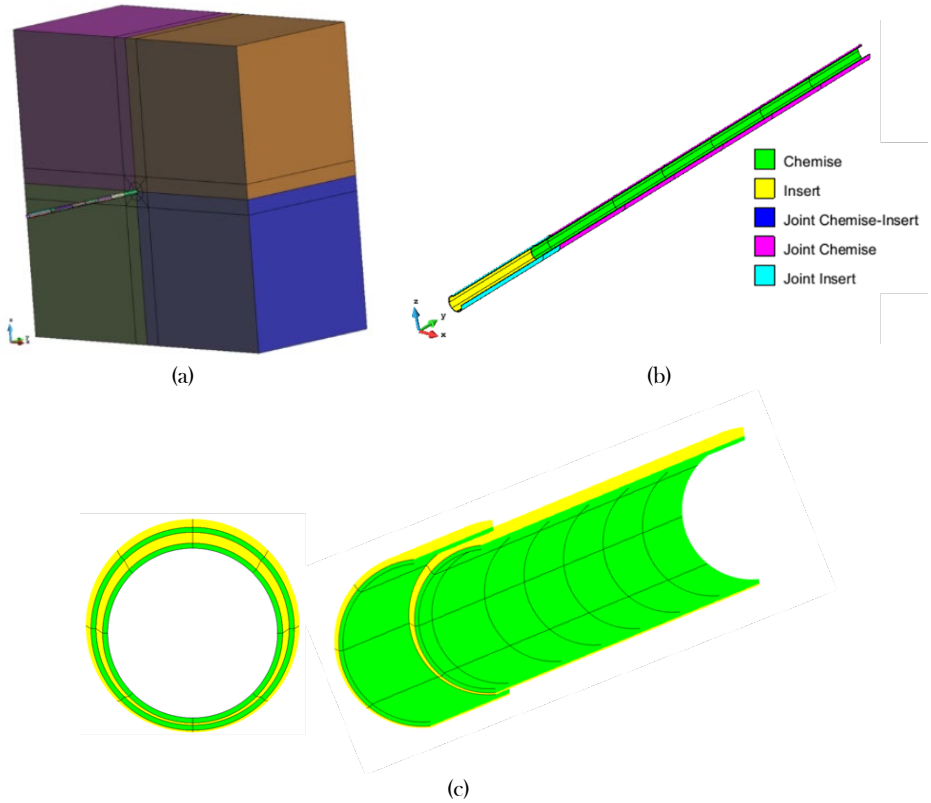

Figure 5.11: Geometry of the 3D model used for the steel casings and gap.

5.3.2 Initial and boundary conditions

The initial and boundary conditions are depicted in Figure 5.12. Heat fluxes have been prevented on all faces, except on the back, where the temperature is prescribed to 21.82°C. A particular aspect relies on the influence of temperature changes of GAN and GRD galleries on the values of temperature at the sensors close to the gallery wall. Consequently, a specific boundary condition has been applied at the loci corresponding to gallery walls (see Figure 5.12). It prescribes a continuous-time evolution of temperature according to measurements taken in gallery OHZ1690. This condition has been applied since 9th September 2010, date of GAN gallery excavation.

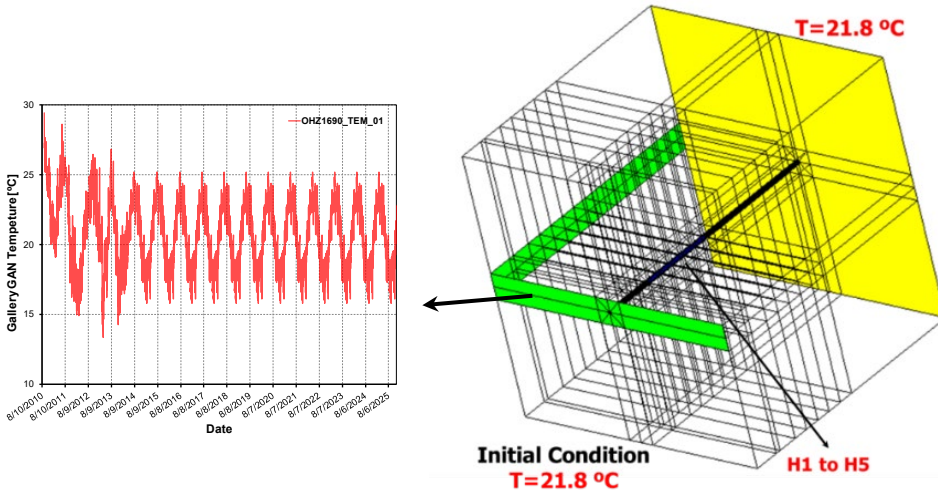

(a) (b)

Figure 5.12. Initial and boundary conditions applied.

Another aspect corresponds to the boundary condition to prescribe in the non-heated part of the cell. As shown in Figure 5.13, there no isolation between the heater and the non-heated part of the cell. As such, part of the power input will heat the air inside, leading to air convection in the empty zone of the cell.

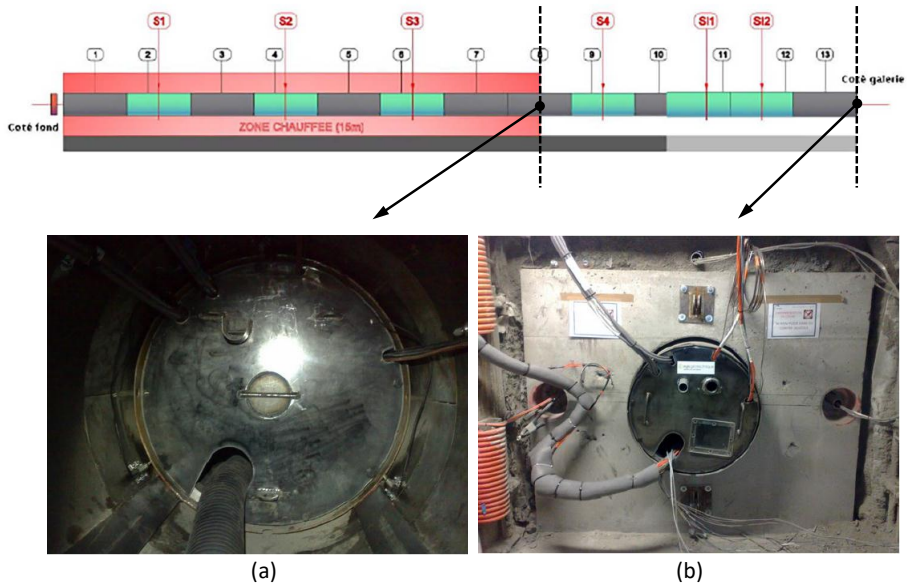

Figure 5.13: layout of ALC1604 insitu test. (a) installed plate at the end of cell body (b) installed plate at the insert head.

Considering this phenomenon several cases have been considered:

- The case in which the heaters are thermally isolated (Figure 5.14a). The total power input is applied directly in the heater zone. Results evidence that temperature measurement in front of the heated zone cannot be well reproduced.
- Different cases where a small part of the power input to the heaters is removed from the heated zone and applied in the non-heated zone (Figure 5.14b). After a trial-error procedure based on the comparison between computed and measured temperatures in front of the heated and non-heated zone, the value of flux to apply in the non-heated zone has been determined.

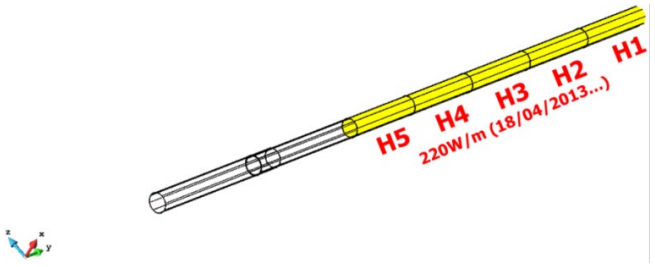

(a)

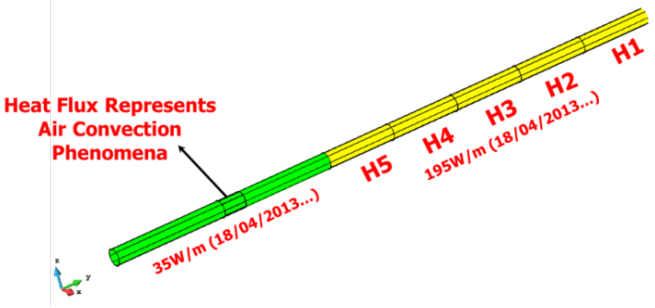

(b)

Figure 5.14. Heat fluxes applied in the heating phase. (a) Isolated heaters (b) Non-isolated heaters.

5.3.3 Material Parameters

The thermal parameters of the COx claystone have been intensively investigated since 1990 by Andra (Andra, 2012). Table 5.1 gives the values obtained in the laboratory for the thermal conductivity along and orthogonal to the bedding plane.

Table 5.1: Laboratory measurements of thermal conductivity in the Callovo-Oxfordian Clay in the TED area (Conil et al., 2010).

		DBE	LAEGO
Thermal conductivity parallel to bedding	$\lambda_{\parallel}$[W/m/K]	1.96±0.07	1.89±0.05
Thermal conductivity perpendicular to bedding	$\lambda_{\parallel}$[W/m/K]	1.28±0.06	1.26±0.05

A specific heat equal to 1025 J/kgK for the saturated material (corresponding to a specific heat equal to 800 J/kgK for the solid phase) has been assigned to the host rock. As discussed before, values of the thermal conductivity along the bedding plane and orthogonal to it have been back analysed to match temperatures at all the

sensors. Values used for the final modelling are indicated in Table 5.2. They are 2.5% higher than the reference values (2 and 1.33 W/m/K, respectively) and within the range of values measured experimentally (Table 5.1). The thermal parameters of the casing and gap are given in Table 5.2. The low value of thermal conductivity assigned to the gap corresponding to the air at 100 kPa.

Table 5.2: Reference parameters of the Callovo-Oxfordian clay adopted in the simulations.

Properties	Parameters	Symbol	Value	Units
Physical	Porosity	ϕ	15	%
Thermal	Thermal Conductivity	$\lambda_{//}$	2.05	W/m/K
		$\lambda_{\perp}$	1.33	W/m/K
	Specific heat of solid	C_s	800	J/kg/K

Table 5.3: Reference parameters of the gaps and steel lining adopted in the simulations.

	Porosity	Thermal Conductivity (W/m/K)	Specific heat of solid (J/kg/K)
Gaps	0.98	0.35	1100
Steel lining	0.01	80	550

5.3.4 A short overview of some numerical results

Before presenting in the next section, a full comparison between computed and measured temperatures at all sensors, some aspects of the model are briefly discussed in this paragraph.

The first aspect concerns the anisotropic character of the thermal field. Figure 5.15a shows a three-dimensional intersection of the temperature bulb with three planes: 1) a horizontal plane passing through the centreline of cell; 2) a vertical plane passing through the centreline of cell and 3) a vertical plane orthogonal to the cell and passing through the end of the heater. Figure 5.15b shows the contour map of temperature iso-values for a vertical plane orthogonal to the alveolus and passing through the middle of the heaters. One can observe in the two figures the elliptical shape of the temperature bulb in the vertical plane.

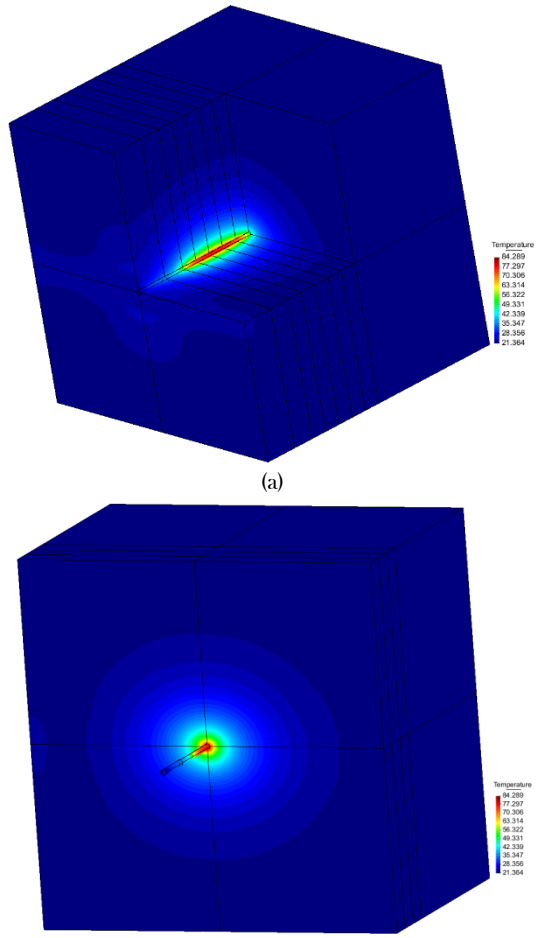

Figure 5.15: Three-dimensional view of computed contours of equal temperature at the end of the computation.

The second aspect concerns the slight eccentricity of the temperature bulb due to the contact existing between the casing and the host rock at the bottom of the cell. This aspect is shown in Figure 5.6, slightly higher width of the heated zone below the cell than on top of it as well as higher temperature at the bottom of the cell in the heated zone.

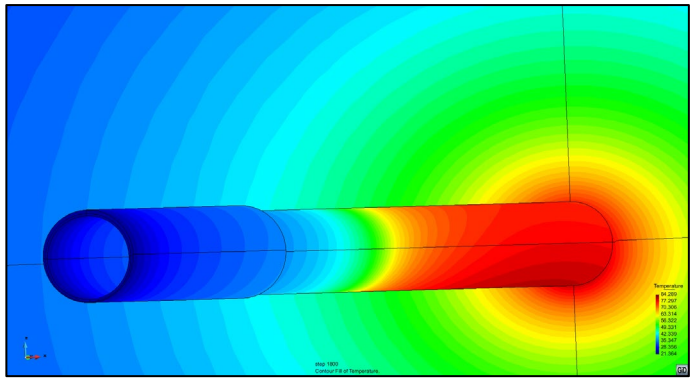

Figure 5.16: Three-dimensional view of computed contours of equal temperature in the steel casings.

The third aspect concerns the distribution of temperatures with and without application of heat flux within the non-heated zone. Figure 5.17 shows a comparison of both models against temperatures measured in front of the non-heated zone (sensors ALC1616_TEM_05 and ALC1633_TEM_05). In both cases, the discontinuous line corresponds to the model with heat flow applied in the non-heated zone. It fits much better the measurements than the model without heat flow (continuous line). The bulb of temperatures in both cases are also shown in Figure 5.18.

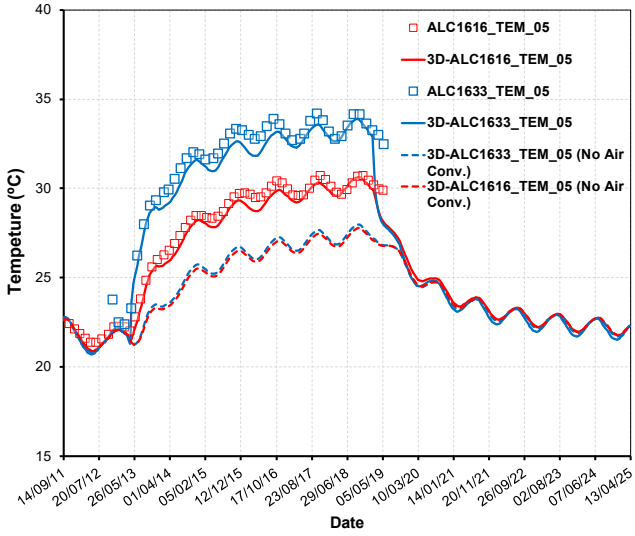

(a)

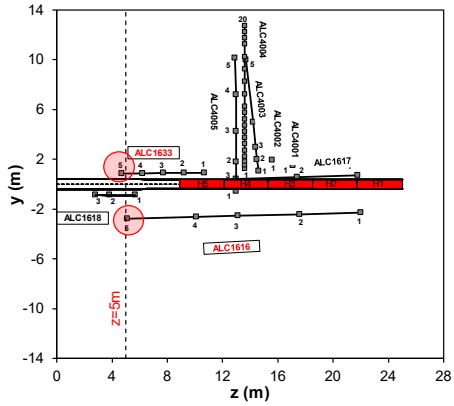

(b)

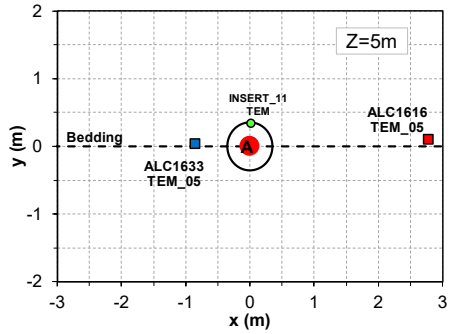

(c)

Figure 5.17: Temperature evolution of sensors located on the same section as the heaters (5 m deep from the gallery). The measurements (dots) are compared with the simulation (lines).

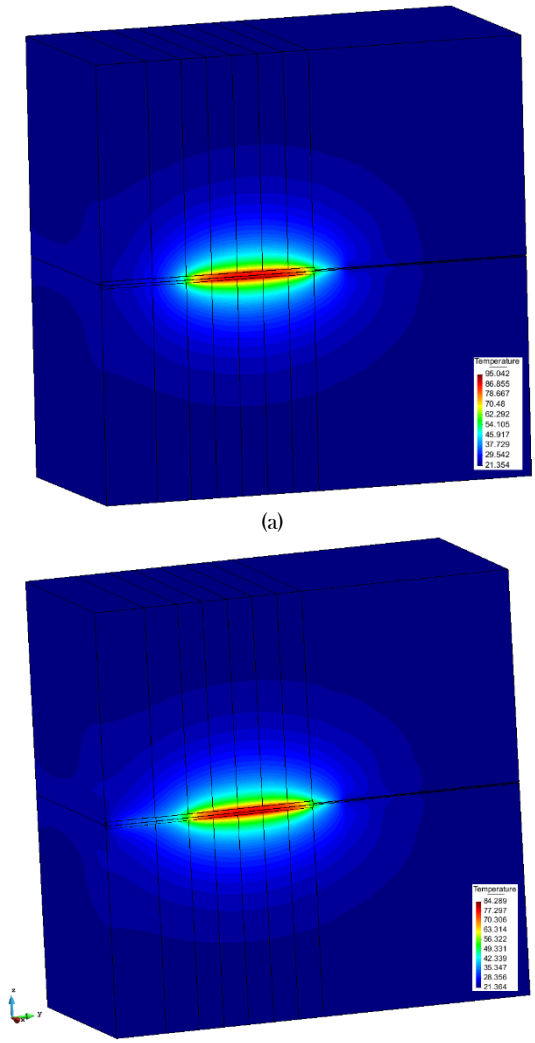

Figure 5.18: Three-dimensional view of computed contours of equal temperature at the end of the computation (a) input power applied only in the heaters and bottom (b) power applied according to the heat distribution in the alveolus.

5.4 COMPARISON BETWEEN SIMULATED AND MEASURED RESULTS

A systematic comparison between simulation results and measurements has been made for each sensor. The temperature has been compared on the vertical cross-sections orthogonal to the cell as well as along each borehole containing temperature boreholes. This part contains the comparison between the numerical results of the final three-dimensional modelling (including heat flow within the non-heated zone) and the measurements at all the sensors in the host rock, on the steel casing and within the gap. Results are organized into two types of figures:

- Comparisons of temperature evolution at all the sensors within specific vertical cross-sections orthogonal to the alveolus and located at z = 3, 4, 4.5, 5, 10, 13, 13.6 14.5 and 17.5 m from the head of the cell at GAN gallery.
- Comparisons of temperature time evolution and temperature profiles for all the sensors belonging to specific boreholes: ALC1616, ALC1617, ALC1618, ALC1633, ALC4001, ALC4002, ALC4003, ALC4004 and ALC4005.

For space reasons, only a summary of the results is presented here. All the temperature evolution graphs for each borehole are plotted in Appendix A – *Temperature results from the reference analysis.* All the simulation results have been obtained for the overall best fitting thermal conductivity couple of 1.96 W/m/K – 1.26 W/m/K.

5.4.1 Section X=13m

There are seven sensors which installed in three boreholes (ALC1616, ALC1617 and ALC4005), in section z=13m cross section across heaters 4 and 5, set at different orientations regarding to bedding, with a maximum distance of 10 m (ALC4005_05) and a minimum distance of 2.5 m (ALC1616_03) to the microtunnel wall. The sensors ALC4005_05 and ALC1617_03 are damaged and therefore, their measurements are discarded for temperature interpretation and are not included to calculate the average temperature increase at each borehole.

The observed evolution of temperatures at section z=13m are shown in Figure 5.19a,b, together with the computed results from the 3D thermal analyses. Horizontal view of these instrumentation and microtunnel arrangement as well as location of observation points at this section are also indicated in Figure 5.19c,d.

The temperature increase is larger at ALC4005_01 than that at ALC4005_04 due to the shorter distance of ALC4005_04 to the heater (see Figure 5.19b). Maximum temperature increases of 40°C and 45°C are observed by the sensors at ALC4005_01 and at ALC1616_03, respectively. The heating and cooling phases are well visible. The temperature drop becomes apparent just after the heater is switched off. It can be noted that, after about one year of heating, temperatures generally rise very slowly throughout the COx claystone. However, anisotropic effects are noticeable; different temperatures are recorded at all points, despite their distance from the tunnel wall. The 3D analysis captures the temperature variation well; of course, thermal conductivity has been back-calculated, and conduction is the dominant form of heat transport. In any case, the whole evolution of temperatures is correctly reproduced.

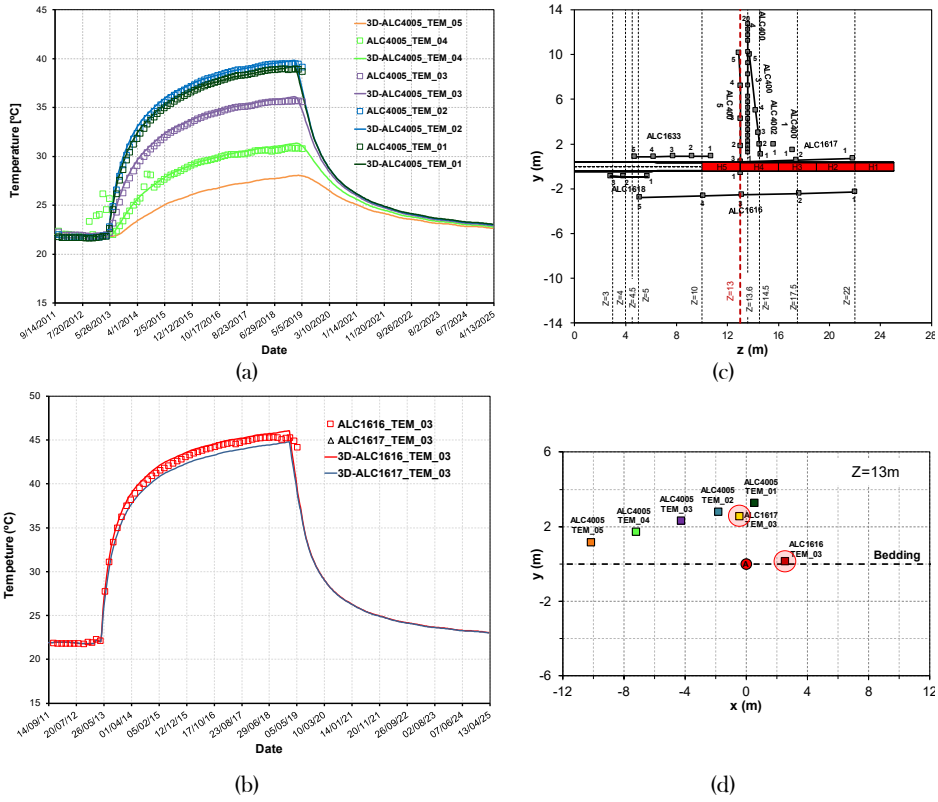

Figure 5.19: Temperature evolution at sensors located within the section at 13 m from the gallery (a) borehole ALC4005 (b) boreholes ALC1616 and ALC1617 (c) Horizontal view of the instrumentation and micro-tunnel arrangement (d) Location of observation points at a depth of 13m.

5.4.2 Section X=17.5m

In this section, the temperatures are measured at about 17.5 m depth. To compare the results, several points were considered, with a maximum distance of 3.2 m (ALC1616_02) and a minimum distance of 1.5 m (ALC4001_01) to the tunnel wall. There are three sensors which installed in three boreholes (ALC1616, ALC1617 and ALC4001), set at different orientations to bedding plane.

The observed evolution of temperatures at sections z=17.5m are shown in Figure 5.20a,b, together with the computed results from the 3D thermal analyses. Horizontal view of these instrumentation and microtunnel arrangement as well as location of observation points at this section are also shown in Figure 5.20b,c. A maximum temperature increases of 56°C is observed at the sensor situated in the symmetry plane of the heater. Temperatures generally rise very slowly throughout the COx claystone after about a year of heating. Anisotropic effects are noticeable, however; different temperatures are recorded at all points despite their distance from the tunnel wall. The figure shows that the values and evolution of the temperatures are predicted well in practically all observation points, indicating again that the thermal conductivity estimate was quite accurate.

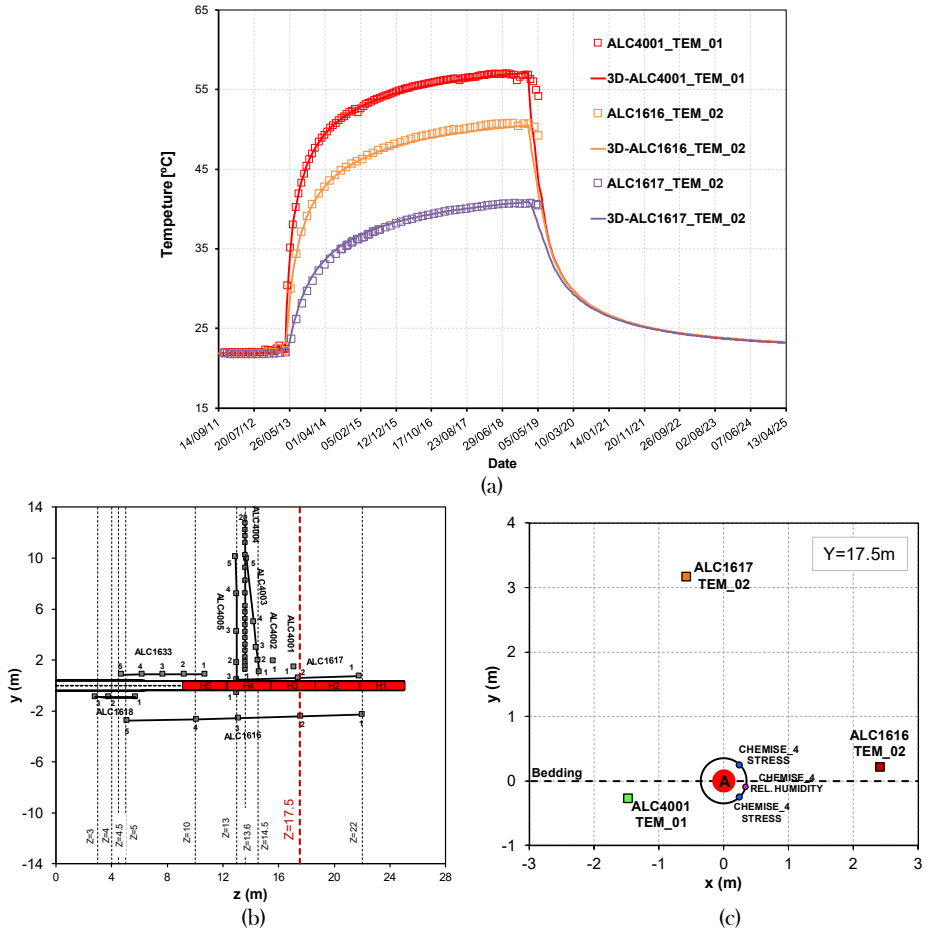

Figure 5.20: (a) Temperature evolution at sensors located within the section at 13 m from the gallery (b) Horizontal view of the instrumentation and micro-tunnel arrangement (c) Location of observation points at a depth of 13m.

5.4.3 Boreholes measurements

Temperature has been also compared along each borehole containing temperature boreholes (see Figure 5.21). For space reasons, only the temperature evolution of the sensors of boreholes ALC1616 and ALC4005 are shown in Figure 5.22. Figure 5.21 and 5.22 show the evolution of the temperature measured in two boreholes. Five temperature sensors at different distances from the tunnel axis were installed in each borehole. Boreholes ALC1616 is parallel whereas borehole ALC4005 is perpendicular to the microtunnel axis.

Borehole ALC1616

A maximum temperature increases of 50°C is observed at the sensor situated in the symmetry plane of the heater. All measured temperatures in borehole (see Figure 5.21) show a delay of the temperature decrease after switching off the heater. Especially the temperature in sensor ALC1617_02, which is located furthest from the heater.

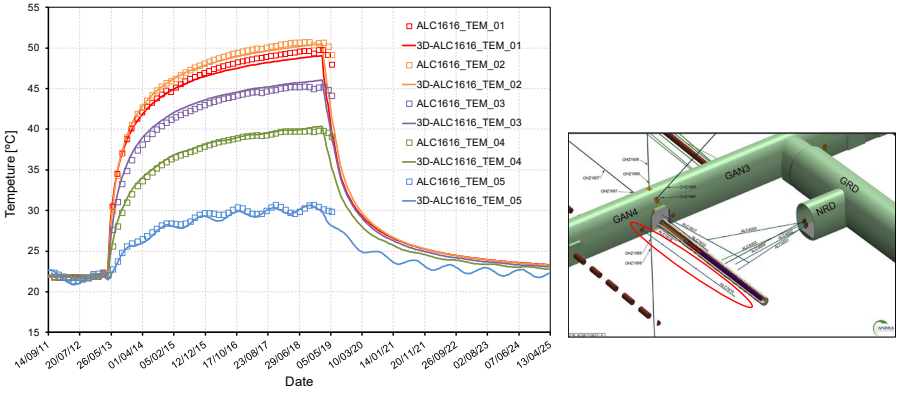

(a)

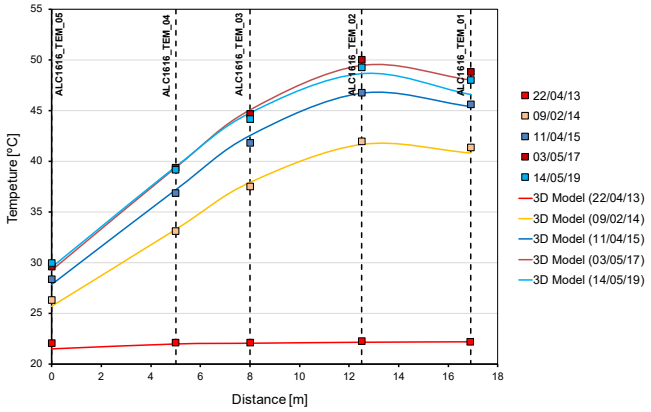

(b)

Figure 5.21: Temperature evolution of the sensors of the borehole ALC1617. The measurements (dots) are compared to the simulation results (lines).

Borehole ALC4005

The tendencies are very similar in both boreholes, higher temperatures for sensors located close to heaters and for sensors located along the bedding plane. All measured temperatures by sensors in borehole ALC4005 (see Figure 5.22) show a

delay of the temperature decrease after switching off the heater. A maximum temperature increases of 40°C is observed at the sensor ALC4005_01 closest to the heater.

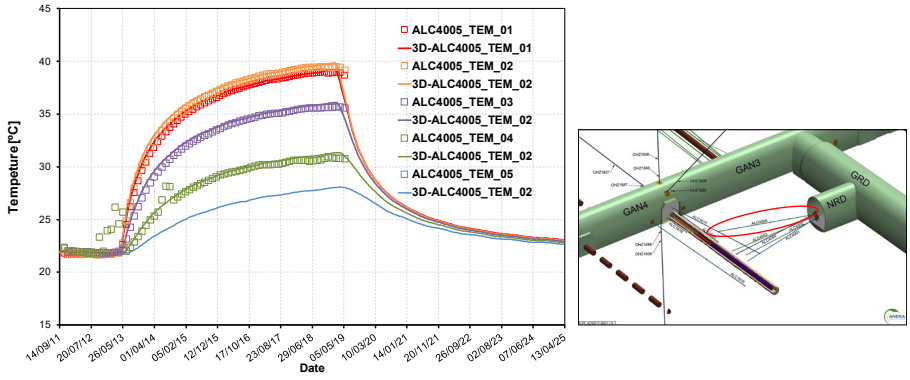

(a)

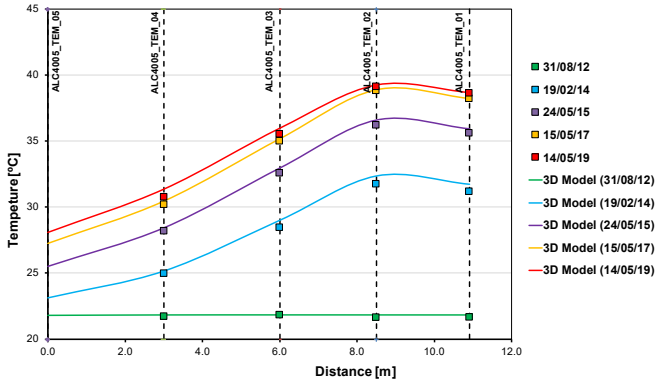

(b)

Figure 5.22: Temperature evolution of the sensors of the borehole ALC4005. The measurements (dots) are compared to the simulation results (lines).

5.4.4 Steel casing (liner and Insert)

The observed evolution of temperatures on the underside of the liner, 15° from the vertical axis, is shown in Figure 5.23 together with the computed results from the 3D analysis. The heating stages and the cooling phases can be clearly identified. The first heating phase with a low power of 30W/m generated an increase of the temperature from 21°C to 30°C at the liner over the 16 days. The following heating phase with a power of 220 W/m caused a maximum temperature of 90°C on the liner at the centre of the heated zone over the next five years. The gradual heat transfer away from the heaters resulted in the build-up of a temperature gradient.

The final cooling phase led to a gradual decrease of the temperature down to the initial level after about five years.

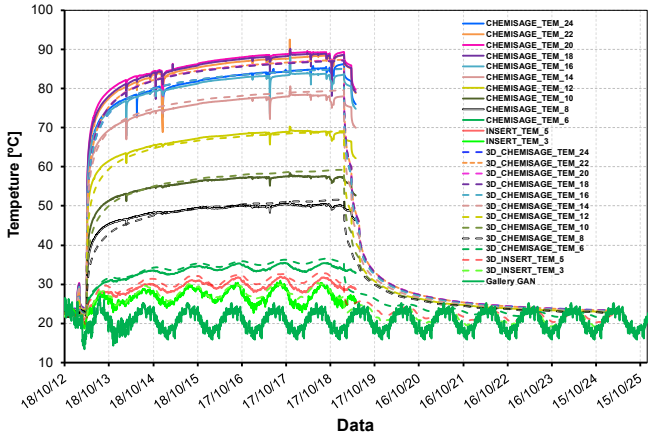

(a)

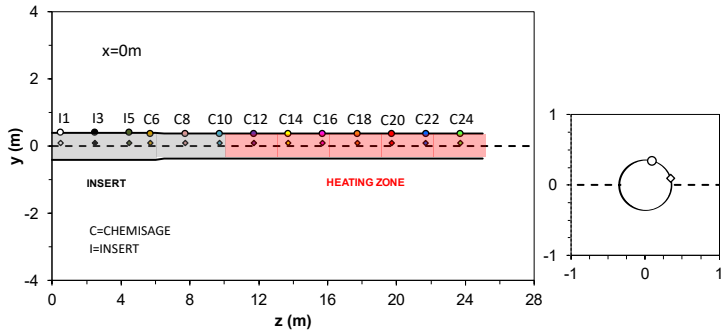

(b)

Figure 5.23: Temperature evolution of the vertical sensors at sleeve. The measurements (lines) are compared to the simulation results (dotted lines).

Figure 5.24 shows the axial temperature profile on the underside of the liner, 15° from the vertical axis and 15° above the horizontal axis, along the cell at different times. As it can be seen on Figure 5.24, the temperature profile on the side of the liner remains still approximately 4°C lower than that measured in the vault during heating. This difference can be explained both by convection occurring inside the casing (hot air rises) and by the influence of the boundary conditions around the casing (the contact between the casing periphery). The highest temperature is located at a depth of approximately 18 m at the centre of the heated zone between.

However, anisotropic effects are hardly noticeable; very similar temperatures are recorded at two points. The whole temperatures evolution is correctly reproduced by the 3D analysis as shown in the figure.

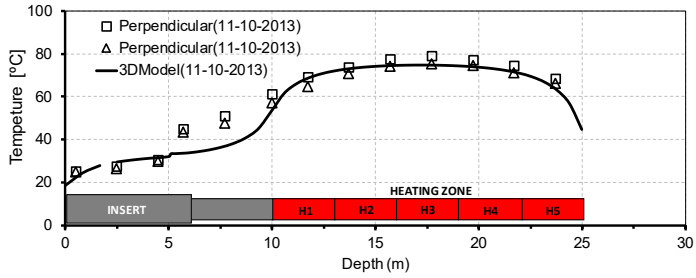

(a)

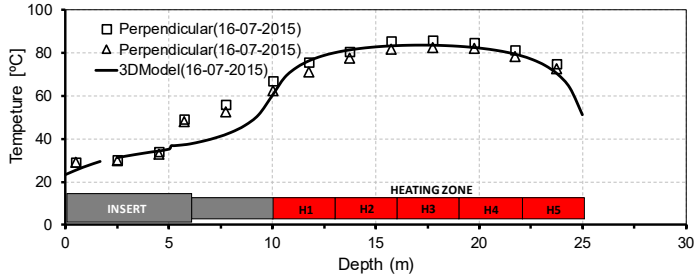

(b)

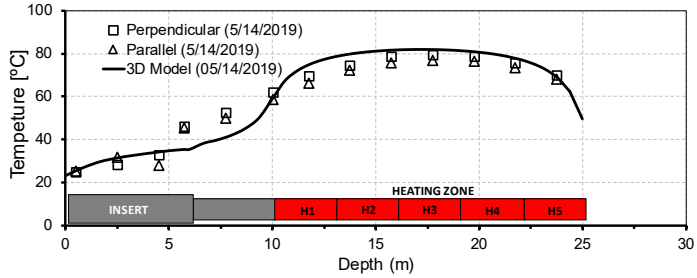

(c)

Figure 5.24: Temperature profile at steel casings. The graph (b), 10 August 2014, shows the comparison with a model in which the heated zone is isolated. The measurements (dots) are compared to the simulation results (lines).

More information from the analyses is given in Figure 5.25 in terms of contours in the casing at various relevant stages. The following times have been selected for plotting: 585 days (One year heating); 985 days (Two years heating); 2297 days (at the end of heating phase); 2358 days (at the end of first cooling phase);

2422 days (at the End of second cooling phase); and 4668 days (towards the end of cooling phase).

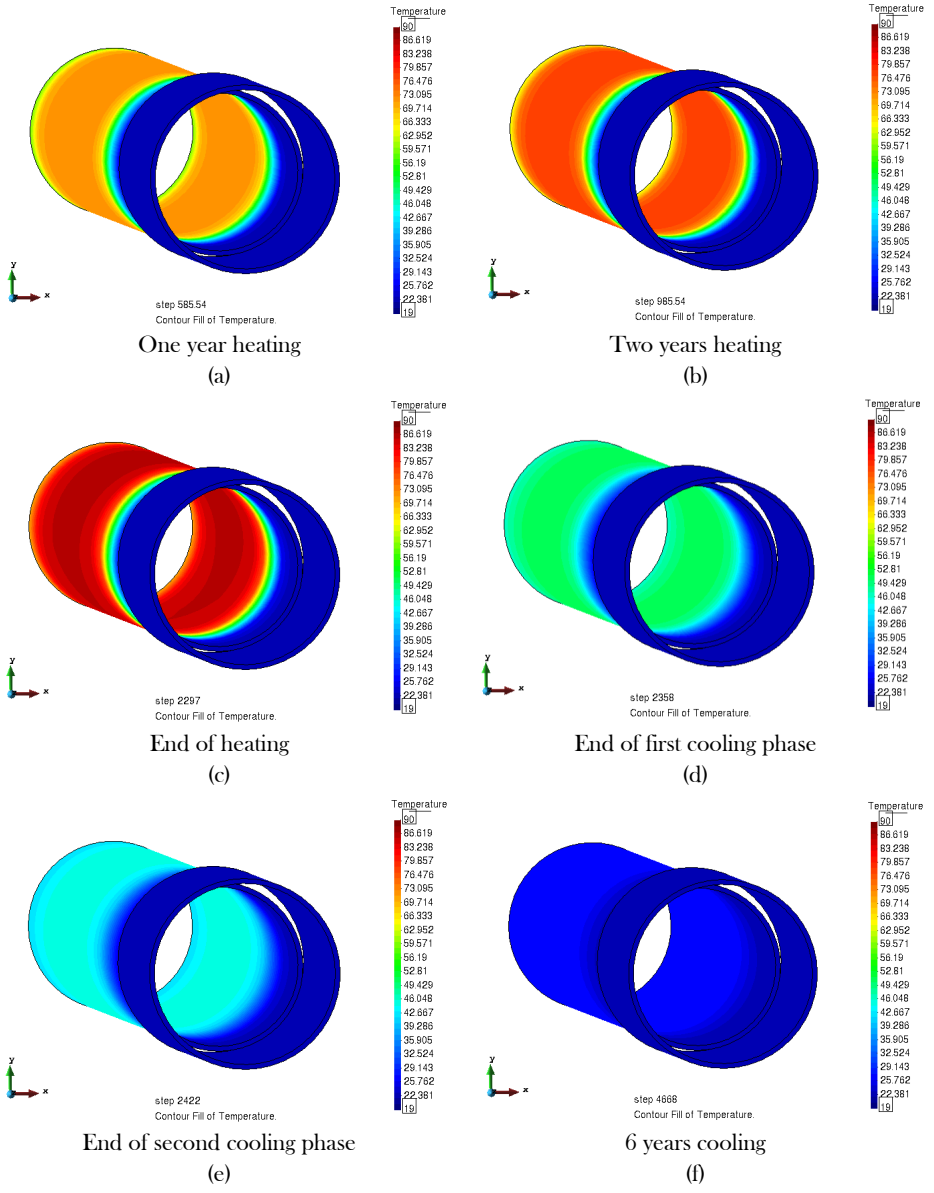

One year heating (a)

Two years heating (b)

End of heating (c)

End of first cooling phase (d)

End of second cooling phase (e)

6 years cooling (f)

Figure 5.25: 3D view of computed contours of equal temperature in steel liner at various times.

Chapter 6: Analysis of THM behaviour

This chapter presents the thermo-hydro-mechanical modelling of the ALC1604 in situ test. After a short description of the evolution of pore pressures registered by the sensors around the experiment (section 6.1), the model itself is presented (section 6.2). It corresponds to the final 3D model carried out of the project, which includes most of experiment geometrical features (host rock, microtunnel, insert, steel lining and the gaps between the steel lining and the host in the operative zone, the steel lining and the insert and the insert and the host rock in the alveolus head).

However, the model includes the thermo-hydraulic influence of the surrounding GAN and GRD gallery, as well as all experiment phases since the excavation of the microtunnel. Section 6.3 presents the comparison of numerical results with all experiment measurements: temperatures pore pressures, casing convergences and mechanical signatures. In some figures, results of the 3D model are compared with those output by a 2D model focusing two vertical cross-sections orthogonal to the microtunnel, to emphasise the importance of three-dimensional effects.

6.1 THE PORE PRESSURE FIELD

As described in Chapter 4, there are 18 piezometers installed in the rock mass to monitor the pore pressure evolution (Figure 6.1).

- Two boreholes with one piezometer chamber (ALC4001 and ALC 4002),
- Two boreholes with three piezometer chambers (ALC1617 and ALC1618),
- Two boreholes with five piezometer chambers associated with temperature sensors to measure the pressure gradient from the gallery into the rock mass and the pressure evolution near to the heated zone. (ALC4005 and ALC 1616).

These boreholes are backfilled with resin in order to ensure that they are impervious and with low incompressibility.

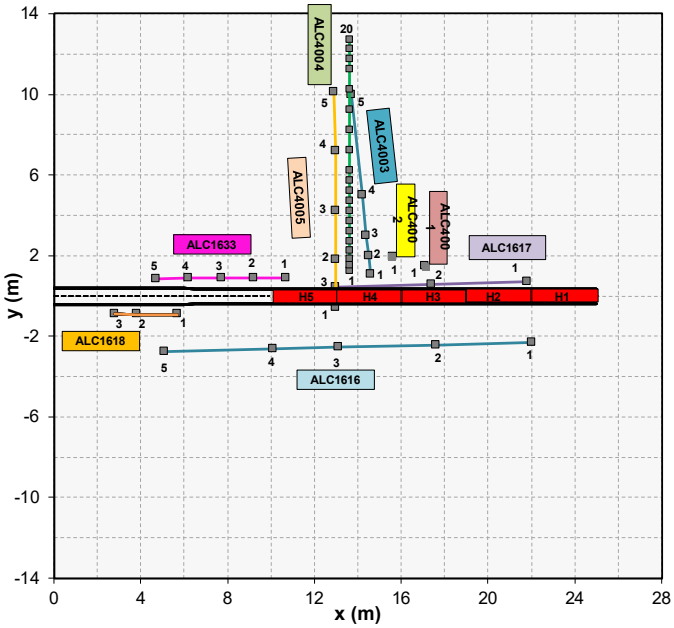

Figure 6.1: Horizontal cross-section indicating of instrumentation. ALC1633 and ALC1618 boreholes are located on the non-heated zone of the ALC1604 experiment and contain various piezometer chambers.

6.1.1 Pore pressure response to a thermal load

In COx claystone, the main hydraulic phenomenon associated with thermal effects is the generation of pore pressure due to changes of temperature. When COx claystone (and other argillaceous rocks) is subjected to a temperature increase, the pore pressure will also increase due to the fact that the thermal expansion of the water is larger than that of the porous skeleton itself. The low permeability of COx claystone ensures that the resulting excess pore pressure does not dissipate rapidly. Nevertheless, the predictions of pore pressures evolution of the host rock (COx claystone) during excavation is of great importance. An important concern in the experiment is a good understanding of the pore pressure response due to excavation operations too.

As shown below, hydro-mechanical coupling, and particularly the configuration and extent of the EDZ, play a significant role in the pore pressure response. Figure 6.2 shows the variation with time of pore pressures, measured with capacitive sensors in section 17.5m deep (z=17.5m). The same graph is shown in Figure 6.2b, but with an emphasis on the first days. Water pressure raises at those locations as the excavation front approaches the measurement points up to a value of about 8 MPa, i.e. 3.3 MPa above the initial value. After that, pressure drops rapidly to

2MPa as soon as the excavation front passes the corresponding measuring points. However, in the zone above the tunnel crown, pressures decrease which is linked to the geometry of the damaged zone around the cell so that is more pronounced horizontally and the EDZ barely grows in this direction. In addition, permeability remains almost constant, by the implemented formulation (see chapter 3, Eq. 3.27). Figure 6.2 shows the evolution of pore pressures at the borehole ALC1617 that is located in the vertical plane of the tunnel (above the tunnel crown), 3.2 m away from the wall outside the EDZ. There is a slight increase of pore pressures as the excavation front approaches the measurement points, which was captured by the analysis.

Interesting insights can be obtained examining a typical evolution of temperature and pore pressure as presented in Figure 6.2. As expected, temperature increases during the thermal load trigger a significant upsurge of pore pressures. It is noticeable that the pore pressure responds to the temperature rise immediately, and the higher the temperature change, the stronger the response. The maximum pore pressure increase, in this case, is 7.5 MPa, a significant magnitude. It can also be observed that the pore pressure evolution does not precisely match that of temperature; at some time, the pore pressure stops rising, even though temperatures increase further. Dissipation by liquid flow overcomes the thermal effect. This phenomenon is especially noticeable at two points located in the bedding plane (ALC1616 and ALC4001). Although in the 140 days after the beginning of the heating, the overpressure peak was observed on the horizontal plane of the tunnel, this peak was not actually achieved in the vertical plane above the curve of the tunnel in over 800 days. The difference in time taken to reach the overpressure peak in the vertical and horizontal planes can be explained by the rock's anisotropic thermal and hydraulic properties (Figure 6.2).

Figure 6.3 shows the evolution of pore pressure in all sensors within the vertical cross-section located at 13 m from GAN gallery. The influence of the thermal load is evident in most of the sensors, except sensor ALC4001_PRE_05, positioned 10 m away from the cell. For the nearest sensors, combined effect of distance and orientation can be appreciated: Sensor ALC4005_PRE_01 and ALC1617_PRE_03, oriented in the direction orthogonal to the bedding present the higher increase in pore pressure and the slowest dissipation, while ALC1616_PRE_03 experiences a lower increase in pore pressure (although closer to the heater) and the quickest dissipation. Other sensors from borehole ALC4005 exhibit an intermediate response between the two previous sensors. This is a clear indication of a higher permeability along the bedding plane. Farthest sensor

ALC4001_PRE_05 shows a response similar to the sensors located in the non-heated zone in front of the alveolus head (ALC1633 and ALC1618). It is interesting to note that the temperature variations imposed by the presence of GAN gallery induce as well as small variations of pore pressure.

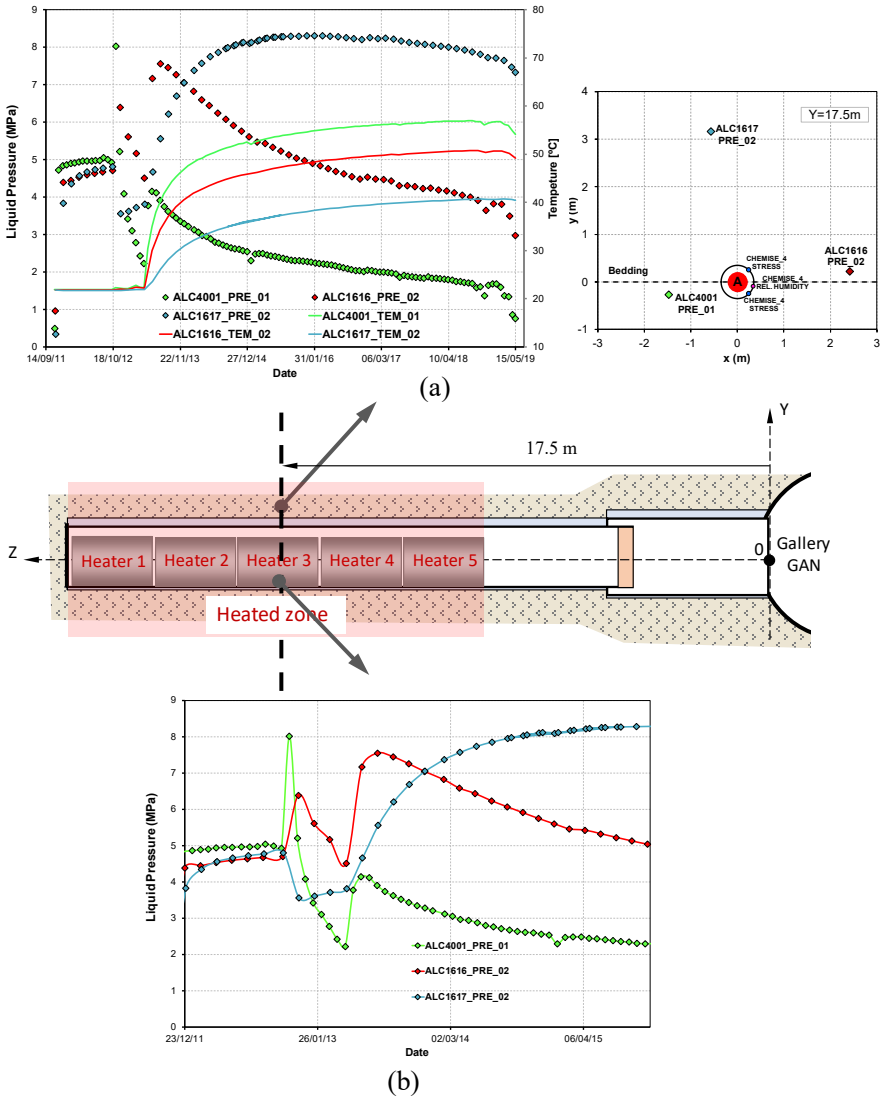

Figure 6.2: Pore pressure and temperature evolution measured in sensors ALC1616_PRE_02, ALC1617_PRE_02 and ALC4001_PRE_01 located on the same section as the heaters (17.5 m deep from the gallery).

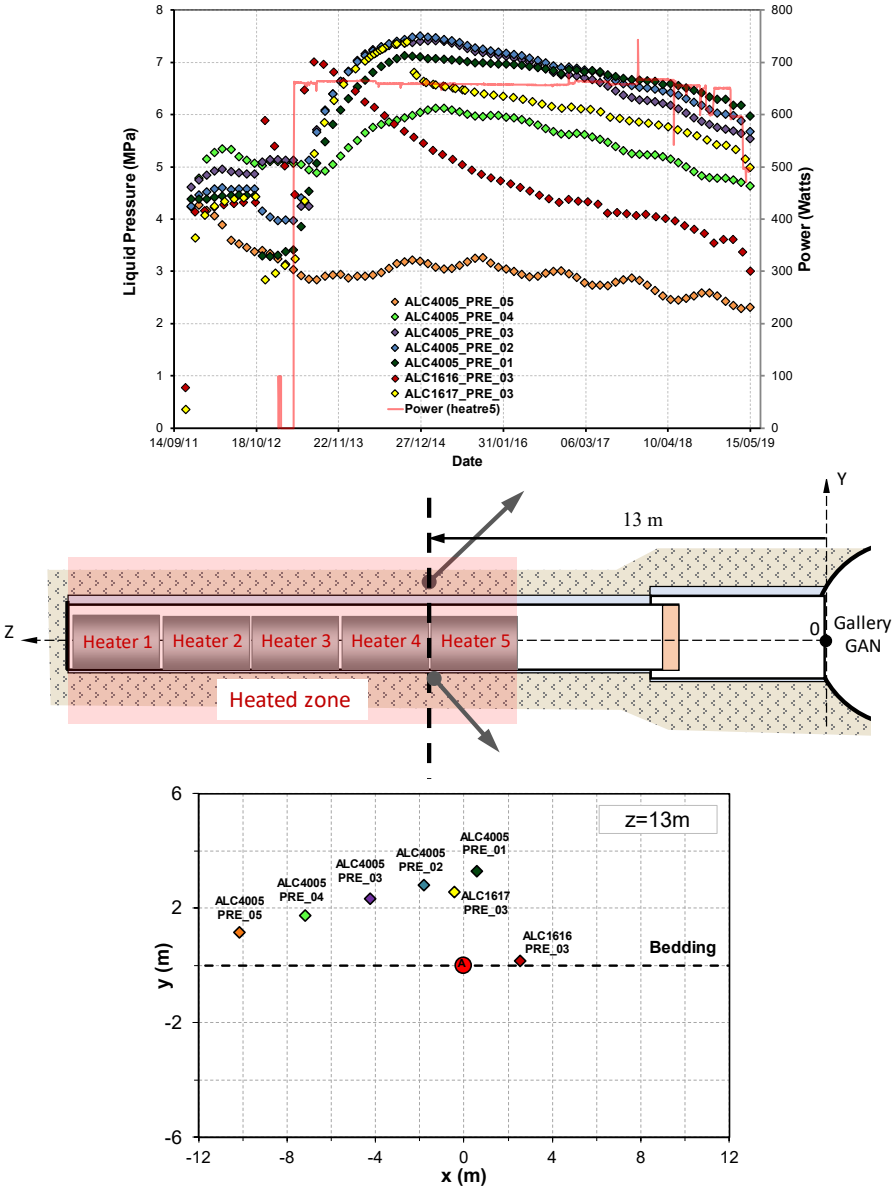

Figure 6.3 Pore pressure measured on sensors ALC4005_PRE_01 to PRE_05, ALC1616_PRE_03 and ALC1617_PRE_03 during all the experiment. The red line indicates changes of power injected in the heaters.

6.2 THERMOMECHANICAL BEHAVIOUR OF CASING

In order to ensure the structural reliability of the casing, several in situ experiments have been performed to analyse the mechanical and thermomechanical behaviour of steel casing and the mechanisms involved in the casing/rock interface at the MHM URL (Bumbieler et al., 2015). The measurements exhibit a strongly anisotropic load, in spite of isotropic in situ stress which was consistent with the convergence anisotropy measured on drifts (Armand et al., 2013) showing that horizontal convergence is twice the vertical convergence.

In ALC1604 in situ test, the evolution of the mechanical behaviour of the casing is monitored by convergence and local strain measurements on the casing (Liner and Insert) inner face. The convergence measurement sections were installed in liner section 9, at a depth of 7 m, and inserts 11 and 12, at respective depths of 4 and 2 m in the cell as given in section 4.4.2.

6.2.1 Convergences

Figure 6.4 shows the overall evolution of convergence measurements of the sleeve, since the connection of the sensors (48 days after the micro-tunnel excavation). Although the in-situ stress field is almost isotropic in the cross-section (orthogonal to micro-tunnel) measurements exhibit an anisotropic load. This behaviour is consistent with the anisotropy of convergence measurements reported by Morel et al. (2013) and Armand et al. (2013).

Concerning liner response, three loading steps can be distinguished in Figure 6.4. In the first one, the radial load is localised in the horizontal direction corresponding to the maximum extension of the excavation induced fracture network. It can be observed that immediately after emplacement, the liner starts to converge in the horizontal direction, meaning that the theoretical initial annular air gap, which is about 3 percent of the excavation diameter, is consumed in this direction in less than 25 days. This loading results in the radial bending of the liner and the decrease in diameter. The heating phase strongly increases the liner convergence rate and thus its deformation, until contact with the microtunnel vault occurs. In this step, the ovalization of the casing continues until it reaches the rock wall in the vertical direction. Once the annular air gap is taken up in the vertical direction, a second loading stage starts; characterized by the fact that mechanical load remains anisotropic with no impact on the liner convergence. This second loading step is followed by the third one, corresponding to a progressive decrease of the load anisotropy, resulting in a decrease of the ovalization. After one year of

heating, the convergence rate is less than 5×10^{-11} s^{-1}, which is of the same order of magnitude as the convergence rate measured in 5 m diameter drifts having the same orientation (Armand et al., 2013).

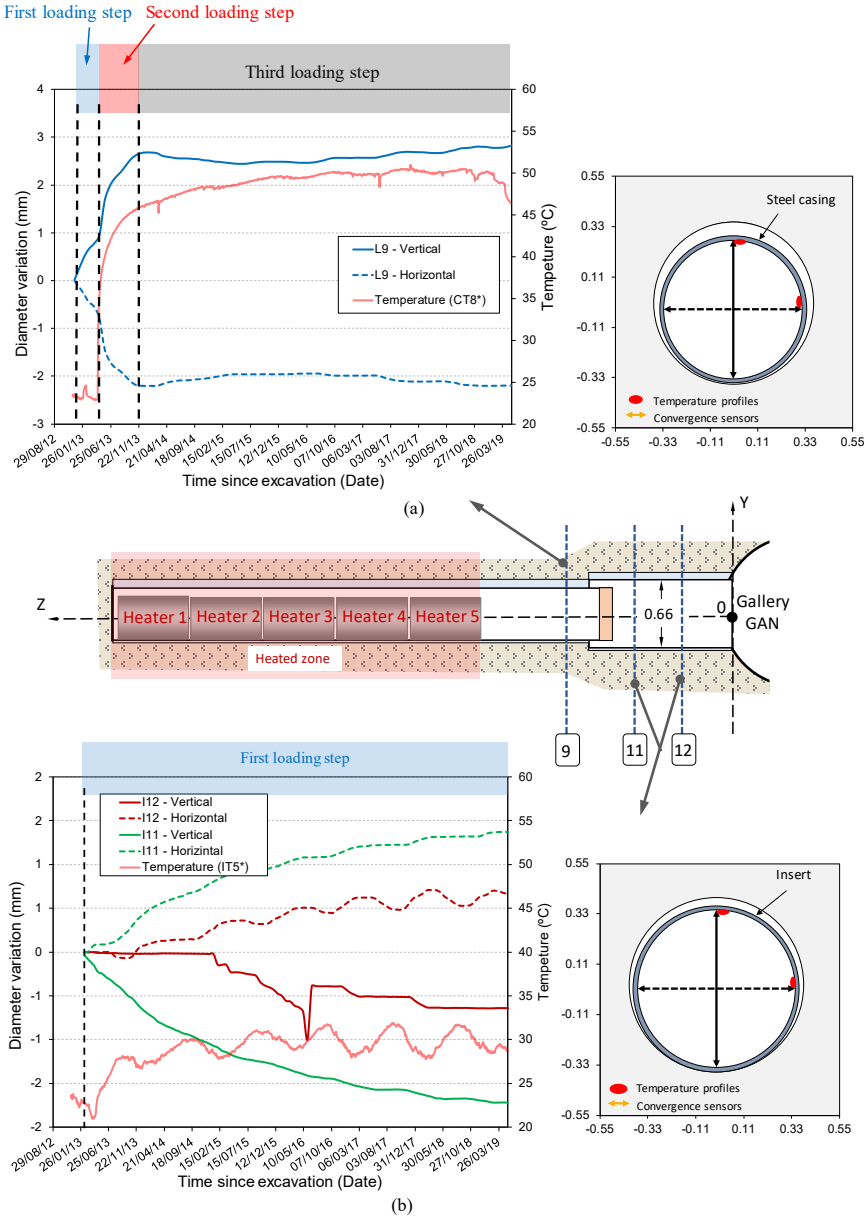

Figure 6.4: Diameter variations measured on the liner at a depth of 7 m and on the insert at a depth of 4 and 2 m (negative values = convergence).

The horizontal and vertical convergence of insert sections 11 and 12 also given in Figure 6.4. A similar short-term mechanical loading of the casing is observed at insert. However, after five years of measurements, the convergence of the insert is not stabilised, which means that they are still in the first loading step mentioned above. The behaviour of the insert sections does not show any significant heating impact (the sections were 8 and 6 meters behind the heated zone).

On both sections, the loading scheme is the inverse of one of the liners, consisting of vertical convergence and noticeably equivalent horizontal divergence. A possible explanation relies on the fact that the annular air gap is much smaller at the insert level (initially 12 mm at the radius, compared with 25 mm around the sleeve). This behaviour could then be caused by the insert being in contact with the rock in the vertical and horizontal planes. As the mechanical strength of the rock was lower horizontally due to the damage generated during excavation, the insert tended to diverge horizontally. For both sections, the loading direction is reversed with respect to the sleeve, i.e. vertical convergence and noticeably equivalent horizontal divergence.

6.2.2 Mechanical signatures measured

The influence of a thermal load on the mechanical behaviour of the casing has been determined by heating the casing more than 5 years after its installation, so that a significant mechanical load is already applied by the rock (Figure 6.5). The evolution of the applied load (Figure 6.5) is estimated from local strain measurements on the inner face of the casing at 18 m depth (z=18m). The strain gauges, which were preinstalled on the casing, were connected 27 days after the cell was excavated. For each section, the gauges are spread out into six sectors, two in the horizontal plane and the other four at 45° angles on either side of it (Figure 6.5). The following dates have been selected: Jun 17, 2013 (two months heating); August 11, 2014 (one year heating); July 16, 2016 (three years heating); September 18, 2017 (4.5 years heating).

A first increase heating step, by 15°C, leads to an increase of the deformation rate of the casing up to the recovery of vertical annular air gap (end of phase 1 as defined in Section 6.2.1) which is related to the anisotropic extent of the EDZ around the cell. This anisotropic loading results in a radial bending of the casing so that significant circumferential mechanical strains appeared. After the second year of heating, when the temperature of the casing reached nearly 55°C, circumferential strain of casing does not evolve, corresponding to a relaxation of the radial load

(third loading step as defined in Section 6.2.1). These evolutions tend towards a stabilised curve, which represents the mechanical signature of the applied load.

Mechanical signatures of the loading applied by the rock (i.e. the evolution of the circumferential strain around the inner face of the casing) confirm the loading anisotropy. However, the casing does not evolve significantly after the second year of heating.

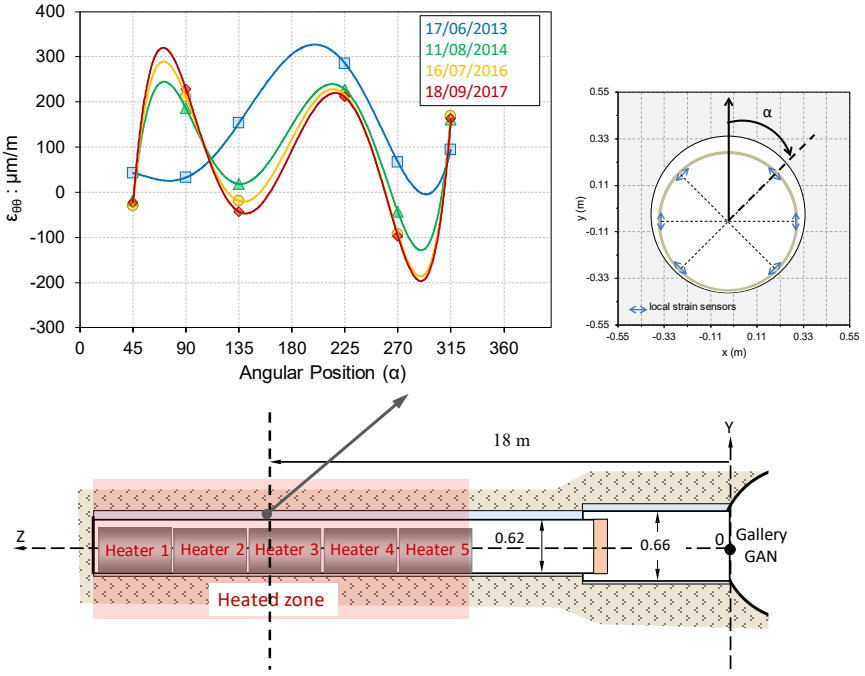

Figure 6.5: Evolution of circumferential mechanical strain at various times on section z=18m depth.

6.3 THERMO-HYDRO-MECHANICAL NUMERICAL MODELLING

The numerical analysis has been carried out using the same mesh used for the 3D thermal analysis. More detail about the model is given hereinafter.

6.3.1 Material parameters

Parameters of the COx claystone

Table 6.1 presents the values of all the THM parameters used for the COx claystone in the model, and the sources cited. The mechanical model is described in Chapter 4. It consists of an anisotropic Visco-elastoplastic model with creep. The transverse elasticity has been used in the previous experiment, either in COx claystone (TER and TED experiments) or in the Opalinus clay (HE-D). Rock strength anisotropy was defined by adopting scaling factors c_N = 1.33 and c_S = 1.0, selected to obtain a reasonable configuration of the damaged zone. The stratification planes in the COx claystone formation are nearly horizontal; therefore, the angles α and β were set equal to zero.

According to measurements of wave velocities in cubic samples (Armand et al., 2013), the ratio between horizontal and vertical Young's modulus has been set to 1.3. Young's modulus and permeability results from a back-calculation of the evolution of pore pressures measured in the ALC1604 experiment. Values obtained were $E_{//}$ = 5200 MPa, $E_{\perp}$ = 4000 MPa for the Young modulus and $k_{//}=2\times10^{-20}$ m^2, $k_{\perp}=1\times10^{-20}$ m^2 for the permeability. Stiffness values differ slightly from the ones used in the simulation of TED experiment ($E_{//}$ = 6000 MPa, $E_{\perp}$ = 3000 MPa). Discrepancy is higher for the permeability, since it is 3 times lower than the one used in TED experiment. Parameters used for the viscoplastic and creep part of the model come from the modelling of CGS excavation performed by (Mánica et al., 2016).

The change in permeability in the Excavation Damage Zone, given by parameter η has been back-analysed in the present modelling to match pore pressure during the excavation phase. Thermal parameters are the ones back-analysed during the three-dimensional thermal modelling. The solid thermal expansion comes from Auvray (2004) and the previous modelling of TER and TED experiments.

Table 6.1: Callovo-Oxfordian claystone parameters used in the THM simulations.

properties	Parameter	Orientation*	Value	
Mechanical	Young's Modulus, E: MPa	Parallel Perpendicular	5200 4000	Back-analysis of ALC1604 test.
	Poisson's ratio, ν	Parallel Perpendicular	0.25 0.35	Reference value
	Peak friction angles, φ_{peak}	-	22.0	
	Initial friction angles, φ_{ini}	-	9.35	
	Mobilised friction angles, φ_{res}	-	14.74	
	peak cohesion,c_{peak} : MPa	-	3.55	
	Constant that controls the curvature of the function in the hardening branch,a_{hard}	-	0.0035	
	Constant that controls the curvature of the function in the softening branch,a_{soft}	-	0.07	
	Coefficient of non-associativity,ω	-	0.6	Calibration of the constitutive model (Miguel Mánica; et al. 2016)
	Equivalent plastic strain at which the maximum strength is reached,ξ_1: MPa	-	0.005	
	Equivalent plastic strain at which softening begins,ξ_2: MPa	-	0.006	
	Equivalent plastic strain at which the residual strength is reached,ξ_3: MPa	-	0.06	
Mechanical (Time-dependent mechanism)	The threshold from which viscoplastic strains are activated,σ_s: MPa	-	4.0	
	Viscosity parameter,γ: day^{-1}	-	1x10^{-7}	
	Material constants,n	-	3.37	
	Material constants,m	-	530	
Hydraulic	Intrinsic Permeability, k	Parallel Perpendicular	2·10^{-20} 1·10^{-20}	
	Material parameters,A		1.0	Back-analysis of ALC1604 test
	Material parameters, Λ		3.0	
	Model parameter,P: MPa		14.3	
	Material parameters,λ		0.33	
TM	Linear Thermal expansion coefficient of the rock, α_T: K^{-1}	-	1.4·10^{-5}	Auvray (2004)
	Biot Coefficient, b	-	0.6	Reference value
HM	Constant controls the rate of change of intrinsic permeability,η	-	300	Back-analysis of ALC1604 test
	Threshold in the plastic multiplier for the change in permeability	-	1.2e-4	
Thermal	Linear Thermal expansion coefficient of the solid grain, α_T: K^{-1}	-	1.4·10^{-5}	Value and anisotropic ratio from Auvray (2004)
	Thermal Conductivity, λ: W/m/K	Parallel Perpendicular	2.05 1.33	Anisotropic back-analysis of thermal field
	Specific heat capacity of the solid, c: J/kg/K	-	800	Auvray (2004)
Petrophysical	Solid compressibility, β_s	-	2.5·10^{-5}	From mineral composition
	Specific weight, ρ_s: kg/m3	-	2.7	Reference value
	Porosity, ϕ	-	0.173	Martin & Lanyon (2003)

Parameters for the casing and the air gap

The selected steel casing has a sufficiently high yield strength (above 400 MPa) to reduce the risk of early-stage plasticity due to host rock anisotropic convergence and to overcome Stress Corrosion Cracking (SCC) (Bumbieler et al., 2015). The casing is considered to be linear elastic with parameters E, ν and α, respectively, for Young's (elastic) modulus, Poisson's ratio and the coefficient of thermal expansion. Mechanical and thermal properties of steel lining are listed in Table 6.2.

As stated above, the model contains a gap between the host rock and the casing. This gap is modelled as a material with very high porosity and permeability (several orders of magnitude larger than the other materials, see Table 6.3). The retention curve is also considered but with a very low value of the reference air entry capillary pressure P_o (P_o = 0.001 MPa), as the gap corresponds is, in essence, a material with very large pores. This implies that saturation takes place sharply as capillary pressure vanishes. To avoid numerical convergence problems, the porosity has been set to a high value (0.8) but less than one. The dependency of both permeability and air entry pressure on porosity has been considered in order to model their evolution towards host rock values when the gap closes.

From the mechanical point of view, the gap was modelled using a bilinear elastic model that uses two values of Young's modulus, one for the opened gap and the other for the closed gap. A large value of Young's modulus (E) was used for the closed gap (representing the contact between gap surfaces), and a relatively low value (E_o) was used for the open gap (Figure 6.6). The volumetric strain was used to check whether the gap was open or closed. As, during the calculations, the gap undergoes a path from an initial open state towards a closed state as the casing expands, the approximation considered was deemed adequate.

Table 6.2: Steel lining properties adopted in the THM analysis.

properties	Parameter	Value
Thermal	Thermal Conductivity,λ: (W/m/K)	80
	Specific heat of solid (J/kg/K)	550
	Linear Thermal expansion coefficient, α_T: K^{-1}	$1.4 \cdot 10^{-5}$
Mechanical	Young's Modulus, E: MPa	0.005
	Poisson's ratio, ν (-)	0.3

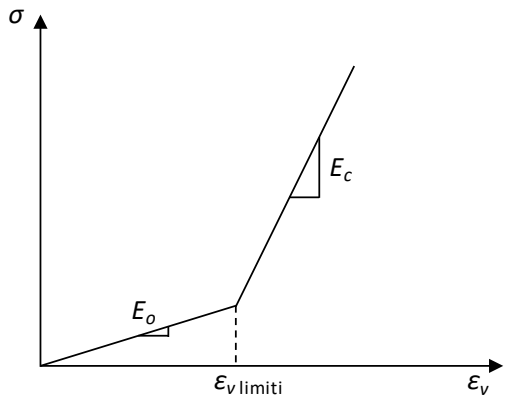

Figure 6.6: Bilinear elastic model.

Heat transfer across the gap will take place by conduction, radiation and convection as described detailed in Chapter 3. At the local scale, the state of the gap (i.e. open/closed gap and degree of saturation) is expected to be an important factor controlling the maximum temperature of the COx claystone and casing. For the conductive flux, the Fourier law is used. In this study, the combined effects of conduction and radiation are included in the conductive flux using an equivalent conductivity. Moreover, thermal conductivity varies with saturation. When the gap is dry, the thermal conductivity is set to 0.035 W/mK (a mixture of air and water vapour) and to 0.6 W/mK (liquid water) when saturated. Table 6.3 summarises air gap parameters used in the analysis.

Table 6.3: Air-gap element properties adopted in the 2D THM analysis.

properties	Parameter	Value
Thermal	Thermal Conductivityλ_{dry}: (W/m/K)	0.035
	Thermal Conductivity, λ_{sat}: (W/m/K)	0.6
Hydraulic	Intrinsic permeability, k_0: (m2)	10^{-16}
	Porosity, ϕ_0 (-)	0.8
	Parameter for van Genuchten model, λ (-)	0.5
	Measured P at certain temperature, $P_0(MPa)$ $P_0(\phi) = P_0\, exp[\alpha(\phi_0 - \phi)]$	0.001
	Parameter for van Genuchten model, α	10
Mechanical	Young's Modulus, E: MPa	200
	Young's Modulus, E: MPa	1.0
	Strain limit, $\varepsilon_{v\,limit}$ (-)	0.005
	Poisson's ratio, ν (-)	0.3

6.3.2 Domain discretisation

A three-dimensional coupled THM analysis has been performed in order to incorporate the anisotropic properties of the COx claystone and the anisotropy of the in-situ stress state. The model domain and the finite element mesh used is depicted in Figure 6.7. Dimensions are 50 m × 50m ×50 m, and the reference axis system has been taken equal to the local system defined for the ALC1604 test (see Chapter 5.4.1 of thermal modelling).

The mesh has been refined near the gallery and near the micro-tunnel, in order to be able to cope with the high temperature (and subsequently pore pressure) gradients in this zone. The distance to the boundary is 25 m, which corresponds to the distance from the microtunnel axis to the gallery GRD.

Besides the host rock domain, the model includes the geometry of the casing and the air gaps formed by the sleeve and the COx claystone, the sleeve and the insert and the insert and the COx claystone. According to the experimental layout, the casing is supported on the bottom of the excavation, and then the casing, insert and gaps are eccentric with respect to cell centreline. This aspect is represented in the geometry. The mesh used in this computation contains about 3312 tetrahedral elements and 6720 nodes. The domain and the finite element mesh used are depicted in Figure 6.7. The initial and boundary conditions are depicted in Figure 6.8 and summarized in Table 6.4.

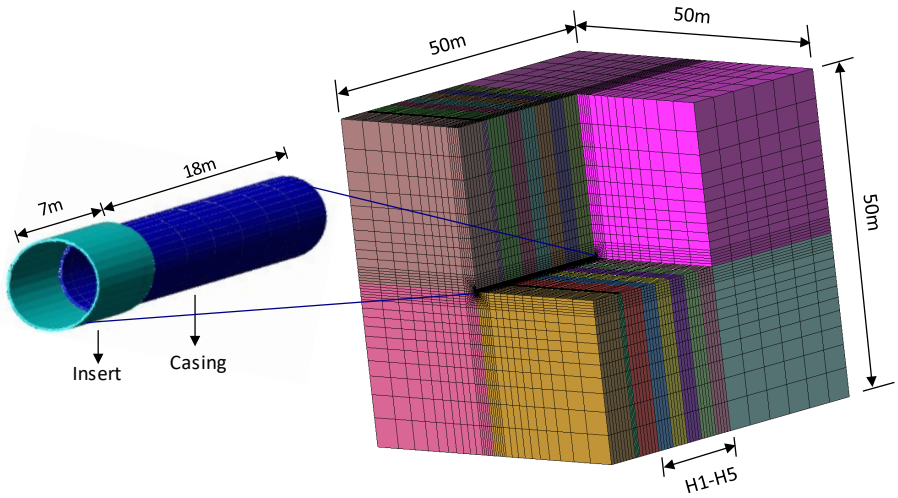

Figure 6.7: Geometry and mesh used for 3D THM simulation. The ALC1604 cell is oriented parallel to the major horizontal stress direction.

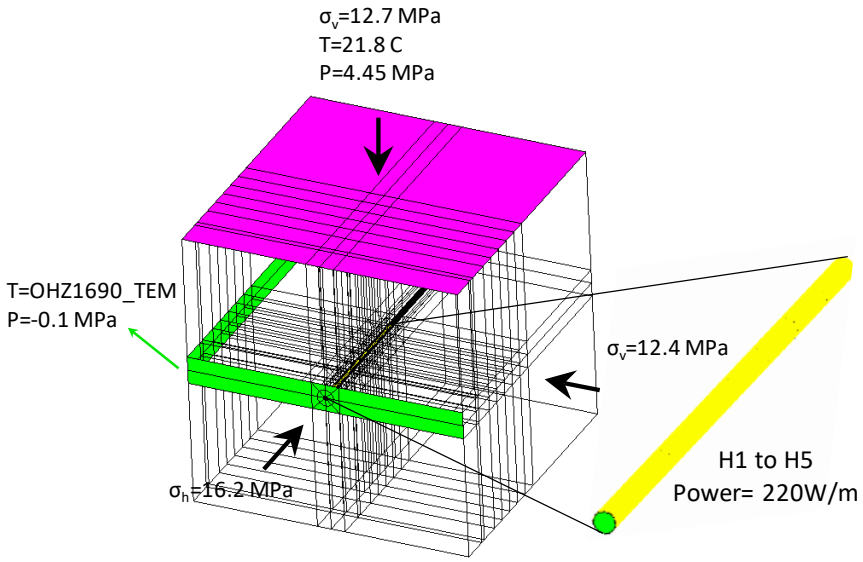

Figure 6.8: Initial and boundary conditions applied for 3D THM simulation.

An initial constant temperature of 21.8°C has been assumed throughout the geometry. Hydrostatic distribution of water pressure was initially defined, with a value equal to the field value (4.7 MPa) at ALC1604 experiment level. Fully anisotropic lithostatic stress distribution has been initially prescribed. Values at experiment level are 16.2 MPa, 12.4 MPa and 12.7 MPa for the vertical, the major and minor horizontal components, respectively. Porosity was set to 17.3% in the COx claystone.

Table 6.4 Initial and boundary conditions applied.

	Condition	Parameters	First point	Final point	Distribution
COx claystone	Initial Liquid pressure	Pl [MPa]	4.45	4.95	Linear
	Initial Temperature	T [°C]	21.82		Constant
	Initial Porosity	ϕ	0.15		Constant
	Initial Stress	X Stress	-9.937	-14.0625	Linear
		Y Stress	-9.937	-14.0625	Linear
		Z Stress	-13.216	-18.703	Linear

The different phases of numerical analyses have mimicked the different stages of the experiment was listed in Table 4.1. The analysis started simulating the tunnel excavation followed by the construction of the casing and the insertion of the heater. After the installation of heaters, an isothermal period of three months was simulated. Afterwards, the main power was applied to the heaters. During the heating stage of the experiment, the input power will be maintained long enough to achieve a quasi-permanent state, in order to separate the transitory and the steady-state. As for the thermal analysis, a small part of the heat input has been prescribed in the non-heated zone to simulate the heating of this zone by conduction/radiation and air convection.

For reference, two 2D plane strain analyses have been performed and the results compared with those of the 3D simulation. The model domain, finite element meshes and main boundary conditions (B.C.) adopted are depicted in Figure 6.9. The analysis "A1" has been run for the section located at a depth of 17.5 m (Cross-section across Heater 3) which is the location of the three boreholes that contain temperature sensors and piezometers. A second analysis "A2" has been run with a different value of heat flux for the section located at a depth of 13 m, which is the location of the three boreholes that contain temperature sensors and piezometers.

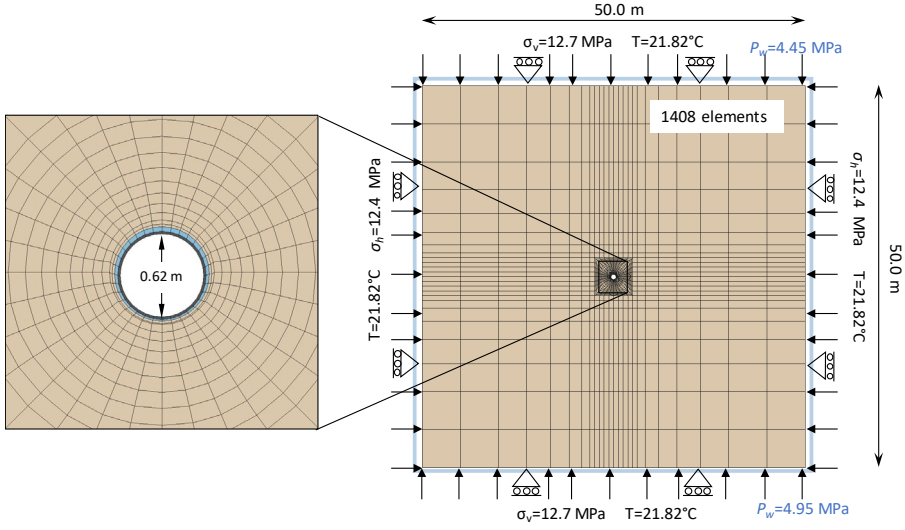

Figure 6.9: Geometry, mesh and boundary conditions from the 2D THM analysis of ALC1604 in situ heating test.

6.4 COMPARISON OF MEASUREMENTS AND SIMULATIONS

6.4.1 Thermal results

There were three sensors in section z=17.5m and seven sensors in Section z=13m, located at different orientations with respect to the bedding plane (indicated in Figure 6.10). The evolution of temperatures at these two sections are shown in Figure 6.10 and compared with the results of the 2D and 3D analyses.

It can be noted that, after about one year of heating, temperatures generally rise very slowly throughout the COx claystone. Moreover, anisotropic effects are noticeable; temperature along the bedding increases more rapidly than in the orthogonal direction. As expected, the 3D THM output the same temperature field and the T-analysis and captures consequently well temperatures variations at all sensors. It is worth noting that the observed stabilization of temperatures at the end of the heating phase (1st semester 2019) and well-captured by the 3D model cannot be reproduced by the 2D models. This indicates that heat dissipation along the z-direction (direction of microtunnel) has a major effect on the temperature field in the rock.

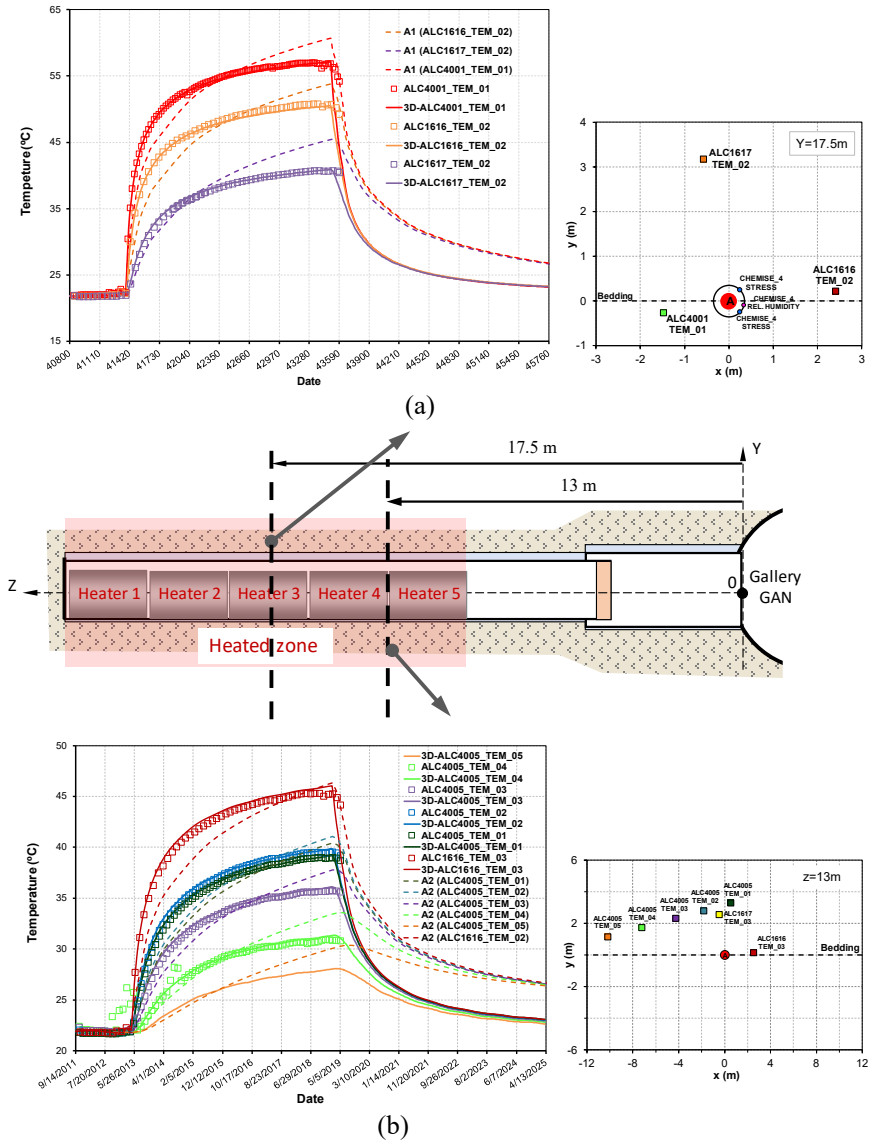

Figure 6.10: Evolution of temperatures in COx claystone, observations and computed results: (a) Section z =17.5 m; (b) section z =13 m.

More information from the analyses is given in Figure 6.11 in terms of contours in a section z =17.5 m at various relevant stages. The following times have been selected: 114 days (end of the first heating stage); 260 days (time at which maximum pore pressures are achieved); 960 days (two years heating); and 2000 days (five years heating, at the end of the simulation).

The anisotropic temperature distribution is apparent, with higher temperatures being reached in the direction of the bedding planes. Similar information about the 3D shape of temperature bulb is presented in Figure 6.12 and 11 in a three-dimensional view.

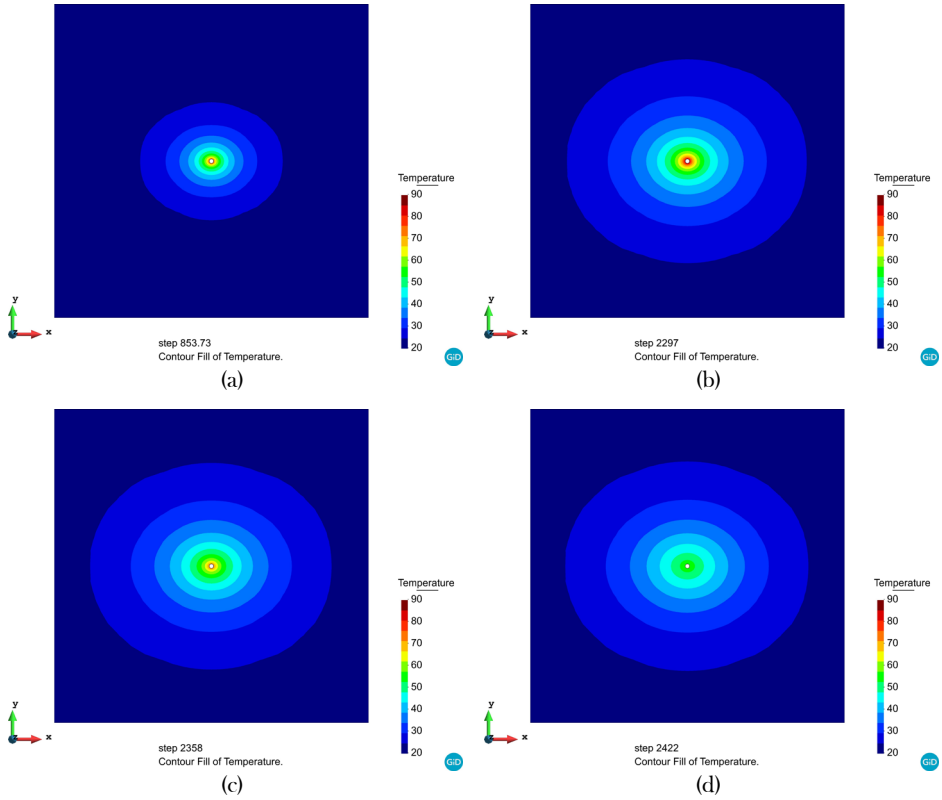

Figure 6.11: Computed contours of equal temperature (^{0}C) in a cross-section across Heater 3 for (a) 985 days (two years heating); (b) 2297 days (end of heating); (c) 2358 days (end of first cooling phase); (d) 2422 days (end of second cooling phase).

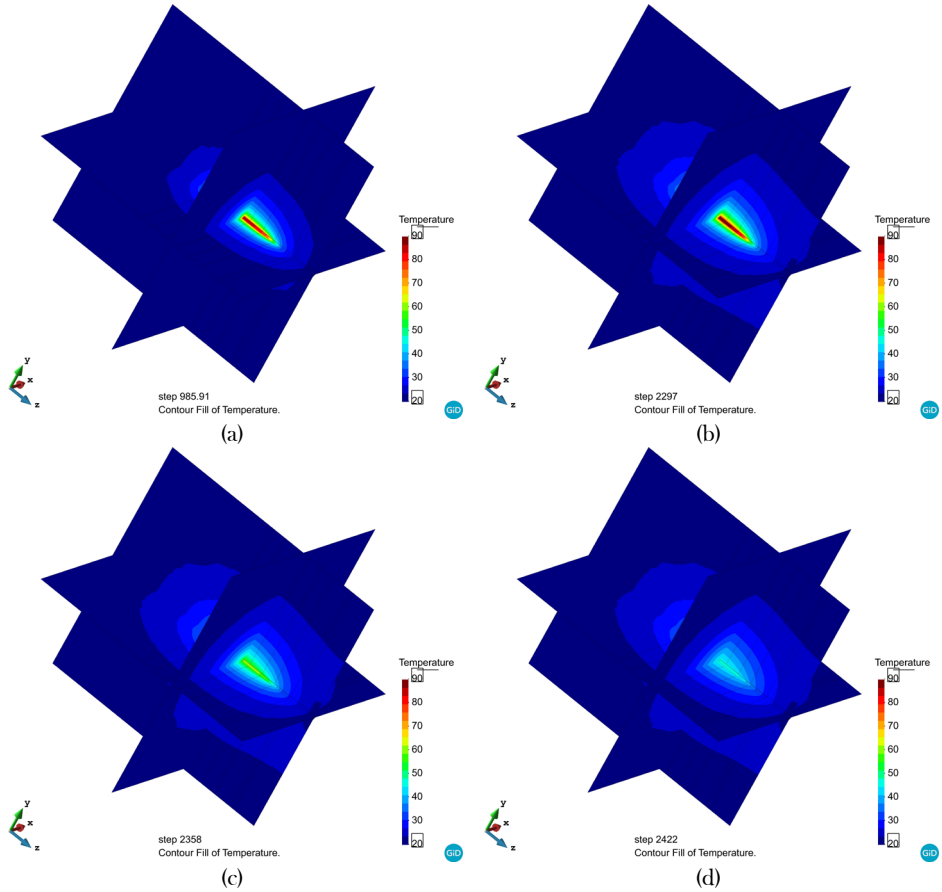

Figure 6.12: Three-dimensional views of computed contours of equal temperature (°C) on section A for (a) 985 days (two years heating); (b) 2297 days (end of heating); (c) 2358 days (end of first cooling phase); (d) 2422 days (end of second cooling phase).

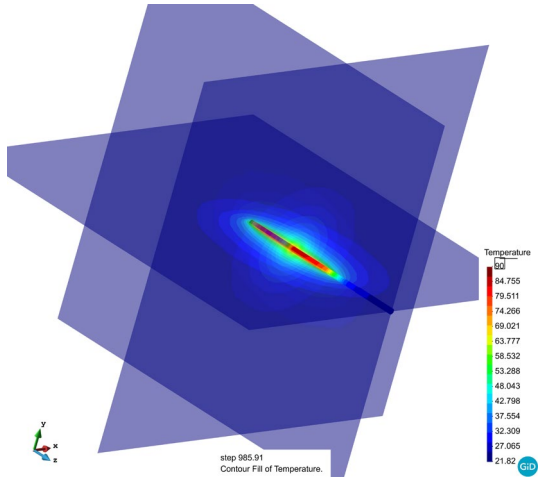

(a)

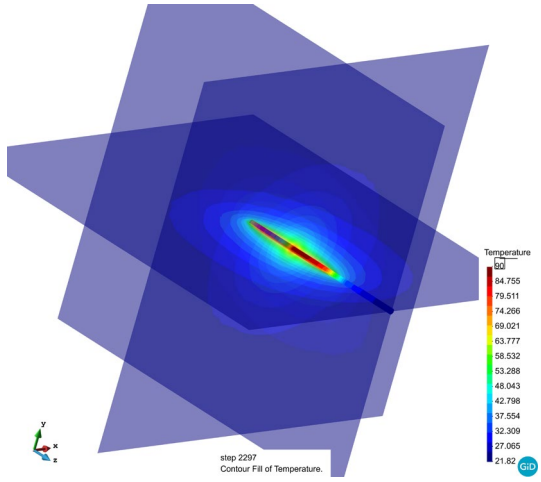

(b)

Figure 6.13: Three-dimensional views of computed contours of equal temperature (°C) on section A for (a) two years heating; (b) end of heating.

Profiles of temperatures within section z=17.5m are plotted in Figure 6.14 for the same times. The progressive rise of temperature can be readily observed. It is interesting to note that the region with a significant temperature increase appears to be limited to a radius of about 5 m around the main borehole.

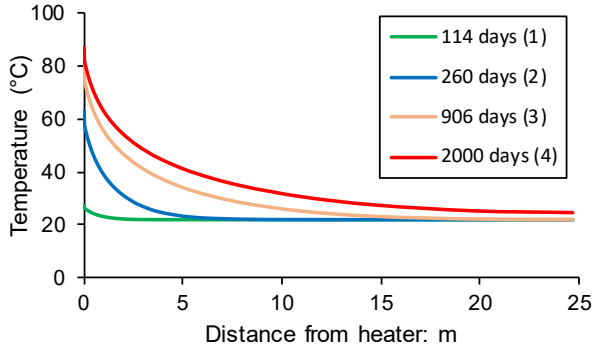

(a)

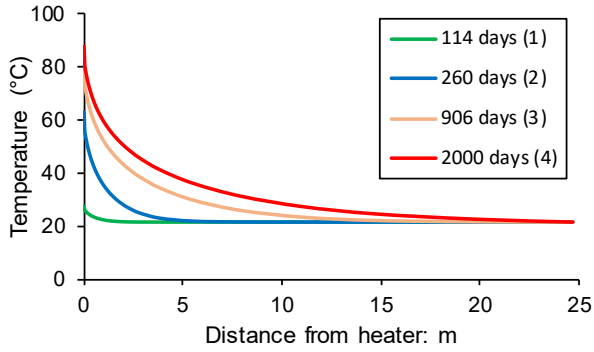

(b)

Figure 6.14: Computed temperature distributions at various times on section A: (a) bedding plane direction; (b) perpendicular to bedding plane direction.

6.4.2 Excavation damaged zone

To design deep geological repositories (DGR) for high-level radioactive waste (HLW), the depth of excavation induced damage is essential. The damages arising from the excavation are well known to increase the permeability of the undamaged rock mass and constitute a potential contaminated transport or leakage path. The depth of excavation damage caused by high stress concentrations in brittle rock masses has been calculated to date on the basis of empirical methods or case-specific numerical modelling.

Numerical back analysis of development and extent of brittle rock damage has been proven as a best captured using methods. In this section we will calculate and predict the configuration of excavation damage zone (EDZ) depths around ALC1604 cell excavation in COx claystone as host material.

Thanks to the improved understanding of how the damage is induced and affects the permeability around the excavations, the terminology linked to damage

zones has evolved from early investigations. The damage zones are traditionally referred to collectively as the EDZs and various zones therein are depicted in Figure 3.7 (Chapter 3). The density of fractures triggered by excavation decreases moving away from the surface of the excavation. Typically, the outer limit of the EIZ is of minimal interest for a single excavation as it occurs at a significant distance from the surface of excavation.

Many studies have been conducted on EDZs with focuses on:

- formation and long-term processes (e.g. Blümling et al., 2007),
- the depth of damage (e.g. Bäckblom, 2008),
- and changes in permeability (e.g. Ababou et al., 2011).

These studies have focused on crystalline (e.g. a review by Bäckblom, 2008), argillaceous (e.g. a review by Lanyon, 2011) and salt rocks (Hou, 2003). These are the most commonly considered rock types for nuclear waste storage.

Numerical simulations to date have largely focused on EDZ development and prediction using a variety of approaches for specific case studies. These have included continuum modeling (Hou, 2003; Rutqvist et al., 2009), discontinuum modeling (Fabian et al., 2007; Hudson et al., 2009), and hybrid modeling (Zhu and Bruhns, 2008; Lisjak et al., 2016).

The experiments have revealed that excavation operations induce damage and fracturing around the MHM URL galleries (Armand et al., 2014), creating an excavation damaged zone (EDZ), where significant changes in flow and transport properties take place (Tsang et al., 2005). Significant efforts have been made to simulate these experimental excavations (Seyedi and Gens, 2017) and to gain insights into the design of the actual repository. The EDZ is identified as one of the critical issues affecting the long-term behaviour of the tunnel near-field (Blümling et al., 2007). The observed configuration of the EDZ depends on the orientation of the excavation concerning the anisotropic in-situ stress state.

As stated above, the ALC1604 cell is parallel to the major horizontal stress σ_H and has a nearly isotropic stress state in the plane normal to the tunnel axis. Despite that, the EDZ extends further in the horizontal direction (Figure 6.15), suggesting strong anisotropic characteristics of the rock mass. Figure 6.15 shows the distribution of fractures around a micro-tunnel (ALC3005) excavated parallel to ALC1604. The breakouts occurred mainly at locations where the bedding planes were orientated tangential to the tunnel circumference and, as a consequence, the

breakouts mainly developed in the vertical direction of the cross-section (Marschall et al., 2006 and Blümling et al., 2007).

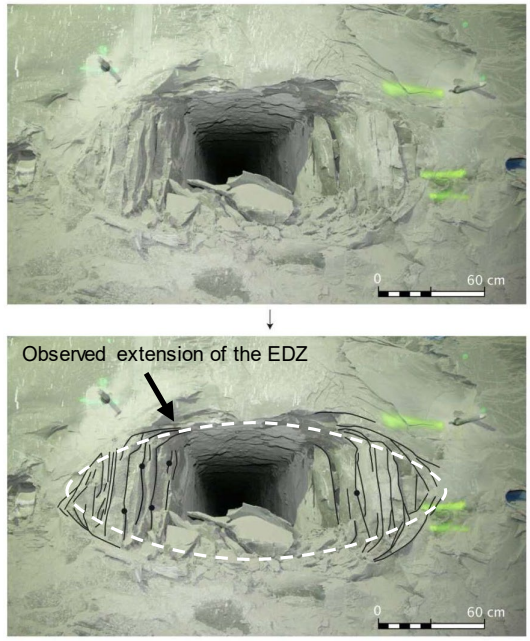

Figure 6.15: Extension of the damaged zone around a HLW cell parallel to major horizontal stress, showing the elliptical distribution of fractures around the opening, with a larger extension in the horizontal direction.

An estimate of the configuration of the excavation damaged zone can be obtained by plotting contours of the cumulative plastic multiplier as it is directly related to the magnitude of irreversible strains (Figure 6.16). The lateral extent of the shear fractures zone for smaller opening was almost equal to one diameter of the opening (Armand et al., 2014) in MHM URL. Model results suggest that a plastic zone of up to 0.7 m away from the microtunnel wall is formed. At the point with the higher plastic multiplier, much more substantial mechanical effects on rock deformability and hydraulic diffusion will be identified. It can be seen that the configuration of the damaged zone is similar to that observed in the previous microtunnel with the same orientation, extending more in the horizontal direction (Armand et al. 2014, 2017).

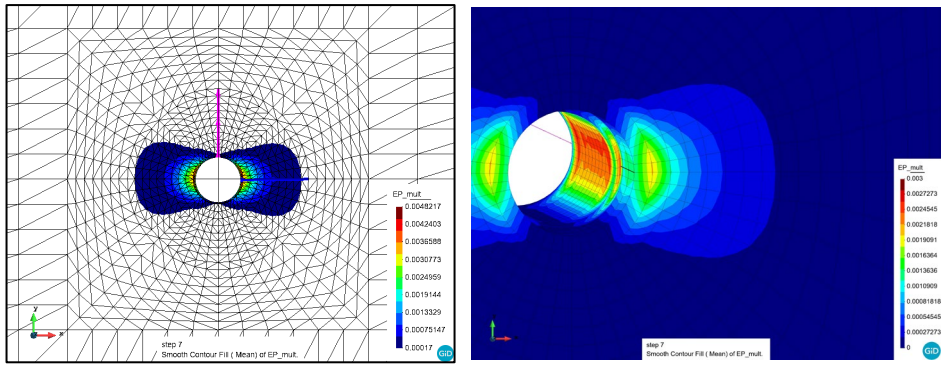

(a) (b)

Figure 6.16: (a) Obtained configuration of the EDZ in terms of the plastic multiplier in the section z=17.5m (b) Three-dimensional view of computed contours of plastic multiplier at the end of excavation.

Figure 6.15 presents the computed plastic multiplier increment distributions at various times on section z=17.5m. The following times have been selected: 1 day after excavation; 7 days (end of the excavation); 176 days (end of heating test); 985 days (two years heating); 2297 days (end of main heating phase); 2358 days (End of first cooling phase); 2455 days (End of second cooling phase); 4668 days (End of 6 years cooling). After seven days from the excavation, almost all the damage has developed in the zone where stresses are higher than the available anisotropic strength. Afterwards, the damage process slowly continues as the result of creep, consolidation and heating. At the end of the heating phase, after six years, the size of the damaged zone has only marginally increased. However, inside it, the intensity of damage was increased. After about six years of cooling, the EDZ will either barely change or not alter at all (Figure 6.17). Similar information is presented in Fig. 12 in a three-dimensional view Figure 6.18 in terms of contours in a section z=17.5m at various relevant stages.

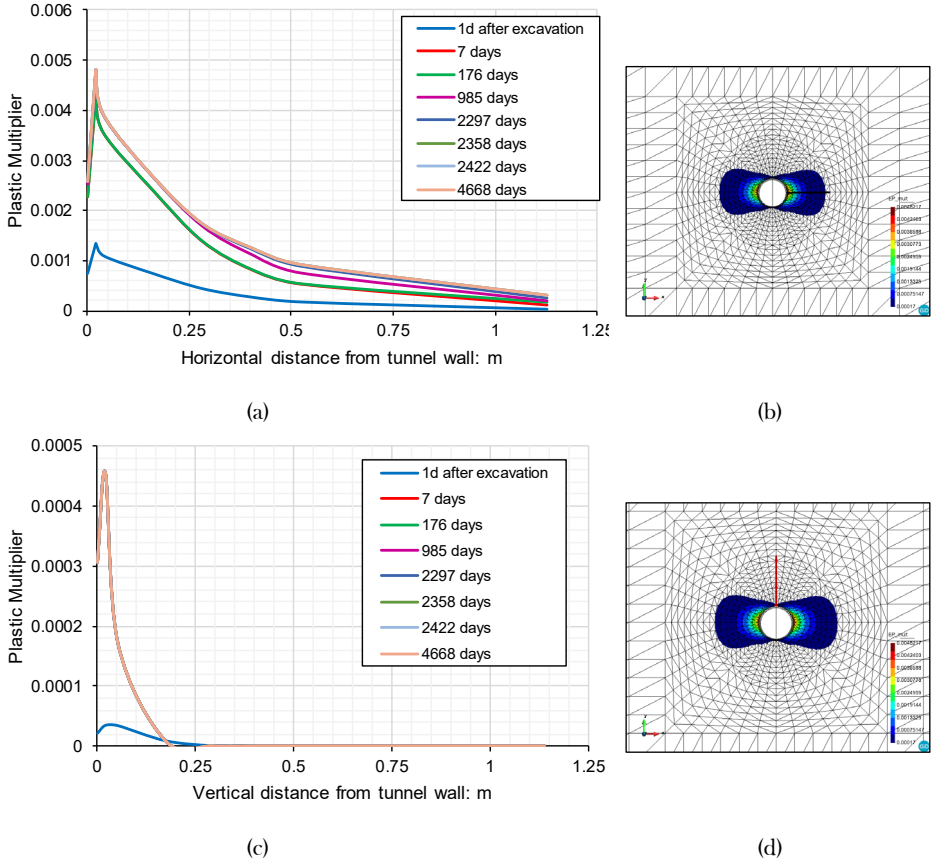

Figure 6.17: Computed *plastic multiplier* increment distributions at various times on section perpendicular to Heater 3 (z=17.5m) (Horizontal distance to tunnel wall).

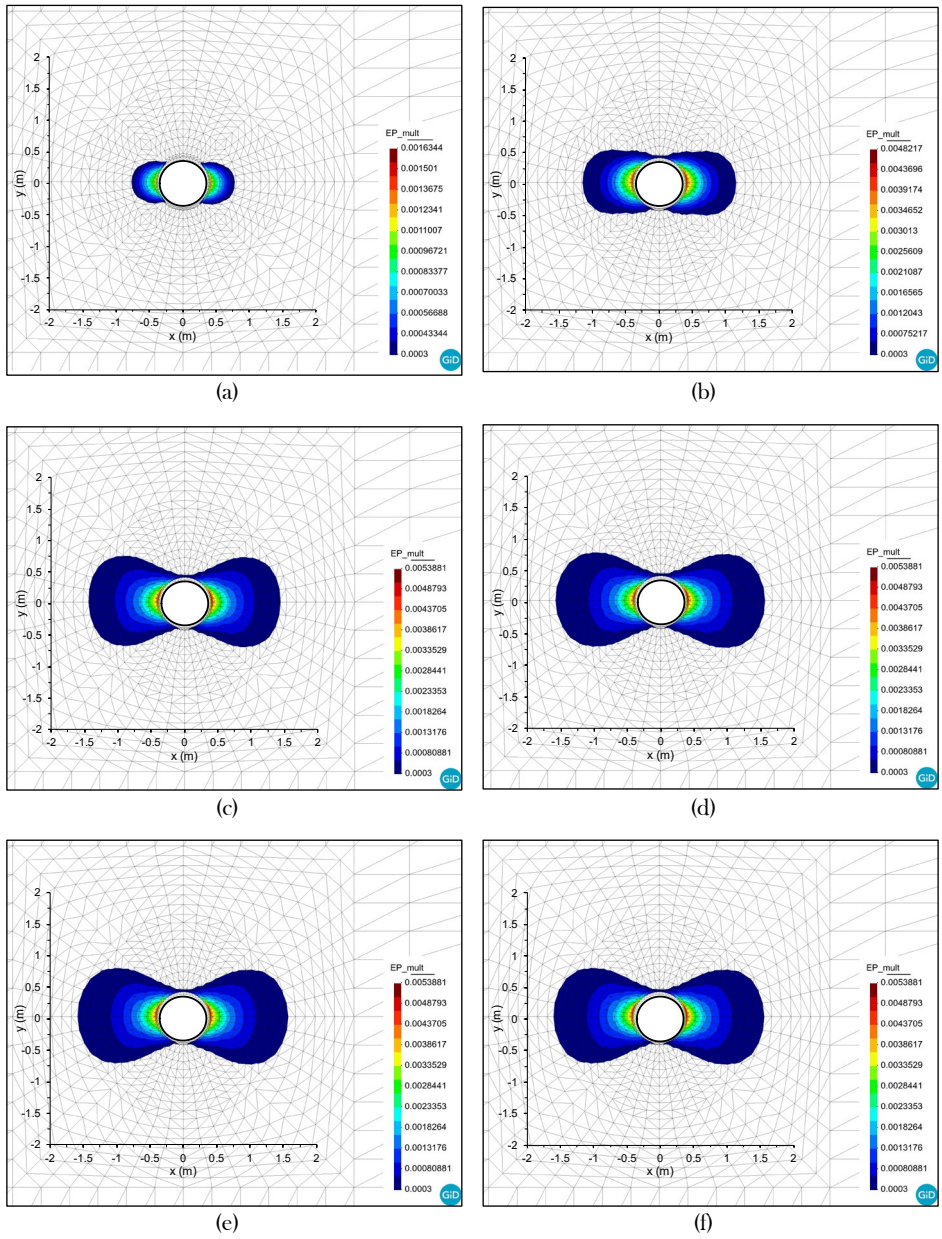

(a) (b) (c) (d) (e) (f)

Figure 6.18: Damage distribution evolution in the model for: (a) cell opening; (b) 7 days; (c) 2297 days; (d) 2358 days; (e) 2455 days; (f) 4668 days.

Figure 6.22 shows horizontal profiles of plastic multiplier along the longitudinal direction in microtunnel for various times and horizontal distances to tunnel wall. The following times have been selected: 1 day (cell opening); 7 days (end of the excavation); 176 days (end of heating test); 985 days (two years heating); 2297 days (end of main heating phase).

Two different zone are distinguished in the figure. Induced fracture caused by excavation and EDZ extension during heating phase. As shown in Figure 6.22, EDZ evolution from day 7 (end of excavation) to the day 176 is negligible. It means that the effect of time-dependent hydromechanical evolution of COx claystone has not an indispensable role in EDZ evolution around the tunnel. However, the heating phase caused thermoplastic strains as indicated in the figure. Figure 6.20 shows the similar results of computed damage distribution for various times and horizontal distances to tunnel wall.

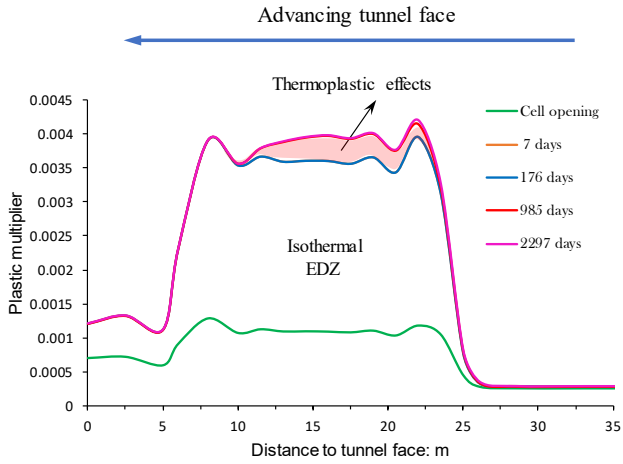

Figure 6.19: Computed damage distribution at various times in horizontal distance to tunnel wall Δx=4cm.

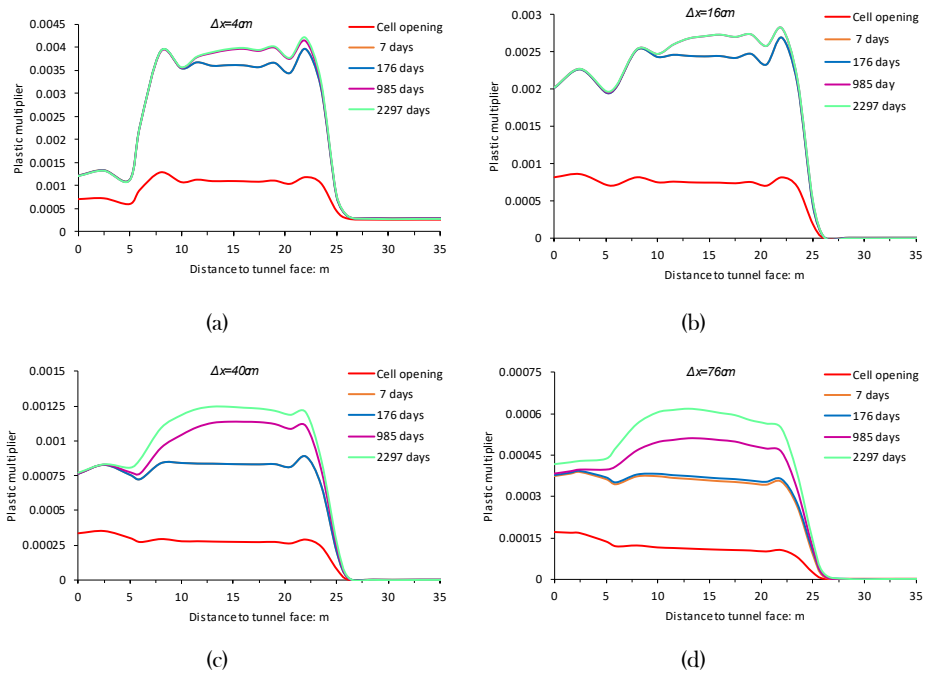

Figure 6.20: Computed damage distribution at various times and horizontal distances to tunnel wall.

Figure 6.21 shows computed damage distribution at various horizontal distances (Δx= 4, 16, 28, 40, 64, 76 cm) to tunnel wall for cell opening, 7 day (end of excavation) and 2297 days (end of heating phase). It can be seen that, the point with Δx= 4m which is the closet to the tunnel wall gives higher values of plastic multiplier. However, the plastic multiplier evolution is negligible for Δx > 10 cm.

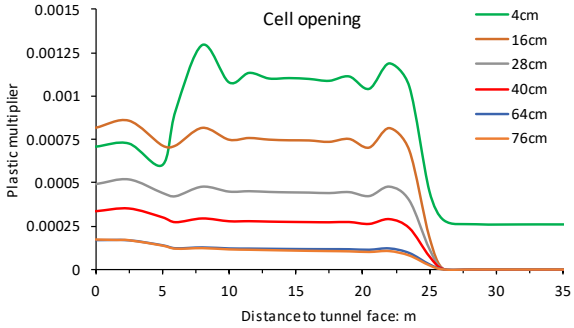

(a)

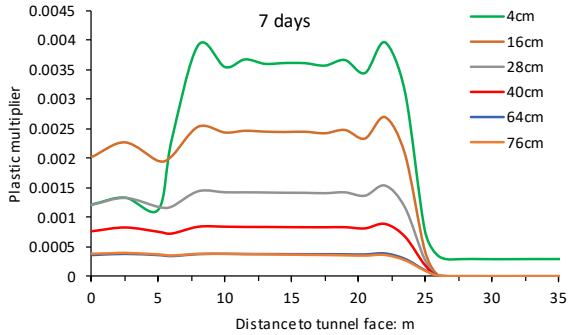

(b)

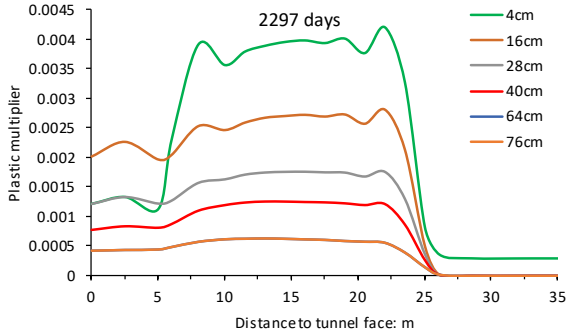

(c)

Figure 6.21: Computed damage distribution at various times and horizontal distances to tunnel wall.

Figure 6.22 shows horizontal profiles of intrinsic permeability on the right side of the cell. They evidenced the dependence of permeability on damage introduced in the model and whose coefficient has been back analysed to reproduce the pore pressure correctly around the excavation. Permeability reaches a maximum value near the cell wall where it appears to increase of five orders of magnitude during

excavation and one additional order of magnitude during heating. These values should not be considered as quantitatively relevant but essentially indicate a high permeable zone because of fracturing close to the excavation wall. More important for an adequate capture of the pore pressures measured in the rock during the ALC1604 experiment is the distance within the EDZ at which permeability experiences a change of at least one order of magnitude. More information from the intrinsic permeability evolution in EDZ is given in Figure 6.23 in terms of contours in the section z=17.5m at the end of excavation and end of heating phase.

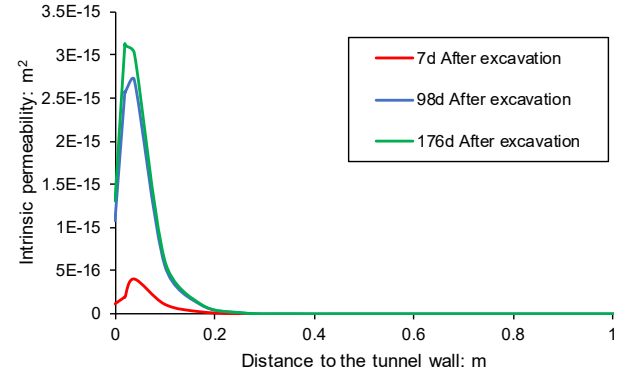

(a)

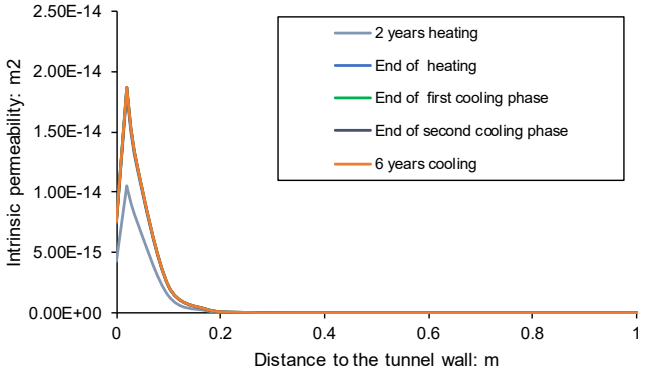

(b)

Figure 6.22: Computed permeability increment distributions at various times (Horizontal distance to tunnel wall).

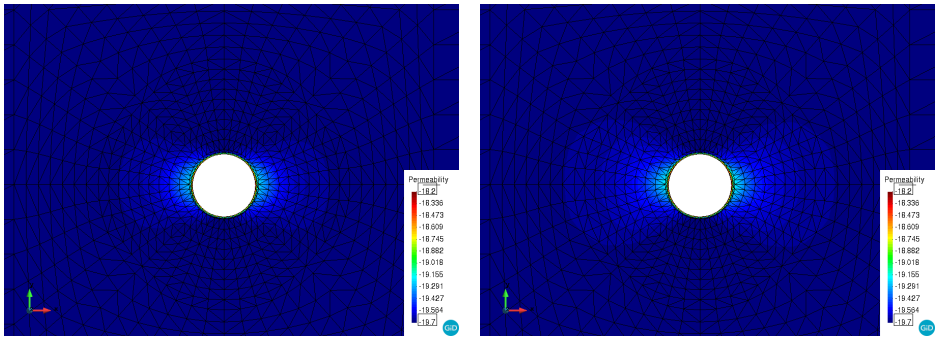

(a) (b)

Figure 6.23: Computed contours of permeability in section z=17.5m for: (a) 7 days (b) 2297 days (log scale).

6.4.3 Pore pressures

Figure 6.24 presents a comparison between the results of the 3D analysis and pore pressure measurements at sections z=17.5 and 13 m. The results of the two 2D analyses have also been added for reference. It is apparent that the pore pressure increase is reasonably well captured by the model for both the excavation and heating phases. The pore pressure rises registered during the heating stage by sensor ALC1616_PRE_02 is, however, sharper than in the model. This could be due to the spatial discretization considered. The discrepancy is not observed for the two other sensors of the same sections.

In Figure 6.24 shows with grey lines the times of peak in pore pressure in the section at 17.5 m. Time becomes larger as the distance to the main borehole increases. These results from the combined effect of the movement of temperature rise outwards and pore pressure dissipation from the inner zones. This evolution can easily be observed in Figure 6.25, where profiles of pore pressure are plotted for various times. The two distributions plotted correspond to two orthogonal directions, one along the bedding plane and the other normal to the bedding. Differences can be observed between the two sets of distributions.

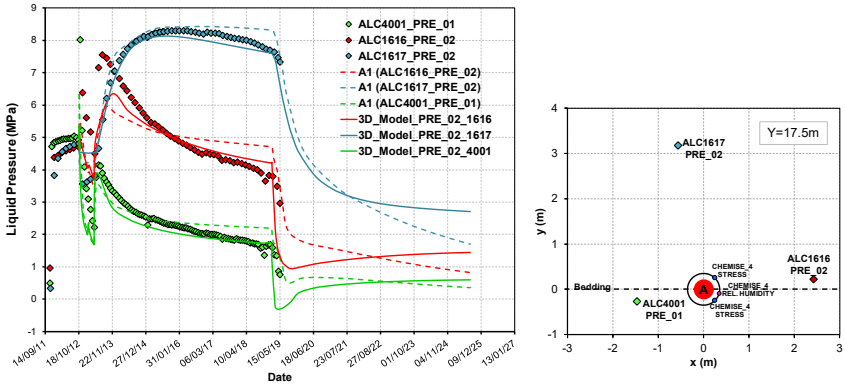

(a)

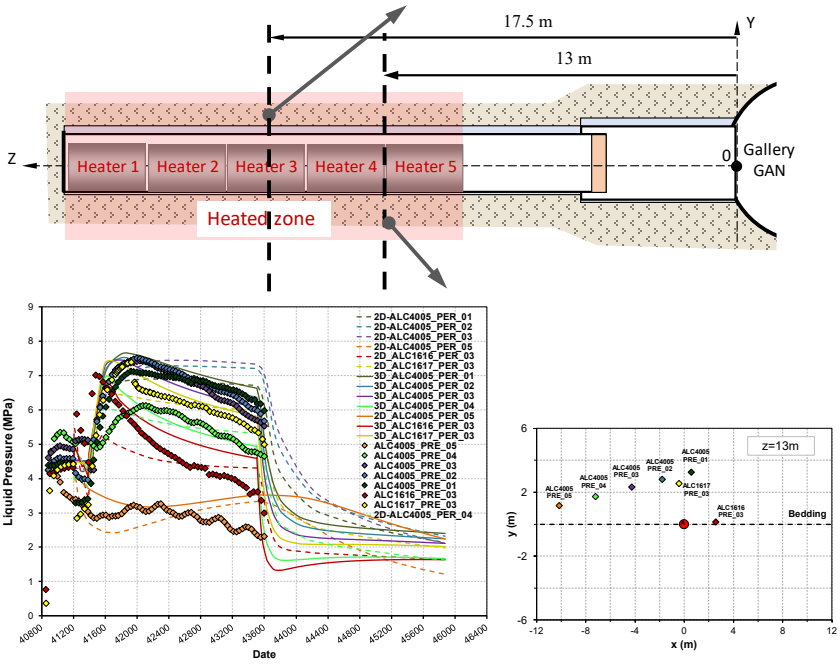

(b)

Figure 6.24: Evolution of pore pressure increments at various points in the COx claystone: observed and computed results.

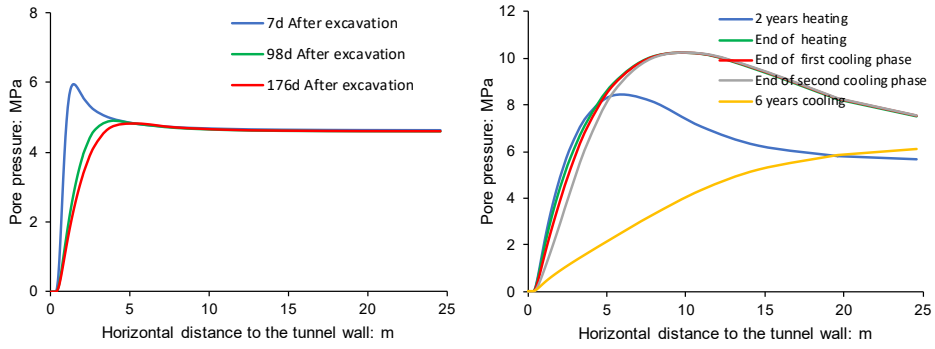

Figure 6.25: Computed pore pressure increment distributions at various times on section A1: (a) bedding plane direction; (b) perpendicular to bedding plane direction.

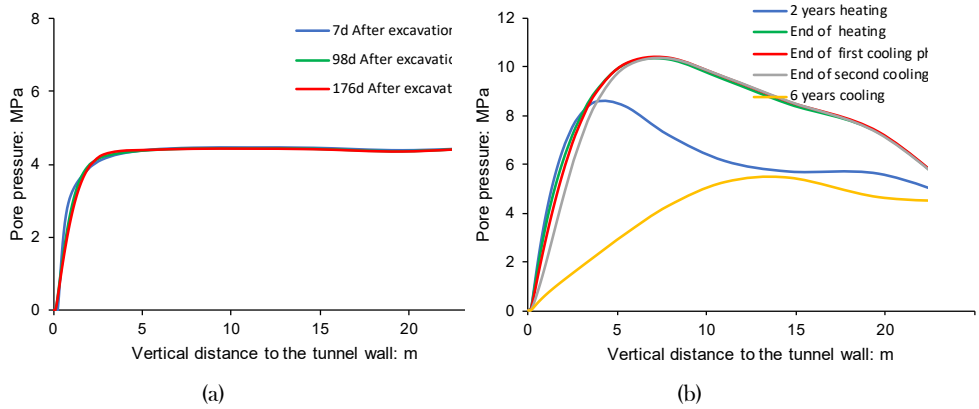

Figure 6.26: Computed pore pressure increment distributions at various times on section A1: (a) bedding plane direction; (b) perpendicular to bedding plane direction.

Finally, a general overview of pore pressure field around the experiment is shown in Figure 6.27, Figure 6.27 , Figure 6.28Figure 6.29. Movement of the locus of maximum pore pressure away from the microtunnel as time goes on is readily apparent. The Figures also evidence the draining effect of the GRD gallery at 2297 d.

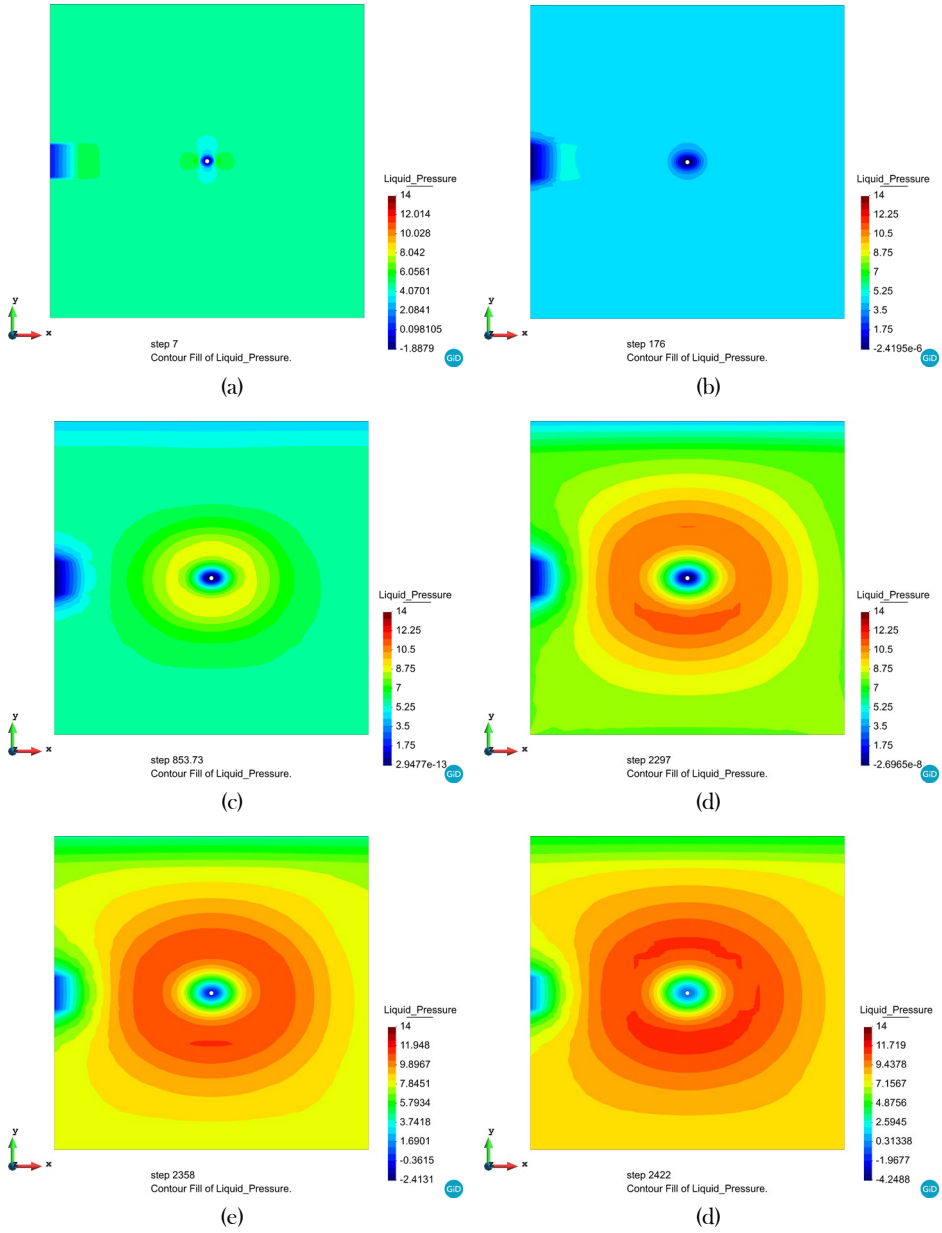

Figure 6.27: Two-dimensional view of computed contours of equal liquid pressure (MPa) in a cross-section across Heater 3 for (a) 7 days (After excavation); (b) 176 days (end of heating test); (c) 853 days two years heating); (d) 2297 days (end of heating).

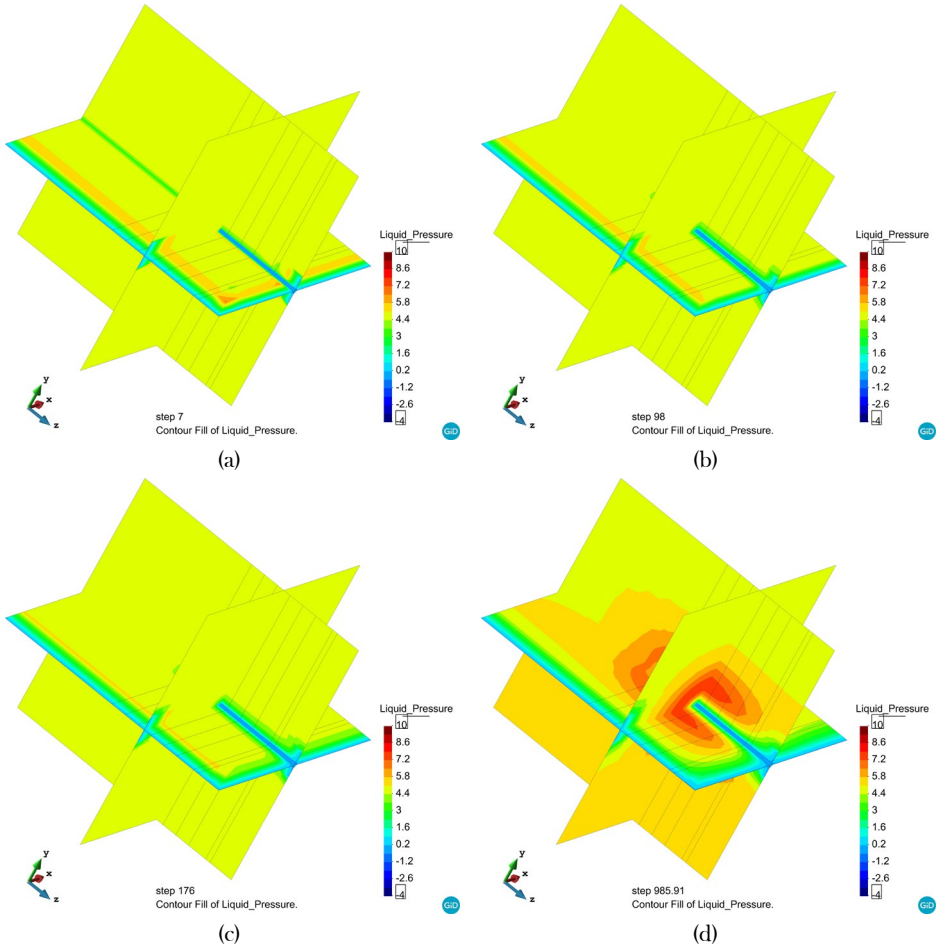

Figure 6.28: Computed contours of equal pore pressure increase (MPa) for: (a) 7 days (After excavation); (b) 98 days; (c) 176 days (end of heating test); (d) 985 days (2 years heating).

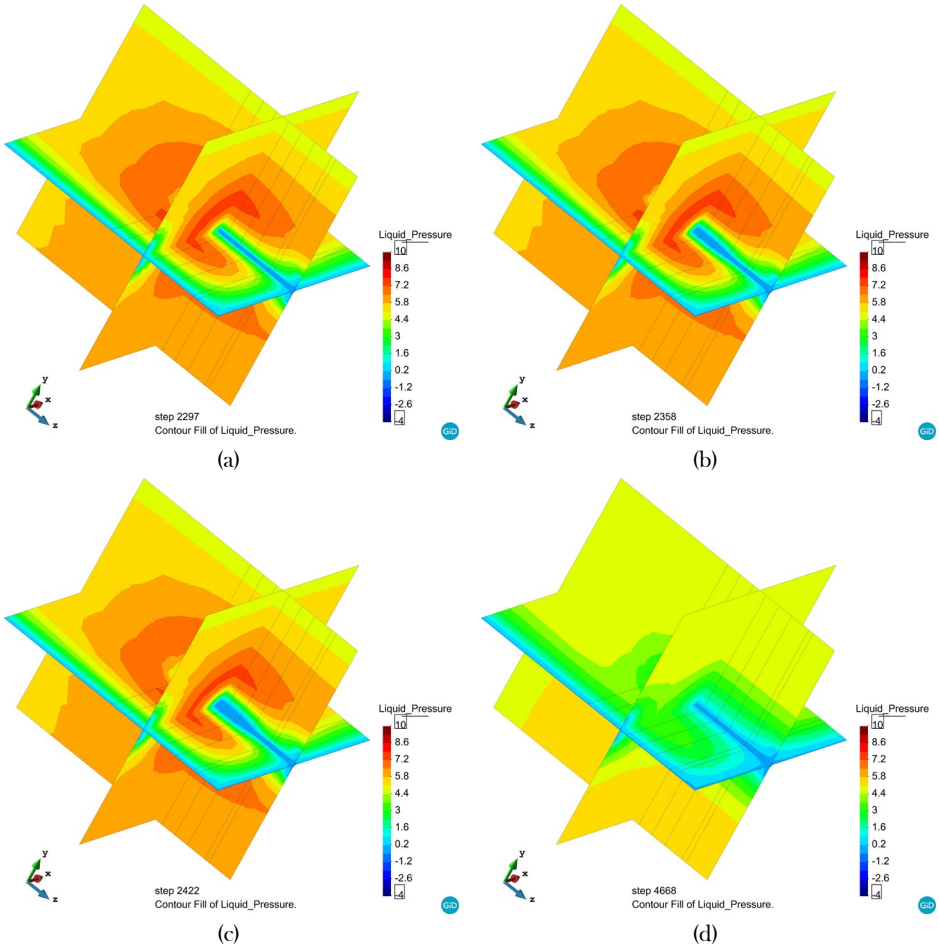

Figure 6.29: Computed contours of equal pore pressure increase (MPa) for (a) 2297 days (End of heating); (b) 2358 days (End of first cooling phase); (c) 2422 days (End of second cooling phase); (d) 4668 days (6 years cooling).

6.4.4 Convergence measurements

Figure 6.30 presents a comparison between the results of the 3D THM analysis and convergence measurements of the liner for section 9 (depth of 7 m), since the connection of the sensors. It is apparent that the overall convergence behaviour is reasonably well captured by the model for the three loading steps as defined above.

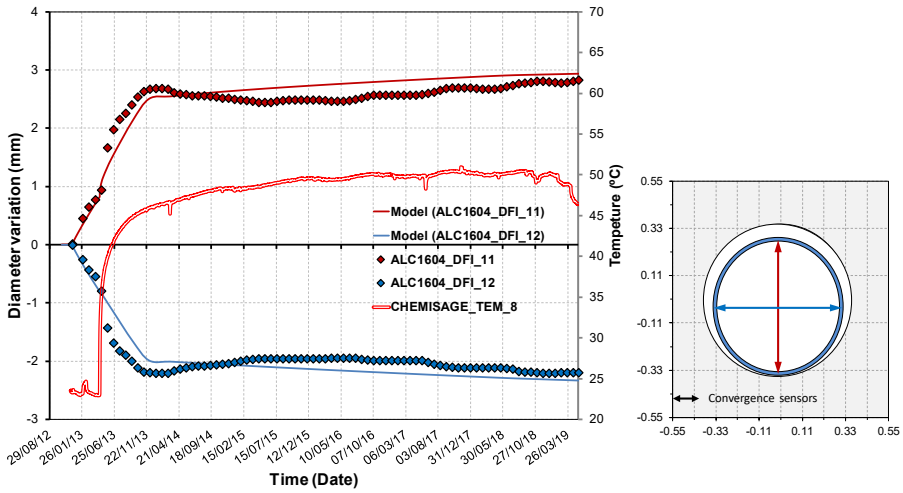

Figure 6.30: Diameter variations measured on the sleeve at a depth of 7 m (negative values correspond to convergence).

The calculated diameter variations of insert at section 11 and 12 (z=2,4m respectively) during in situ test are shown in Figure 6.32 and Figure 6.31. In all the cases, evolution and maximum convergence are reasonably well captured by the model. It can be seen that the calculated results are in good agreement with the measured values. The model is shown to be capable of predicting both qualitatively and quantitatively the above phenomena.

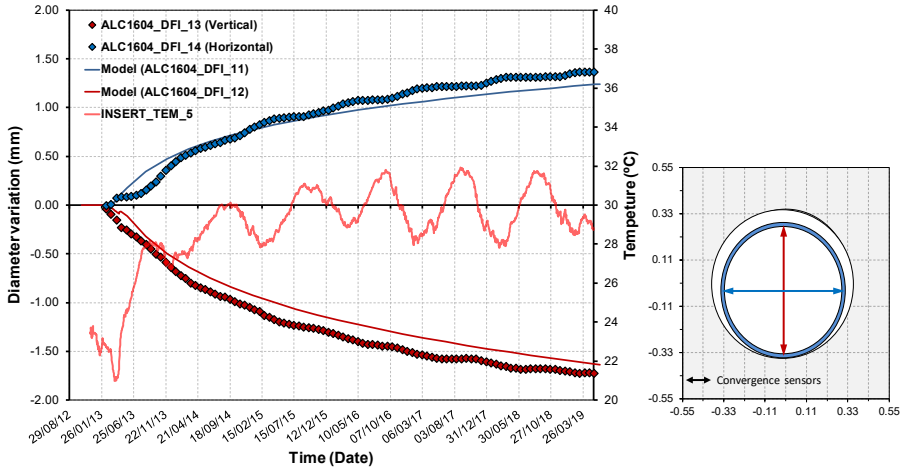

Figure 6.31: Diameter variations measured on the insert at a depth of 2m (negative values correspond to convergence).

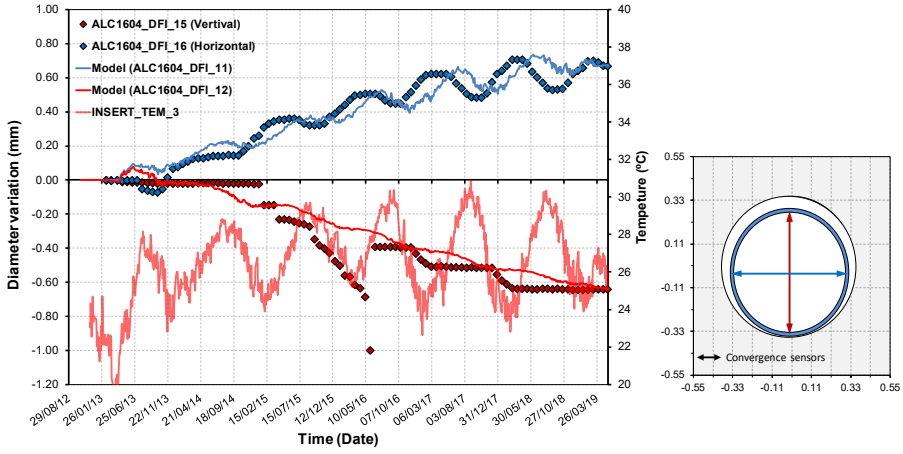

Figure 6.32: Diameter variations measured on the insert at a depth of 4m (negative values correspond to convergence).

More information from the numerical analysis is given in Figure 6.33 in terms of displacement contours and vectors in a section across Heater 3 (section 17.5m) at various times. The following times have been selected for plotting: 176 days (end of the test heating stage a day before heating stage); 1285 days (three years heating); 2500 days (six-year heating); 4500 days (five years cooling). The anisotropic load distribution and ovalization of the casing are apparent in the figures. The figure also shows that the liner follows deforming during the cooling phase, as a result of creep effect.

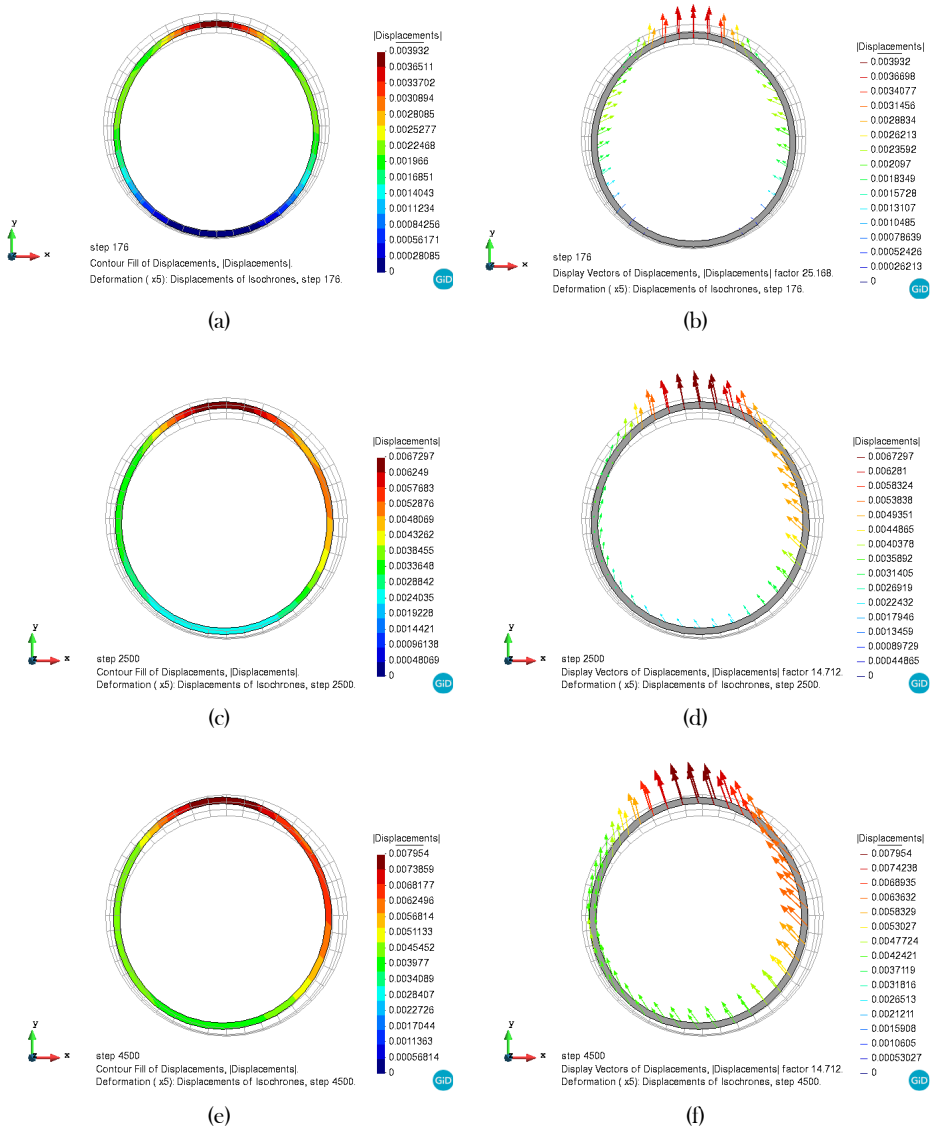

Figure 6.33: Computed contours and display vectors of displacement in casing at section 17.5m for: (a) 176 days (before heating phase started); (b) (2500 days (six-year heating); (c) 4500 days (five years cooling).

6.4.5 Mechanical signatures

Figure 6.34 presents the evolution of the circumferential strain ($\varepsilon_{\theta\theta}$) around the inner face of the casing at different times and 18 m depth (section 4) with the computed results from the analysis. It is apparent that the evolution of the circumferential strain is reasonably well captured with the formulation and parameters used.

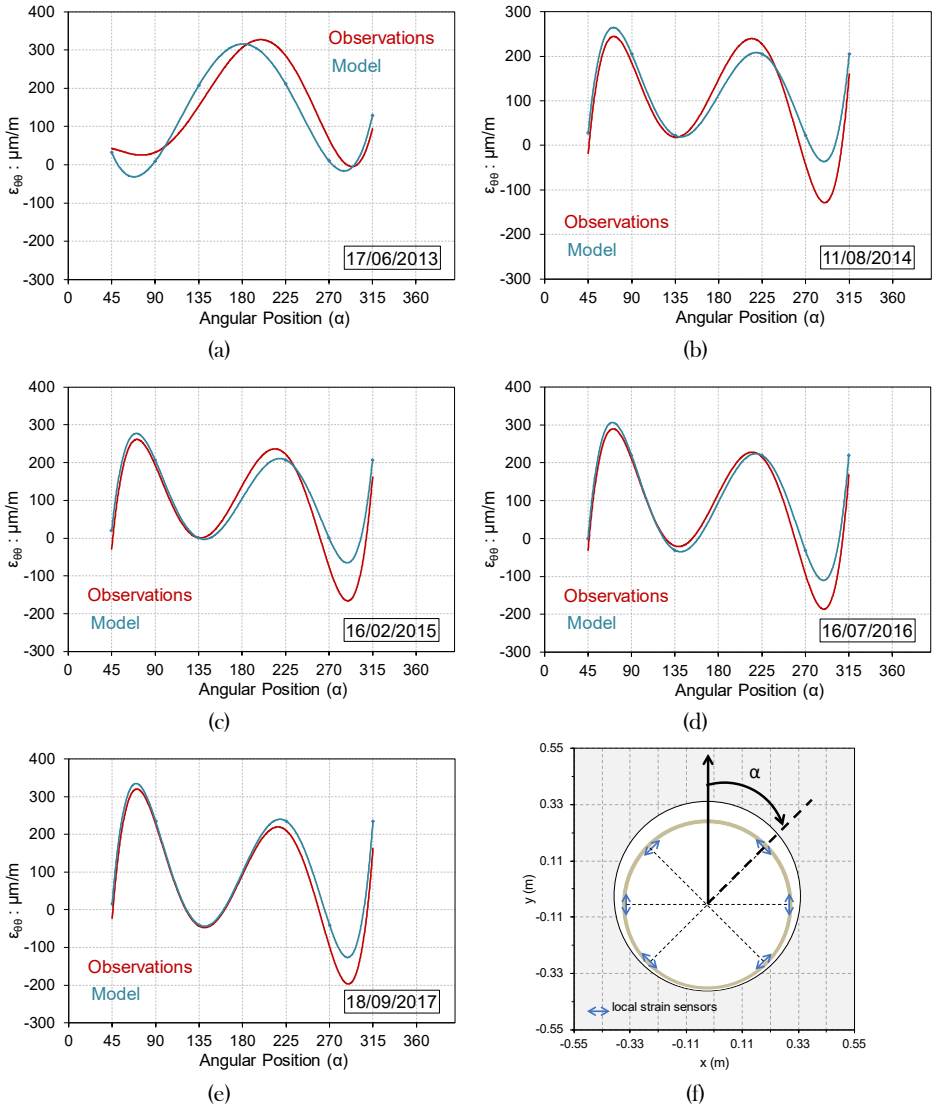

Figure 6.34: Evolution of circumferential mechanical strain at 18m depth for various times during the insitu test.

Chapter 7: Thermomechanical model for argillaceous rocks

The chapter is centred on the enhancement of an existing time-dependent anisotropic isothermal elastoplastic model for argillaceous rocks to enhance its predictive capability with respect to temperature changes, in the light of new experimental evidence. The reference model is cast within a constitutive framework that considers deviatoric strain hardening and includes a number of features that are relevant for a satisfactory description of hydromechanical behaviour of argillaceous rocks. Some development of the original temperature-independent formulation is proposed. In particular, functions describing the yield locus, stiffness and the strength parameters are improved to consider the elastic domain shrinking and the degradation of stiffness and strength parameters with heating. The adequacy of the presented model is confirmed by results of thermal triaxial tests on COx claystone. The thermomechanical constitutive model developed is then applied, via a suitable coupled THM formulation, to the coupled THM analysis of an in-situ heating test performed in the Meuse/Haute-Marne Underground Research Laboratory. The relevance and importance of the temperature effect in the damaged zone around the in-situ heating tunnel are clearly demonstrated.

7.1 BACKGROUND

Argillaceous rocks are considered as a potential host rock for high-level radioactive waste disposal. Given the exothermic nature of radioactive wastes, a temperature elevation will affect the Excavation Damaged Zone (EDZ) around the disposal cells. In this regard potential effects of the thermal impact on the EDZ in the near field are an important aspect regarding the performance assessment of deep geological repositories. The host rock around the repository cells containing the exothermic waste canisters will be submitted to various coupled mechanical, hydraulic and thermal phenomena including the development of an excavation damaged zone (EDZ). The temperature elevation might have some effects on the crack network of the EDZ as well as overall rock permeability in the close field, resulting in possible thermomechanical failure. For a proper understanding and appropriate modelling of the excavation damaged zone around repository cells at elevated temperatures, the combined effects of those phenomena should be considered in a constitutive model.

Thermomechanical models that are able to reproduce most of the observed behaviour of saturated clays at increased temperatures have been developed by several researchers. Hueckel and Borsetto (1990) developed one of the first thermomechanical constitutive models by modifying the well-known Cam-Clay model to take thermo-elastoplastic behaviour into account. They proposed a simple, yet conceptually powerful, approach to tackle the mechanical response of a soil exposed to variable heat conditions by defining the yield surface as a function of temperature as well as the plastic volumetric strain. In fact, most subsequent models are based on the same principle. Robinet et al. (1996) subsequently modified this model by attributing the thermal evolution of the yield limit to irreversible expansion thermal strain. Cui et al. (2000) added a volumetric thermal plastic mechanism, within the framework proposed by Hueckel and Borsetto, to predict thermal plastic strain for overconsolidated states. Graham et al. (2001) also introduced a non-isothermal modified Cam-Clay model within the framework of Hueckel and Borsetto. Modaressi and Laloui (1997) and Laloui and Cekerevac (2003) developed a thermoplastic model, based on multi-surface plasticity, wherein a one-parameter equation is used to capture the thermal evolution of the preconsolidation stress. Abuel-Naga et al. (2009) and Hueckel et al. (2009) incorporated the temperature-dependent shape of the state boundary surface (SBS) to accurately model the influence of temperature on the undrained stress path and peak shear strength. Some thermomechanical constitutive models consider the effect of temperature on viscous behaviour and cyclic loading (Modaressi and Laloui, 1992).

Most developed thermomechanical models are versions of the Cam-clay family models, in which thermo-plastic mechanism is developed using temperature-dependent preconsolidation stress function. In fact, soft clays thermomechanical behaviour is well modelled using the Cam-clay family models (in the critical state framework) because the preconsolidation is the main mechanism in these materials, whereas this is not the case for argillaceous rocks since strong post-sedimentation diagenetic bonds characterize argillaceous rocks thermo-plastic behaviour. Indeed, a Mohr-Coulomb type of failure criterion, with two strength parameters (cohesion c and friction angle φ) to describe the plastic behaviour, is more appropriate for argillaceous rocks.

When compared with the work on the thermomechanical modelling of clays, a limited number of thermomechanical models are developed for argillaceous rocks. The main aim of this work is to provide a thermomechanical model for argillaceous rocks, which predicts not only the qualitative effects of temperature on

the argillaceous rocks behaviour but also correctly captures a continuous variation of mechanical characteristics (e.g. stiffness and strength parameters) with temperature variation.

Although there are notable differences between different argillaceous formations (Gens, 2004, 2010), reflecting their various origins and geological histories, there are also a number of common key features that should be considered in any description of their thermomechanical behaviour. The peculiarities of the mechanical response of argillaceous rocks to heating established in experiments consist in a thermal hardening, with an elastic thermal expansion observed below the maximum supported temperature, followed by a plastic contraction at yielding once the maximum temperature is reached, as well as more ductile behaviour with an apparent decrease in peak strength at elevated temperature (Zhang et al., 2007; Monfared et al., 2012; Zhang et al., 2014; Menaceur et al., 2015; Zhang et al., 2016; Liu et al., 2019).

These experimental results led to the idea of extending a reference constitutive model (Mánica et al., 2017) to non-isothermal conditions. The core of the mechanical part of the reference model is taken from the Mohr-Coulomb yield criterion generalized to include anisotropy of strength and stiffness, behaviour nonlinearity and occurrence of plastic strains before peak strength, softening after the peak, time-dependent creep deformations and permeability increase due to damage in both saturated and unsaturated conditions. The proposed thermo-elastoplastic model consists of an elasticity law, plastic flow rule, hardening law, and yield condition. These elements are generalized here to depend explicitly on temperature, suitably modified to reproduce the main features of the thermomechanical behaviour of the argillaceous rocks mentioned above.

In the following sections, the proposed thermo-elastoplastic model is introduced. Then the validation of the proposed model is investigated using test results reported in the literature. Finally, the proposed model is then applied to the THM modelling of an in-situ heating test carried out in Callovo-Oxfordian (COx) claystone in the Meuse/Haute-Marne (MHM) underground research laboratory (URL).

7.2 THERMO-PLASTICITY OF ARGILLACEOUS ROCKS

There are quite comprehensive experimental data on the thermomechanical behaviour of clays. In general, heating a saturated clay under drained conditions induces strength and volumetric changes that depend on the clay's stress history

condition. The temperature-induced volume change tends to be contractive and irreversible for normally consolidated clays, whereas it becomes reversible and expansive for highly overconsolidated clays.

On the other hand, experimental data on the thermomechanical behaviour of argillaceous rocks (claystone) are more scarce in the scientific literature (Zhang et al., 2007; Monfared et al., 2012; Zhang et al., 2014; Menaceur et al., 2015; Zhang et al., 2016; Liu et al., 2019). The following main characteristics of the thermal behaviour of argillaceous rocks appear to be the most important:

- modification of mechanical behaviour; quantitatively, this corresponds to a continuous variation of mechanical characteristics (e.g. strength parameters and stiffness) with temperature, and qualitatively it represents a transition to more ductile behaviour,
- temperature-induced reversible expansive strains followed, at some temperature value, by irreversible contracting strains.

7.2.1 Temperature-induced changes in strength parameters

Experimental evidence

Experimental studies of the triaxial strength of clays show that natural Boom Clay exhibit temperature dependence of their internal friction. In 1996, De Bruyn (De Bruyn and Thimus, 1996) performed several series of CIU (isotropically consolidated, undrained with pore water pressure measurement) tests triaxial tests at different temperatures on Boom clay samples (Figure 7.1a). It was observed that heating to about 90°C has led to a significant loss (30%) of cohesion (in five years) and eventually led to a decrease in shear strength. This strength reduction was later confirmed by Hueckel et al. (2009). With regard to thermal shear resistance changes in argillaceous rocks namely Opalinus clay and COx claystone, more ductile behaviour with a clear decrease in strength (under undrained condition) at elevated temperature, initially observed by Zhang et al. (2007) on Opalinus clay (Figure 7.1b), was confirmed by Zhang et al. (2014) (under drained condition) and Menaceur et al. (2015) (under drained condition) on COx claystone (Figure 7.2a). More recently, Liu et al. (2019) (under drained condition) conducted a series of lateral decompression tests (LD) with constant mean stress on the COx claystone samples. Reduction of the shear strength due to the increase of temperature was evidenced on COx claystone samples confirming previous obtained thermomechanical strength degradation performed in the conventional triaxial tests (Figure 7.2a).

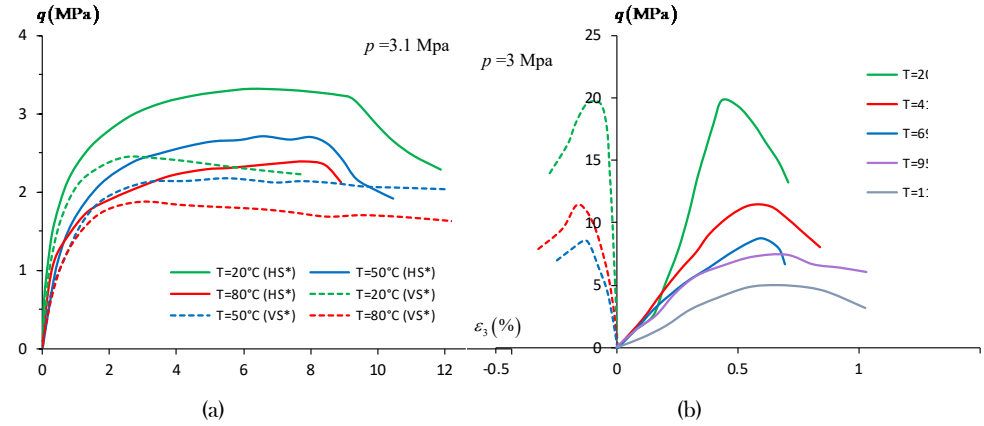

Figure 7.1: (a) Results of triaxial CIU test at 20, 50 and 80°C on Boom clay (De Bruyn and Thimus, 1996) ; (b) Results of an undrained shear test at 20, 41, 69, 95 and 116°C on Opalinus clay: representations in the $q-\varepsilon_1$, $q-\varepsilon_3$ planes Zhang et al. (2007).

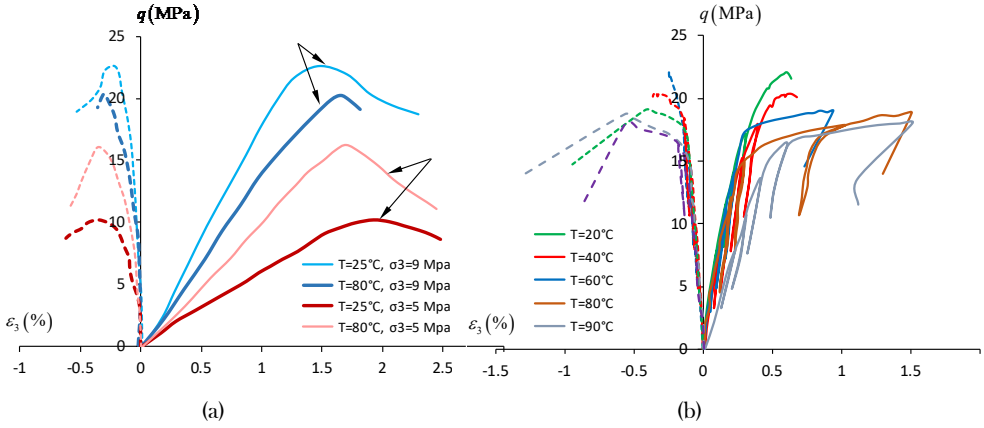

Figure 7.2: (a) Results of drained shear test at 25°C and 80°C (Menaceur et al., 2015) (b) Results of lateral decompression tests at 20, 40, 60, 80 and 90°C on COx claystone: representations in the $q-\varepsilon_1$, $q-\varepsilon_3$ plans (Liu et al., 2019).

Dependency law for the thermal evolution of shear strength

As shown in Figure 7.3, each set of experimental results (Figure 7.1and Figure 7.2) has roughly the same shape, and it appears that the $\tilde{q}-T$ relationship for the argillaceous hard soils - weak rocks can be normalised: $\tilde{q}(T)$ (peak strength at a given temperature T) with respect to the peak strength at a reference temperature $\tilde{q}(T_0)$, and T with respect to the reference temperature T_0, assumed here to be the minimal testing temperature.

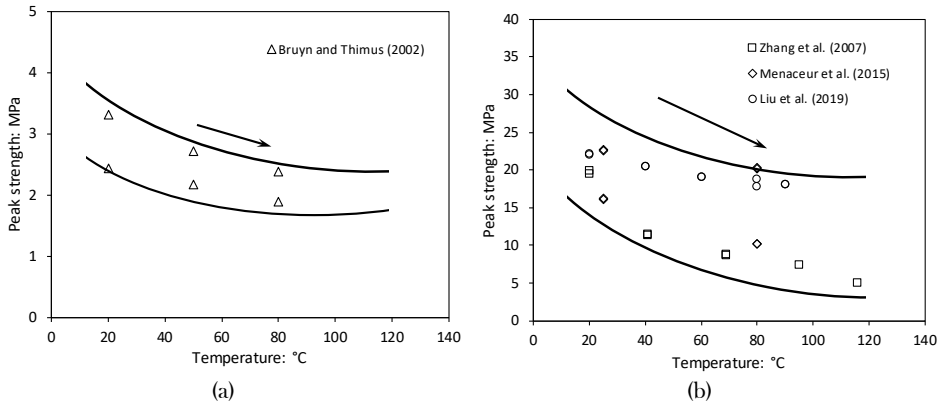

Figure 7.3: Evolution of peak strength $\tilde{q}$ with temperature (a) Results from tests on Boom clay samples; (b) Results tests on Opalinus clay and COx claystone samples.

Figure 7.4 represents results of Figure 7.3 in the normalised form. From this figure, it can be deduced that the normalised $\tilde{q}(T)/\tilde{q}(T_0)$ versus $\ln(T/T_0)$ relationship becomes unique for argillaceous materials. This relationship is mostly linear and can be expressed by the following equation:

$$\tilde{q}(T) = \tilde{q}(T_0)\left[1 - \mu \ln\left(T/T_0\right)\right] \tag{7.33}$$

where $\tilde{q}(T_0)$ is peak strength at initial temperature (T_0) and μ is a temperature-independent constant.

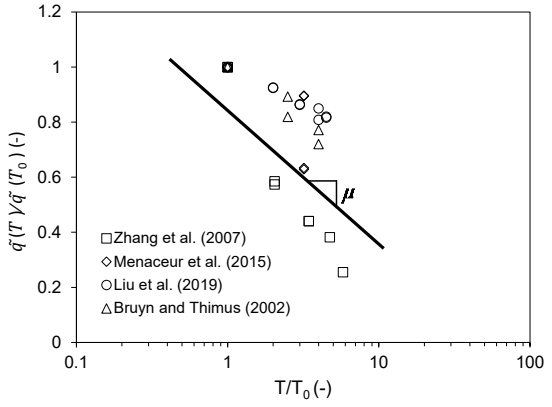

Figure 7.4: Evolution of peak strength with temperature (re-plotting of all experimental results from Figure 7.3).

Figure 7.5 shows schematic variations of $\tilde{q}(T)$ by temperature for different values of μ.

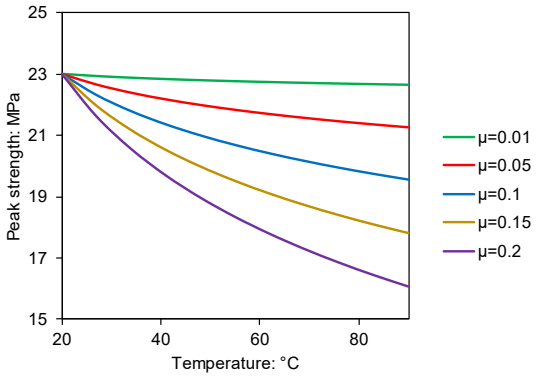

Figure 7.5: Variations of peak strength ($\tilde{q}$) for different values of μ (for $T_0 = 20\,^0C$ and $\tilde{q}(T_0) = 23$ MPa).

Considering an extension of thermal extension of Mohr-Coulomb model, as a single yield surface plasticity, the material behaviour upon shearing depends on the strength parameters (*internal friction angle* and *cohesion strength*) which modify the yield locus. Figure 7.6 schematically illustrates the variation of peak strength with temperature; temperature increase leads to a reduction of peak strength (Figure 7.6a). Besides assuming the yield locus of the original Mohr-Coulomb model, the effect of temperature on the internal friction angle and cohesion can be deduced from the evolution of the peak deviatoric stress q with T (Figure 7.6b). Then the theoretical variation of peak strength with temperature can be concluded from (Figure 7.6). The thermal evolution of the internal friction angle is expressed using a similar linear relation to Eq. 7.1 as follow

$$\varphi_{mob}(T) = \varphi(T_0)\left[1 - \alpha \ln\left(T / T_0\right)\right] \tag{7.34}$$

where $\varphi(T_0)$, $\varphi_{mob}(T)$ are the friction angle at the reference temperature (T_0) and elevated temperature (T). The coefficient α is a model parameter that controls the thermal evolution of the internal friction angle. The other parameter controlling the yield locus evolution is the cohesion strength which it is assumed that it varies with temperature in the same way as the friction angle.

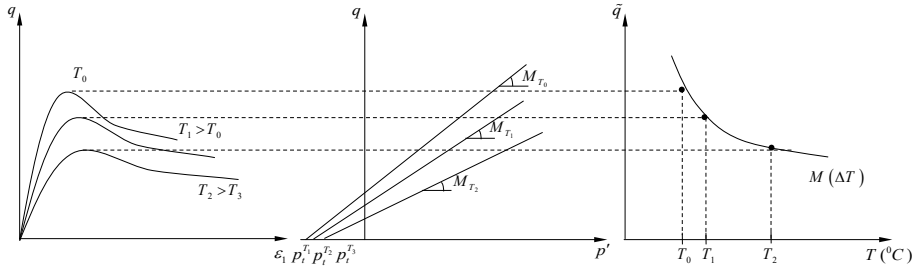

Figure 7.6: Evolution of peak strength with temperature.

Dependency law for the thermal evolution of stiffness

Regarding the thermal dependency of stiffness, a reduction of Young's modulus with temperature increase is observed in the all experiments presented above (Figure 7.1 and Figure 7.2). Figure 7.7 shows a schematic variation of Young's modulus due to temperature elevation.

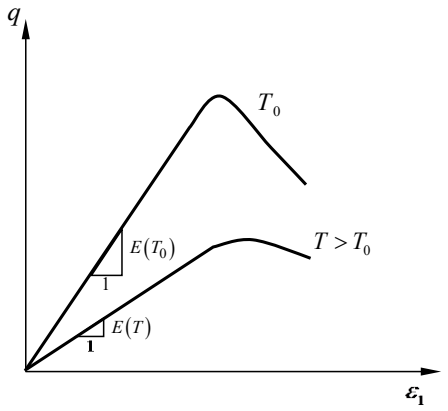

Figure 7.7: Schematic evolution of Young's modulus with temperature.

As shown in Figure 7.8, each set of experimental results has roughly the same trend, and it appears that the $E-T$ relationship for the argillaceous hard soils - weak rocks can be normalised: $E(T)$ (young modulus at a given temperature T) with respect to the Young's modulus at a reference temperature $E(T_0)$, and T with respect to the reference temperature T_0.

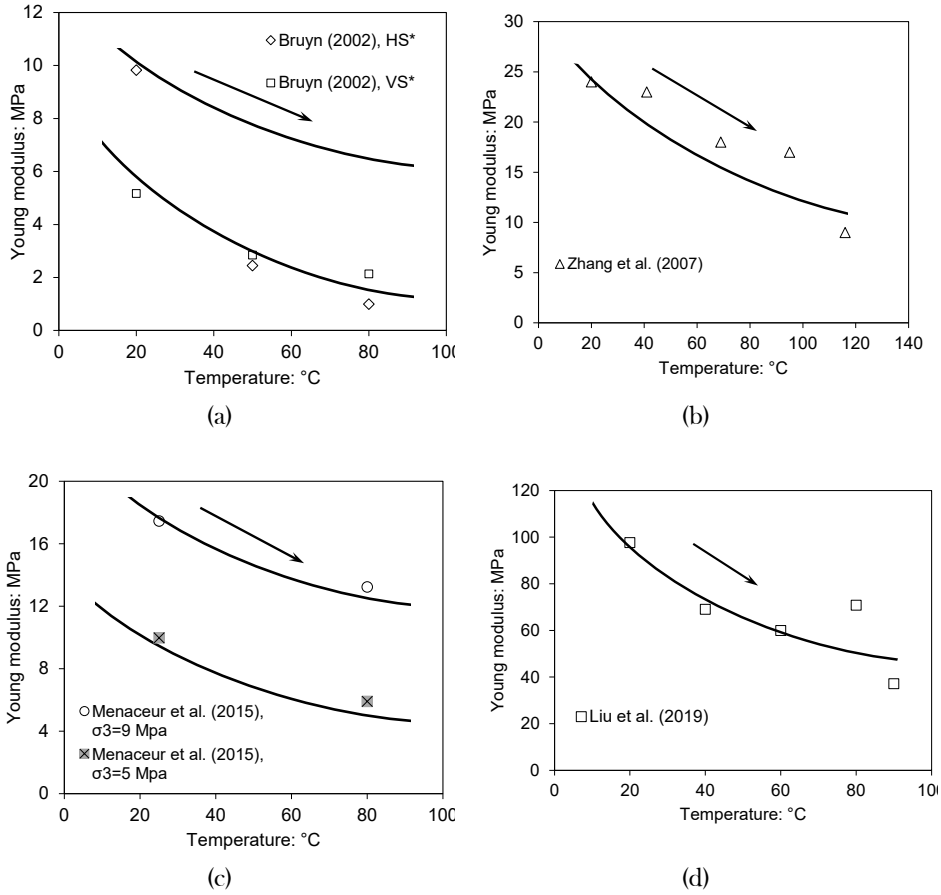

Figure 7.8: Evolution of young modulus $\tilde{q}$ with temperature results tests on (a) Boom clay (b) Opalinus claystone (c) COx claystone (d) COx claystone samples.

Figure 7.9 represents results of Figure 7.8 in the normalised form. The continuous lines are drawn using Eq. (7.1) and interpolation of the laboratory data.

$$E(T) = E(T_0)\left[1 - \gamma \ln\left(T / T_0\right)\right] \tag{7.35}$$

where E_0 is Young's modulus at initial temperature (T_0) and γ is a temperature-independent constant. The coefficients γ is the model constant that controls the thermal evolution of Young's modulus.

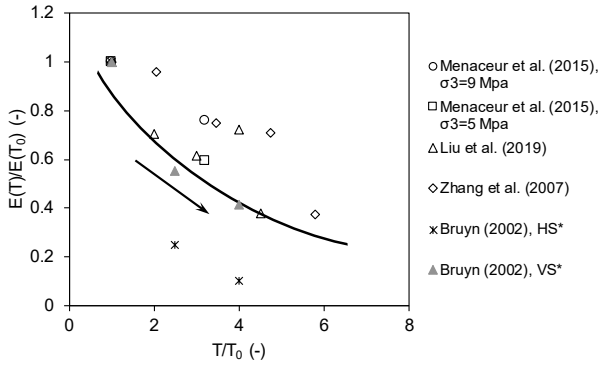

Figure 7.9: Evolution of Young's modulus with temperature (re-plotting of all experimental results from Figure 7.3).

7.2.2 Temperature-induced strains

The thermal volume changes of clays submitted to temperature elevation under constant stress depend on their degree of consolidation, with thermoelastic expansion in overconsolidated clays and thermoplastic contraction in normally consolidated clays. In claystones, less data is available. With regard to the thermal volumetric response of the COx claystone, a contracting behaviour (thermo-plastic) was first reported by Mohajerani et al. (2014) and Menaceur et al., (2015) which is comparable to the response of normally consolidated clays. However, most numerical predictions of the behaviour of claystones around waste disposal systems consider a thermo-elastic response (Gens et al., 2007). Actually, this trend is not in agreement with the in-situ measurements of thermally induced pore pressure that appeared to be correctly modelled under a thermoelastic (dilating) hypothesis.

Zhang et al. (2016) determined thermal expansion behaviour of the claystones by heating and cooling the samples under different isostatic stresses and undrained conditions, which was consistent with the in situ observations during heating experiments. Figure 7.10 shows the strain evolution measured on a COx claystone sample during a heating/cooling cycle under sequentially lowered confining stress. The data show that each temperature increases generated expansion in all directions; the expansion did not change much with time at each constant temperature below 47°C, and then a gradual contraction reversely occurred at higher temperatures, and cooling down yielded contraction and then was followed by a small swelling as shown in Figure 7.10. The thermal volumetric response of the COx claystone was studied later in (Belmokhtar et al., 2017) by using a thermal isotropic compression cell. A drained heating test under constant stress carried out up to 80°C exhibited a thermo-elastic expansion followed by thermo-plastic

contraction. The transition appeared at a temperature of 48°C, close to the maximum burial temperature supported during the geological history of the material, estimated at 50°C.

Regarding the argillaceous rock's volumetric behaviour with temperature elevation, an elastic thermal expansion observed below the maximum supported temperature, followed by a plastic contraction at yielding once the maximum temperature is reached.

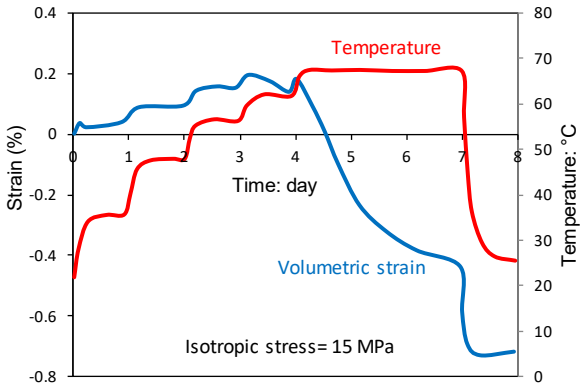

Figure 7.10: Thermal expansion and contraction of a COx claystone sample (modified after Zhang et al., 2016).

7.3 CONSTITUTIVE THERMO-ELASTOPLASTIC MECHANISM

The model presented here comprises two main deformation mechanisms: an instantaneous response related to stress and temperature change and a time-dependent response occurring under constant stress. The instantaneous response is described within the framework of elastoplasticity so that under low deviatoric stresses, the response is linear elastic but characterised through a transverse isotropic form of the Hooke's law. For higher deviatoric stresses, plastic deformations can take place. An initial, a peak and a residual yield limits are considered. The first one defines a surface in the stress space that separates the elastic and plastic regions, but further loading can be sustained by the material. On the other hand, the peak limit represents the maximum strength of the material and states beyond this boundary are not allowed. From this point, strength is gradually reduced to its residual value modelled through softening plasticity. A generalised effective stress expression has been adopted here:

$$\boldsymbol{\sigma}' = \boldsymbol{\sigma} + S_e s B \mathbf{I} \tag{7.36}$$

where σ' is the effective stress tensor, σ is the total stress tensor, S_e is the equivalent degree of saturation (defined below), s is suction, B is Biot's coefficient, and $\mathbf{I}$ is the identity tensor. In the following, the term "stress" always denotes effective stress.

7.3.1 Thermo-mechanical formulation

The induced thermal strains can be reversible (dilatation) as well as irreversible (compaction). An elasto- plastic approach is used here with a decomposition of the thermo-mechanical strains in two parts: thermo- elastic and thermo-plastic.

Thermoelastic components

Assuming that the coefficient of thermal expansion is independent of stress, the hypo-elastic (incrementally reversible) volumetric strain increments are the sum of the thermal and mechanical components. However, the elastic shear strain is assumed to be completely mechanical with no thermal component

$$d\varepsilon_v^e = d\varepsilon_v^{pe} + d\varepsilon_v^{Te} \tag{7.37}$$

where $d\varepsilon_v^e$ is increment of elastic volumetric strain; $d\varepsilon_v^{pe}$ elastic volumetric strain caused by stress changes and $d\varepsilon_v^{Te}$ is elastic volumetric strain caused by temperature. The elastic volumetric strain increment caused by temperature can be calculated by Eq. (7.6)

$$d\varepsilon_v^{Te} = 3 b_s dT \tag{7.38}$$

where dT is increment of temperature change and b_s is thermal expansion coefficient of the medium. This coefficient is dependent on the material mineralogy, temperature, and pressure changes. However, for most practical purposes, this coefficient can be considered constant and equal to $10^{-5}°C^{-1}$ (Bolzon and Schrefler 2005).

Thermoplastic components

A core of the mechanical part of the model is taken from the Mohr-Coulomb criterion, which produces a cone in the principal stress space, with a hexagonal cross-section in the deviatoric plane. The model leads to an incremental elastoplastic model, consisting of an elasticity law, plastic flow rule, hardening law, and yield condition. These elements are generalized here to depend explicitly on

temperature, consistent with a thermoplasticity theory suitably modified for argillaceous rocks. The key thermal effects in argillaceous rocks, at least in the concept of the geological disposal of high-level radioactive waste, are those that lead to irreversible deformation, particularly thermo-plastic behaviour of the EDZ. To address the irreversible strain in thermal conditions, the classical notion of the elasticity domain in the elastoplastic context must be revised. The main new feature is the sensitivity of the plastic limit to temperature. This finding is expected, as argillaceous rocks exhibit such sensitivity. However, other prominent thermomechanical characteristics of claystones that need to be considered in this context that is clearly different from those of other materials, and are discussed in detail. On the basis of those observations, the elasticity domain is thought of as temperature-dependent, shrinking when claystone is heated and expanding during cooling (Figure 7.11).

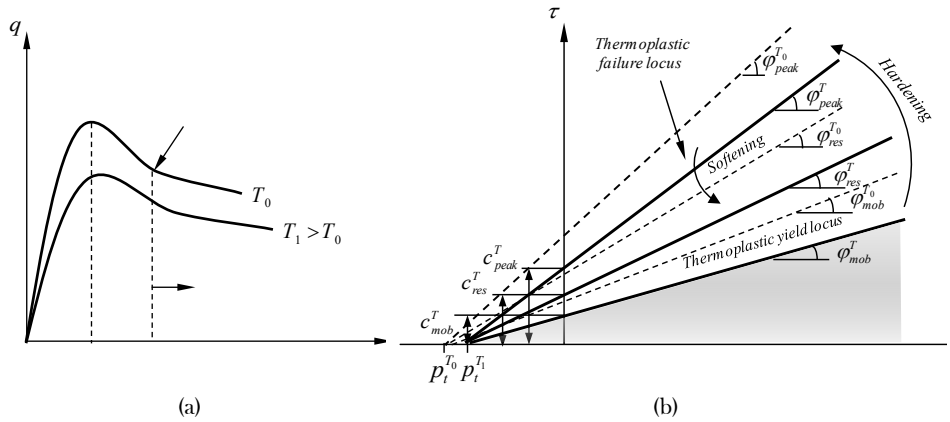

Figure 7.11: Evolution of yield locus with temperature increase.

As in a single yield surface plasticity, the claystone behaviour upon shearing depends on the current strength parameters, thermal changes will affect their evolution. Hence a specific form of the temperature dependence of the internal friction angle and cohesion has to be considered. An elastoplastic strain hardening and softening model with a Mohr-Coulomb yield criterion (Figure 7.11) are used for the considered material.

$$f(T) = \left(\cos\theta + \sin\theta \sin\varphi / \sqrt{3}\right) J - \sin\varphi \left(p + c \cot\varphi\right) = 0 \qquad (7.39)$$

where φ is the friction angle, c is the cohesion and the remaining variables are stress invariants given by the following expressions,

$$p' = \frac{1}{3}\left(\sigma'_{xx} + \sigma'_{yy} + \sigma'_{zz}\right) \tag{7.40}$$

$$J = \left(\frac{1}{2} tr\mathbf{s}^2\right)^{1/2} \tag{7.41}$$

$$\theta = \frac{1}{3} sin^{-1}\left(\frac{3\sqrt{3}\det\mathbf{s}}{2J^3}\right) \tag{7.42}$$

where $\mathbf{s}$ is the deviatoric stress tensor $\mathbf{s} = \boldsymbol{\sigma}' - p'\mathbf{I}$.

The initial yield limit is denoted by using $\varphi_{ini}^{T_0}$ and $c_{ini}^{T_0}$ in Eq. (7.7) which are material parameters. In the same way, the failure limit is obtained by replacing φ and c by the peak values φ_{peak}^{T} and c_{ini}^{T} at elevated temperature T. The fact that there are two different sources of the sensitivity of the yield locus to temperature affects the form of the flow rule. In particular,

$$\varphi = \varphi(\varepsilon_{eq}^{p}, \Delta T) \tag{7.43}$$

$$c = c(\varepsilon_{eq}^{p}, \Delta T) \tag{7.44}$$

where ε_{eq}^{p} is the plastic strain tensor

$$\varepsilon_{eq}^{p} = \int_0^t \sqrt{\frac{2}{3}\left(\dot{\varepsilon}_{ij}^{p} - \frac{\dot{\varepsilon}_{v}^{p}}{3}\delta_{ij}\right)\left(\dot{\varepsilon}_{ij}^{p} - \frac{\dot{\varepsilon}_{v}^{p}}{3}\delta_{ij}\right)} dt \tag{7.45}$$

The friction angle varies in a piecewise manner as shown in Figure 7.12; the evolution laws corresponding to zone 1, 2, 3 and 4 are given in hyperbolic functions Eq.7.14, 7.15, 7.16 and 7.17 respectively.

$$\varphi_{mob}^{T} = \left[\varphi(T_0) + \frac{\varepsilon_{eq}^{p}}{a_{hard} + \varepsilon_{eq}^{p}} \Delta\varphi_{hard}^{T}\right] \tag{7.46}$$

$$\varphi_{mob}^{T} = \varphi_{peack}^{T} \tag{7.47}$$

$$\varphi_{mob}^{T} = \left[\varphi_{peak} + \frac{\varepsilon_{eq}^{p} - \xi_2}{a_{soft} + \left(\varepsilon_{eq}^{p} - \xi_2 \right) / \Delta\varphi_{soft}^{T}} \right] \tag{7.48}$$

$$\varphi_{mob}^{T} = \varphi_{res}^{T} \tag{7.49}$$

$$\Delta\varphi_{hard} = \frac{\xi_1}{\xi_1 / \left(\varphi_{peack}^{T} - \varphi_{ini} \right) - a_{hard}} \tag{7.50}$$

$$\Delta\varphi_{soft} = \frac{\xi_3 - \xi_2}{\left(\xi_3 - \xi_2 \right) / \left(\varphi_{peack}^{T} - \varphi_{res} \right) - a_{soft}} \tag{7.51}$$

where

$$\varphi_{peak}^{T} = \varphi_{peack}^{T_0} \left[1 - \alpha \ln\left(T / T_0 \right) \right] \tag{7.52}$$

and

$$\varphi_{res}^{T} = \varphi_{res}^{T_0} \left[1 - \alpha \ln\left(T / T_0 \right) \right] \tag{7.53}$$

where φ_{mob} = mobilized friction angle, φ_{res} = residual friction angle, ξ_1 = equivalent plastic strain at which the maximum strength is reached, ξ_2 = equivalent plastic strain at which softening begins, ξ_3 = equivalent plastic strain at which the residual strength is reached, a_{hard} = constant that controls the curvature of the function in the hardening branch, a_{soft} = constant that controls the curvature of the function in the softening branch.

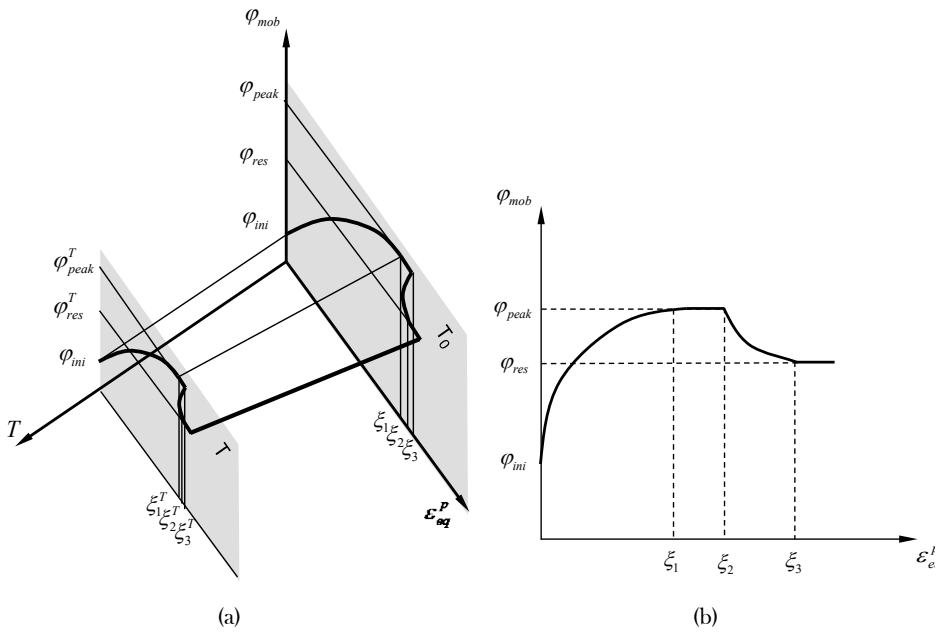

Figure 7.12: Evolution of friction angle in hardening and softening regimes with temperature increase.

Cohesion evolves in parallel but not equal with the friction angle according to:

$$c^T_{mob} = c^T_{peak} \cot \varphi^{T_0}_{ini} \tan \varphi^T_{mob} \tag{7.54}$$

where c^T_{mob} is the mobilized cohesion at temperature T, c^T_{peak} is the peak cohesion, and $\varphi^{T_0}_{ini}$ and φ^T_{mob} are the initial and mobilized friction angles at initial and elevated temperature, respectively.

then Prager's consistency condition requires that, to maintain the yielding process,

$$\mathrm{d}f = \frac{\partial f}{\partial \boldsymbol{\sigma}'} : \mathrm{d}\boldsymbol{\sigma}' + \frac{\partial f}{\partial \varphi} d\varphi + \frac{\partial f}{\partial c} dc = 0 \tag{7.55}$$

where

$$d\varphi = \frac{\partial \varphi}{\partial \varepsilon^p} d\varepsilon^p + \frac{\partial \varphi}{\partial T} dT \tag{7.56}$$

and

$$dc = \frac{\partial c}{\partial \varepsilon^p} d\,\varepsilon^p + \frac{\partial c}{\partial T} dT \tag{7.57}$$

Beside a non-associated flow, rule is adopted in the model. Rather than deriving a specific function for the plastic potential, the flow rule is directly obtained from the yield criterion in the following way:

$$\mathrm{d}g = \omega \frac{\partial f}{\partial p'} \frac{\partial p'}{\partial \boldsymbol{\sigma}'} + \frac{\partial f}{\partial J} \frac{\partial J}{\partial \boldsymbol{\sigma}'} + \frac{\partial f}{\partial \theta} \frac{\partial \theta}{\partial \boldsymbol{\sigma}'} = 0 \tag{7.58}$$

where g is the plastic potential and ω is a constant that controls the volumetric component of plastic deformations. With $\omega = 1$ an associated flow rule is recovered, while with $\omega = 0$ no volumetric plastic strains occur. Hence, if the flow rule is assumed to be non-associated, that is if

$$d\,\varepsilon^p = d\,\lambda \frac{\partial g}{\partial \boldsymbol{\sigma}'} \tag{7.59}$$

as $\mathrm{d}\varphi = \mathrm{d}\varphi(\mathrm{d}\,\varepsilon^p_{eq}, \mathrm{d}T)$ and $\mathrm{d}c = \mathrm{d}c(\mathrm{d}\,\varepsilon^p_{eq}, \mathrm{d}T)$ the plastic multiplier λ, which controls the amount of the plastic strain rate, is affected by the change in φ and c:

$$\begin{aligned} d\,\lambda &= \frac{1}{H}\left[\frac{\partial f}{\partial \boldsymbol{\sigma}'} : \boldsymbol{\sigma}' + \left(\frac{\partial f}{\partial \varphi} \frac{\partial \varphi}{\partial T} + \frac{\partial f}{\partial c} \frac{\partial c}{\partial T} \right) dT \right] \geq 0 \\ H &= -\frac{\partial f}{\partial \varphi} \frac{\partial g}{\partial \boldsymbol{\sigma}'} \frac{\partial \varphi}{\partial \varepsilon^p_v} + \frac{\partial f}{\partial c} \frac{\partial g}{\partial \boldsymbol{\sigma}'} \frac{\partial c}{\partial \varepsilon^p_v} \end{aligned} \tag{7.60}$$

Therefore the plastic strain increment is affected by the thermal variation of internal friction and cohesion, as long as $\mathbf{s} \neq 0$. Otherwise, this dependence disappears, as for both forms of the yield locus (equations 7.7) $\partial\varphi/\partial T = 0$ and $\partial c/\partial T = 0$.

At any constant effective stress during heating along with continuing plastic yielding, there is a specific plastic strain increment generated per increment of temperature,

$$\frac{d\,\varepsilon^p}{dT} = \frac{1}{H} \frac{\partial g}{\partial \boldsymbol{\sigma}'} \left[\left(\frac{\partial f}{\partial \varphi} \frac{\partial \varphi}{\partial T} + \frac{\partial f}{\partial c} \frac{\partial c}{\partial T} \right) \right] \tag{7.61}$$

Equation (7.27) describes a compensatory thermoplastic hardening mode in which plastic strain-hardening compensates for thermal softening. Also, in the case of heating at constant effective stress ($\mathbf{s} = 0$), the consistency condition (Eq. 7.21) restrains the evolution of c and φ during the temperature change:

$$d\varphi = \left(\frac{\partial f}{\partial c} \Big/ \frac{\partial f}{\partial \varphi} \right) dc \tag{7.62}$$

In other words, changes in φ need to be compensated for by necessary adjustments in terms of changes in c.

7.3.2 Viscoplastic components

The time-dependent response characterized by a modified form of the Lemaitre's law.

$$d\boldsymbol{\varepsilon}^{vp} = dt\left(\dot{\boldsymbol{\varepsilon}}^{vp}\right) \tag{7.63}$$

where $d\varepsilon^{vp}$ is the visco-plastic strain increment (time-dependent response), dt is the time increment and $\dot{\varepsilon}^{vp}$ is the visco-plastic strain rate tensor. It is assumed that visco-plastic deformations are mainly caused by deviatoric stresses, with strain rates given by:

$$\dot{\boldsymbol{\varepsilon}}^{vp} = \frac{2}{3}\frac{\dot{\varepsilon}^{vp}}{q}\mathbf{s} \tag{7.64}$$

$$q = \left(\frac{3}{2}\mathbf{s} : \mathbf{s} \right)^{1/2} \tag{7.65}$$

$$\dot{\varepsilon}^{vp} = \gamma \left\langle q - \sigma_s \right\rangle^n \left(1 - \varepsilon_{eq}^{vp}\right)^m \tag{7.66}$$

where γ is a viscosity parameter, σ_s is a threshold from which viscoplastic strain is activated, $\langle\ \rangle$ are the Macaulay brackets n and m are material constants and ε_{eq}^{vp} is the state variable of the time-dependent response given by:

$$\varepsilon_{eq}^{vp} = \int_0^t \left(\frac{2}{3}\dot{\varepsilon}^{vp} : \varepsilon^{vp} \right)^{1/2} dt \tag{7.67}$$

In this way, larger viscoplastic strain rates are obtained for higher deviatoric stresses, and those rates decrease as viscoplastic strains accumulate in time, as observed in laboratory tests.

7.4 VALIDATION OF THE PROPOSED MODEL

The sufficiency of the constitutive model has been verified by the three sets of laboratory results on COx claystones using thermal triaxial tests. Parameters derived from this exercise are later applied to the analysis of the ALC1604 in situ heating test. In all cases, the major principal stress was orthogonal to the bedding planes of the sample.

7.4.1 Tests on COx claystone reported by Menaceur et al. (2015)

The fully saturated and fully drained triaxial thermal tests were carried out under confinement pressures of 5 Mpa (half to in-situ stress) and 9 Mpa (close to in-situ stress) at 25°C and 80°C have been modelled. Four different loading paths were considered on three hollow cylinder specimens that were machined with the axis perpendicular to bedding to investigate some aspects of the THM behaviour of the COx claystone, as described in Table 7.1.

Table 7.1: Experimental programme.

Test	Specimen	Programme
T2	S2	Isotropic unloading to 4 MPa, shear at 25 °C
T6	S5	Isotropic unloading to 4 MPa, drained heating up to 80 °C, shear at 80 °C
T1	S1	Shear under 8 MPa at 25 °C
T5	S1	Drained heating up to 80 °C, shear under 8 MPa at 80 °C

The specimens of tests T2 were then sheared under a constant confining stress equal to half the in-situ effective stress (4 MPa) in drained conditions with axial displacement rates of 0.5 µm/mn. Figure 7.13 shows the axial, and radial strains changes with respect to shear stress for both specimens. A peak strength value of 10.5 MPa at axial and radial strains of 1.06% and 0.24% respectively is observed for T2. The shear test at 80 °C carried out under half the in-situ effective stresses (4 MPa) is presented in Figure 7.14. These curves show that the shear stress reaches its maximum value of16 MPa at 1.25% and 0.35% of axial and radial strain respectively. From both figures a satisfactory agreement between the simulation results and the laboratory data can be noted.

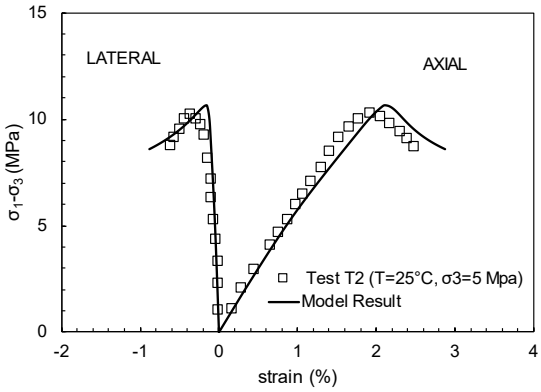

Figure 7.13: Stress-strain curves in triaxial tests on COx claystone. Observations (Menaceur et al., 2015) and constitutive model results , test T2 on Specimen S2.

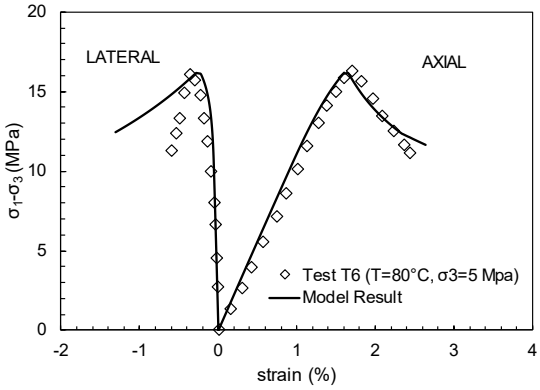

Figure 7.14: Stress-strain curves in triaxial tests on COx claystone. Observations (modified after Menaceur et al., 2015) and constitutive model results, test T6 on Specimen S5.

Test T1, a drained shear test at constant confining stress close to the in-situ effective stress, was carried out with a constant axial displacement rate of 0.4 µm/mn. Figure 7.13 shows the changes in axial and radial strains with respect to the shear stress. The curves show that the maximum value of the shear stress at peak is 23 MPa. Once the drained heating phase completed, specimen of tests T5 was submitted to drained shearing with a constant axial displacement rate of 0.3 µm/min. Figure 7.15 shows that the shear stress at 80 °C under in-situ stress condition reached a peak value of 20 MPa at 0.75% of axial strain and 0.31% of radial strain in test T5. From both figures a satisfactory agreement between the simulation results and the laboratory data can be noted. Table 7.2 summarizes the parameters of the thermomechanical and hydraulic constitutive model employed.

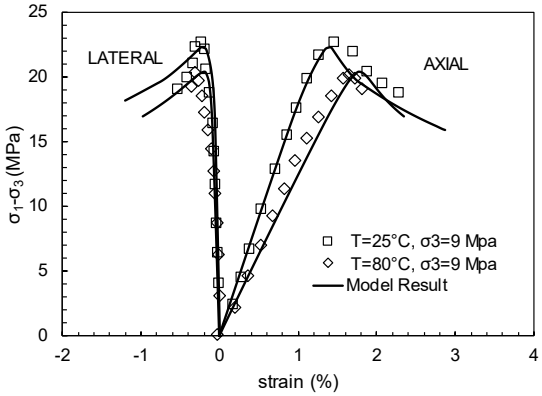

Figure 7.15: Stress-strain curves in triaxial tests on COx claystone. Observations (modified after Menaceur et al., 2015) and constitutive model results, test T1 and T5 on specimen S1.

Table 7.2: Thermomechanical constitutive law parameters used for validation of the proposed model.

Parameter	Units	Value	Parameter	Units	Value
Mechanical			*Mechanical (cont.)*		
E (5 MPa)	(MPa)	1200	a_{hard}	(-)	0.0035
E (9 MPa)	(MPa)	2000	a_{soft}	(-)	0.07
ν	(MPa)	0.1	ξ_1	(-)	0.005
φ_{peak} (5 MPa)	(-)	21.0	ξ_2	(-)	0.006
φ_{peak} (9 MPa)	(-)	24.5	ξ_3	(-)	0.045
			Thermomechanical		
φ_{in} (5 MPa)	(-)	9.35	α_φ (5 MPa)	(-)	0.37
φ_{in} (9 MPa)	(-)	9.35	α_φ (9 MPa)	(-)	0.05
φ_{res} (5 MPa)	(-)	11.74	γ_E (5 MPa)	(-)	0.43
φ_{res} (9 MPa)	(-)	17.7	γ_E (9 MPa)	(-)	0.27
c_{peak} (5 MPa)	(MPa)	3.5	α_T	(K^{-1})	$1.4 \cdot 10^{-5}$
c_{peak} (9 MPa)	(MPa)	3.5	λ	(W/m/K)	2.05
ω	(-)	1	c_s	(J/kg/K)	800

7.4.2 Tests on COx claystone reported by Liu et al. (2019)

In the second case, a series of lateral decompression (LD) tests under five different values of temperature from 20 to 90°C at constant mean stress have been modelled. The first test was under room temperature (20°C) to characterize the basic response of the COx claystone. The other four tests were carried out respectively at T = 40, 60, 80, 90°C, which are the representative temperature range for the host claystone specified in the French radioactive waste disposal project for the investigation of thermal effects. The samples were first subjected to an isostatic stress of 12 MPa,

which is progressively increased with a rate of 1 bar/min. The axial strain rate during the deviatoric loading phase was 2.10−6/s. Figure 7.16 shows the stress-strain curves obtained from the simulated triaxial tests together with the laboratory test results. From both figures a satisfactory agreement between the simulation results and the laboratory data can be noted. Table 7.3 summarizes the parameters of the thermomechanical and hydraulic constitutive model employed.

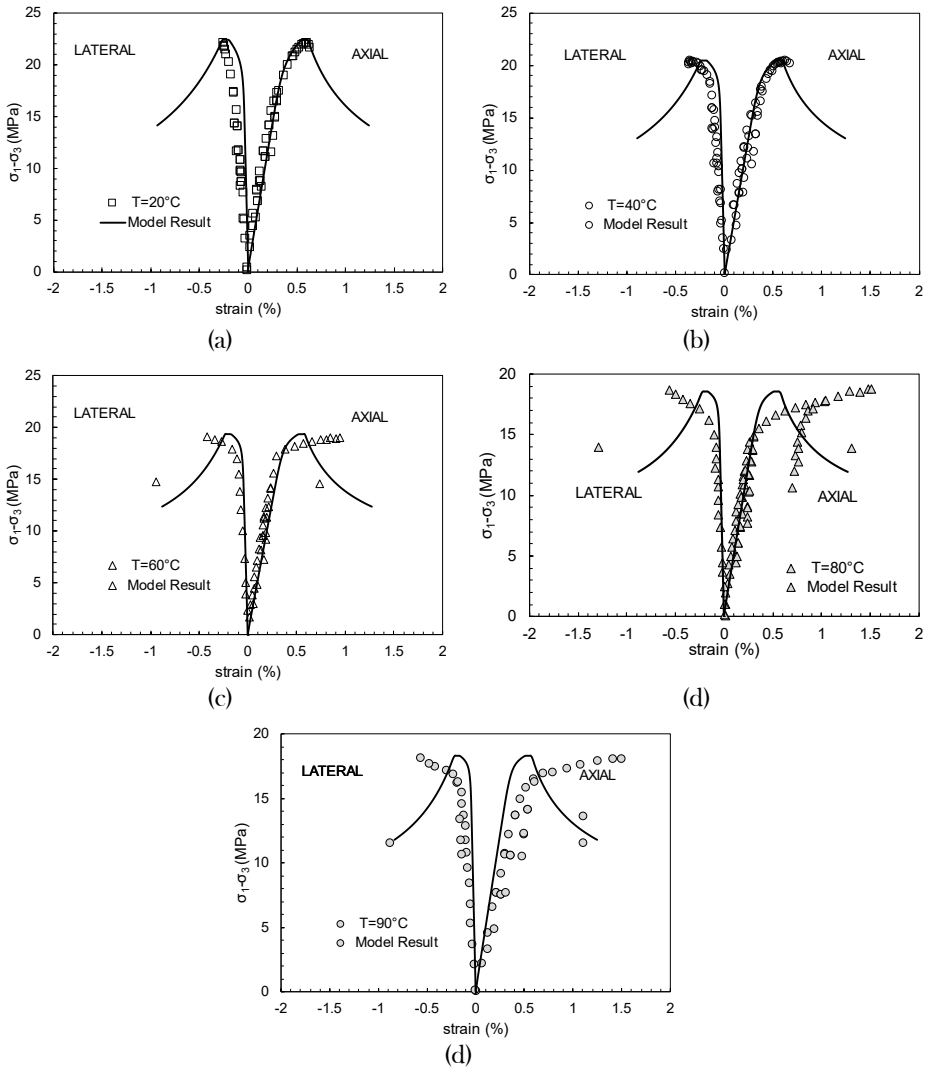

Figure 7.16: Stress-strain curves in triaxial tests on COx claystone. Observations (modified after Liu et al., 2019) and constitutive model results.

Table 7.3: Thermomechanical constitutive law parameters used for validation of the proposed model.

Parameter	Units	Value	Parameter	Units	Value
Mechanical			*Mechanical (cont.)*		
E	(MPa)	6000	ξ_1	(-)	0.005
ν	(MPa)	0.1	ξ_2	(-)	0.006
φ_{peak}	(-)	21.0	ξ_3	(-)	0.045
φ_{ini}	(-)	9.35	*Thermomechanical*		
φ_{res}	(-)	11.74	α_φ	(-)	0.13
			γ_E	(-)	0.07
c_{peak}	(MPa)	3.5	α_T	(K^{-1})	$1.4 \cdot 10^{-5}$
ω	(-)	1	λ	(W/m/K)	2.05
a_{hard}	(-)	0.0035	c_s	(J/kg/K)	800
a_{soft}	(-)	0.07			

7.5 APPLICATION TO THE ALC1604 IN SITU HEATING TEST

In order to illustrate the applicability of the proposed model, a finite element simulation has been performed. In this regard, the coupled THM behaviour of ALC1604 in situ heating test has been simulated using a two-dimensional model domain. As mentioned above, the ALC1604 test is not focused on a specific plane and it is possible to obtain several sections in which different sensors can be compared. In this case, the model has been run for the section located at a distance into the tunnel of z=17.5m (cross-section across the centre of Heater 3) which is the location of the three boreholes that contain six temperature sensors and piezometers.

The model domain and the finite element mesh used are depicted in Figure 7.17 where the reference system of axes is indicated. Axis y is in the vertical direction and axis x defines the horizontal plane. The origin of coordinates is located at the centre of the tunnel. The dimensions of the model are 50m × 50m. The distance of the microtunnel wall to the boundary is 25m, which corresponds to the distance from the microtunnel axis to the gallery GRD. Naturally, the model also incorporates the geometry of the sleeve and the air gap between the sleeve and the COx claystone (Figure 7.17). In accordance with the experimental arrangement, the sleeve is supported by the bottom of the excavation, so the width of the gap is not uniform. The mesh contains 1408 quadrilateral elements and 1425 nodes; it has been refined near the gallery and near the micro-tunnel, in order to be able to deal with the high temperature and pore pressure gradients in those zones.

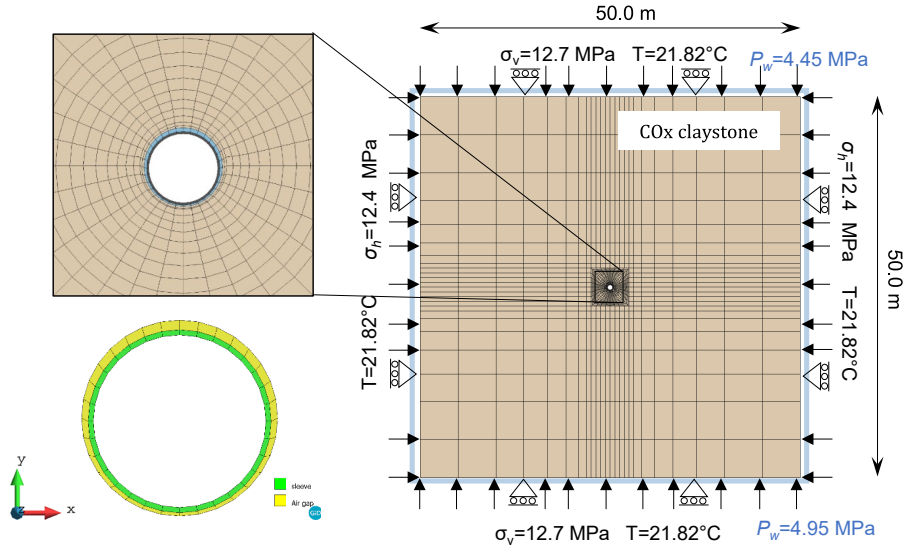

Figure 7.17: Domain modelled, finite element mesh and boundary conditions used in 2D analyses.

An initial constant temperature of 21.8°C has been assumed throughout the geometry. An anisotropic lithostatic initial stress distribution has been prescribed. Values at experiment level are 16.2 MPa, 12.4 MPa and 12.7 MPa for the vertical, the major and minor horizontal components, respectively. A hydrostatic distribution of water pressure was initially defined, with a value equal to the field value (4.7 MPa) at test level.

On the left lateral side, different boundary condition is selected. The surface which corresponds to the cavities GAN and GRD assumes a constant stress boundary, whereas the condition of constrained lateral displacements is adopted at the opposite lateral boundary. Although galleries GAN and GRD are not geometrically represented in the mesh, the observed variation of temperatures and pore pressures are applied as boundary conditions at their locations. A prescribed liquid pressure (- 0.1 MPa) was applied to the excavation surface to represent the process of ventilation. The numerical analysis has simulated the various phases of the experiment, as listed in Table 7.4.

Table 7.4: Stages of ALC1604 in situ test.

Step	Phase	Date	Duration
1	Galleries GAN-GRD Excavation	September 9, 2010 → October 23, 2012	775 days
2	Alveoli Excavation	October 23, 2012 → October 31, 2012	56h
3	Boreholes/Instrumentation	October 31, 2012 → January 30, 2013	94 days
4	Heating Test (30W/m)	January 30, 2013 → February 15, 2013	16 days
5	Cooling	February 15, 2013 → April 18, 2013	61 days
6	Heating Stage (220W/m)	April 18, 2013 → February 6 2019	~6 years
7	First cooling phase (85W/m)	February 6, 2019 → April 8, 2019	61 days
8	Second cooling phase (35W/m)	April 8, 2019 → June 11, 2019 (planned)	64 days

Table 7.5 contains the thermal, thermomechanical, hydraulic and petrophysical parameters for the host rock and their sources. The permeability values have been obtained from the backanalysis of the measured evolution of pore pressures in the test.

Table 7.5: Callovo-Oxfordian claystone parameters used in the simulations.

properties	Parameter	Orientation*	Value	
Hydraulic	Intrinsic permeability, k	Parallel	$2{\cdot}10^{-20}$	Back-analysis of ALC1604 test
		Perpendicular	$1{\cdot}10^{-20}$	
	Biot coefficient, b	-	0.6	Reference value
	Material parameters, A	-	1.0	
	Material parameters, Λ	-	3.0	
	Model parameter, P: MPa	-	14.3	
	Material parameters, λ	-	0.33	
TM	Linear thermal expansion coefficient of the rock, α_R: K^{-1}	-	$1.4{\cdot}10^{-5}$	Auvray (2004)
	Linear thermal expansion coefficient of the solid grain, α_R: K^{-1}	-	$1.4{\cdot}10^{-5}$	Value and anisotropic ratio from Auvray (2004)
Thermal	Thermal conductivity, λ: W/m/K	Parallel	2.05	Anisotropic back-analysis of thermal field
		Perpendicular	1.33	
	Specific heat capacity of the solid, c.: J/kg/K	-	800	Auvray (2004)
Petrophysical	Solid compressibility, β_s	-	$2.5{\cdot}10^{-5}$	From mineral composition
	Specific weight, ρ_s: kg/m3	-	2.7	Reference value
	Porosity, ϕ	-	0.173	Martin & Lanyon (2003)

* Orientation to bedding.

Model parameters for the thermomechanical constitutive model are listed in Table 7.6. They are the same as in Chapter 6 except for the temperature related parameters.

Table 7.6: Mechanical constitutive law parameters used in the simulations.

Parameter	Value	Parameter	Value
Young's modulus (Parallel), E: MPa	5200	Coefficients that controls the thermal evolution of the Young's modulus, γ	0.27
Young's modulus (Perpendicular), E: MPa	4000	Constant that controls the curvature of the function in the softening branch, a_{soft}	0.07
Poisson's ratio (Parallel), ν	0.25	Coefficient of non-associativity, ω	0.6
Poisson's ratio (Perpendicular), ν	0.35	Equivalent plastic strain at which the maximum strength is reached, ξ_1 : MPa	0.005
Instantaneous mechanism		Equivalent plastic strain at which the residual strength is reached, ξ_3 : MPa	0.006
Peak friction angles, φ_{peak}	22.0	*Time-dependent mechanism*	0.06
Initial friction angles, φ_{ini}	9.35	The threshold from which viscoplastic strains are activated, σ_s : MPa	4.0
Mobilized friction angles, φ_{res}	14.74	Viscosity parameter, γ : day^{-1}	1x10^{-7}
peak cohesion, c_{peak} : MPa	3.55	Material constants, n	3.37
Constant that controls the curvature of the function in the hardening branch, a_{hard}	0.0035	Material constants, m	530
Thermomechanical mechanism		Scaling factors, c_N	1.33
Coefficients that controls the thermal evolution of the internal friction angle, α	0.37	Scaling factors, c_S	1.0

Mechanical and thermal properties of the steel casing are listed in Table 7.7 whereas Table 7.8 contains the gap parameters.

Table 7.7: sleeve properties adopted in the analysis.

Properties	Parameter	Value
Thermal	Thermal Conductivity λ : (W/m/K)	80
	Specific heat of solid (J/kg/K)	550
	Linear Thermal expansion coefficient, α_T: K^{-1}	1.4·10^{-5}
Mechanical	Young's Modulus, E: MPa	0.005
	Poisson's ratio, ν (-)	0.3

Table 7.8: Air-gap element properties adopted in the analysis.

Properties	Parameter	Value
Thermal	Thermal Conductivity λ_{dry} : (W/m/K)	0.035
	Thermal Conductivity, λ_{sat} : (W/m/K)	0.6
Hydraulic	Intrinsic permeability, k_0 : (m2)	10^{-16}
	Porosity, ϕ_0 (-)	0.8
	Parameter for van Genuchten model, λ (-)	0.5
	$P_0(MPa)$	0.001
	material parameter, a	10
Mechanical	Young's Modulus, E.: MPa	1000
	Young's Modulus, E.: MPa	1.0
	Strain limit, $\varepsilon_{v\ \mathrm{limit}}$ (-)	Variable 0.005 – 0.21
	Poisson's ratio, ν (-)	0.3

7.5.1 Thermal results

There were three temperature sensors in section z=17.5m, located at different orientations with respect to the bedding plane. The observed evolution of temperatures at this section is shown in Figure 6.10 and compared with the results of the analyses. It can be noted that, after about one year of heating, temperatures generally rise very slowly throughout the COx claystone. Moreover, anisotropic effects are noticeable; temperature along the bedding increases more rapidly than in the orthogonal direction. More information from the analyses is given in Figure 7.19 in terms of contours in a section z =17.5 m at various relevant stages. The anisotropic temperature distribution is apparent, with higher temperatures being reached in the direction of the bedding planes.

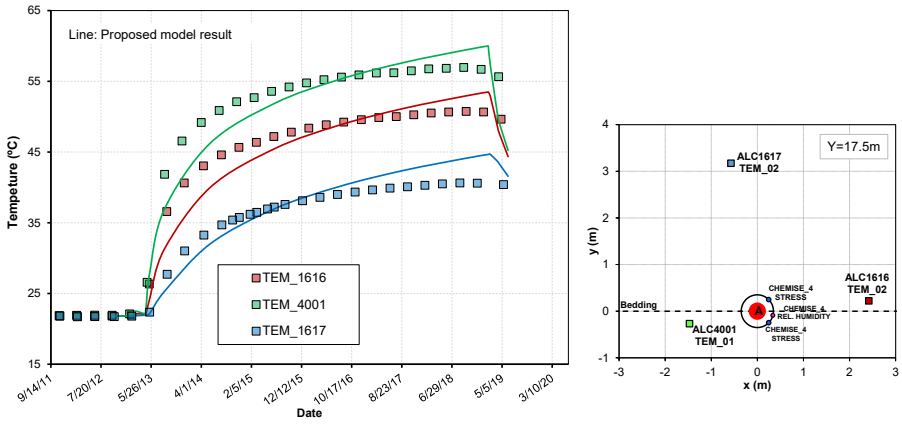

Figure 7.18: Evolution of temperatures in COx claystone, observations and computed results (section z =17.5 m).

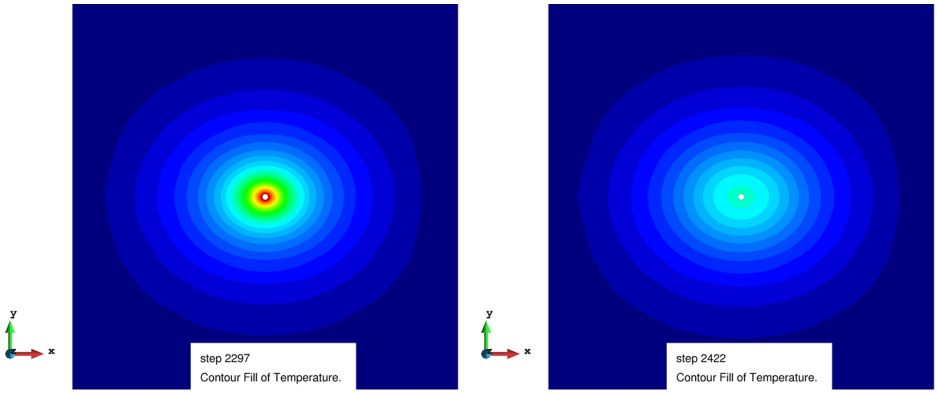

(a) (b)

Figure 7.19: Computed contours of equal temperature (°C) in a cross-section across Heater 3 for (a) 2297 days (end of heating); (b) 2422 days (end of second cooling phase).

7.5.2 Excavation damaged zone

The heat emitted by the high-level radioactive waste will increase temperature in the host rock, with a maximum admitted temperature of 90°C around the waste canisters in the French concept (Armand et al. 2017). As stated above, the ALC1604 cell is parallel to the major horizontal stress σ_H and has a nearly isotropic stress state in the plane normal to the tunnel axis. Despite that, the EDZ extends further in the horizontal direction (Figure 7.20a), suggesting strong anisotropic characteristics of the rock mass. Figure 7.20a shows the distribution of fractures

around a similar micro-tunnel (ALC3005) excavated in COx claystone parallel to ALC1604 cell.

An estimate of the configuration of the excavation damaged zone can be obtained by plotting contours of the cumulative plastic multiplier as it is directly related to the magnitude of irreversible strains (Figure 7.20b). It is interesting to note that the lateral extent of the shear fractures zone calculated for the ALC1604 micro tunnel (about 0.7 m) is very similar to that observed in microtunnel ALC3005 (Figure 7.20).

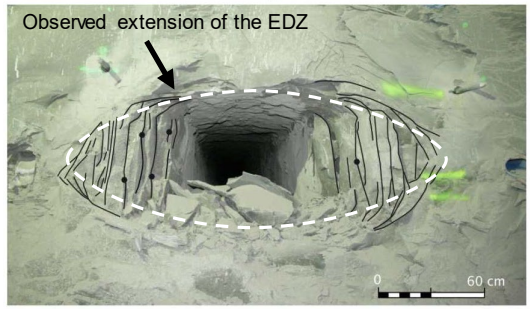

(a)

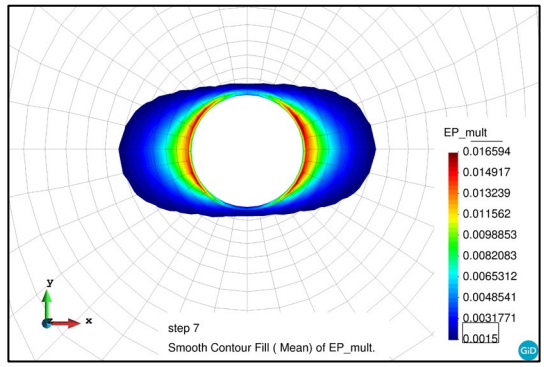

(b)

Figure 7.20: Extension damaged zone around an HLW cell parallel to major horizontal stress (Armand et al., 2014) (b) Obtained configuration of the EDZ in terms of the plastic multiplier in the section z=17.5m (7 days).

Figure 7.21 and Figure 7.22 present the computed plastic multiplier increment distributions at various times in section z=17.5m. The following times have been selected: 7 days (end of the excavation); 176 days (before main heating phase); 2297 days (end of main heating phase); 2455 days (End of cooling phase). Before main heating phase, after 176 days from the excavation, the EDZ has only marginally increased as the result of creep and consolidation. However considerable effect of

heating on size and magnitude of plastic zone is evidenced. Thermoplastic evolution of EDZ can also be observed in the contours of plastic multiplier in Figure 7.23, dotted line shows the excavation damaged zone (EDZ), and dashed line defines extended EDZ due to heating. Moreover, it seems that the EDZ has barely changed during cooling phase which lasted four months (Figure 7.21 and Figure 7.22).

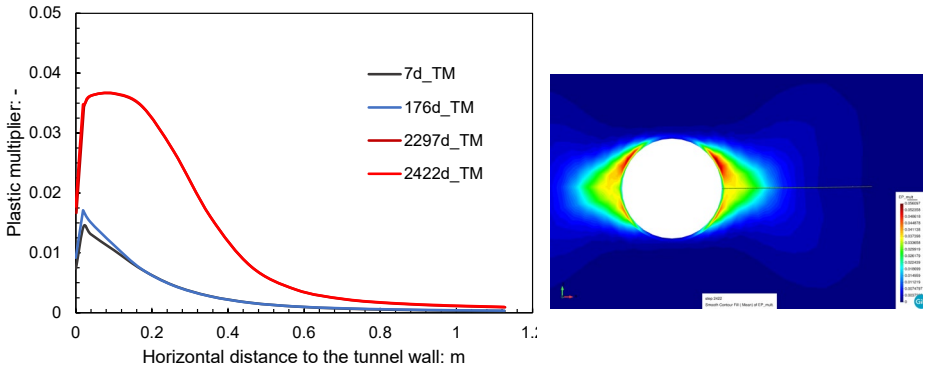

(a) (b)

Figure 7.21: Computed plastic multiplier increment distributions at various times on section perpendicular to Heater 3 (z=17.5m) in (a) Horizontal distance to the tunnel wall for 3 for 7 days (After excavation), 176 days (end of heating test), 2297 days (end of heating), 2422 days (end of cooling phase); (b) Obtained configuration of the EDZ in terms of the plastic multiplier in the section z=17.5m (end of heating phase).

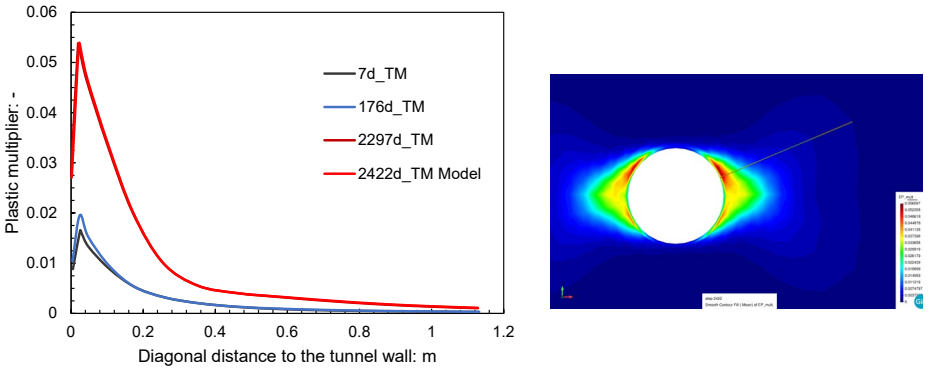

(a) (b)

Figure 7.22: (a) Computed plastic multiplier increment distributions at various times on section perpendicular to Heater 3 (z=17.5m) in diagonal distance to the tunnel wall for 7 days (After excavation), 176 days (end of heating test), 2297 days (end of heating), 2422 days (end of cooling phase); (b) Obtained configuration of the EDZ in terms of the plastic multiplier in the section z=17.5m (end of heating phase).

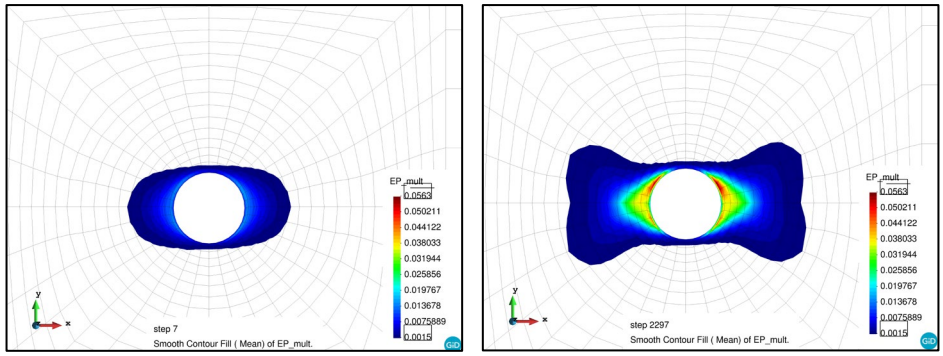

(a) (b)

Figure 7.23: Obtained configuration of the EDZ in terms of the plastic multiplier (a) after excavation (b) end of heating phase.

The comparison of the computed plastic multiplier increment distributions at the end of heating with those obtained from reference model (Chapter 6) is shown in Figure 6.17. Thermoplastic induced fracture caused by EDZ extension during heating phase are distinguished in the plots.

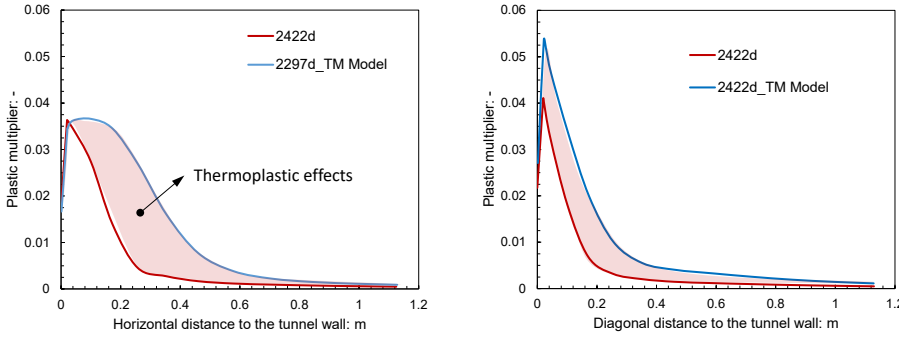

(a) (b)

Figure 7.24: Computed plastic multiplier increment distributions at the end of heating (a) in horizontal distance to the tunnel wall; (b) in diagonal distance to the tunnel wall.

Figure 6.21 shows the comparison of computed damage distribution at various horizontal distances (Δx= 17, 35, 57, 84 cm) to tunnel wall for 2297 days (end of heating phase) with those obtained from reference model. It can be seen that, the point with Δx= 17 cm which is the closet to the tunnel wall gives higher values of plastic multiplier. However, the plastic multiplier change is negligible for Δx > 85 cm. Note that the highest difference between the proposed model and reference model (Chapter 6) result occurs in the point with Δx= 35cm, indicating significant effect on the thermally extended plastic zone. Thermoplastic evolution

of the obtained configuration of the EDZ can also be observed in the contours of the plastic multiplier resulted from proposed model and reference model presented in Figure 7.26.

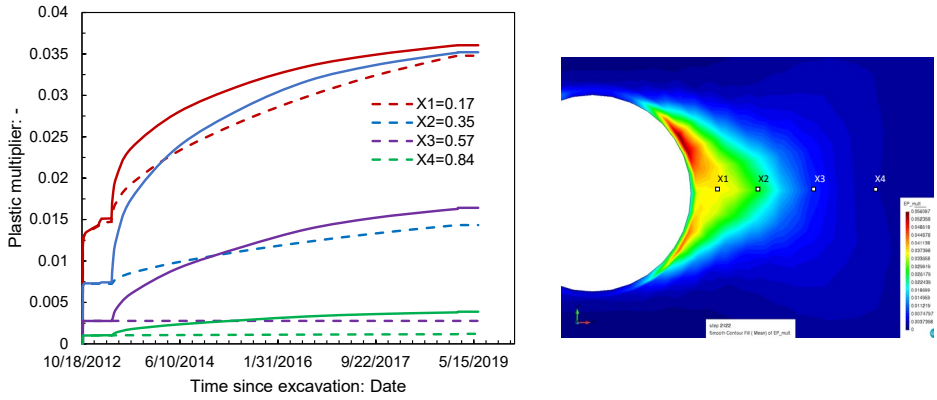

(a) (b)

Figure 7.25: Computed damage distribution at various times and horizontal distances to tunnel wall (Line: Proposed model result; Dashed line: reference model result).

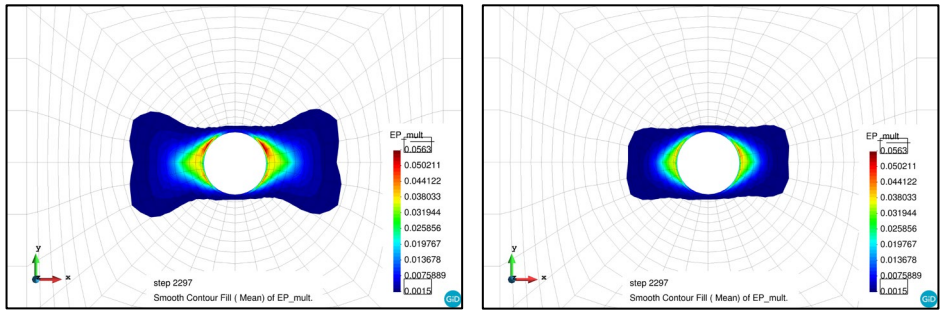

(a) (b)

Figure 7.26: Obtained configuration of the EDZ in terms of the plastic multiplier resulted from (a) proposed model; (b) reference model.

Figure 6.22 shows horizontal profiles of computed intrinsic permeability on the right-hand side of the cell resulted from proposed model and previous model. The differences between the proposed model result and those of the reference model results from the thermoplastic evolution of EDZ and the permeability dependence on damage introduced in the model. The maximum permeability increase in the proposed model is $1.2e^{-15}$ m^2, higher than that of the reference model.

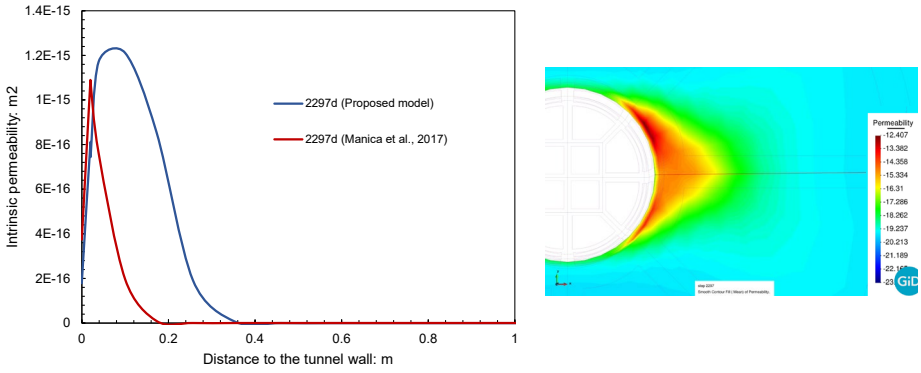

(a) (b)

Figure 7.27: Computed permeability increment distributions at various times (Horizontal distance to tunnel wall).

7.5.3 Pore pressures

The essential hydraulic phenomenon associated with thermal effects in COx claystone is the generation of the pore pressure due to temperature changes. The low permeability of COx claystone ensures that the resulting excess pore pressure does not dissipate rapidly. Figure 6.24 presents a comparison between the results of the analysis and pore pressure measurements. The results of the analysis using reference model have also been added. It is apparent that the pore pressure increase is reasonably well captured by the presented model for both excavation and heating phases. As shown in the figure, the closer to the plastic zone the point is, the more accurate the model result is, indicating that the proposed model is able to capture the main features of the mechanical and hydraulic behaviours associated with thermomechanical evolution of EDZ. Finally, a general overview of the pore pressure field around the experiment is shown in Figure 6.27. Movement of the location of the maximum pore pressure away from the microtunnel as time goes on is readily apparent. The Figures also shows the draining effect of the GRD gallery.

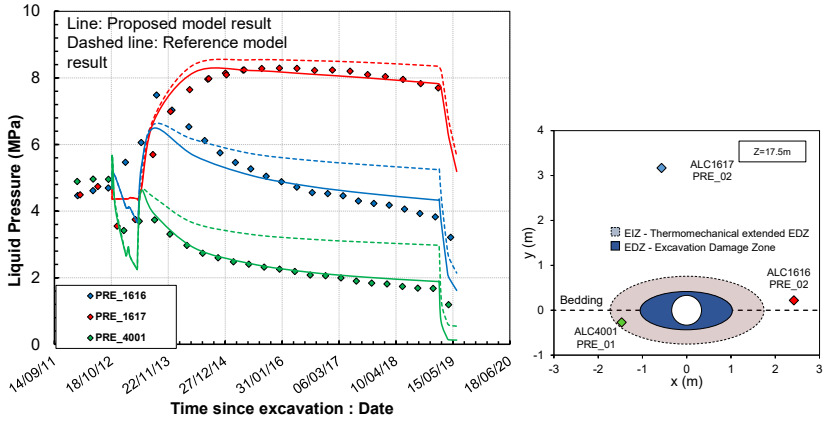

Figure 7.28: Evolution of pore pressure increments at various points in the COx claystone: observed and computed results.

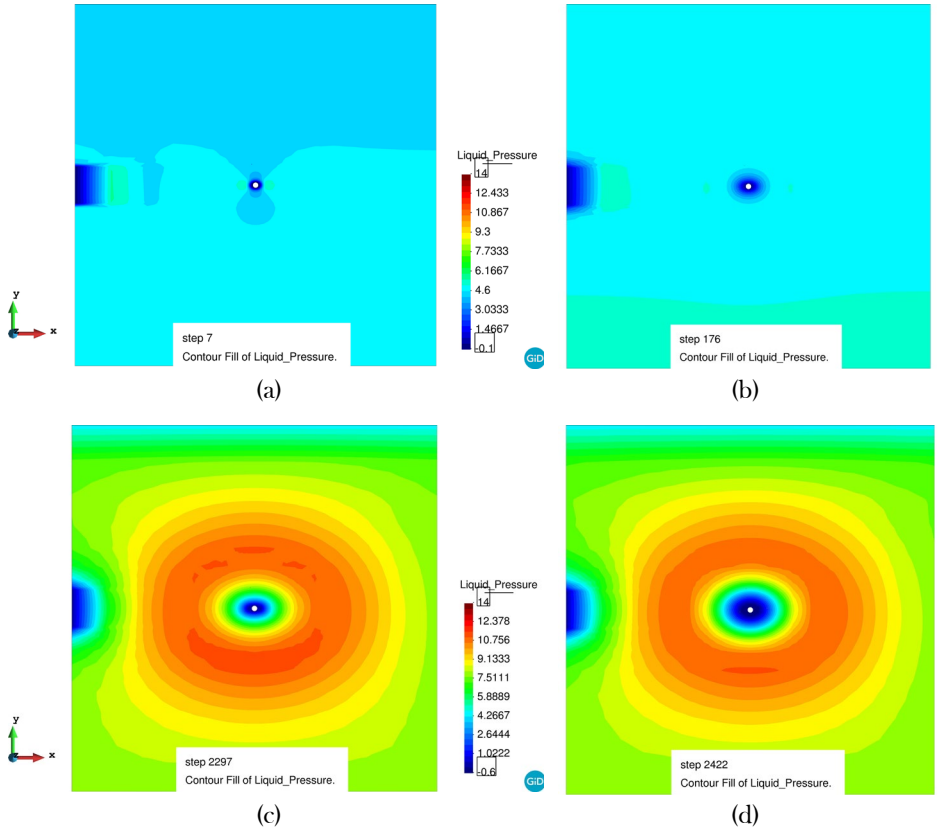

Figure 7.29: Two-dimensional view of computed contours of equal liquid pressure (MPa) in a cross-section across Heater 3 for (a) 7 days (After excavation); (b) 176 days (end of heating test); (c) 2297 days (end of heating).; (d) 2422 days (end of cooling phase).

7.6 CONCLUDING REMARKS

This chapter presents a Thermomechanical model for argillaceous rocks, developed within the framework of elastoplasticity that includes a number of features that are relevant for a satisfactory description of their thermomechanical behaviour: thermal dependency of strength parameters, thermal dependency of stiffness as well as hydromechanical features that have been taken from Mánica et al. (2017) including anisotropy of strength and stiffness, behaviour nonlinearity and occurrence of plastic strains prior to peak strength, significant softening after peak, time-dependent creep deformations and permeability increase due to damage. Both saturated and unsaturated conditions are envisaged. The comparison of the experimental data on COx claystone samples with the model predictions shows that all observed phenomena are correctly described.

The constitutive model has been successfully used in the simulation of triaxial tests on COx claystone. The constitutive model has then been applied, via a suitable coupled THM formulation, to the analysis of the in-situ heating test conducted in the MHM URL, at a depth of 490 m. The pattern of observed pore water pressure as well as the shape of the damaged zone, are generally satisfactorily reproduced. It has been shown that it is essential to incorporate thermal dependency of strength parameters and stiffness if the field observations, pore pressures, are to be adequately represented. Field observations (for example por pressures) also show the paramount importance of geometry and thermoplastic development of the excavation damaged zone on the behaviour of the rock mass close to the tunnel wall. Especially when tunnels of large diameters are excavated or excavation is under unfavourable conditions, significant thermoplastic development of damage could be induced, which would lead to a change in strength and elastic modulus.

Chapter 8: Conclusions

The findings for each section of the thesis have been summarized in this chapter. This thesis presents the final modelling work carried out as a support to the interpretation of the HA-ALC1604 experiment to achieve a better understanding of thermo-hydro-mechanical processes and material properties that influence the behaviour, during and after installation in the repository, of the components of the radioactive waste disposal facility. The models and methodologies developed in this thesis have provided a more thorough understanding of the THM processes in the radioactive waste fuel disposal system and have provided strategies for improvement in the design, selection and optimisation of material.

The model is the outcome of the different simulations performed during the project, including:

1. 3D thermal analysis aiming at back-analysing the COx claystone thermal parameters,
2. 2D thermo-hydro-mechanical analysis for a preliminary interpretation of pore pressures around the experiment during the excavation and heating phases and deformation of the steel lining during heating,
3. Preliminary 3D thermo-hydro-mechanical modelling of the experiment.

One of the main contributions of the thesis is to combine comprehensive and complex models to perform the calculations of a single deposition scheme:

- A time-dependent anisotropic elastoplastic model combined with elasticity to represent Callovo-Oxfordian claystone,
- Porosity-dependent permeability and water retention curve. Thermal conductivity depending of degree of saturation,
- Full scale 3D THM modelling with elastoplastic parameters (BBM) is also an important contribution.

Moreover, the final modelling considers a three-dimensional geometry and includes utmost of material and experiment features:

- Transverse anisotropy for the host rock thermal conductivity, permeability and elastic stiffness.

- An anisotropic viscoplastic hardening/softening constitutive law with creep to model the Callovo-Oxfordian claystone.
- A dependency of permeability on rock damage.
- Experiment geometry, including the host rock, excavated microtunnel, steel lining, insert and the gaps between the steel lining and the rock, the steel lining and the insert and the insert and the rock.
- The different stages of the experiment (microtunnel excavation, heating and cooling) in the same modelling.
- The thermo-hydraulic effect of the surrounding gallery
- The full anisotropy stress state.
- Material parameters are generally consistent with previous field and laboratory experiments or with values reported in the literature.

Comparison between numerical outcomes and observations provides good accuracy of the model in all sensors. Satisfactory agreement is generally achieved between numerical and measured results. The code used in this dissertation may therefore be a useful analysis and design method for modelling a repository of radioactive waste disposal facility. Insights from the thesis suggest, however, that numerical models can be constrained.

The adoption and calibration of THM parameters for gap elements was among the most crucial challenges. Due to the closure during the heating process, the gap component has a complex THM behaviour. This obviously produces local hydraulic and thermal changes that affect temperature and liquid pressure at an early stage, i.e. before a gap closure.

A bi-elastic model has been used to model gap elements and elastoplastic model for rock. The water retention curve, thermal conductivity and permeability of the materials have also been defined according to material behaviour. Thermal conductivity parameters of the materials have been calibrated in a most suitable way to create as realistic as possible simulations.

3D THERMAL ANALYSIS

The maximum temperature of system must not exceed 100°C. This also applies to the HA-ALC1604 concept. However, there are several material data uncertainties. For example, some variability in the values for rock heat capacity and rock thermal conductivity. Therefore, there is a 10°C safety margin that has been

introduced to account for parameter uncertainty. Consequently, the permitted maximum temperature on liner surface is limited to 90°C. This is a design criterion, which determines the thermal dimensioning of the deep repository.

The power of the heaters, the thermal properties of the engineered barrier, the occurrence of gaps and their properties, the orientation of the heaters and the rock thermal properties are the main factors that control the temperature on the canister surfaces.

The thermal calculations included in this thesis are an extension of the modelling task reported in Tourchi et al. (2019) where the following aspects were investigated:

- Influence of gallery on system temperature evolution,
- calibration of heater power function,
- numerical solution for thermal boundary conditions,
- overall thermal evolution of the liner and gap elements,
- overall longitudinal thermal evolution of system,
- effect of gap between steel liner and host rock on canister temperature.

FULL-SCALE 2D NUMERICAL ANALYSES

In order to interpret the patterns of observed behaviour, a series of finite element simulation have been performed. Due to a large number of coupling THM simulations to be performed, two-dimensional THM models were performed to incorporate THM evolution of test in several sections. These simulations were performed for cross-sections located at a position determined to be of special interest with respect to THM coupled behaviour. Thus, for this purpose, the following models and the sections were selected:

- cross-section across Heater 3 (depth of 17.5 m),
- cross-section across Heater 4 and Heater 5 (depth of 13 m),
- section located at the depth of 7, 4 and 2 which is the location of the convergence and local strain sensors in the liner.

For each section the behaviours of different material groups were analysed numerically. In addition to the study of the material parameters, special attention was paid to the thermal and pore pressure behaviour of rock, EDZ behaviour of

rock, thermomechanical behaviour of liner, and the THM behaviour of gap element. Moreover, the anisotropic properties of the COx claystone owing to the presence of the bedding were considered. Different phases were simulated including the tunnel excavation (7 days), the 94-day emplacement of instrumentation, a 16-days heating test, a 61-days first cooling phase and the 6-year main heating phase. Besides, the modelling was extended to 6 years after the heater shutdown aiming at prediction of the long-time behaviours in clay host rock.

FULL-SCALE 3D NUMERICAL ANALYSES

A three-dimensional coupled THM analysis has been performed in order to incorporate the anisotropic properties of the Callovo-Oxfordian claystone and the anisotropy of the in-situ stress state. In 2D geometry, the volume of the backfill tunnel is underestimated which causes faster saturation of the backfill. In the provision of a systematic interpretation framework the performance of three-dimensional coupled THM analysis has proved very useful. In the 3D simulation, anisotropic material properties and in situ stress state anisotropic have been incorporated. By comparing the results of the 3D thermal computations with those of 2D analyses, it is possible to conclude that the anisotropic effects are certainly noticeable although not large.

Thermal conductivity anisotropy has been identified as having major effects on temperature fields and the magnitude of peak temperatures. In particular, the temperature fields are shifted in the direction of the highest thermal conductivity. It is of interest to note that the predicted damaged zone appears to be quite consistent with the test observations. Eventually, even from a quantitative point of view, the theoretical formulation and analyses carried out were able to satisfactorily reproduce in situ test observations.

Aspects of particular interest are:

- Parameters specifically back analysed from experiment field measurements were the thermal conductivity, permeability, Young moduli and parameter of change in permeability with damage. Values obtained for the anisotropic parameters are:

  - $\lambda_{//} = 2.05\ W/m/K$
  - $\lambda_{\perp} = 1.33\ W/m/K$
  - $k_{//} = 2.10^{-20}\ m^2$

- $k_{\perp} = 10^{-20}\ m^2$
- $E_{//} = 5200\ MPa$
- $E_{\perp} = 4000\ MPa$

- The simulation predicts an Excavated Damaged Zone similar in size and shape to the ones observed in the excavation of the same diameter that develops during the excavation of the alveolus. Further thermal loading appears not to affect the size of the EDZ and to increase marginally the damage intensity.
- Accounting for change of permeability within the EDZ is fundamental to reproduce well the pore pressure measurements.
- The deformation of steel lining can be well reproduced by the model.

Future improvements of the model would include a better representation of the EDZ accounting for deformation localization and the implementation of temperature dependency in the mechanical law of the host rock.

References

Ababou, R., Cañamón Valera, I., and Poutrel, A. (2011). "Macro-permeability distribution and anisotropy in a 3D fissured and fractured clay rock: 'Excavation Damaged Zone' around a cylindrical drift in Callovo-Oxfordian Argilite (Bure)." *Physics and Chemistry of the Earth*, Elsevier Ltd, 36(17–18), 1932–1948.

Abuel-Naga, H. M., Pender, M., Bergado, D. T., and Bouazza, A. (2009). "Thermomechanical model for saturated clays." *Géotechnique*, 59(3), 273–278.

Akagi, H., and Komiya, K. (1995). "Constant rate of strain consolidation properties of clayey soil at high temperature." *Proc. Int. Symp. Compression and Consolidation of Clayey Soils--IS--Hiroshima*, 3–8.

Alkhalifah, T. (1997). "Velocity analysis using nonhyperbolic moveout in transversely isotropic media." *Geophysics*, Society of Exploration Geophysicists, 62(6), 1839–1854.

Amadei, B. (1996). "Importance of anisotropy when estimating and measuring in situ stresses in rock." *International Journal of Rock Mechanics and Mining Sciences & Geomechanics Abstracts*, 293–325.

Amorosi, A., and Rampello, S. (2007). "An experimental investigation into the mechanical behaviour of a structured stiff clay." *Géotechnique*, Thomas Telford Ltd, 57(2), 153–166.

Anandarajah, A. (2000). "On influence of fabric anisotropy on the stress--strain behavior of clays." *Computers and geotechnics*, Elsevier, 27(1), 1–17.

Andra. (2005). *Dossier 2005, Référentiel du site Meuse/Haute-Marne. Report CRPADS040022B.* Châtenay-Malabry: ANDRA.

Andra. (2012). *Référentiel du comprotement des formations sur le site de Meuse/Haute Marne. Report D.RP.AMFS.1 2.0024.* Châtenay-Malabry: ANDRA.

Andra. (2013). *Alveole chauffante ALC1604. Rapport d'installation et premier resultats. Document technique D.RP.AMFS.13.0013.* Châtenay-Malabry: ANDRA.

Armand, G., Bumbieler, F., Conil, N., de la Vaissière, R., Bosgiraud, J. M., and Vu, M. N. (2017). "Main outcomes from in situ thermo-hydro-mechanical experiments programme to demonstrate feasibility of radioactive high-level waste disposal in the Callovo-Oxfordian claystone." *Journal of Rock*

Mechanics and Geotechnical Engineering, 9(3), 415–427.

Armand, G., Leveau, F., Nussbaum, C., De La Vaissiere, R., Noiret, A., Jaeggi, D., Landrein, P., and Righini, C. (2014). "Geometry and properties of the excavation-induced fractures at the meuse/haute-marne URL drifts." *Rock Mechanics and Rock Engineering*, 47(1), 21–41.

Armand, G., Noiret, A., Zghondi, J., and Seyedi, D. M. (2013). "Short- and long-term behaviors of drifts in the Callovo-Oxfordian claystone at the Meuse/Haute-Marne Underground Research Laboratory." *Journal of Rock Mechanics and Geotechnical Engineering*, Taibah University, 5(3), 221–230.

Armand, G., Su, K., Wileveau, Y., and Delay, J. (2005). "Expérimentation REP Résultats des mesures après la phase de fonçage du puits entre les cotes-454 m et-480 m." *ANDRA report DRPADPE050855A, Paris, France*.

Auvray, C. (2004). "Thermomechanical tests on opalinus clays of the Mont Terri, ANDRA Report C." *RP. OENG*, 4–239.

Bäckblom, G. (2008). "Excavation damage and disturbance in crystalline rock-results from experiments and analyses." (November), 1–85.

Bai, M., and Abousleiman, Y. (1997). "Thermoporoelastic Coupling With Application To Consolidation." 21(June 1996), 121–132.

Baldi, G., Hueckel, T., and Pellegrini, R. (1988). "Thermal volume changes of the mineral–water system in low-porosity clay soils." *Canadian geotechnical journal*, NRC Research Press, 25(4), 807–825.

Banks, D. C., Strohm, W. E., De Angulo, M., and Lutton, R. J. (1975). *Study of clay slopes along the Panama canal, Report No3, Engineering analyses of slides and strength properties of clay shales along the Gaillard Cut*.

Bass, J. D. (1995). "Elasticity of minerals, glasses, and melts." *Mineral physics and crystallography: A handbook of physical constants*, Wiley Online Library, 2, 45–63.

Bastiaens, W., and Bernier, F. (2006). "25 years of underground engineering in a plastic clay formation: the HADES underground research laboratory." *Geotechnical aspects of underground construction in soft ground. Proceedings of the 5th international conference of TC 28 of the ISSMGE, the Netherlands, 15-17 june 2005*, 795–801.

Bastiaens, W., Bernier, F., and Li, X. L. (2006). "An overview of long-term HM measurements around HADES URF." *Proceedings of EUROCK*, 9–12.

Bauer, C., Pouya, A., and Ghoreychi, M. (1997). "Propriétés thermo-mécaniques des argilites silto-carbonatées de lest." *Andra report BRP0G3S97-001*.

Belanteur, N., Tacherifet, S., and Pakzad, M. (1997). "Etude des comportements mécanique, thermo-mécanique et hydro-mécanique des argiles gonflantes et

non gonflantes fortement compactées." *Revue française de géotechnique*, EDP Sciences, (78), 31–50.

Belmokhtar, M., Delage, P., Ghabezloo, S., and Conil, N. (2017a). "Thermal Behaviour and Creep of the Callovo-Oxfordian Claystone." *Poromechanics 2017 - Proceedings of the 6th Biot Conference on Poromechanics*.

Belmokhtar, M., Delage, P., Ghabezloo, S., and Conil, N. (2017b). "Thermal Volume Changes and Creep in the Callovo-Oxfordian Claystone." *Rock Mechanics and Rock Engineering*, Springer Vienna, 50(9), 2297–2309.

Belmokhtar, M., Delage, P., Ghabezloo, S., and Conil, N. (2018). "Drained Triaxial Tests in Low-Permeability Shales: Application to the Callovo-Oxfordian Claystone." *Rock Mechanics and Rock Engineering*, Springer Vienna, 51(7), 1979–1993.

Bernier, F., Li, X. L., and Bastiaens, W. (2007). "Twenty-five years' geotechnical observation and testing in the Tertiary Boom Clay formation." *Géotechnique*, Thomas Telford Ltd, 57(2), 229–237.

Bernier, F., and Neerdael, B. (1996). "Overview of in-situ thermomechanical experiments in clay: Concept, results and interpretation." *Engineering Geology*, 41(1–4), 51–64.

Bhandari, A. R., Flemings, P. B., Polito, P. J., Cronin, M. B., and Bryant, S. L. (2015). "Anisotropy and stress dependence of permeability in the Barnett shale." *Transport in porous media*, Springer, 108(2), 393–411.

Bian, H. B., Jia, Y., Armand, G., Duveau, G., and Shao, J. F. (2012). "3D numerical modelling thermo-hydromechanical behaviour of underground storages in clay rock." *Tunnelling and Underground Space Technology*, Elsevier Ltd, 30, 93–109.

Biot, M. A., and Willis, D. G. (1957). "The elastic coefficients of the theory of consolidation: Journal of Applied Mechanics." JAMCAV.

Biot, M. a. (1941). "REPRINT SERIES GENERAL THEORY OF THREE-DIMENSIONAL By." *Physics*, 12(2), 155–164.

Bishop, A. W., and Blight, G. E. (1963). "Some aspects of effective stress in saturated and partly saturated soils." *Geotechnique*, Thomas Telford Ltd, 13(3), 177–197.

Blümling, P., Bernier, F., Lebon, P., and Derek Martin, C. (2007). "The excavation damaged zone in clay formations time-dependent behaviour and influence on performance assessment." *Physics and Chemistry of the Earth*, 32(8–14), 588–599.

Bock, H. (2001). *Mont Terri Project. RA experiment: Rock mechanics analyses and synthesis; data report on rock mechanics. Mont Terri Consortium*.

Bolzon, G., and Schrefler, B. A. (2005). "Thermal effects in partially saturated soils: A constitutive model." *International Journal for Numerical and Analytical Methods in Geomechanics*, 29(9), 861–877.

Bossart, P., Meier, P. M., Moeri, A., Trick, T., and Mayor, J. C. (2002). "Geological and hydraulic characterisation of the excavation disturbed zone in the Opalinus Clay of the Mont Terri Rock Laboratory." *Engineering Geology*, 66(1–2), 19–38.

Bossart, P., Trick, T., Meier, P. M., and Mayor, J.-C. (2004). "Structural and hydrogeological characterisation of the excavation-disturbed zone in the Opalinus Clay (Mont Terri Project, Switzerland)." *Applied clay science*, Elsevier, 26(1–4), 429–448.

Boudali, M., Leroueil, S., and Srinivasa Murthy, B. R. (1994). "Viscous hebaviour of natural clays." *International conference on soil mechanics and foundation engineering*, 411–416.

Brace, W. F. (1980). "Permeability of crystalline and argillaceous rocks." *International Journal of Rock Mechanics and Mining Sciences & Geomechanics Abstracts*, 241–251.

Bruyn, D. (1999). "Influence d'une élévation de température sur le comportement physique et mécanique de l'argile de Boom dans le cadre de la problématique de galeries d'enfouissement de déchets radioactifs." UCL-Université Catholique de Louvain.

De Bruyn, D., and Labat, S. (2002). "The second phase of ATLAS: The continuation of a running THM test in the HADES underground research facility at Mol." *Engineering Geology*, 64(2–3), 309–316.

De Bruyn, D., and Thimus, J. F. (1996). "The influence of temperature on mechanical characteristics of boom clay: The results of an initial laboratory programme." *Engineering Geology*, 41(1-4 SPEC. ISS.), 117–126.

Bumbieler, F., Necib, S., Morel, J., Crusset, D., and Armand, G. (2015). "Mechanical And SCC Behavior Of An API5L Steel Casing Within The Context Of Deep Geological Repositories For Radioactive Waste." *ASME 2015 Pressure Vessels and Piping Conference*, 1–11.

Burland, J. B. (1990). "On the compressibility and shear strength of natural clays." *Géotechnique*, 40(3), 329–378.

Campanella, and Mitchell, J. K. (1968). "Influence of temperature variations on soil behavior."

Carcione, J. M. (2000). "A model for seismic velocity and attenuation in petroleum source rocksAn Acoustic Model for Petroleum Source Rocks." *Geophysics*, GeoScienceWorld, 65(4), 1080–1092.

Cekerevac, C., and Laloui, L. (2004). "Experimental study of thermal effects on

the mechanical behaviour of a clay." *J . Numer . Anal . Meth . Geomech*, 28(April 2003), 209–228.

Chen, G. J., Sillen, X., Verstricht, J., and Li, X. L. (2011). "ATLAS III in situ heating test in boom clay: Field data, observation and interpretation." *Computers and Geotechnics*, 38(5), 683–696.

Chen, W. Z., Ma, Y. S., Yu, H. D., Li, F. F., Li, X. L., and Sillen, X. (2017). "Effects of temperature and thermally-induced microstructure change on hydraulic conductivity of Boom Clay." *Journal of Rock Mechanics and Geotechnical Engineering*.

Cho, J.-W., Kim, H., Jeon, S., and Min, K.-B. (2012). "Deformation and strength anisotropy of Asan gneiss, Boryeong shale, and Yeoncheon schist." *International journal of rock mechanics and mining sciences (1997)*, 50, 158–169.

Clayton, C. R. I. (1997). "General Report, Session 2: The mechanical properties and behaviour of hard soils and soft rocks." *Geotechnical Engineering of Hard Soils and Soft Rocks*, Balkema, 3, 1839–1877.

Conil, N., and Armand, G. (2012). "IN SITU HEATING TEST IN CALLOVO-OXFORDIAN CLAYSTONE :"

Conil, N., Gatmiri, B., and Armand, G. (2010). *Premiers résultats de l'expérimentation TED*. Centre de Meuse/Haute-Marne, Rapport Andra D.RP.AMFS.10.0067.

Coop, M. R., and Cotecchia, F. (1995). "The compression of sediments at the archaeological site of Sibari." *Proc. 11th Eur. Conf. Soil Mech. Found. Engng, Copenhagen*, 19–26.

Corkum, A. G., and Martin, C. D. (2007). "Modelling a mine-by test at the Mont Terri rock laboratory, Switzerland." *International Journal of Rock Mechanics and Mining Sciences*, Elsevier, 44(6), 846–859.

Cotecchia, F., and Chandler, R. J. (2000). "A general framework for the mechanical behaviour of clays." *Géotechnique*, Thomas Telford Ltd, 50(4), 431–447.

Coussy, O. (2004). *Poromechanics*. John Wiley & Sons.

Crilly, T. (1996). "Unload-reload tests on saturated illite specimens at elevated temperature."

Cui, Y.-J., Terpereau, J.-M., Marcial, D., Delage, P., Antoine, P., Marchadier, G., and Ye, W.-M. (2004). "A geological and geotechnical characterisation of the loess of Northern France." *Advances in geotechnical engineering: The Skempton conference: Proceedings of a three day conference on advances in geotechnical engineering, organised by the Institution of Civil Engineers and held at the Royal Geographical Society, London, UK, on 29--31*, 417–

428.

Cui, Y. J., Sultan, N., and Delage, P. (2000). "A thermomechanical model for saturated clays." *Canadian Geotechnical Journal*, NRC Research Press, 37(3), 607–620.

Delage, P. (2013). "On the thermal impact on the excavation damaged zone around deep radioactive waste disposal." *Journal of Rock Mechanics and Geotechnical Engineering*, Taibah University, 5(3), 179–190.

Delage, P., Sultan, N., and Cui, Y. J. (2000). "On the thermal consolidation of Boom clay." *Canadian Geotechnical Journal*, NRC Research Press, 37(2), 343–354.

Delay, J., Vinsot, A., Krieguer, J.-M., Rebours, H., and Armand, G. (2007). "Making of the underground scientific experimental programme at the Meuse/Haute-Marne underground research laboratory, North Eastern France." *Physics and Chemistry of the Earth, Parts A/B/C*, Elsevier, 32(1–7), 2–18.

Demars, K. R., and Charles, R. D. (1982). "Soil volume changes induced by temperature cycling." *Canadian geotechnical journal*, NRC Research Press, 19(2), 188–194.

Despax, D. (1976). "Influence de la température sur les propriétés mécaniques des argiles saturées." Ph. D. thesis, Ecole Centrale de Paris, Paris, France.

Donath, F. (1964). "Strength variation and deformational behavior in anisotropic rock." *State of Stress in the Earth's Crust*, American Elsevier, 281.

Eriksson, L. G. (1989). "Temperature effects on consolidation properties of sulphide clays." *International Conference on Soil Mechanics and Foundation Engineering: 13/08/1989-18/08/1989*, 2087–2090.

Fabian, D., Peter, C., Daniel, B., and Torsten, G. (2007). "Evaluation of damage-induced permeability using a three-dimensional Adaptive Continuum/Discontinuum Code (AC/DC)." *Physics and Chemistry of the Earth*, 32(8–14), 681–690.

Farouki, O. T. (1981). "Thermal Properties of Soils." *CRREL Monograph (US Army Cold Regions Research and Engineering Laboratory)*.

Fei, Y. (1995). "Thermal expansion." *Mineral physics and crystallography: a handbook of physical constants*, Wiley Online Library, 2, 29–44.

Fox, P. J., and Edil, T. B. (1996). "Effects of stress and temperature on secondary compression of peat." *Canadian Geotechnical Journal*, NRC Research Press, 33(3), 405–415.

François, B., Laloui, L., and Laurent, C. (2009). "Thermo-hydro-mechanical simulation of ATLAS in situ large scale test in Boom Clay." *Computers and*

Geotechnics, 36(4), 626–640.

Franklin, J. A., and Gruspier, J. E. (1983). *Evaluation of shales for construction projects-an ontario shale rating system*.

Freivogel, M., and Huggenberger. (2003). "Freivogel M, Huggenberger P. Modellierung bilanzierter Profile im Gebiet Mont Terri–La Croix (Kanton Jura). Mont Terri Project–Geology, paleohydrogeology and stress field of the Mont Terri region. Federal Office for Water and Geology Rep." 4, 7–44.

Fromentin, A., Pahud, D., Laloui, L., and Moreni, M. (1999). "Pieux échangeurs: conception et règles de prédimensionnement." *Revue française de génie civil*, Taylor & Francis, 3(6), 387–421.

Garitte, B., Gens, A., Vaunat, J., and Armand, G. (2014). "Thermal conductivity of argillaceous rocks: Determination methodology using in situ heating tests." *Rock Mechanics and Rock Engineering*, 47(1), 111–129.

Gasc-Barbier, M., Chanchole, S., and Bérest, P. (2004). "Creep behavior of Bure clayey rock." *Applied Clay Science*, Elsevier, 26(1–4), 449–458.

Gawin, D., Baggio, P., and Schrefler, B. A. (1995). "Coupled heat, water and gas flow in deformable porous media." *International Journal for numerical methods in fluids*, Wiley Online Library, 20(8 9), 969–987.

Gens, A. (2004). *The role of Geotechnical Engineering for nuclear energy utilisation*.

Gens, A. (2010). "Soil-environment interactions in geotechnical engineering." *Geotechnique*, 60(1), 3–74.

Gens, A. (2013). *On the hydromechanical behaviour of argillaceous hard soils-weak rocks*.

Gens, A., Garcia Molina, A. J., Olivella, S., Alonso, E. E., and Huertas, F. (1998). "Analysis of a full scale in situ test simulating repository conditions." *International Journal for Numerical and Analytical Methods in Geomechanics*, Wiley Online Library, 22(7), 515–548.

Gens, A., Guimaraes, L. do N., Garcia-Molina, A., and Alonso, E. E. (2002). "Factors controlling rock clay buffer interaction in a radioactive waste repository." *Engineering Geology*, Elsevier, 64(2–3), 297–308.

Gens, A., and Olivella, S. (2000). "Non isothermal multiphase flow in deformable porous media. Coupled formulation and application to nuclear waste disposal." Balkema, A.

Gens, A., Sánchez, M., Guimarães, L. D. N., Alonso, E. E., Lloret, A., Olivella, S., Villar, M. V., and Huertas, F. (2009a). "A full-scale in situ heating test for high-level nuclear waste disposal: observations, analysis and interpretation."

Géotechnique, 59(4), 377–399.

Gens, A., Sánchez, M., Guimarães, L. D. N., Alonso, E. E., Lloret, A., Olivella, S., Villar, M. V., and Huertas, F. (2009b). "A full-scale in situ heating test for high-level nuclear waste disposal: Observations, analysis and interpretation." *Geotechnique*, 59(4), 377–399.

Gens, A., Vaunat, J., Garitte, B., and Wileveau, Y. (2007a). "In situ behaviour of a stiff layered clay subject to thermal loading: Observations and interpretation." *Stiff Sedimentary Clays: Genesis and Engineering Behaviour - Geotechnique Symposium in Print 2007*, (2), 123–144.

Gens, A., Vaunat, J., Garitte, B., and Wileveau, Y. (2007b). "In situ behaviour of a stiff layered clay subject to thermal loading: observations and interpretation." *Géotechnique*, 57(2), 207–228.

Gens, A., Wieczorek, K., Gaus, I., Garitte, B., Mayor, J. C., Schuster, K., Armand, G., García-Siñeriz, J. L., and Trick, T. (2017). "Performance of the Opalinus Clay under thermal loading: experimental results from Mont Terri rock laboratory (Switzerland)." *Swiss Journal of Geosciences*, 110(1), 269–286.

Ghabezloo, S., and Sulem, J. (2010). "Effect of the volume of the drainage system on the measurement of undrained thermo-poro-elastic parameters." *International Journal of Rock Mechanics and Mining Sciences*, Elsevier, 47(1), 60–68.

Graham, J., Tanaka, N., Crilly, T., and Alfaro, M. (2001). "Modified Cam-Clay modelling of temperature effects in clays." *Canadian Geotechnical Journal*, 38(3), 608–621.

Gräsle, W. (2009). "Long-term behaviour of Opalinus clay--a new experimental approach involving undrained and drained triaxial creep tests." *Proceedings of the European Commission TIMODAZ-THERESA International Conference, Luxembourg*, 343–347.

Habibagahi, K. (1973). "Temperature Effect on Consolidation Behavior of Overconsolidated Soils." *Proceedings, 8th International Conference on Soil Mechanics and Foundation Engineering*, 159–163.

Habibagahi, K. (1976). "Temperature effects on primary consolidation." *Page Behaviour of a Malaysian Residual Granite Soil as a Sand-Silt-Clay Composite Soil*, 7, 95.

Hallsworth, C. R., and Knox, R. (1999). "BGS rock classification scheme. Volume 3, classification of sediments and sedimentary rocks." British Geological Survey.

Hawkins, A. B. (2000). "General report: The nature of hard rocks/soft soils." *The geotechnics of hard soils-soft rocks*, 1391–1402.

Hawkins, A. B., and Pinches, G. M. (1992). "Engineering description of mudrocks." *Quarterly Journal of Engineering Geology and Hydrogeology*, Geological Society of London, 25(1), 17–30.

Heitz, J.-F., and Hicher, P.-Y. (2002). "The mechanical behaviour of argillaceous rocks--Some questions from laboratory experiments." *Proc. Int. Symp. Hydromechanical and Thermohydromechanical Behaviour of Deep Argillaceous Rock*, 99–108.

Hornby, B. E. (1998). "Experimental laboratory determination of the dynamic elastic properties of wet, drained shales." *Journal of Geophysical Research: Solid Earth*, Wiley Online Library, 103(B12), 29945–29964.

Horseman, S. T., Winter, M. G., and Enwistle, D. C. (1987). *Geotechnical characterization of Boom clay in relation to the disposal of radioactive waste*.

Hou, Z. (2003). "Mechanical and hydraulic behavior of rock salt in the excavation disturbed zone around underground facilities." *International Journal of Rock Mechanics and Mining Sciences*, 40(5), 725–738.

Houston, S. L., Houston, W. N., and Williams, N. D. (1985). "Thermo-mechanical behavior of seafloor sediments." *Journal of Geotechnical Engineering*, American Society of Civil Engineers, 111(11), 1249–1263.

Hu, D. W., Zhang, F., and Shao, J. F. (2014). "Experimental study of poromechanical behavior of saturated claystone under triaxial compression." *Acta Geotechnica*, 9(2), 207–214.

Hudson, J. A., Bäckström, A., Rutqvist, J., Jing, L., Backers, T., Chijimatsu, M., Christiansson, R., Feng, X. T., Kobayashi, A., Koyama, T., Lee, H. S., Neretnieks, I., Pan, P. Z., Rinne, M., and Shen, B. T. (2009). "Characterising and modelling the excavation damaged zone in crystalline rock in the context of radioactive waste disposal." *Environmental Geology*, 57(6), 1275–1297.

Hueckel, T., and Baldi, G. (1991). "THERMOPLASTICITY OF SATURATED C L A Y S : EXPERIMENTAL CONSTITUTIVE STUDY By T. Hueckel 1 and G. Baldi 2." *Journal of Geotechnical and Geoenvironmental Engineering ASCE*, 116(12), 1778–1796.

Hueckel, T., and Borsetto, M. (1990). "Thermoplasticity of saturated soils and shales: Constitutive equations." *Journal of Geotechnical Engineering*, 116(12), 1765–1777.

Hueckel, T., Francois, B., and Laloui, L. (2009). "Explaining thermal failure in saturated clays." *Geotechnique*, 59(3), 197–212.

Hvorslev, M. J. (1937). *Über die Festigkeitseigenschaften gestörter bindiger Böden: With an abstract in English*. Danmarks naturvidenskabelige samfund, i kommission has GEC Gad.

IAEA. (2003). "The Long Term Storage of Radioactive Waste: Safety and Sustainability." *Vienna, Austria: IAEA*.

Jardine, R. J. (2011). "Characterization of mudrocks: a practical application of advanced laboratory testing." *Journal of Zhejiang University-SCIENCE A*, Springer, 12(1), 1–14.

Jardine, R. J., Gens, A., Hight, D. W., and Coop, M. R. (2004a). "Developments in understanding soil behaviour." *Advances in geotechnical engineering: The Skempton conference: Proceedings of a three day conference on advances in geotechnical engineering, organised by the Institution of Civil Engineers and held at the Royal Geographical Society, London, UK, on 29--31*, 103–206.

Jardine, R. J., Gens, A., Hight, D. W., and Coop, M. R. (2004b). "Developments in understanding soil behaviour, Advances in Geotechnical Engineering, The Skempton Conference." Thomas Telford.

Khemissa, M. (1998). "Mesure de la perméabilité des argiles sous contrainte et température." *Revue française de Géotechnique*, EDP Sciences, (82), 11–22.

Kim, J. S., Kwon, S. K., Sanchez, M., and Cho, G. C. (2011). "Geological storage of high level nuclear waste." *KSCE Journal of Civil Engineering*, 15(4), 721–737.

Knowles, N. C., Jeffries, R. M., and Come, B. (1996). "Benchmarking the thermomechanical behaviour of clays a progress report the CEC interclay project." *Engineering geology*, Elsevier, 41(1–4), 65–71.

Kuntiwattanakul, P., Towhata, I., Ohishi, K., and Seko, I. (1995). "Temperature effects on undrained shear characteristics of clay." *Soils and Foundations*, The Japanese Geotechnical Society, 35(1), 147–162.

Kwon, O., Kronenberg, A. K., Gangi, A. F., Johnson, B., and Herbert, B. E. (2004). "Permeability of illite-bearing shale: 1. Anisotropy and effects of clay content and loading." *Journal of Geophysical Research: Solid Earth*, Wiley Online Library, 109(B10).

Lachenbruch, A. H. (1980). "Frictional heating, fluid pressure, and the resistance to fault motion." *Journal of Geophysical Research: Solid Earth*, Wiley Online Library, 85(B11), 6097–6112.

Ladd, C. C., and Varallyay, J. (1965). *The influence of stress system on the behavior of saturated clays during undrained shear*.

Laloui, L., and Cekerevac, C. (2003). "Thermo-plasticity of clays: An isotropic yield mechanism." *Computers and Geotechnics*, 30(8), 649–660.

Lanyon, G. . (2011). "Excavation Damaged Zones Assessment." *OPG's Deep Geologic Respository for Low & Intermediate waste*, NWMO DGR-

T(March).

Lemueil, S., and Vaughan, P. R. (1990). "The general and congruent effects of structure in natural soils and weak rocks." *Geotechnique*, 40(3), 467–488.

Leroueil, S., and Vaughan, P. R. (1991). "Discussion: The general and congruent effects of structure in natural soils and weak rocks." *Géotechnique*, Thomas Telford Ltd, 41(2), 281–284.

Li, X. (2013). "TIMODAZ: A successful international cooperation project to investigate the thermal impact on the EDZ around a radioactive waste disposal in clay host rocks." *Journal of Rock Mechanics and Geotechnical Engineering*, Taibah University, 5(3), 231–242.

Li, X. L., Bastiaens, W., and Bernier, F. (2006). "The hydromechanical behaviour of the Boom Clay observed during excavation of the connecting gallery at Mol site." *Proceedings of EUROCK2006-Multiphysics Coupling and Long Term Behaviour in Rock Mechanics, Liege, Belgium*, Balkema Rotterdam, The Netherlands, 467–472.

Li, X., and Yu, H.-S. (2009). "Influence of loading direction on the behavior of anisotropic granular materials." *International Journal of Engineering Science*, Elsevier, 47(11–12), 1284–1296.

Lima, A., Romero, E., Gens, A., Muñoz, J., and Li, X. L. (2010). "Heating pulse tests under constant volume on Boom clay." *Journal of rock mechanics and geotechnical engineering*, Elsevier, 2(2), 124–128.

Lisjak, A., Tatone, B. S. A., Mahabadi, O. K., Grasselli, G., Marschall, P., Lanyon, G. W., Vaissi??re, R. de la, Shao, H., Leung, H., and Nussbaum, C. (2016). "Hybrid Finite-Discrete Element Simulation of the EDZ Formation and Mechanical Sealing Process Around a Microtunnel in Opalinus Clay." *Rock Mechanics and Rock Engineering*, 49(5), 1849–1873.

Liu, Z., Shao, J., Xie, S., Conil, N., and Talandier, J. (2019). "Mechanical Behavior of Claystone in Lateral Decompression Test and Thermal Effect." *Rock Mechanics and Rock Engineering*, Springer Vienna, 52(2), 321–334.

Mánica, M. A. (2018). "Analysis of underground excavations in argillaceous hard soils - weak rocks." *UPC*.

Mánica, M., Gens, A., Vaunat, J., and Ruiz, D. F. (2016). "A time-dependent anisotropic model for argillaceous rocks. Application to an underground excavation in Callovo-Oxfordian claystone." *Computers and Geotechnics*.

Mánica, M., Gens, A., Vaunat, J., and Ruiz, D. F. (2017). "A time-dependent anisotropic model for argillaceous rocks. Application to an underground excavation in Callovo-Oxfordian claystone." *Computers and Geotechnics*, 85, 341–350.

Marschall, P., Distinguin, M., Shao, H., Bossart, P., Enachescu, C., and Trick, T.

(2006). “Creation and evolution of damage zones around a microtunnel in a claystone formation of the Swiss Jura Mountains.” *SPE International Symposium and Exhibition on Formation Damage Control*, Society of Petroleum Engineers.

Masri, M., Sibai, M., Shao, J. F., and Mainguy, M. (2014). “Experimental investigation of the effect of temperature on the mechanical behavior of Tournemire shale.” *International Journal of Rock Mechanics and Mining Sciences*, Elsevier, 70, 185–191.

McLamore, R., and Gray, K. E. (1967). “The mechanical behavior of anisotropic sedimentary rocks.”

McTigue, D. F. (1986). “Thermoelastic response of fluid-saturated porous rock.” *Journal of Geophysical Research: Solid Earth*, Wiley Online Library, 91(B9), 9533–9542.

Menaceur, H., Delage, P., Tang, A. M., and Conil, N. (2015a). “The thermo-mechanical behaviour of the Callovo-Oxfordian claystone.” *International Journal of Rock Mechanics and Mining Sciences*, 78, 290–303.

Menaceur, H., Delage, P., Tang, A. M., and Conil, N. (2015b). “The thermo-mechanical behaviour of the Callovo-Oxfordian claystone.” *International Journal of Rock Mechanics and Mining Sciences*, Elsevier, 78, 290–303.

Mesri, G., and Shahien, M. (2003). “Residual shear strength mobilized in first-time slope failures.” *Journal of Geotechnical and Geoenvironmental Engineering*, American Society of Civil Engineers, 129(1), 12–31.

Miguel Mánica;, Gens;, A., Vaunat;, J., and Ruiz, D. F. (2016). “A time-dependent anisotropic model for argillaceous rocks . Application to an underground excavation in Callovo-Oxfordian claystone.” *Computers and Geotechnics*.

Modaressi, H., and Laloui, L. (1992). “A cyclic thermoviscoplastic constitutive model for clays.” *International symposium on numerical models in geomechanics*, 125–134.

Modaressi, H., and Laloui, L. (1997). “a Thermo-Viscoplastic Constitutive Model for Clays.” 21(April 1995), 313–335.

Mohajerani, M. (2011). “Etude expérimentale du comportement thermo-hydro-mécanique de l’argilite du Callovo-Oxfordien.”

Mohajerani, M., Delage, P., Sulem, J., Monfared, M., Tang, A. M., and Gatmiri, B. (2012). “A laboratory investigation of thermally induced pore pressures in the Callovo-Oxfordian claystone.” *International Journal of Rock Mechanics and Mining Sciences*, Elsevier, 52, 112–121.

Mohajerani, M., Delage, P., Sulem, J., Monfared, M., Tang, A. M., and Gatmiri, B. (2014). “The thermal volume changes of the callovo-oxfordian claystone.” *Rock Mechanics and Rock Engineering*, 47(1), 131–142.

Monfared, M., Sulem, J., Delage, P., and Mohajerani, M. (2012). "On the THM behaviour of a sheared Boom clay sample: Application to the behaviour and sealing properties of the EDZ." *Engineering Geology*, Elsevier B.V., 124(1), 47–58.

Morel, J., Bumbieler, F., Conil, N., Armand, G., and others. (2013). "Feasibility and behavior of a full scale disposal cell in a deep clay layer." *ISRM International Symposium-EUROCK 2013*.

Morin, R., and Silva, A. J. (1984). "The effects of high pressure and high temperature on some physical properties of ocean sediments." *Journal of Geophysical Research: Solid Earth*, Wiley Online Library, 89(B1), 511–526.

Muñoz, J., Alonso, E. E., and Lloret, a. (2009). "Thermo-hydraulic characterisation of soft rock by means of heating pulse tests." *Géotechnique*, 59(4), 293–306.

Naumann, M., Hunsche, U., and Schulze, O. (2007). "Experimental investigations on anisotropy in dilatancy, failure and creep of Opalinus Clay." *Physics and Chemistry of the Earth, Parts A/B/C*, Elsevier, 32(8–14), 889–895.

NEA. (2001). *The role of underground laboratories in nuclear waste disposal programmes*. *Nuclear Energy Agency*, Paris.

Neuzil, C. E. (1994). "How permeable are clays and shales?" *Water resources research*, Wiley Online Library, 30(2), 145–150.

Niandou, H., Shao, J. F., Henry, J. P., and Fourmaintraux, D. (1997). "Laboratory investigation of the mechanical behaviour of Tournemire shale." *International Journal of Rock Mechanics and Mining Sciences*, Elsevier, 34(1), 3–16.

Nygård, R., Gutierrez, M., Bratli, R. K., and Høeg, K. (2006). "Brittle--ductile transition, shear failure and leakage in shales and mudrocks." *Marine and Petroleum Geology*, Elsevier, 23(2), 201–212.

Olivella, S., Carrera, J., Gens;, A., and Alonso, E. (1994). "Non-isothermal multiphase flow of brine and gas through saline media." *Transport in Porous Media*, 15(3), 271–293.

Olivella, S., Gens, A., Carrera, J., and Alonso, E. E. (1996). "Numerical formulation for a simulator (CODE_BRIGHT) for the coupled analysis of saline media." *Engineering Computations*, 13(7), 87–112.

Palciauskas, V. V, and Domenico, P. A. (1982). "Characterization of drained and undrained response of thermally loaded repository rocks." *Water Resources Research*, Wiley Online Library, 18(2), 281–290.

Pettijohn, F. J. (1957). "Sedimentary Rocks. 3 Indian edition." New York: Harper & Row Publishers, Inc.

Picard, J. M., Bazargan, B., and Rousset, G. (1994). *Essai thermohydro-mecanique dans une argile profonde: Essai CACTUS*. Luxembourg: CEC.

Plum, robert l., and Esrig, melvin I. (1969). "Some temperature effects on soil compressibility and pore water pressure." *Special Report*, The Board., (103), 231.

Potts, D. M., and Zdravkovic, L. (1999). "Finite element analysis in geotechnical engineering. Theory." 440.

Rice, J. R. (2006). "Heating and weakening of faults during earthquake slip." *Journal of Geophysical Research: Solid Earth*, Wiley Online Library, 111(B5).

Robinet, J.-C., Rahbaoui, A., Plas, F., and Lebon, P. (1996). "A constitutive thermomechanical model for saturated clays." *Engineering Geology*, Elsevier, 41(1–4), 145–169.

Rotta Loria, A. F., and Laloui, L. (2017). "Thermally induced group effects among energy piles." *Géotechnique*, 67(5), 374–393.

Rutqvist, J., B??rgesson, L., Chijimatsu, M., Hernelind, J., Jing, L., Kobayashi, A., and Nguyen, S. (2009). "Modeling of damage, permeability changes and pressure responses during excavation of the TSX tunnel in granitic rock at URL, Canada." *Environmental Geology*, 57(6), 1263–1274.

Salager, S. (2008). *Expertise sur les mesures sur échantillons dargilites du coefficient de dilatation thermique, du module et du coefficient de Biot*.

Sayers, C. M. (2013). "The effect of anisotropy on the Young's moduli and Poisson's ratios of shales." *Geophysical Prospecting*, European Association of Geoscientists & Engineers, 61(Rock Physics for Reservoir Exploration, Characterisation and Monitoring), 416–426.

Seyedi, D. M., and Gens, A. (2017). "Numerical analysis of the hydromechanical response of Callovo-Oxfordian claystone to deep excavations." *Computers and Geotechnics*, 85, 275–276.

Simpson, B. (1979). "Design Parameters for stiff clays general report." *7th European Conference On Soil Mechanics and Foundation Engineering*, Brighton, 91–125.

Skempton, A. W. (1954). "The pore-pressure coefficients A and B." *Geotechnique*, Thomas Telford Ltd, 4(4), 143–147.

Skempton, A. W. (1964). "Long-term stability of clay slopes, Geo-technique." XIV.

Skempton, A. W. (1969). "The consolidation of clays by gravitational compaction." *Quarterly Journal of the Geological Society*, Geological Society of London, 125(1–4), 373–411.

Skempton, A. W. (1970). "The consolidation of clays by gravitational compaction." *Quarterly Journal of the Geological Society*, Geological Society of London, 125(1–4), 373–411.

Spang, B. (2002). "Excel add-in for properties of water and steam in SI-units." *Water97_v13. xla. Hamburg*.

Sulem, J., Lazar, P., and Vardoulakis, I. (2007). "Thermo-poro-mechanical properties of clayey gouge and application to rapid fault shearing." *International journal for numerical and analytical methods in geomechanics*, Wiley Online Library, 31(3), 523–540.

Sulem, J., Vardoulakis, I., Ouffroukh, H., Boulon, M., and Hans, J. (2004). "Experimental characterization of the thermo-poro-mechanical properties of the Aegion fault gouge." *Comptes Rendus Geoscience*, Elsevier, 336(4–5), 455–466.

Sultan, N. (1997). "Etude du comportement thermo-mécanique de l'argile de Boom: expériences et modélisation." *THESE DE DOCTORAT PRESENTEE A L'ECOLE NATIONALE DES PONTS ET CHAUSSEES-SPECIALITE: GEOTECHNIQUE*.

Sultan, N., Delage, P., and Cui, Y. J. (2002). "Temperature effects on the volume change behaviour of Boom clay." *Engineering Geology*, 64(2–3), 135–145.

Tanaka, N. (1995). "Thermal elastic plastic behaviour and modelling of saturated clay [Ph. D. Thesis][D]." *Winnipeg, Man: University of Manitoba*.

Terzaghi, K., Peck, R. B., and Mesri, G. (1996). *Soil mechanics in engineering practice*. John Wiley & Sons.

Terzaghi, K. van. (1923). "Die berechnung der durchlassigkeitsziffer des tones aus dem verlauf der hydrodynamischen spannungserscheinungen." *Sitzungsberichte der Akademie der Wissenschaften in Wien, Mathematisch-Naturwissenschaftliche Klasse, Abteilung IIa*, 132(34), 125–138.

Thomas, H. R., and He, Y. (1995). "Analysis of coupled heat, moisture and air transfer in a deformable unsaturated soil." *Geotechnique*, Thomas Telford Ltd, 45(4), 677–689.

Thury, M., and Bossart, P. (1999). "The Mont Terri rock laboratory, a new international research project in a Mesozoic shale formation, in Switzerland." *Engineering Geology*, Elsevier, 52(3–4), 347–359.

Tidfors, M., and Sällfors, G. (1989). "Temperature effect on preconsolidation pressure." *Geotechnical Testing Journal*, ASTM International, 12(1), 93–97.

Tiedemann, B. (1937). "Uber die Schubfestigkeit bindiger boden." *Bautechnik*, 15, 433–435.

TIMODAZ. (2007). "Thermal impact on the damaged zone around a radioactive

waste disposal in clay host rocks. Deliverable 2. State of the art on THMC. Euratom European Project."

Tourchi, S., Vaunat, J., and Gens, A. (2019). *THM modelling of the ALC1604 experiment. Final report.* Barcelona.

Towhata, I., Kuntiwattanaku, P., Seko, I., and Ohishi, K. (1993). "Volume change of clays induced by heating as observed in consolidation tests." *Soils and Foundations*, The Japanese Geotechnical Society, 33(4), 170–183.

Tsang, C. F., Bernier, F., and Davies, C. (2005). "Geohydromechanical processes in the Excavation Damaged Zone in crystalline rock, rock salt, and indurated and plastic clays - In the context of radioactive waste disposal." *International Journal of Rock Mechanics and Mining Sciences*, 42(1), 109–125.

Valès, F., Minh, D. N., Gharbi, H., and Rejeb, A. (2004). "Experimental study of the influence of the degree of saturation on physical and mechanical properties in Tournemire shale (France)." *Applied Clay Science*, Elsevier, 26(1–4), 197–207.

Vardoulakis, I. (2002). "Dynamic thermo-poro-mechanical analysis of catastrophic landslides." *Geotechnique*, Thomas Telford Ltd, 52(3), 157–171.

Vernik, L., and Liu, X. (1997). "Velocity anisotropy in shales: A petrophysical study." *Geophysics*, Society of Exploration Geophysicists, 62(2), 521–532.

Wang, Z. (2002a). "Seismic anisotropy in sedimentary rocks, part 2: Laboratory data: Geophysics." GPYSA7.

Wang, Z. (2002b). "Seismic anisotropy in sedimentary rocks, part 1: A single-plug laboratory method." *Geophysics*, Society of Exploration Geophysicists, 67(5), 1415–1422.

Yu, L., Weetjens, E., Sillen, X., Vietor, T., Li, X., Delage, P., Labiouse, V., and Charlier, R. (2014). "Consequences of the thermal transient on the evolution of the damaged zone around a repository for heat-emitting high-level radioactive waste in a clay formation: a performance assessment perspective." *Rock mechanics and rock engineering*, Springer, 47(1), 3–19.

Zhang, C. L. (2011). "Experimental evidence for self-sealing of fractures in claystone." *Physics and Chemistry of the Earth*, Elsevier Ltd, 36(17–18), 1972–1980.

Zhang, C. L. (2015). "Deformation of clay rock under THM conditions. Geomech Tunn 8: 426--435."

Zhang, C. L. (2018). "Thermo-hydro-mechanical behavior of clay rock for deep geological disposal of high-level radioactive waste." *Journal of Rock Mechanics and Geotechnical Engineering*, Elsevier Ltd, 10(5), 992–1008.

Zhang, C. L., Conil, N., and Armand, G. (2017). "Thermal effects on clay rocks

for deep disposal of high-level radioactive waste." *Journal of Rock Mechanics and Geotechnical Engineering*, Elsevier Ltd, 1–16.

Zhang, C. L., Rothfuchs, T., Su, K., and Hoteit, N. (2007a). "Experimental study of the thermo-hydro-mechanical behaviour of indurated clays." *Physics and Chemistry of the Earth*, 32(8–14), 957–965.

Zhang, C. L., Rothfuchs, T., Su, K., and Hoteit, N. (2007b). "Experimental study of the thermo-hydro-mechanical behaviour of indurated clays." *Physics and Chemistry of the Earth*, 32(8–14), 957–965.

Zhang, C., and Rothfuchs, T. (2004a). "Experimental study of the hydro-mechanical behaviour of the Callovo-Oxfordian argillite." *Applied Clay Science*, Elsevier, 26(1–4), 325–336.

Zhang, C., and Rothfuchs, T. (2004b). "Experimental study of the hydro-mechanical behaviour of the Callovo-Oxfordian argillite." *Applied Clay Science*, 26(1–4), 325–336.

Zhang, F., Hu, D. W., Xie, S. Y., and Shao, J. F. (2014). "Influences of temperature and water content on mechanical property of argillite." *European Journal of Environmental and Civil Engineering*, 18(2), 173–189.

Zhu, W. C., and Bruhns, O. T. (2008). "Simulating excavation damaged zone around a circular opening under hydromechanical conditions." *International Journal of Rock Mechanics and Mining Sciences*, 45(5), 815–830.

Zhu, W., and Wong, T. (1997). "The transition from brittle faulting to cataclastic flow: Permeability evolution." *Journal of Geophysical Research: Solid Earth*, Wiley Online Library, 102(B2), 3027–3041.

Zimmerman, R. W. (2000). "Coupling in poroelasticity and thermoelasticity." *International Journal of Rock Mechanics and Mining Sciences*, 37(1–2), 79–87.

Appendices

Appendix A

Temperature results from the thermal analysis

A.1 COMPARISON BETWEEN SIMULATED AND MEASURED RESULTS

This part contains the comparison between the numerical results of the final three-dimensional modelling and the measurements at all the sensors in the host rock, on the steel lining and within the gap. Results are organized into two types of figures:

- Comparisons of temperature evolution at all the sensors within specific vertical cross-sections orthogonal to the microtunnel and located at z = 3, 4, 4.5, 5, 10, 13, 13.6 14.5 and 17.5 m from the head of the microtunnel at GAN gallery.
- Comparisons of temperature time evolution and temperature profiles for all the sensors belonging to specific boreholes: ALC1616, ALC1617, ALC1618, ALC1633, ALC4001, ALC4002, ALC4003, ALC4004 and ALC4005.

For the sake of clarity, Figure A.1 summarizes again the location of instrumentation around ALC1604 experiment.

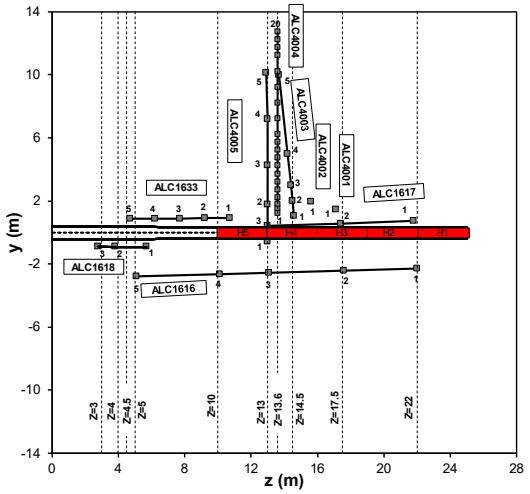

Figure A.1: Horizontal view (bedding plane) of the instrumentation boreholes and perpendicular sections.

A.1.1 Comparisons in sections perpendicular to the alveolus

Comparison of temperature in sections perpendicular to the microtunnel (sections 3, 4, 4.5, 5, 10, 13, 13.6, 14.5, 17.5 and 22m) between measurement and model simulations are presented in Figure A.2 to Figure A.11.

Section Z=3m

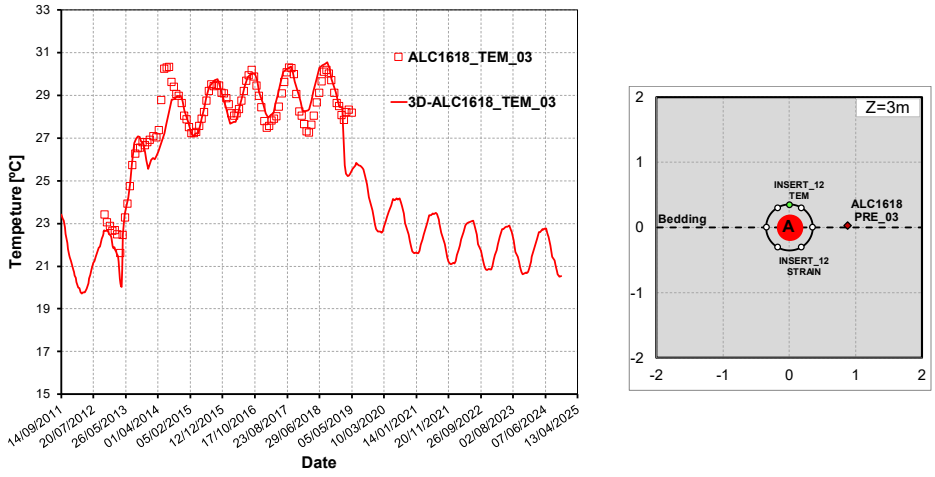

(a) (b)

Figure A.2: Temperature evolution at sensors located within the section at 3 m from the gallery. The measurements (dots) are compared with the simulation (lines).

Section Z=4m

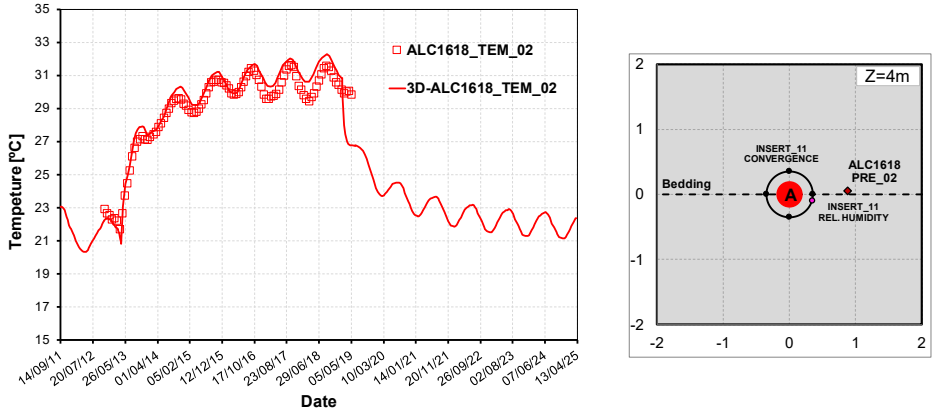

(a) (b)

Figure A.3: Temperature evolution at sensors located within the section at 4 m from the gallery. The measurements (dots) are compared with the simulation (lines).

Section Z=4.5m

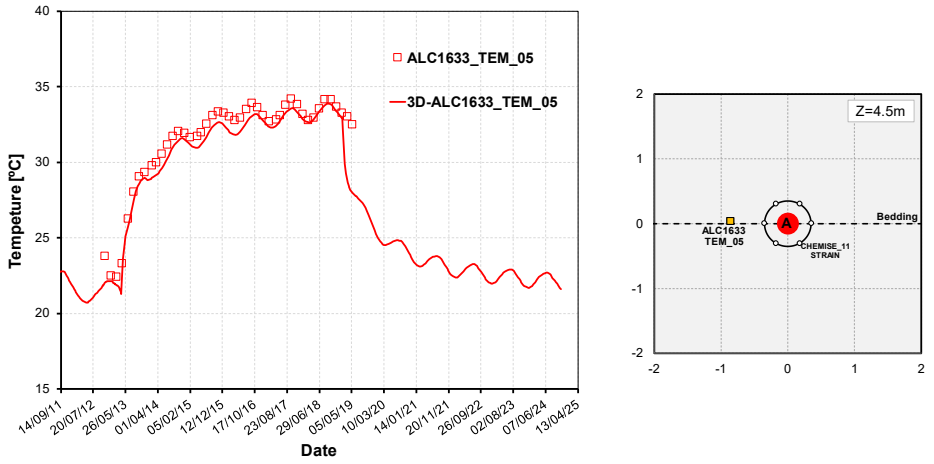

(a) (b)

Figure A.4: Temperature evolution at sensors located within the section at 4.5 m from the gallery. The measurements (dots) are compared with the simulation (lines).

Section Z=5m

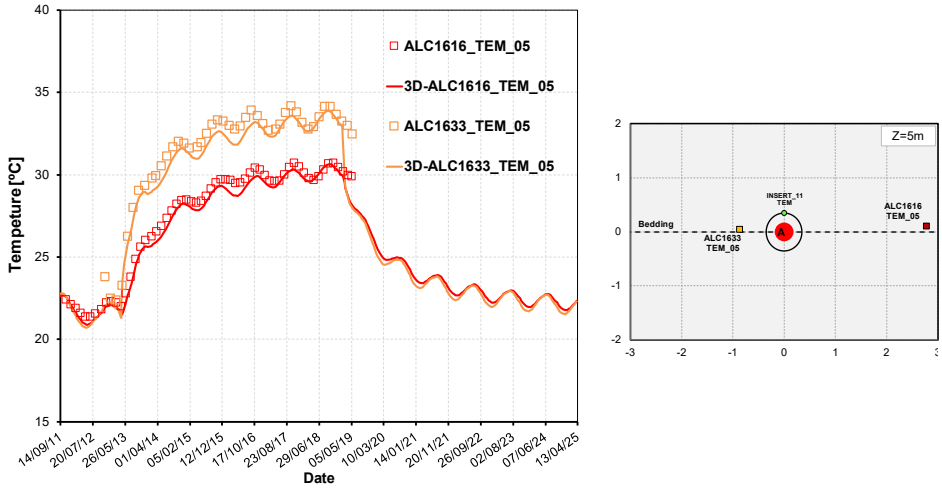

(a) (b)

Figure A.5: Temperature evolution at sensors located within the section at 5 m from the gallery. The measurements (dots) are compared with the simulation (lines).

Section Z=10m

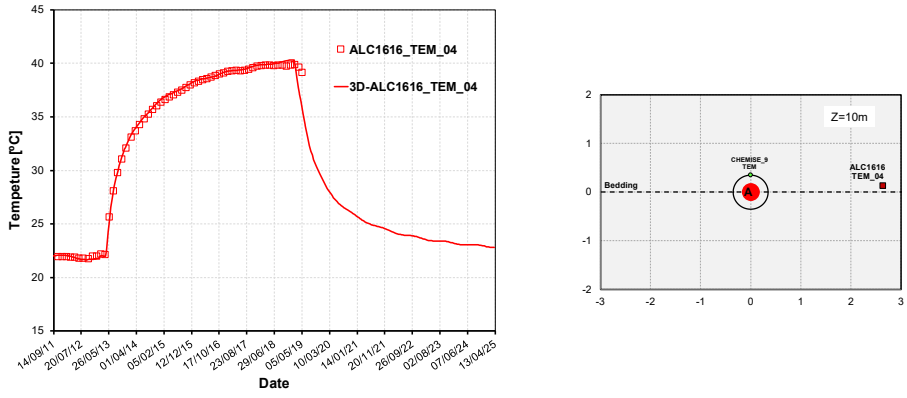

(a) (b)

Figure A.6: Temperature evolution at sensors located within the section at 10 m from the gallery. The measurements (dots) are compared with the simulation (lines).

Section Z=13m

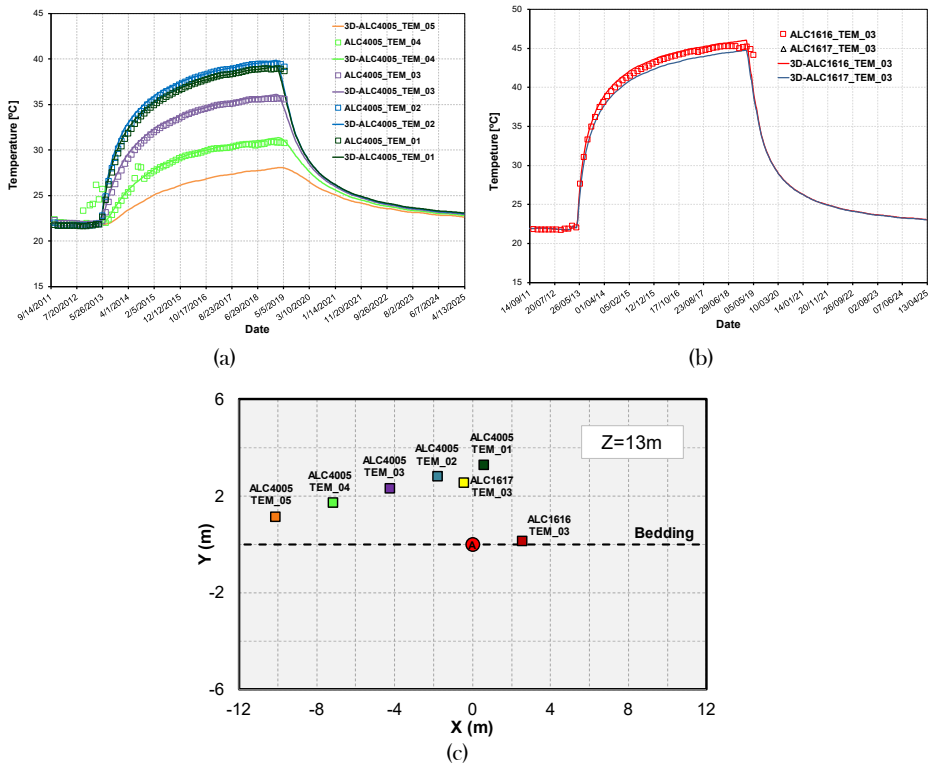

Figure A.7: Temperature evolution at sensors located within the section at 13 m from the gallery. The measurements (dots) are compared with the simulation (lines).

Section Z=13.6m

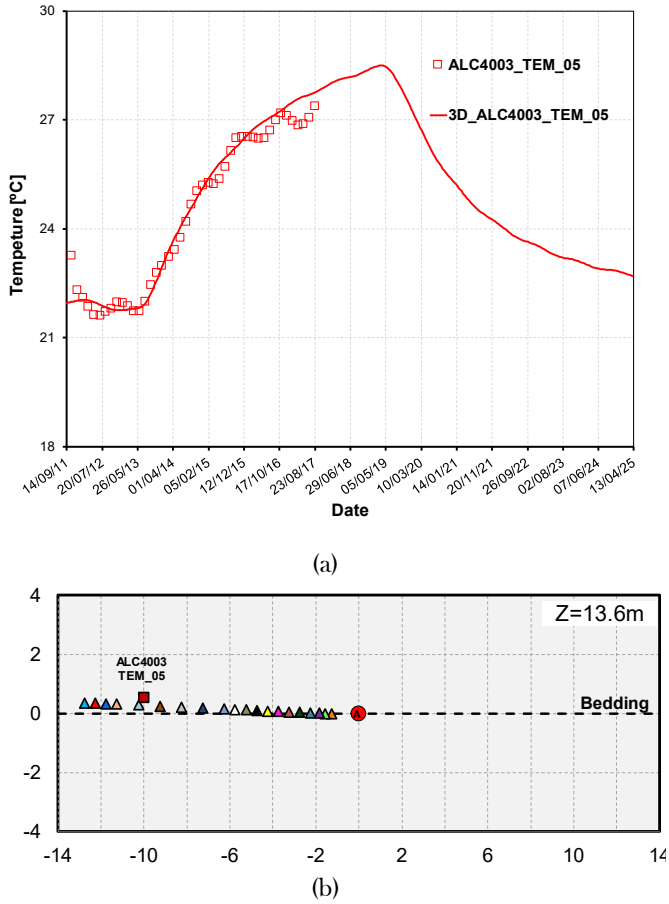

Figure A.8: Temperature evolution at sensors located within the section at 13.6 m from the gallery. The measurements (dots) are compared with the simulation (lines).

Section Z=14.5m

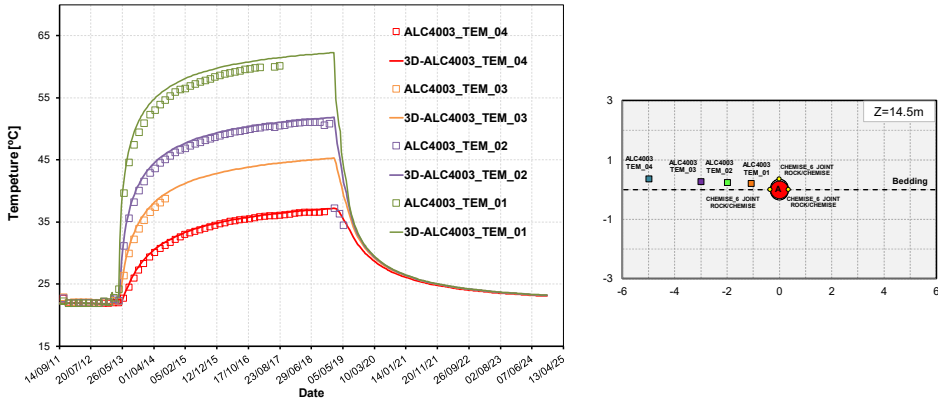

(a) (b)

Figure A.9: Temperature evolution at sensors located within the section at 14.5 m from the gallery. The measurements (dots) are compared with the simulation (lines).

Section Z=17.5m

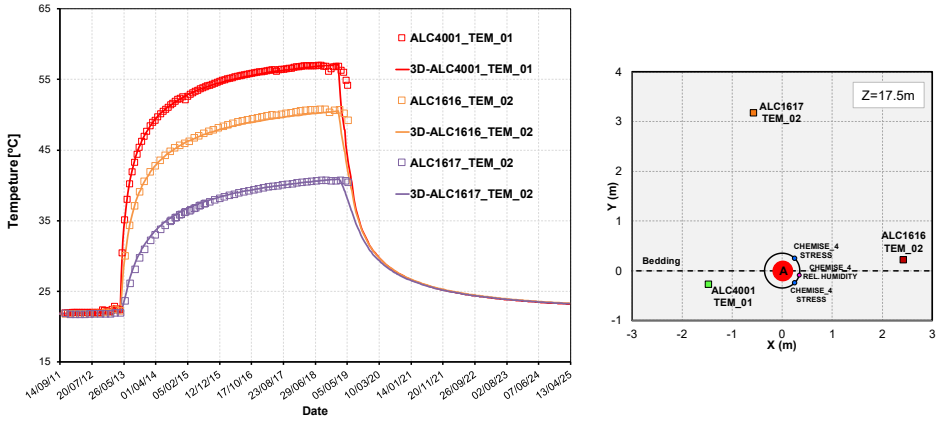

(a) (b)

Figure A.10: Temperature evolution at sensors located within the section at 17.5 m from the gallery. The measurements (dots) are compared with the simulation (lines).

Section Z=22m

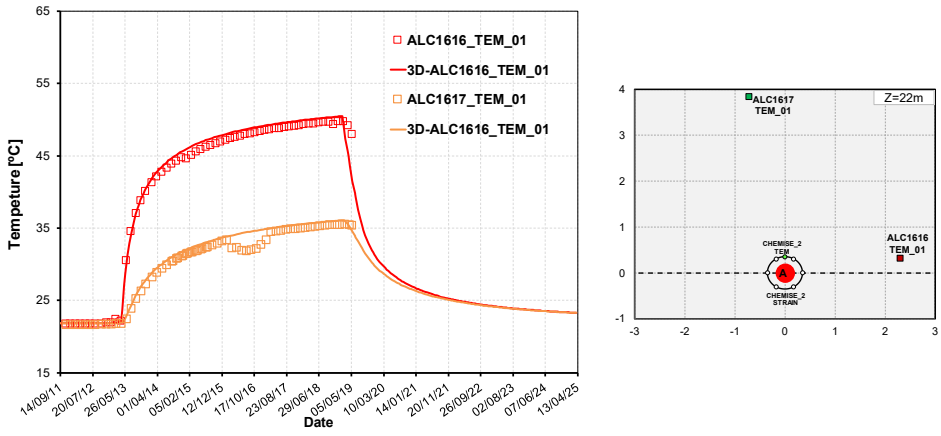

(a) (b)

Figure A.11: Temperature evolution at sensors located within the section at 22 m from the gallery. The measurements (dots) are compared with the simulation (lines).

A.1.2 Comparisons along boreholes

Comparison of temperature along boreholes (boreholes1616, boreholes1617, boreholes1618, boreholes1633, boreholes 4003, boreholes4005 and boreholes4001) between measurement and model simulations are presented in Figure A.12 to Figure A.18.

Borehole ALC1616

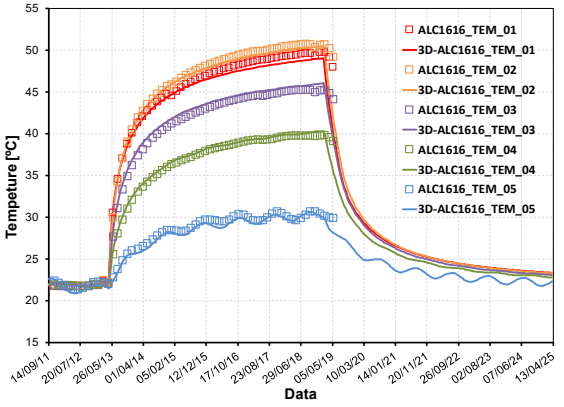

(a)

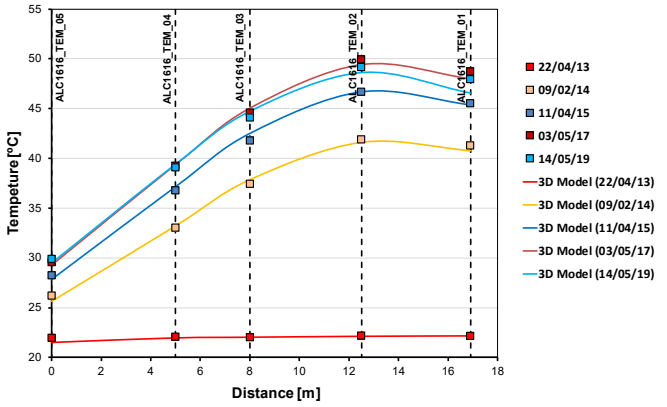

(b)

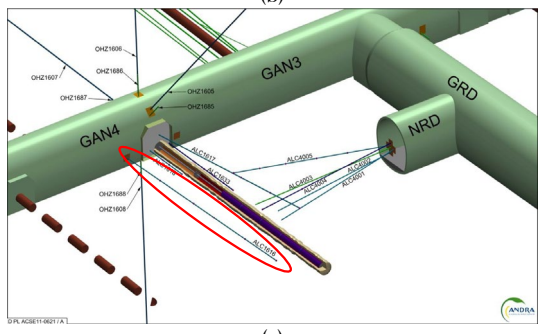

(c)

Figure A.12: Temperature a) time evolution and b) profiles at sensors along borehole ALC1616. The measurements (dots) are compared to the simulation results (lines).

Borehole ALC1617

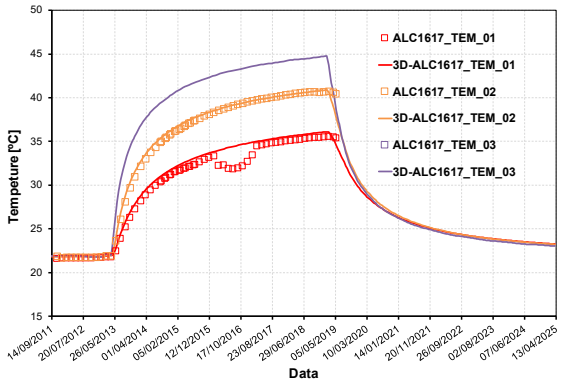

(a)

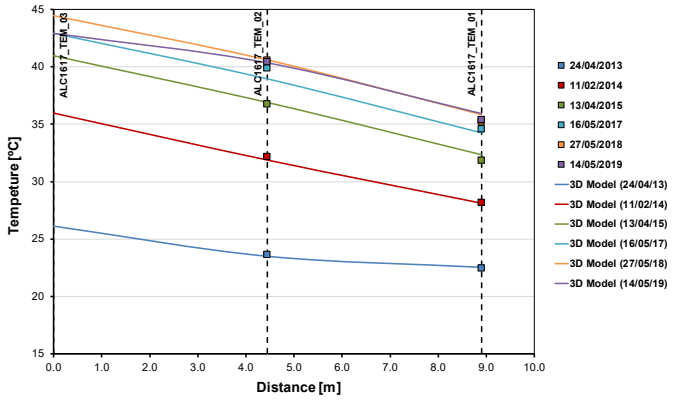

(b)

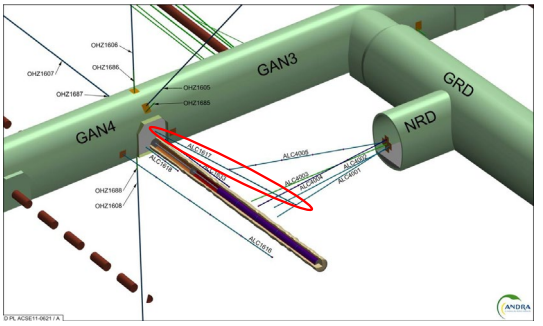

(c)

Figure A.13: Temperature a) time evolution and b) profiles at sensors along borehole ALC1617. The measurements (dots) are compared to the simulation results (lines).

Borehole ALC1618

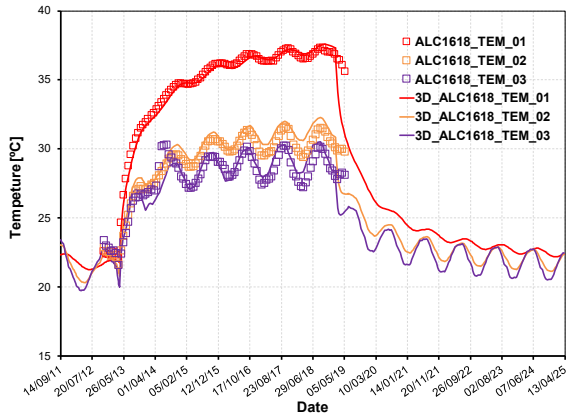

(a)

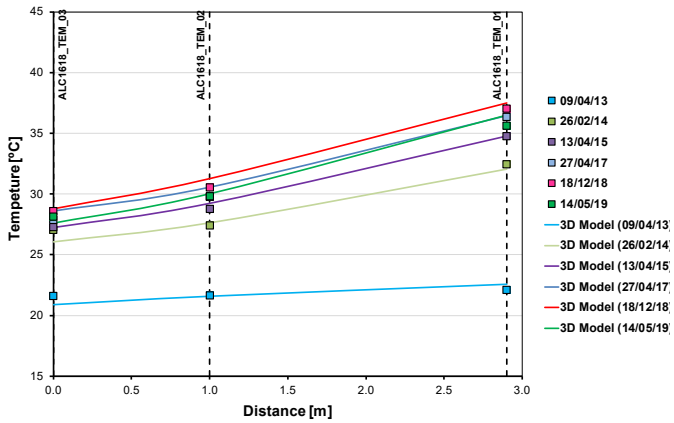

(b)

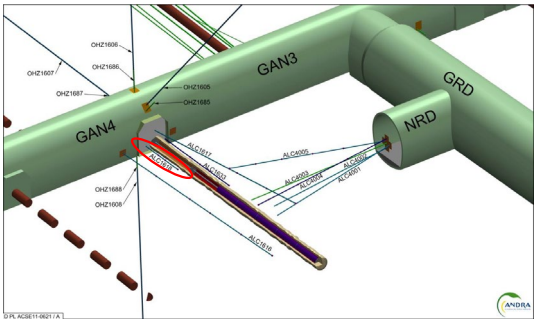

(c)

Figure A.14: Temperature a) time evolution and b) profiles at sensors along borehole ALC1618. The measurements (dots) are compared to the simulation results (lines).

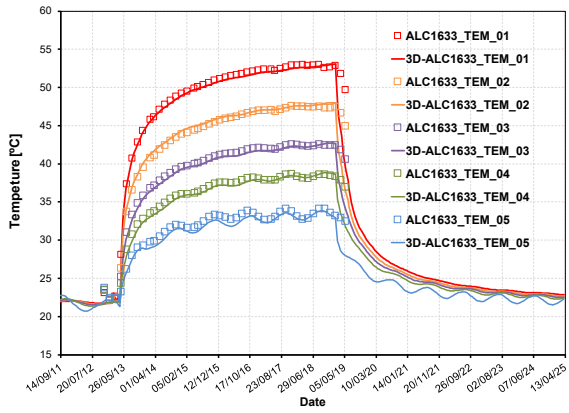

(a)

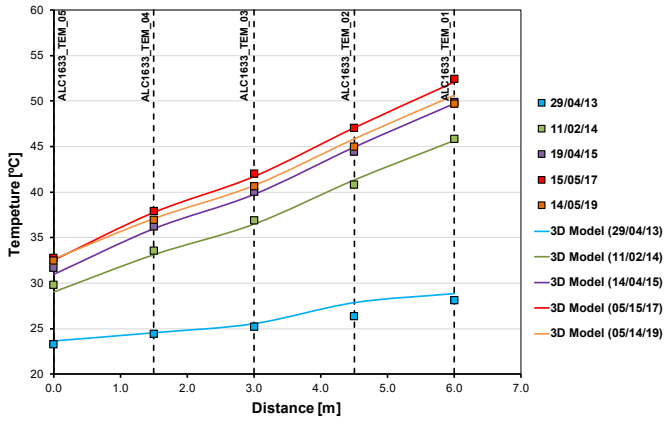

(b)

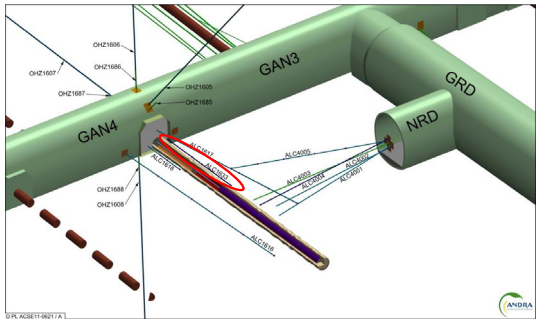

(c)

Figure A.15: Temperature a) time evolution and b) profiles at sensors along borehole ALC1633. The measurements (dots) are compared to the simulation results (lines).

Borehole ALC4003

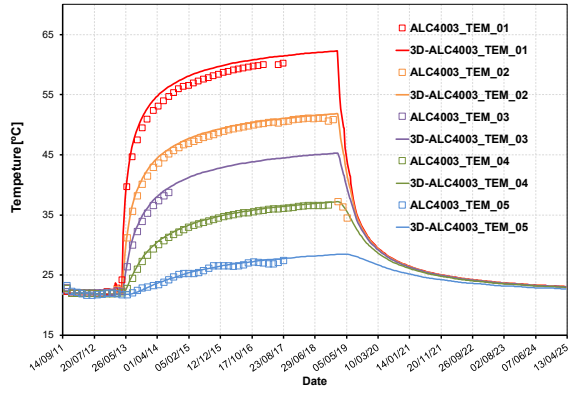

(a)

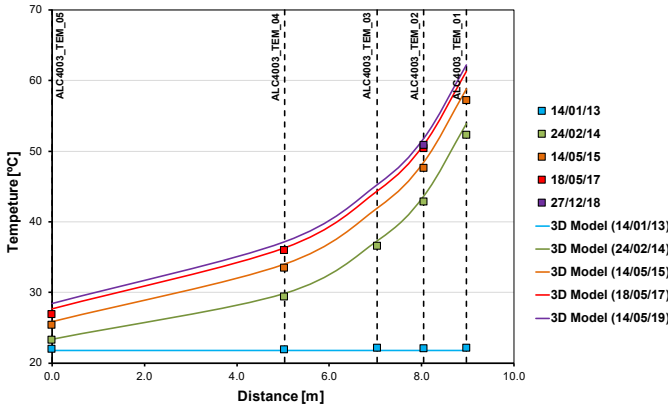

(b)

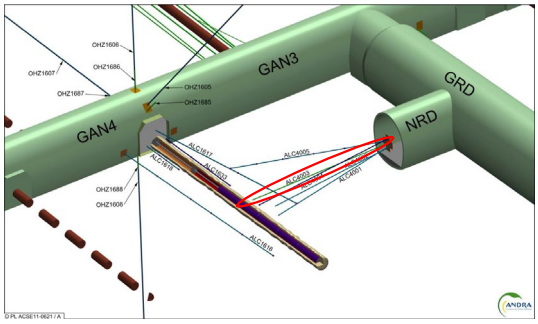

(c)

Figure A.16: Temperature a) time evolution and b) profiles at sensors along borehole ALC4003. The measurements (dots) are compared to the simulation results (lines).

Borehole ALC4005

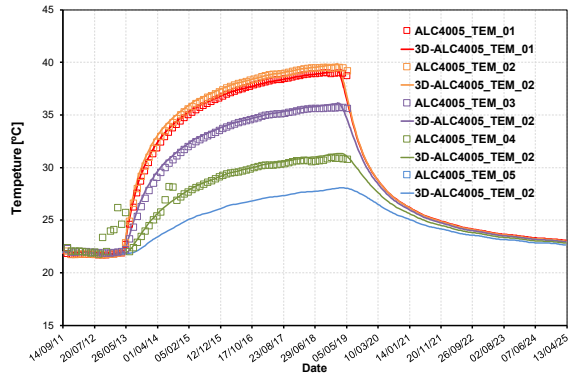

(a)

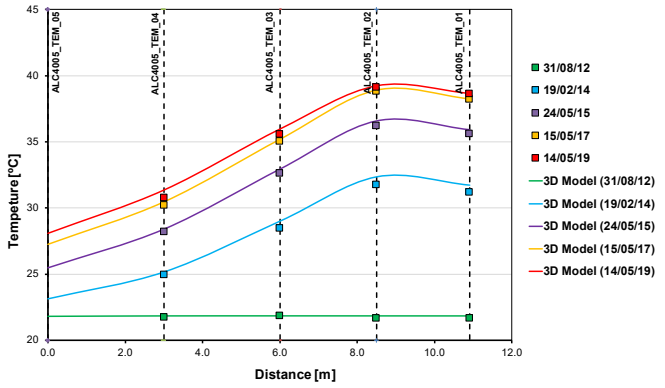

(b)

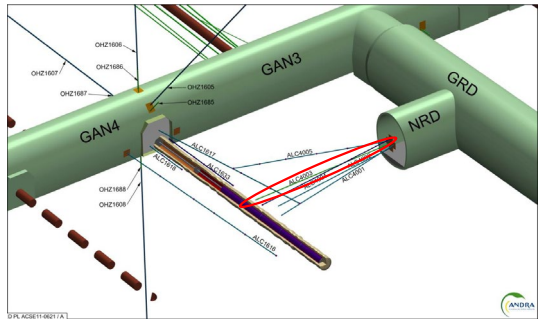

(c)

Figure A.17: Temperature a) time evolution and b) profiles at sensors along borehole ALC4005. The measurements (dots) are compared to the simulation results (lines).

Borehole ALC4001

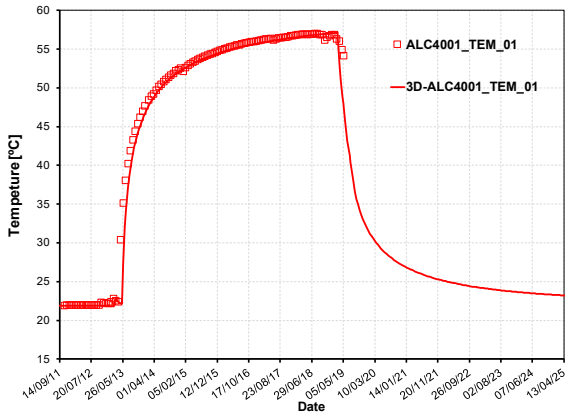

(a)

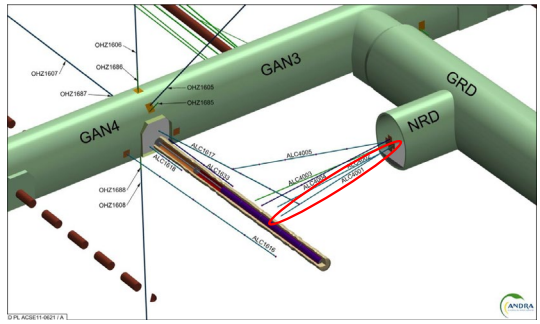

(b)

Figure A.18: Temperature a) time evolution and b) profiles at sensors along borehole ALC4001. The measurements (dots) are compared to the simulation results (lines).

A.1.3 Steel liner temperature measurement and simulations

Comparison of temperature profile (Figure A.19) on steel lining between measurement and model simulations are presented in Figure A.20 to Figure A.23.

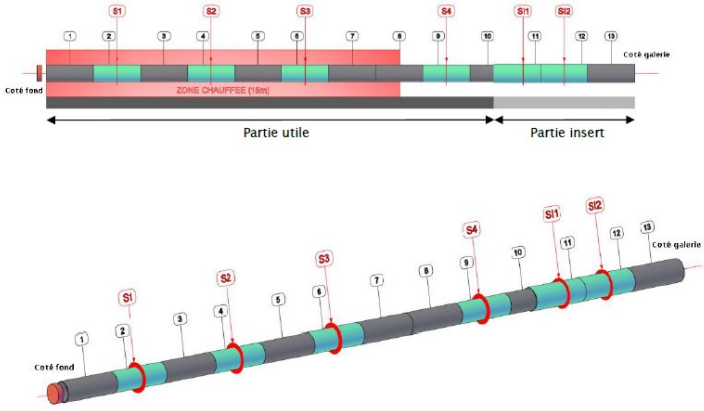

(a)

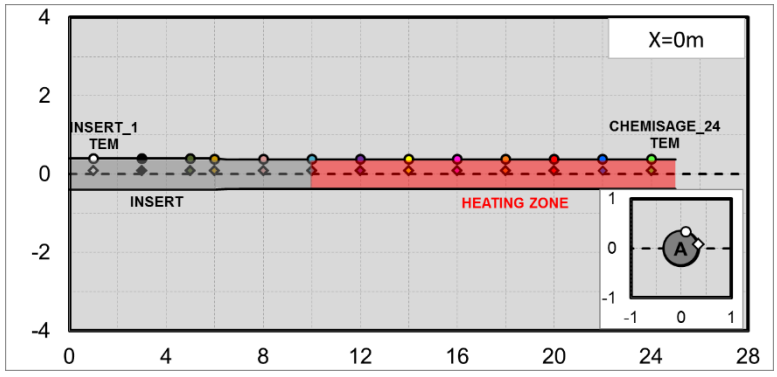

(b)

Figure A.19: Temperature sensor located at steel casings.

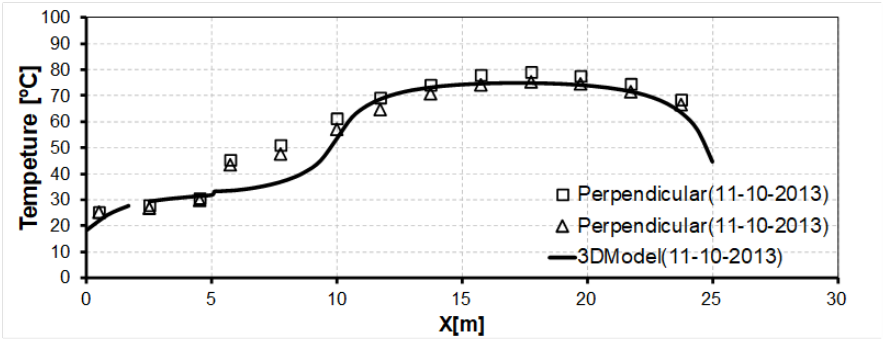

(a)

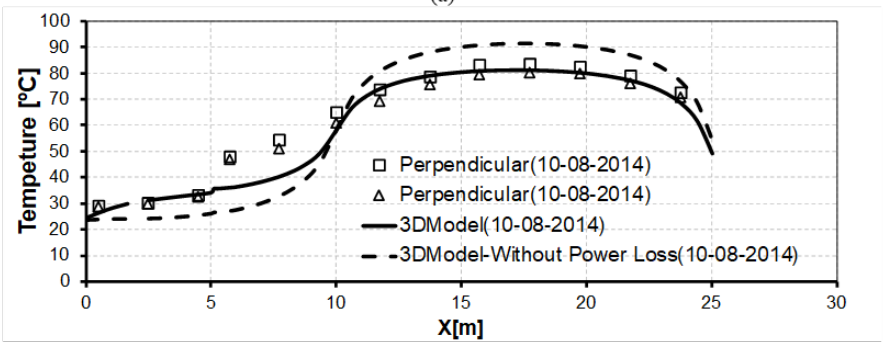

(b)

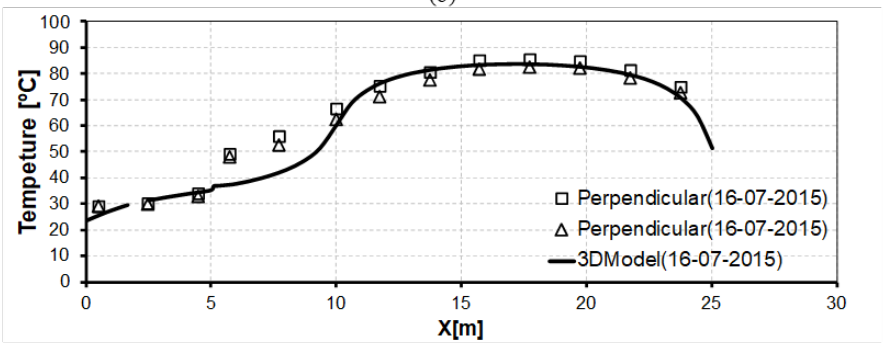

(c)

Figure A.20: Temperature profile on steel lining. The graph (b), 10 August 2014, shows the comparison with a model in which the heated zone is isolated (dot line). The measurements (dots) are compared to the simulation results (lines).

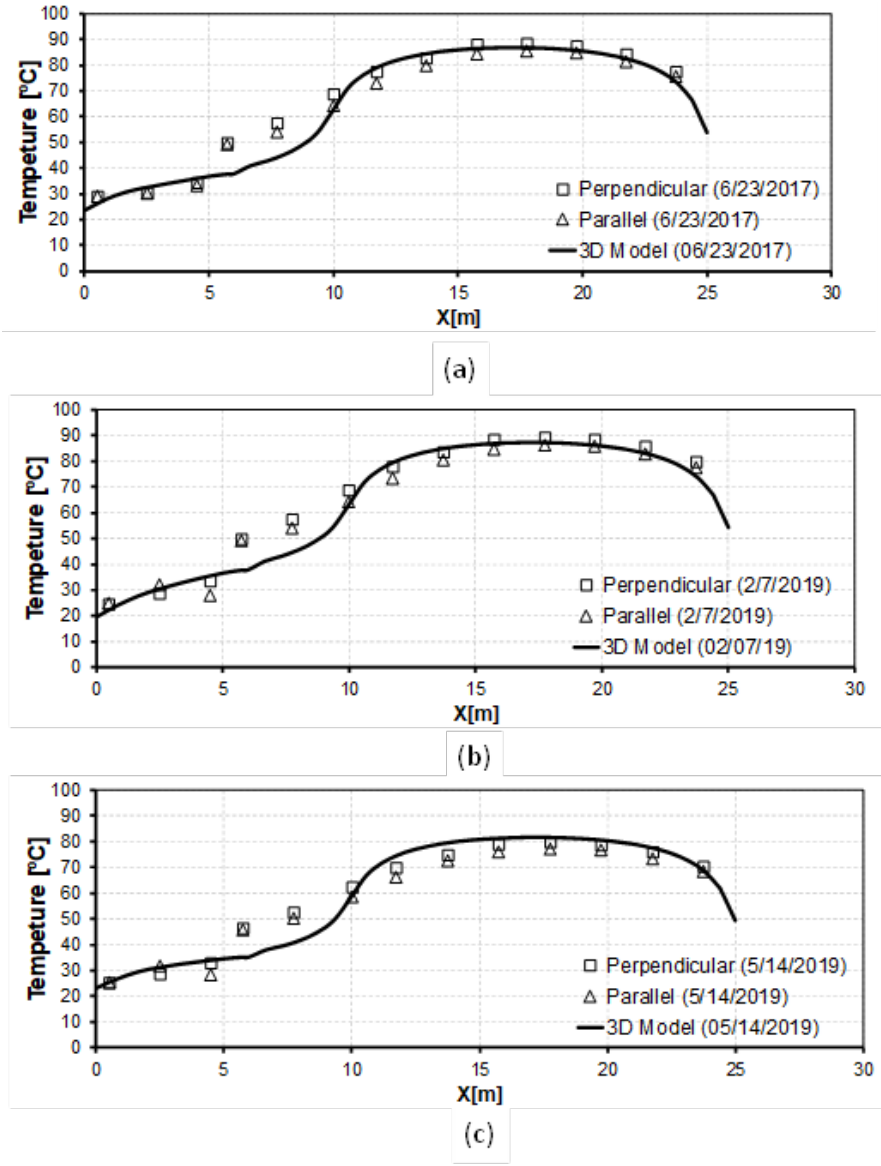

Figure A.21: Temperature profile on steel lining. The graph (b), 10 August 2014, shows the comparison with a model in which the heated zone is isolated (dot line). The measurements (dots) are compared to the simulation results (lines).

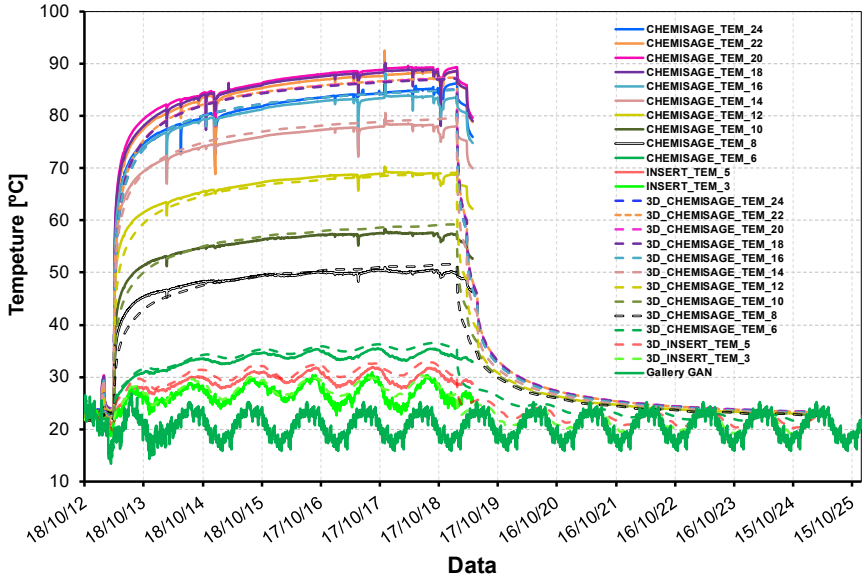

Figure A.22: Temperature evolution of the vertical sensors at steel casing. The measurements (lines) are compared to the simulation results (dotted lines).

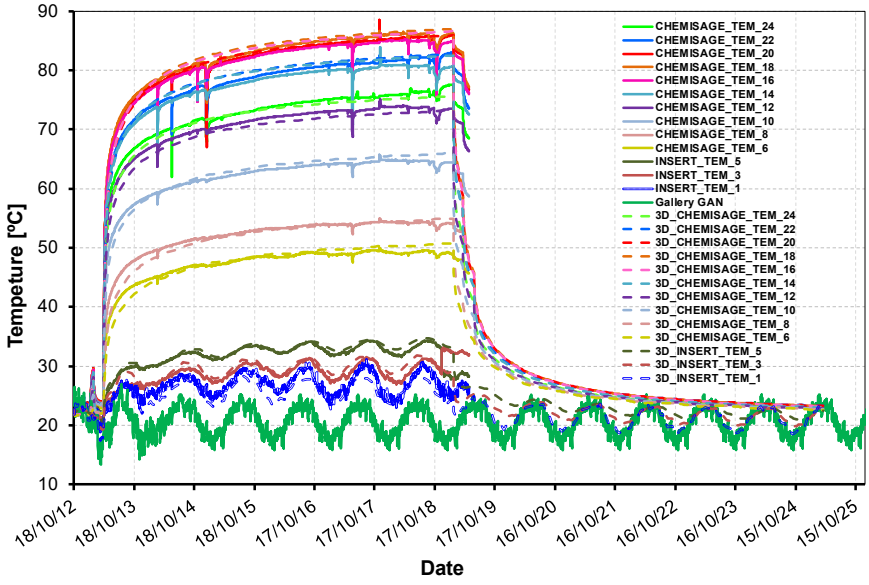

Figure A.23: Temperature evolution at the lateral sensors on steel lining. The measurements (lines) are compared to the simulation results (dotted lines).

A.1.4 Joint temperature measurement and simulations

Comparison of temperature evolution of the sensors at the gap (Figure A.24) on steel lining between measurement and model simulations are presented in Figure A.25.

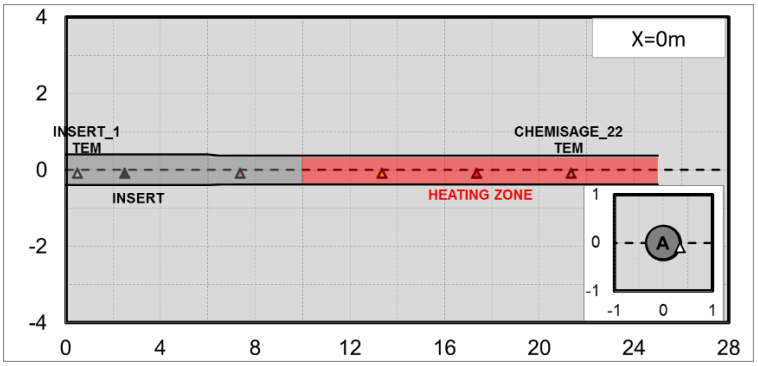

Figure A.24: Temperature sensor located at the gap between steel casings and COx claystone.

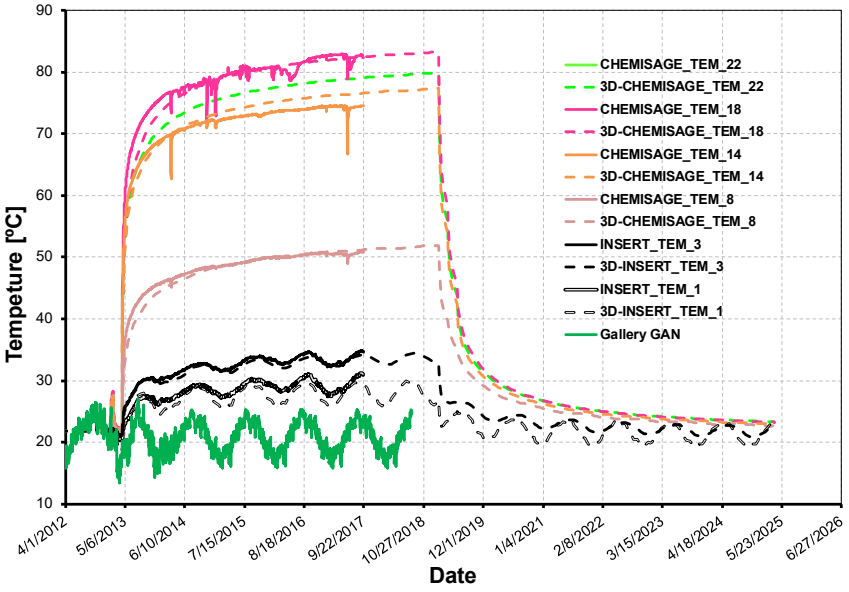

Figure A.25: Temperature evolution of the sensors at the gap. The measurements (lines) are compared to the simulation results (dotted lines).

Appendix B

Pore pressure results from the reference 3D THM analysis

B.1 COMPARISON BETWEEN SIMULATED AND MEASURED RESULTS

In this section, a comprehensive comparison between computed and measured pore pressures at all the sensors is presented to highlight the consistency of the model. Two sets of results will be output:

- Pore pressures within the sections perpendicular to the bedding planes: z = 13 m, and z = 17 m.
- Pore pressures along the boreholes lines: ALC1616 and ALC1617. Time evolutions and profiles at different times are shown.

For the sake of clarity, Figure B.1 summarizes again the location of instrumentation around ALC1604 experiment.

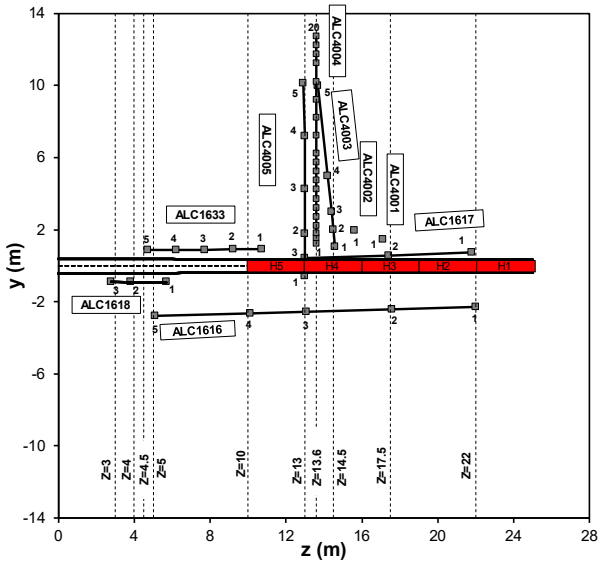

Figure B.1: Horizontal view (bedding plane) of the instrumentation boreholes and perpendicular sections.

B.1.1 Comparisons in sections perpendicular to the alveolus

Section Z=13m

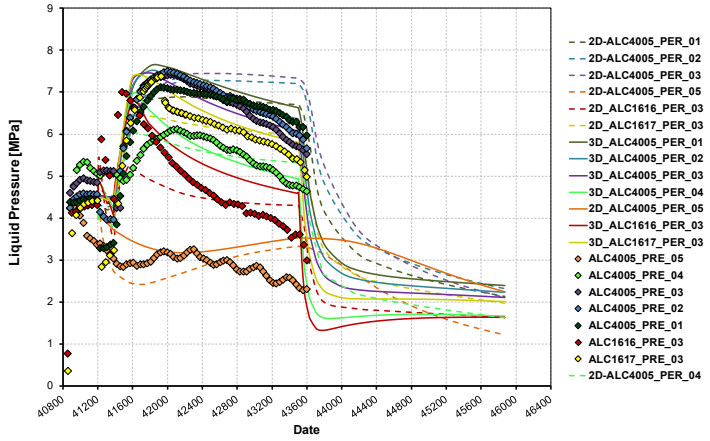

(a)

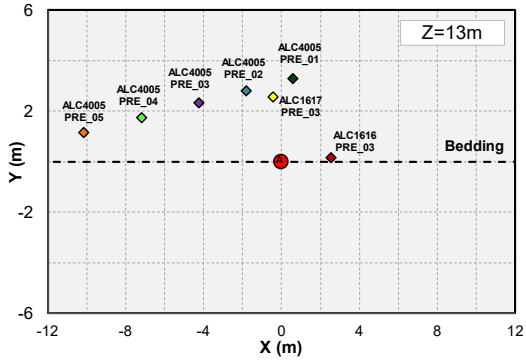

(b)

Figure B.2: (a) Pore pressure evolution of sensors located in borehole ALC4005, ALC1616 and ALC1617 in section A2 at 13m from the entrance of the tunnel. (b) Pore pressure profile of sensors located in borehole ALC1616. The measurements (lines) performed are compared to the simulation results (dots).

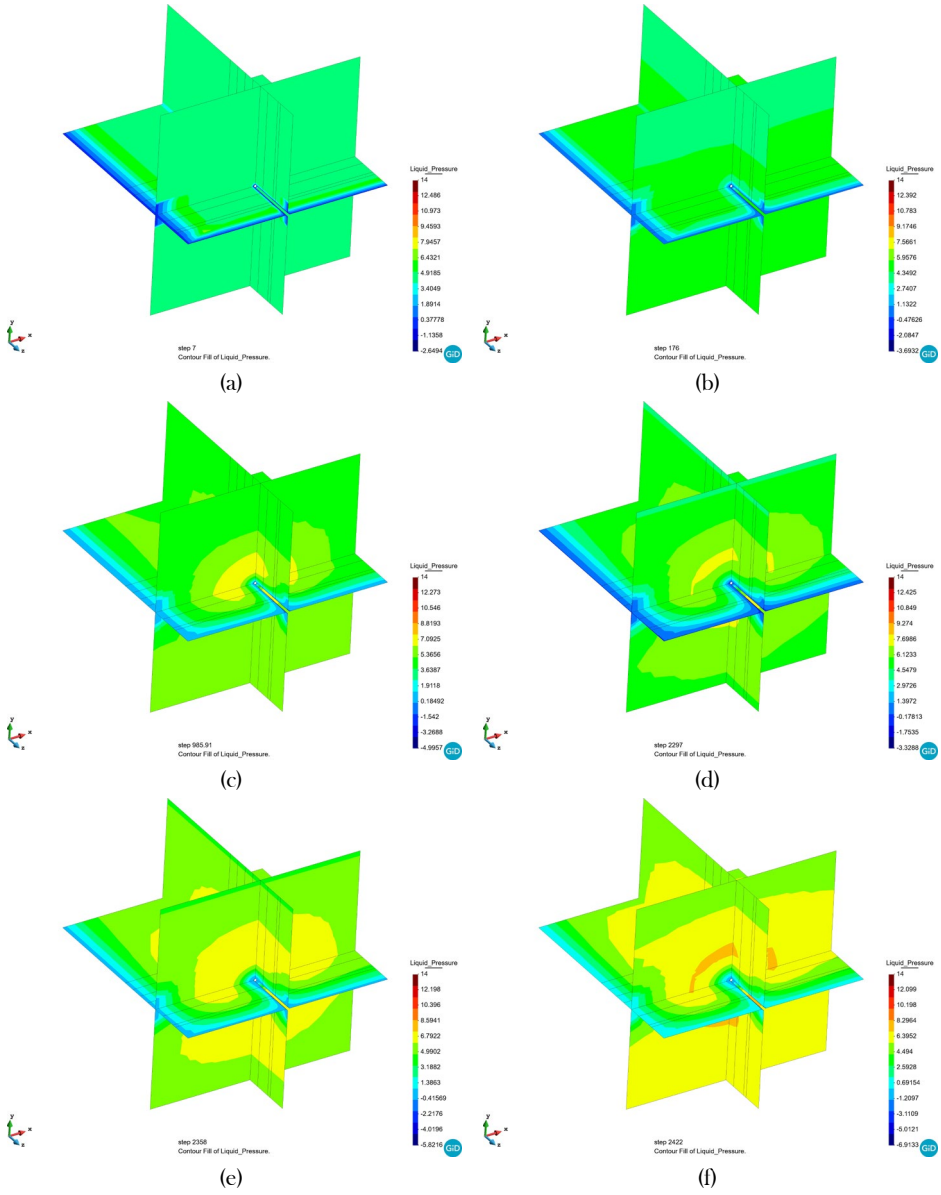

Figure B.3: Computed contours of equal pore pressure increase (MPa) at various times.

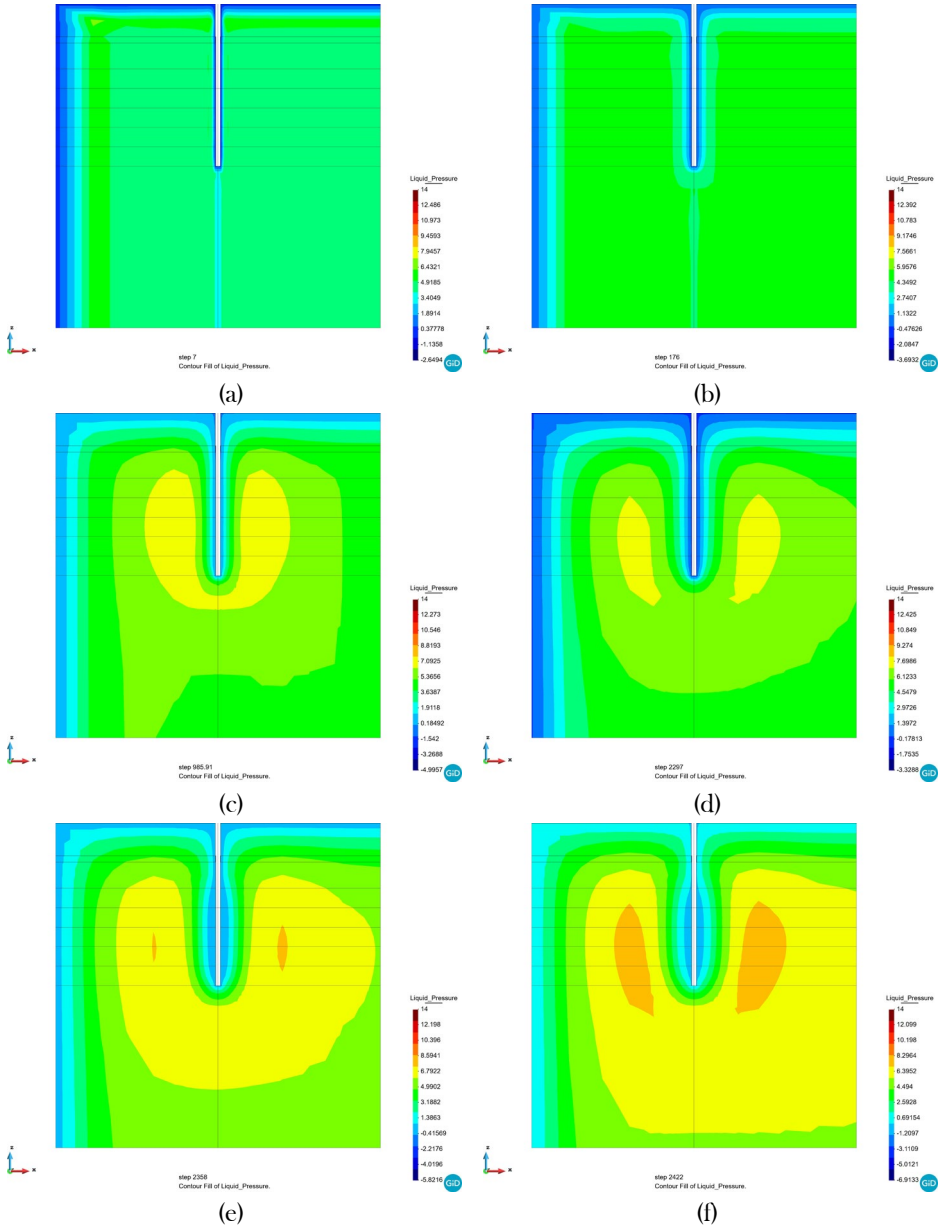

Figure B.4: Computed contours of equal pore pressure increase (MPa) in cross-section z=13m at various times (xz plane).

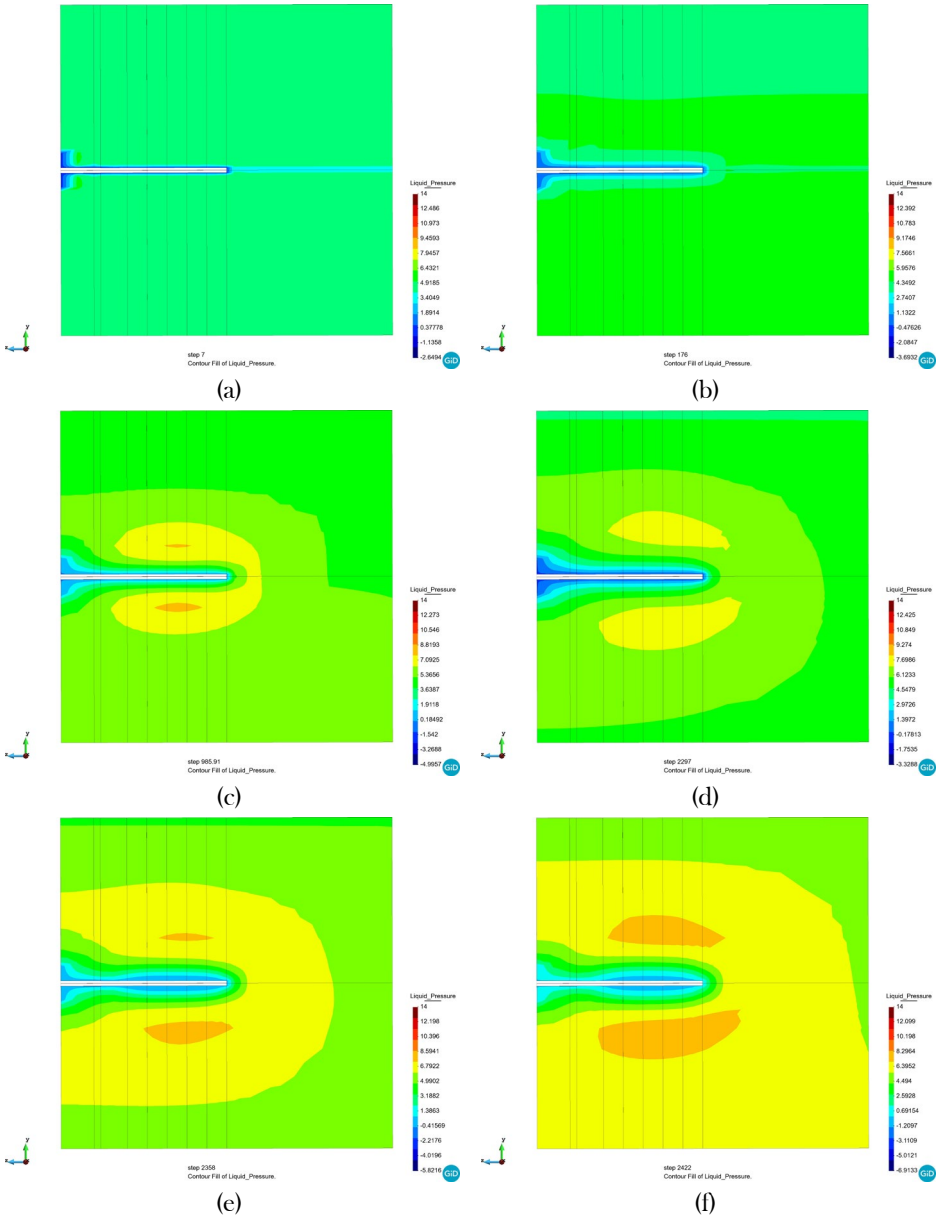

Figure B.5: Computed contours of equal pore pressure increase (MPa) in cross-section z=13m at various times (zy plane).

Section Z=17.5m

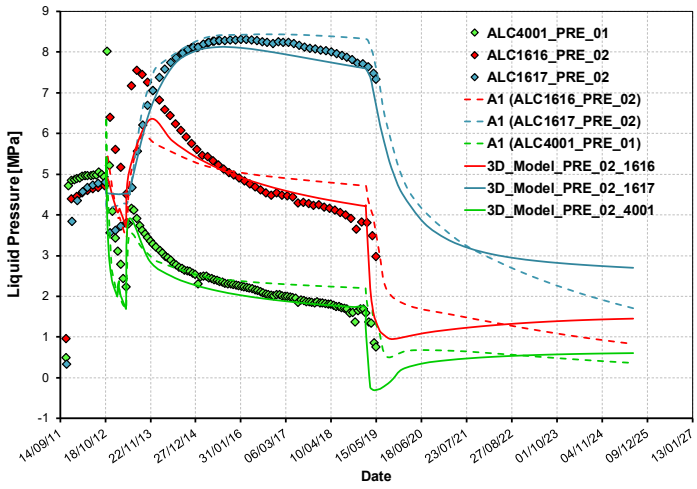

(a)

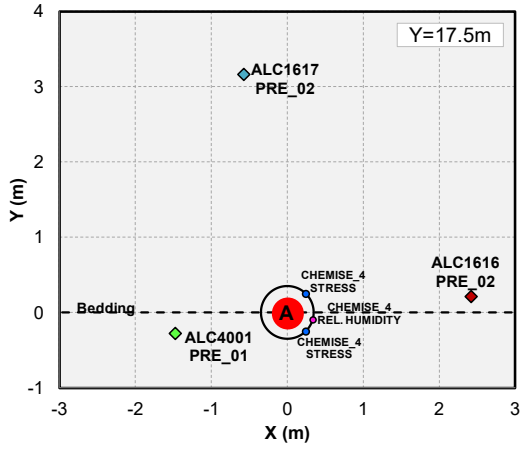

(b)

Figure B.6: (a) Pore pressure evolution of sensors located in borehole ALC1616, ALC1617 and ALC4001 in section A1 at 17.5m from the entrance of the tunnel. (From instrumentation emplacement to end of six years cooling).) The measurements (lines) performed are compared to the simulation results (dots).

Borehole ALC1616

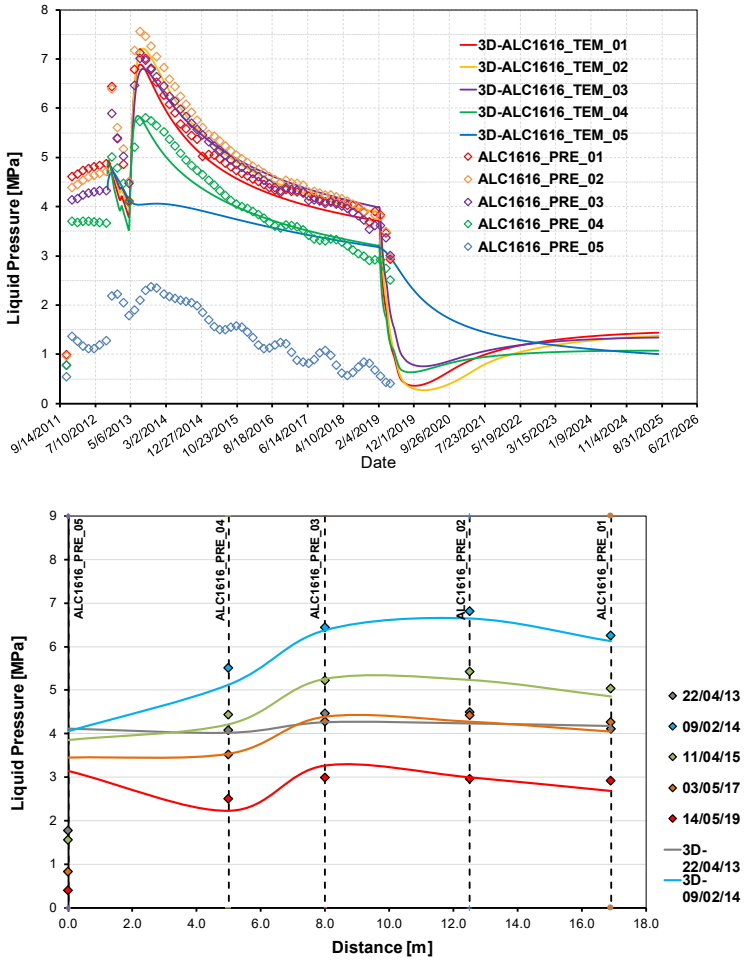

Figure B.7: (a) Pore pressure evolution of sensors located in borehole ALC1616. (b) Pore pressure profile of sensors located in borehole ALC1616. The measurements (lines) performed are compared to the simulation results (dots).

Borehole ALC1617

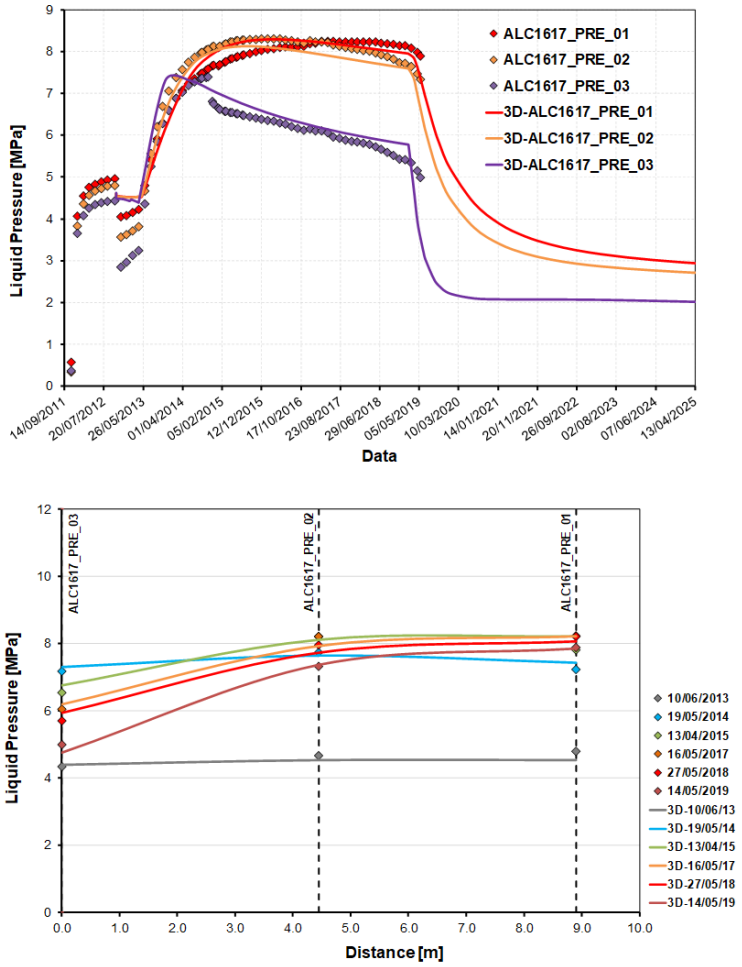

Figure B.8: (a) Pore pressure evolution of sensors located in borehole ALC1617. (b) Pore pressure profile of sensors located in borehole ALC1617. The measurements (lines) performed are compared to the simulation results (dots).

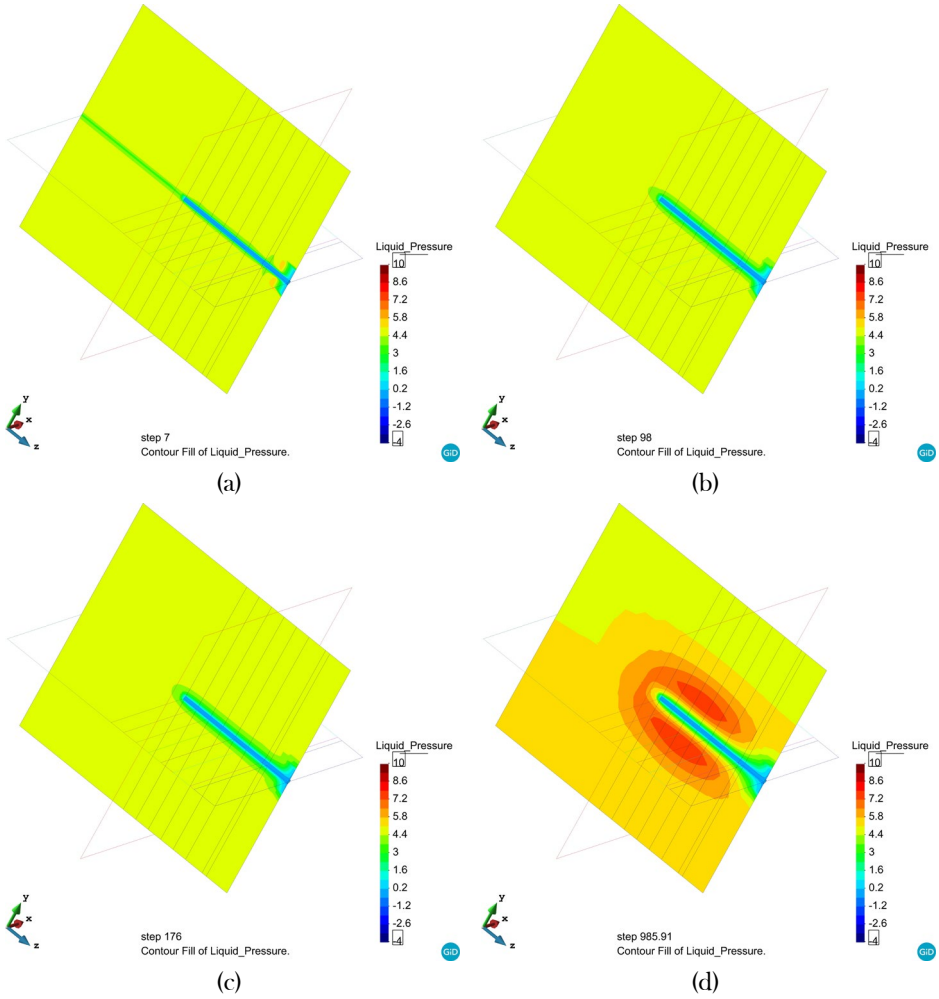

Figure B.9: Computed contours of equal pore pressure increase (MPa) for: (a) 7 days (After excavation); (b) 98 days; (c) 176 days (end of heating test); (d) 985 days (2 years heating) in section ZY.

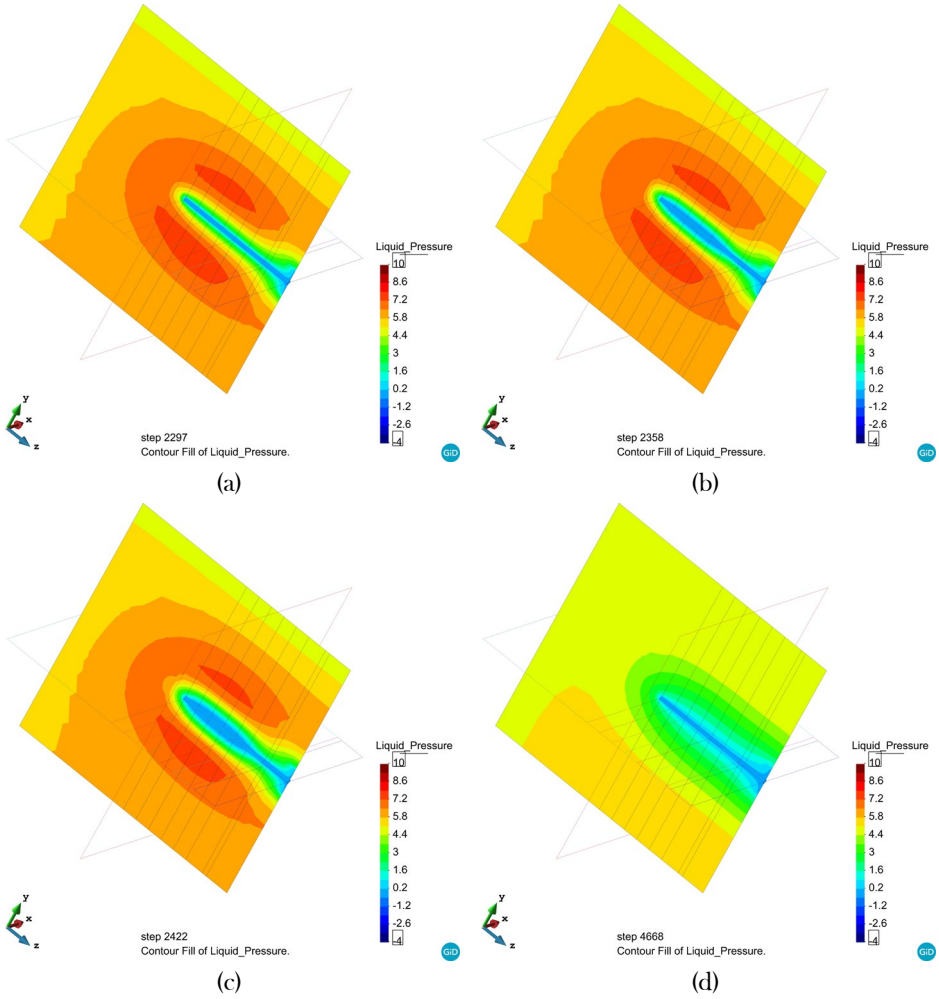

Figure B.10: Computed contours of equal pore pressure increase (MPa) for (a) 2297 days (End of heating); (b) 2358 days (End of first cooling phase); (c) 2422 days (End of second cooling phase); (d) 4668 days (6 years cooling) in section ZY.

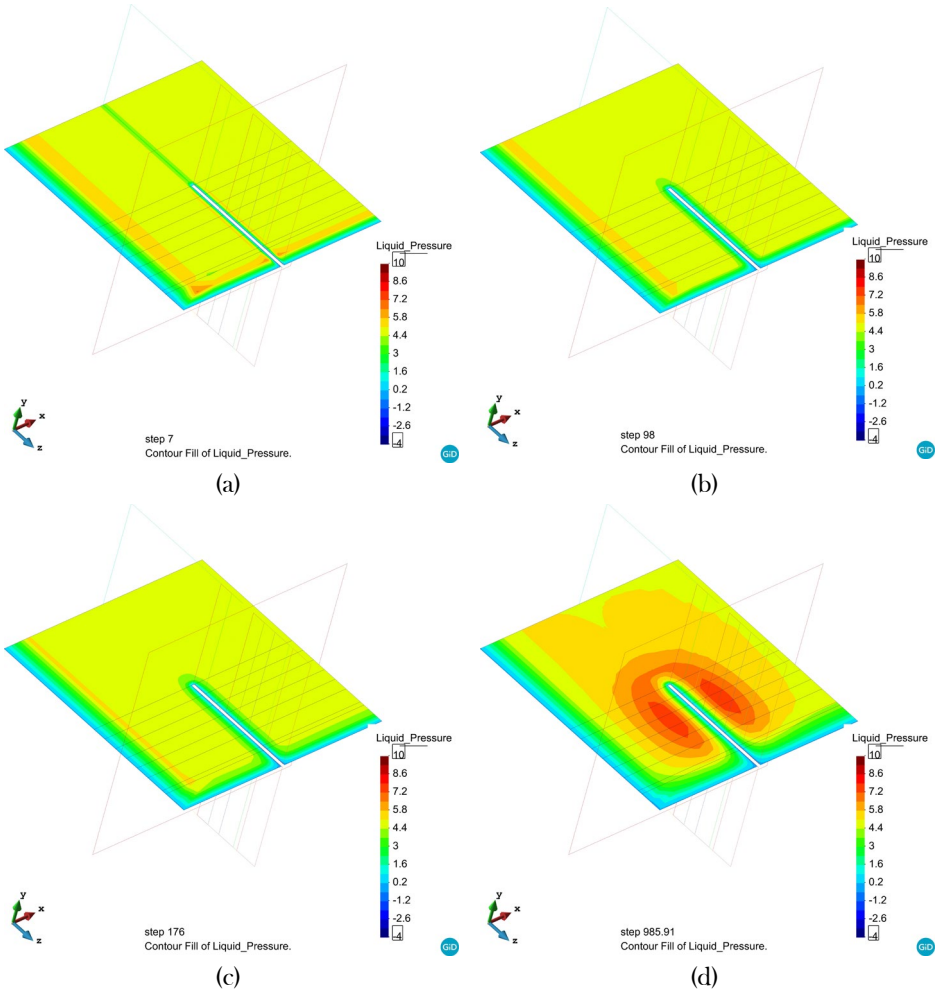

Figure B.11: Computed contours of equal pore pressure increase (MPa) for: (a) 7 days (After excavation); (b) 98 days; (c) 176 days (end of heating test); (d) 985 days (2 years heating) in section XZ.

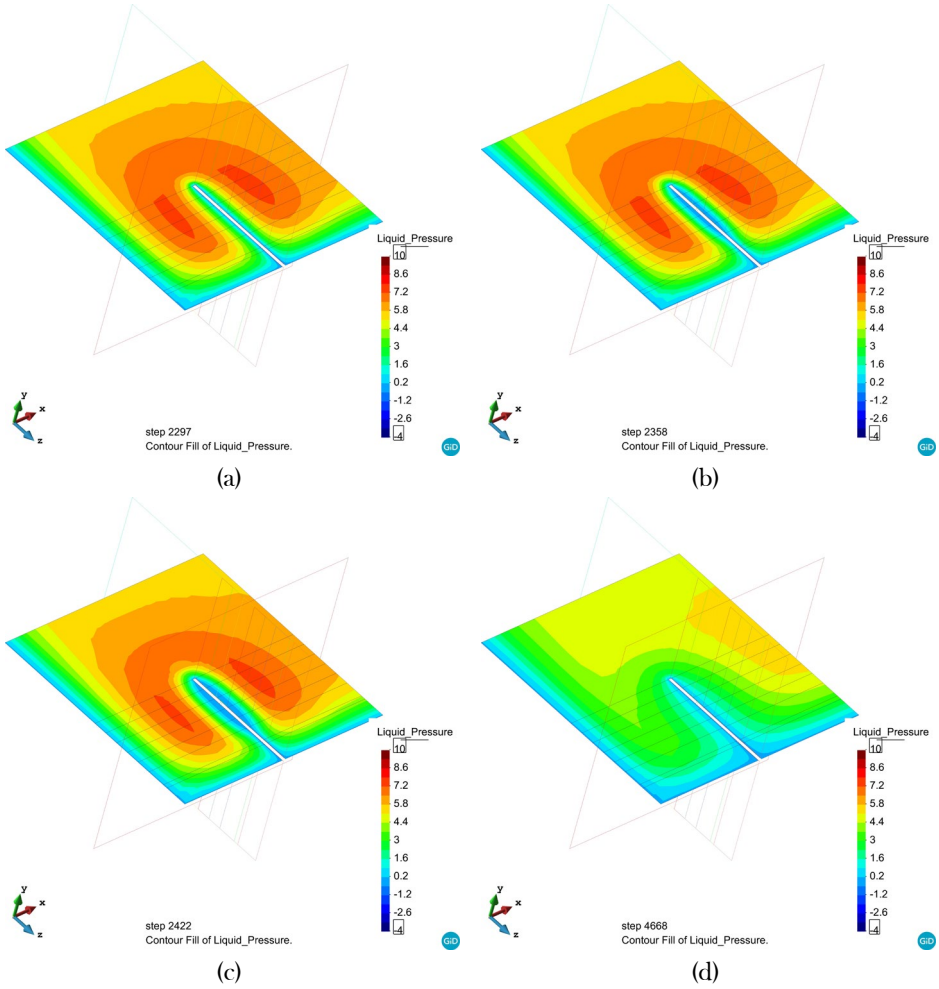

Figure B.12: Computed contours of equal pore pressure increase (MPa) for (a) 2297 days (End of heating); (b) 2358 days (End of first cooling phase); (c) 2422 days (End of second cooling phase); (d) 4668 days (6 years cooling) in section ZY.

Appendix C

Thermal pressurization effect on the shaft bearing capacity of energy piles

C.1 INTRODUCTION

One of the vital issues of the 21st century is managing energy resources. As the global population trend rises and living standards improve, primary energy consumption continues to evolve. Although no short-term energy exhaustion is expected, the environmental effects of the overuse of natural energy resources may well be troublesome. The greenhouse effect, associated with the obvious rise in carbon dioxide, remains perhaps the most acute of the issues.

This research considers a new sustainable technology for the intermittent energy storage in heat exchanger piles. Heat exchanger piles use the soil as an energy storage system. The heat exchange system consists of absorbing and transporting thermal energy from soil to buildings through fluid that circulates in the pipes within the piles; in other words, geothermal piles are used to exchange heat from the ground for heating and cooling of superstructures. During their cooling mode, circulating liquid temperature is higher than soil temperature, thereby increasing the latter's temperature. Under normal operating conditions, the fluid might be up to 30 ° C, although higher temperatures have been reported.

The Swiss Federal Institute of Technology in Lausanne (EPFL) conducted an in-situ test of a heat exchangers pile under actual conditions. Some of the significant results of the study were used to evaluate the usability of a thermo-hydro-mechanical final component system to simulate thermal soil-structure interactions. This allows the use of the numerical approach for the evaluation of the optimum soil energy storage system design, the specification of typical design parameters and the creation, for design purposes, of a standard calculation method and validation criteria.

C.2 THE PILE FOUNDATION AND SITE

For an in-situ test of a heat exchanger pile a four-story building was selected at the EPFL (Switzerland). The building is 100 m in length and 30 m in width (Figure C-1a) and is founded on 97 piles approximately 25 m in length. The tested pile was located at the side of the building. The drilled pile diameter was 88 cm and the length was 25.8 m: The schematic soil stratigraphy profile is presented in Figure C-1b and described in Table C-1 (adapted from Rotta Loria and Laloui., 2017).

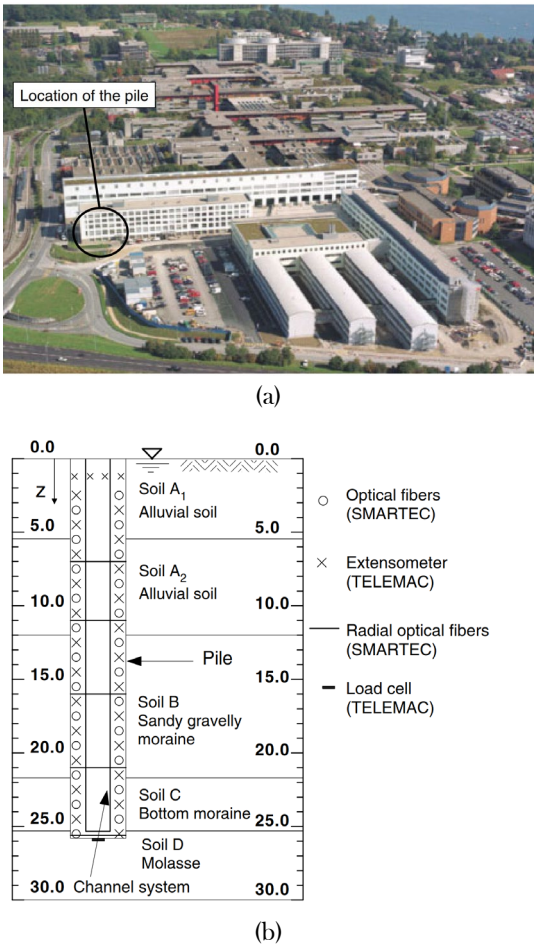

Figure C-1. View of the test site in Lausanne (Switzerland), the soil profile and the instrumentation of the tested pile.

This soil profile was obtained on the basis of various geotechnical investigations and two static pile tests. The values of the ultimate shaft friction q_s and the tip

capacity q_p are given in Table I. The groundwater table in this zone is very close to the ground surface.

Table C-1. Material properties used for the numerical modelling (modified after Rotta Loria and Laloui., 2017)

Soil layers	Young's modulus, E: MPa	Poisson ratio, ν	Porosity, n	Density of solid particles, ρ.: kg/m3	Specific heat of solid particles, cp,s: J/(kg °C)	Thermal conductivity of solid particles, λ.: W/ (m °C)	Linear thermal expansion coefficient, α: 1/°C
A	190	0.22	0.1	2769	880	1.49	3.3×10^{-6}
B	84	0.4	0.35	2735	890	3.68	3.3×10^{-6}
C	90	0.4	0.3	2740	890	3.46	3.3×10^{-6}
D	3000	0.3	0.1	2167	923	3.82	2.3×10^{-5}
Reinforced concrete piles and slab							
Piles	28000	0.25	0.1	2722	837	1.628	1×10^{-5}
Slab	35000	0.25	0.1	2722	837	1.628	1×10^{-5}

C.3 LOADING HISTORY

The pile was subjected to two types of test loading: mechanical and thermal (Figure C-2). The mechanical load is caused by the dead weight of the building under construction; the thermal load is induced by a heating device controlling the water temperature in the PE tubes installed in the pile. The two types of loads were applied separately and alternately in order to decouple the thermal and mechanical effects. Thus, at the end of the construction of each storey, a thermal loading cycle was applied to the pile (see Figure C-2 for the complete loading history). In addition to the measurements made during the casting of the pile (Test 0), seven tests were carried out. The maximum mechanical load on the pile head was about 1300 kN.

Test 1 differs from the others as the pile had a free displacement boundary condition at the head. For the other tests, the pile was constrained in its movement by the applied load due to the incremental addition of the storeys under construction. In addition, the thermal loads were on the order of ΔT=21°C in Test 1, while they were 15°C for the others (values usually encountered in heat exchanger piles). The measurements in Test 8 were made at the natural temperature of the ground.

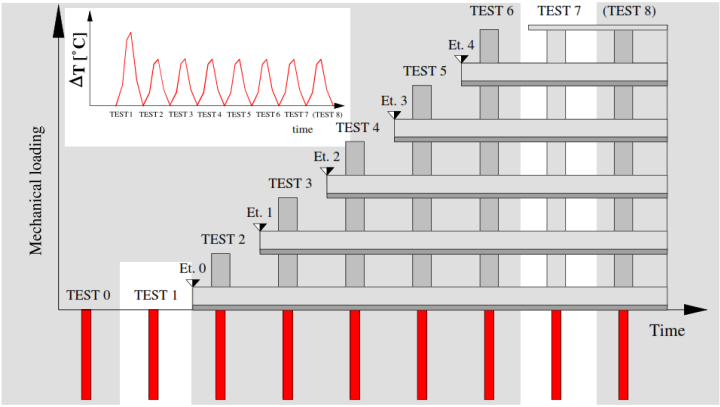

Figure C-2. Thermo-mechanical loading history.

C.4 THEORETICAL AND NUMERICAL MODEL

In order to examine the in situ observed behaviour, a series of numerical analyses have been performed. In particular, a coupled thermo-hydraulic-mechanical theoretical formulation solved by a coupled finite element algorithm has been utilised (particular case of the general formulation presented in Olivella et al., 1994). Full details of the theoretical formulation and the numerical solution have been presented in detail elsewhere (Gens et al., 2007).

In particular, the elastoplastic constitutive presented by Mánica et al., (2016) has been used. The model developed within the framework of elastoplasticity that includes a number of features that are relevant for a satisfactory description of their hydromechanical behaviour: anisotropy of strength and stiffness, behaviour nonlinearity and occurrence of plastic strains prior to peak strength, significant softening after the peak, time-dependent creep deformations and permeability increase due to damage. Both saturated and unsaturated conditions are envisaged.

C.5 FEATURES OF ANALYSIS AND MATERIAL PROPERTIES

The test pile was part of a pile group interacting statically but the only one to be heated. It will therefore be treated as a single pile for the sake of simplicity. It appears however useful to consider this analysis, which is similar to but less complex than the full analysis of the whole group of surrounding piles. As the considered pile was circular in cross section and installed vertically in the ground, which has a horizontal lithology and horizontal water table, an axisymmetric geometry was

adopted. The mesh takes into account a heat exchanger pile with a radius of 0.5 m (instead of 0.44 m as in the experiment) and a length of 26 m; as well as the five soil layers. The bottom of the mesh is located at a depth of 52 m (Figure C-3). The elements (168 in total) are quadratic for displacements and bi-linear for pore water pressures and temperatures.

The contact between pile shaft and soil is considered as perfectly rough. This implies that the finite element nodes of the pile and the soil are constrained by no relative movement. The material behaviour of the contact area was simulated by the material behaviour of the soil. To overcome the problems that can rise at this interface, a refined finite element mesh was used at that location.

C.5.1 Features of analysis

The material parameters are summarized in Table C-1. The soil is represented by five layers represented by the generalized Mohr–Coulomb model. The pile itself is modelled as a thermo-elastoplastic material. The mechanical parameters were determined from triaxial tests at three confining pressures for each soil layer (Fromentin et al. 1999). The pile is considered impervious, as is the soil layer D (molassic formation) while the other soil layers are considered drained.

The horizontal permeability coefficients were determined from in situ measurements and isotropic permeability was further assumed. The thermal parameters; were estimated based on the geotechnical characteristics while the porosity was determined from collected samples for each layer. In order to interpret the patterns of observed behaviour, a series of finite element simulation have been performed. The models were performed to incorporate thermal, thermomechanical and THM evolution of test during a heating–cooling cycle.

C.5.2 Initial and boundary conditions

The mechanical boundary conditions are shown in Figure C-3. Restrictions are applied to both vertical and horizontal displacements on the base of the mesh and to horizontal displacements on the sides. The initial stress due to gravity in the pile, as well as in the soil layers, is calculated assuming saturated bulk unit weights and a coefficient of earth pressure at rest K_0=1.

The hydraulic boundary conditions result from assuming the pile as impervious, allowing the drainage of the soil layers to take place at the top surface as well as on the right-hand side of the mesh. Undrained conditions are applied along the axis of symmetry and for the layer D. The initial pore water pressure corresponds to the hydrostatic profile with a water table located at the top surface.

The thermal boundary conditions consist in allowing the heat to flow through the right-hand side of the mesh as well as through the bottom of the mesh. Constant temperatures are imposed on the top surface of the mesh and the heat flux is assumed to be null along the axis of symmetry.

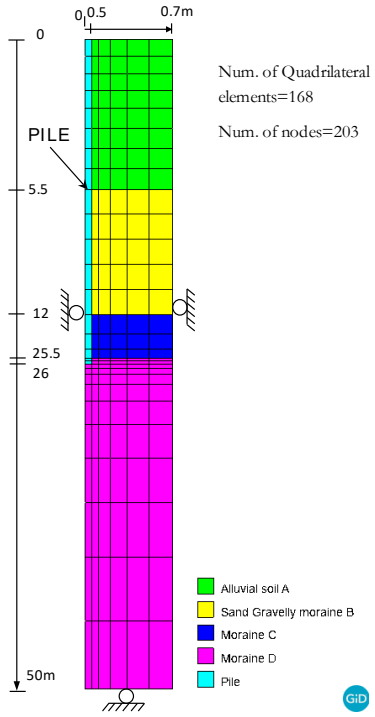

Figure C-3. Finite element mesh and mechanical boundary conditions.

C.6 TEST OBSERVATION AND INTERPRETATION

In this section, the thermo-hydro-mechanical finite element results are presented and compared with the experimental ones. The behaviour of the concrete pile is considered first and then that of the soil layers.

C.6.1 Thermal behaviour

To analyse the thermal behaviour of the pile, Test 1 is considered (Figure C-2). In this test, a heating–cooling cycle was imposed (12 days of heating then 16 days of cooling). Two types of thermal boundary conditions were applied:

- constant temperature at the top surface;

- imposed incremental temperatures in the concrete pile. The values are determined from the measured ones (Figure C-7a). Time variation of the thermal load is shown in Figure C-7b.

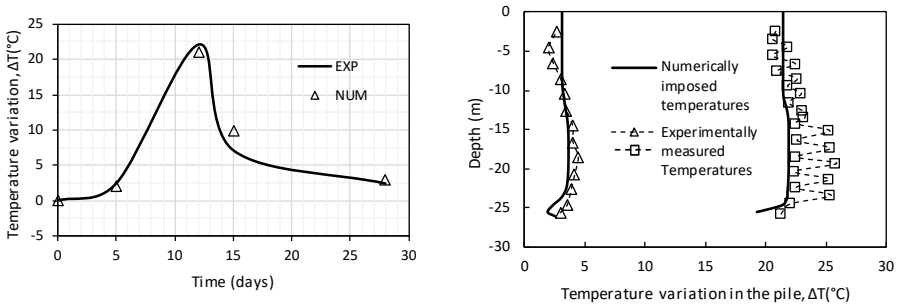

(a) (b)

Figure C-4. Temperature values imposed in the pile.

Figure C-5 shows the temperature field after the heating period. It should be noted that due to the thermal characteristics of the molasse layer, thermal diffusion is mainly horizontal. As a result, the part of the mesh affected by the applied loads is limited to the depth of the pile. Some of the next results will be thus presented only for the upper portion of the mesh.

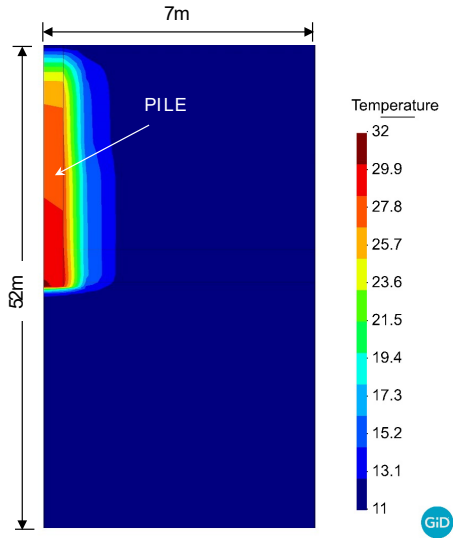

Figure C-5. Computed contours of temperature at the end of the heating period.

C.6.2 Thermal effect on the mechanical behaviour of the pile

Thermal strains

In Test 1 (Figure C-2), only the thermal heating–cooling cycle was applied to the pile. No mechanical load was imposed at the pile top and the pile was free to move upwards. The imposed thermal field generated strains in the pile. Figure C-9a compares the simulated thermo-elastic vertical strains compared to the measured ones for the heating and cooling periods. Strains are not uniform during the heating period and are influenced by the friction along the pile shaft.

Thermo-elastic linear behaviour is observed and computed during the cooling phase. This reversibility means that the stress level induced by the displacement of the pile with respect to the soil has not yet reached the threshold where the friction would no longer permit the pile to return to its initial state. The modelled radial strains fit the measured ones well, as may be seen for one of them (at depth of 16 m) in Figure C-9b. The radial strain behaviour shows that lateral contact is still maintained between the pile and the ground after a thermal cycle. It should be noted that because the final temperature values are different from the initial ones, the strains do not return to zero at the end of the heating–cooling cycle.

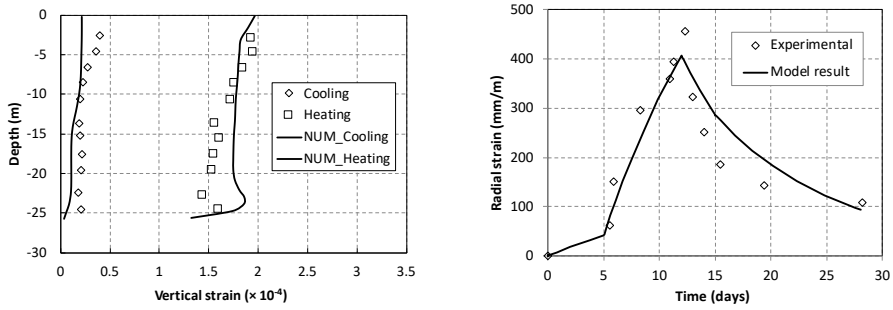

Figure C-6. Thermal strains during a heating and cooling period.

Pile uplift

Test 1 enabled the measurement of the maximum uplift produced by a temperature increase of 21°C. Values obtained by precision levelling (extensometers and the optical fibres) compared well with the numerical results (Figure C-7,8).

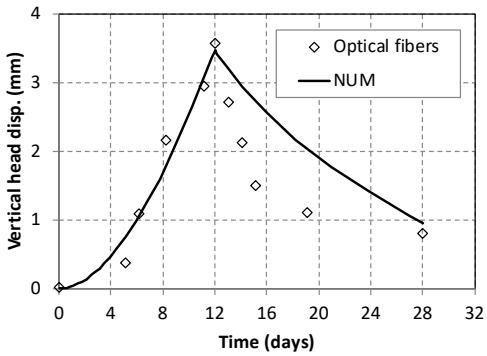

Figure C-7. Thermal pile uplift during a heating–cooling cycle.

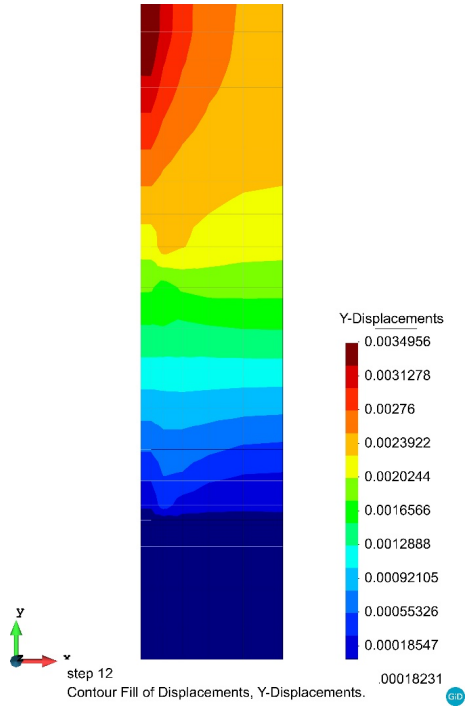

Figure C-8. Computed contours of displacement at the end of the heating period.

Induced thermal stresses

Under the effect of a temperature increase, a pile with free boundary conditions dilates. In the case where it is not entirely free to move (e.g. due to side friction or blocked head and toe), part or all of the deformation will be prevented. The constrained strains produce thermal stresses.

Figure C-12a shows a comparison between measured and simulated variations in vertical stresses corresponding to Test 1 at a temperature difference of 13.4 °C. Different stress levels result from different types of the surrounding soil, and the layer boundaries (A, B, C and D) may be identified in Figure C-12a. The model is able to reproduce this effect. Figure C-12b presents the vertical effective stresses during the heating–cooling cycle. The difference in properties of layers B and C clearly are reflected in the thermal response.

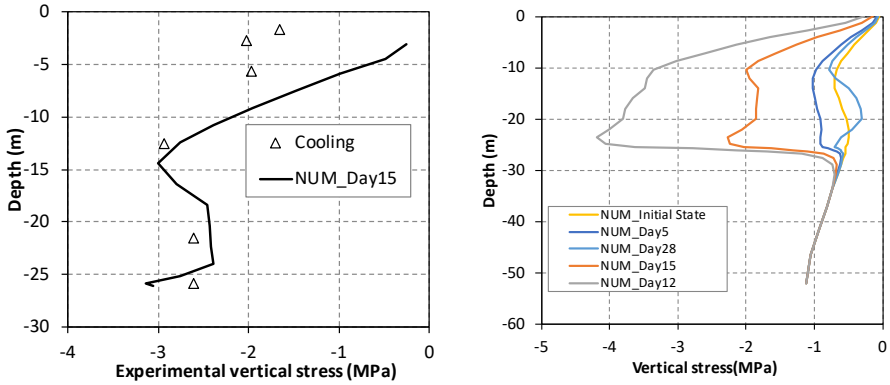

(a) (b)

Figure C-9. Thermal vertical stresses: (a) under a thermal load of 13:48C; and (b) during a heating–cooling cycle.

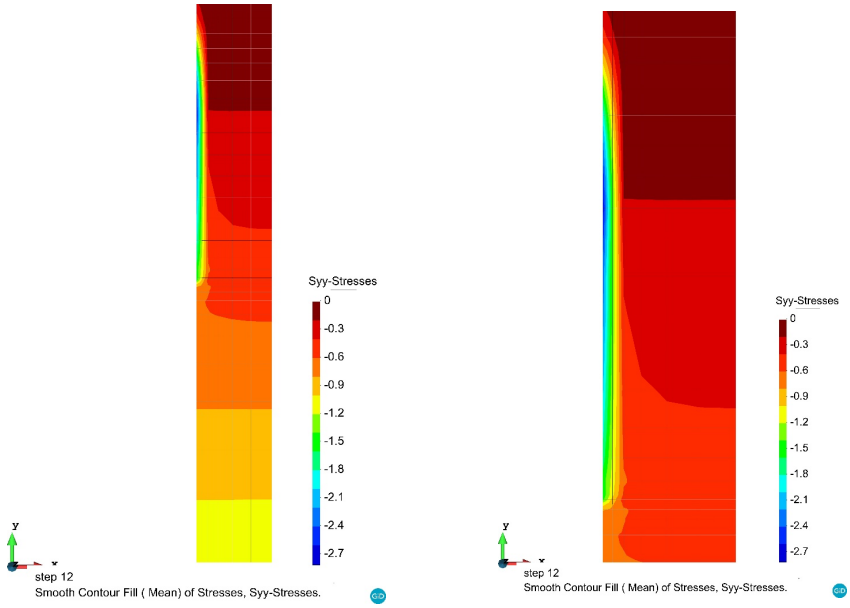

(a) (b)

Figure C-10. Computed contours of stress (σ_{yy}) at the end of the heating period.

C.6.3 Thermo-mechanical behaviour of the pile

As an example of the thermo-mechanical behaviour of the pile, Test 7 (Figure C-2) will now be considered. The experimental results clearly show the differences between the response to the mechanical and thermal loading (Figure C-14a). Even though the mechanical vertical stress is large at the pile top and diminishes with depth, the thermal load is larger and rather uniform. The experimental data show an overstress on the order of 1.2 MPa at the pile head and strongly solicits the toe (2 MPa). Data from Tests 5 and 6 indicate that a temperature increment of 1°C results in an additional temperature-induced vertical force on the order of 100 kN. As a consequence, the total axial load in the pile is twice as large as the one due to purely mechanical loading, with a large solicitation of the toe.

The mechanical loading is modelled by applying increments of vertical stress to the top of the pile. The thermal loading is imposed in the pile as discussed previously. The model is able to reproduce the decrease in the mechanical vertical stresses with depth as well as the increase in the thermally-induced vertical stresses with depth (Figure C-14(b)).

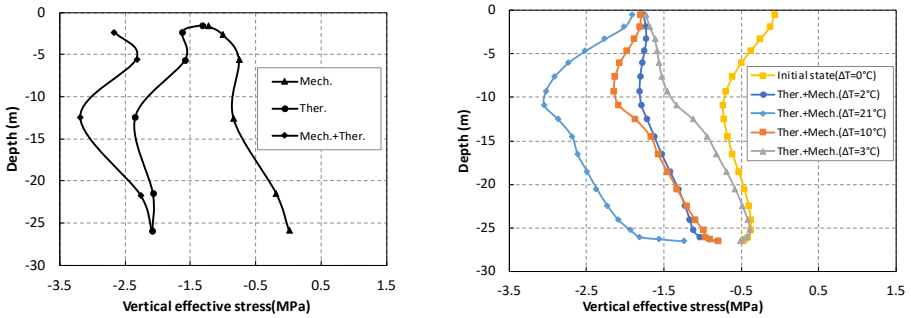

(a) (b)

Figure C-11. Thermal vertical stresses: (a) under a thermal load of 13:48C; and (b) during a heating–cooling cycle.

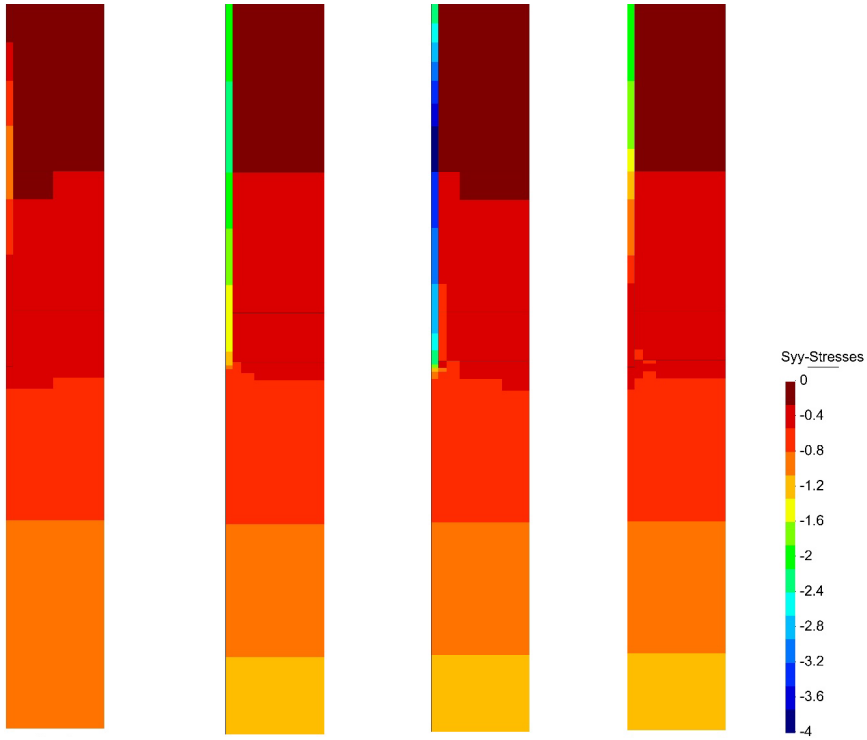

Figure C-12. Computed contours of stress (σ_{yy}) for: (a) 5 days (b) 12 days (c)15 days (d) 28 days.

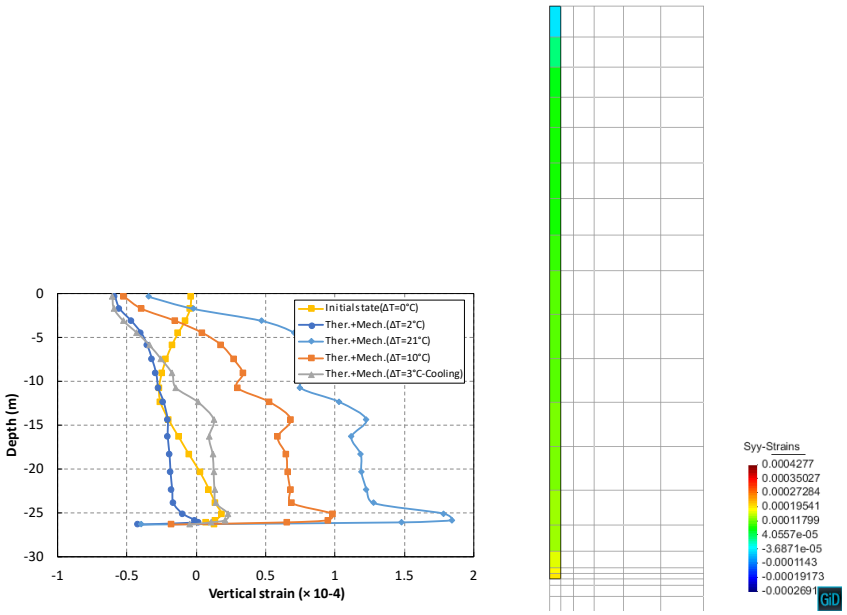

Figure C-13. (a) Thermo-mechanical vertical strains in the pile at various times (b) Computed contours of strain at the end of the heating period.

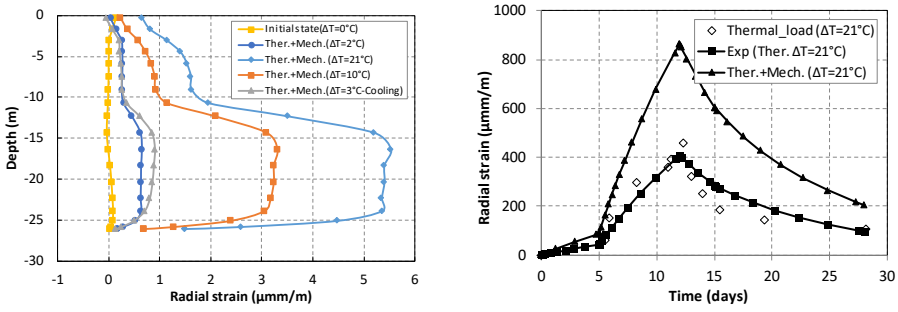

Figure C-14. Thermo-mechanical radial strain in the pile for various times.

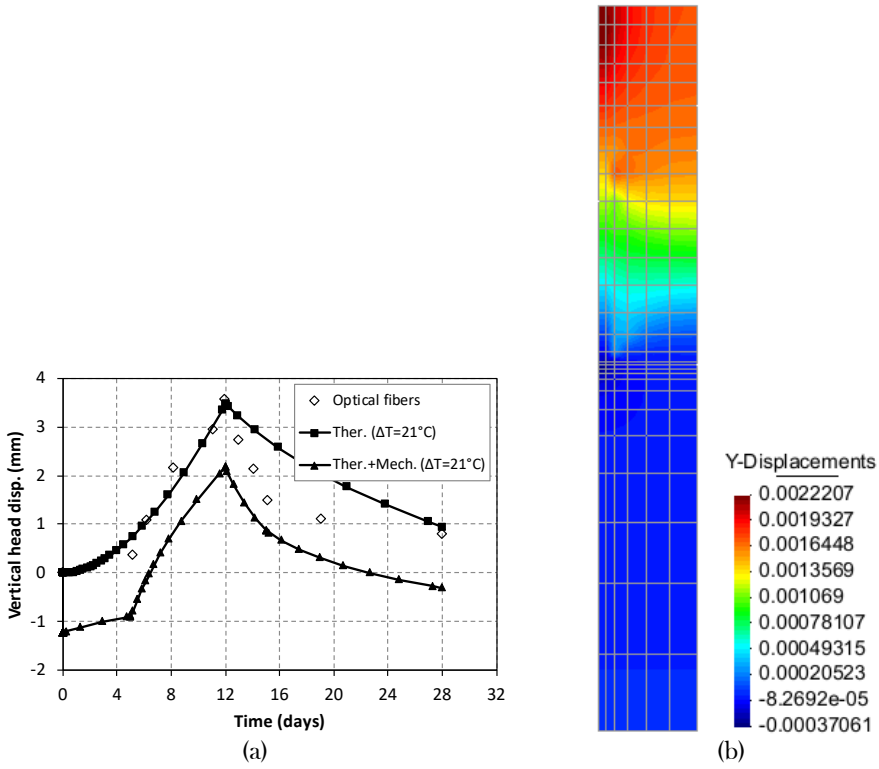

Figure C-15. (a) Thermal pile uplift during a heating–cooling cycle. (b) Computed contours of displacement at the end of the heating period (12 days).

C.6.4 Thermo-hydro-mechanical behaviour of the soil

The thermo-hydro-mechanical finite element modelling shows the following results:

In the case of Test 1 (thermal load only)

- heating of the pile produces a global swelling of the top surface of the soil (Figure C-19). The calculated displacement at the pile top corresponds well to the measured value (Figure C-10);
- the induced vertical strains are mainly dilative. However, as was experimentally observed, compressive strains are generated at the bottom of the pile.

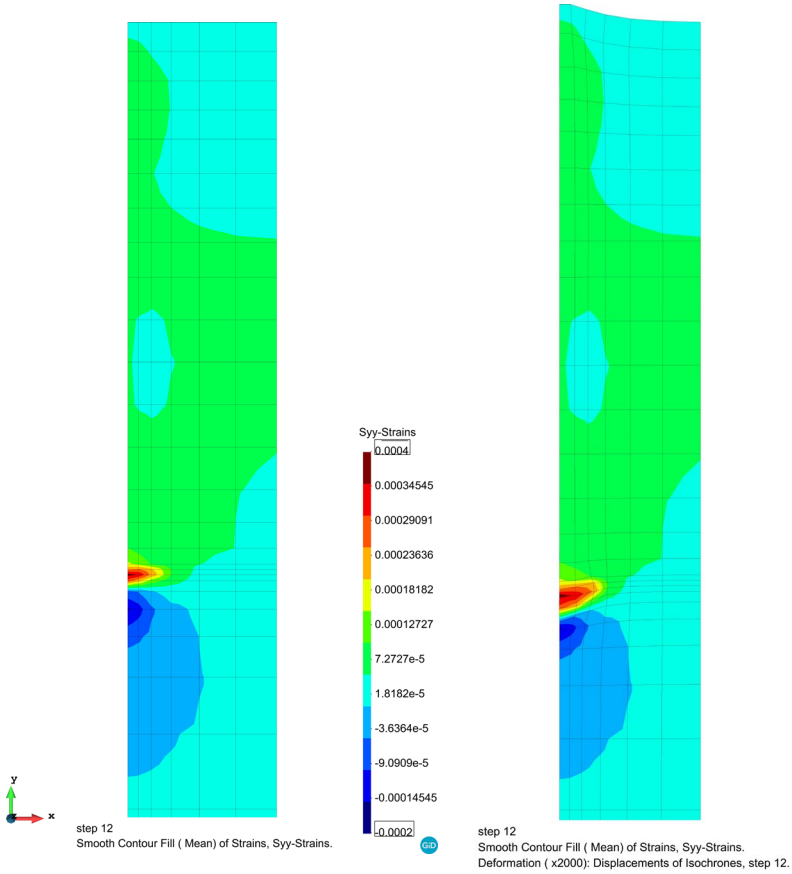

(a) (b)

Figure C-16. (a) Simulation of Test 1---heat-induced deformations (×2000).

In the case of Test 7 (thermo-mechanical load)

- the mechanical load (induced by the weight of the building) on the pile does not produce any strain in the soil at a distance as short as 1 m from the pile shaft;
- the heat effect is more pronounced and induces small strains at 1 m from the pile shaft (Figure C-21);
- The temperature induced excess porewater pressures in the base of thermal pile can be significant. Values in excess of 8 MPa have been proven in this study (Figure C-22Figure C-23).

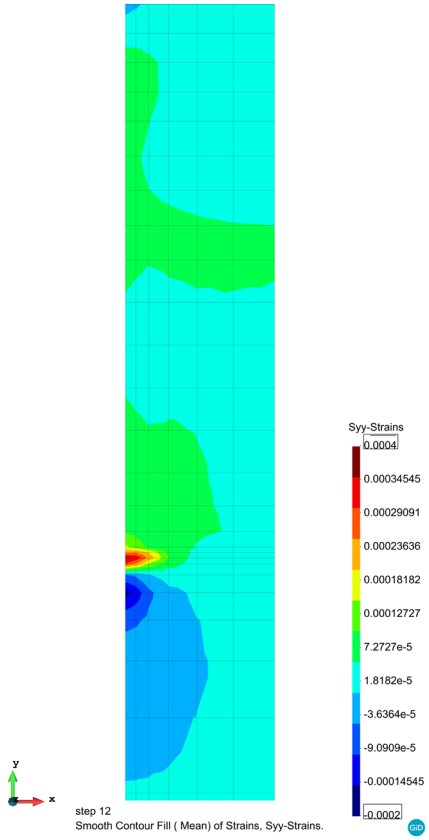

Figure C-17. Computed contours of vertical strains at the end of the heating period (computed results of Test 7).

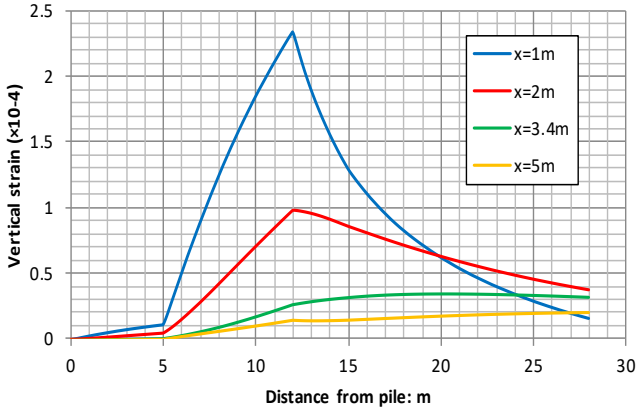

Figure C-18. Evolution of vertical strains increments at various points in the soil (computed results of Test 7).

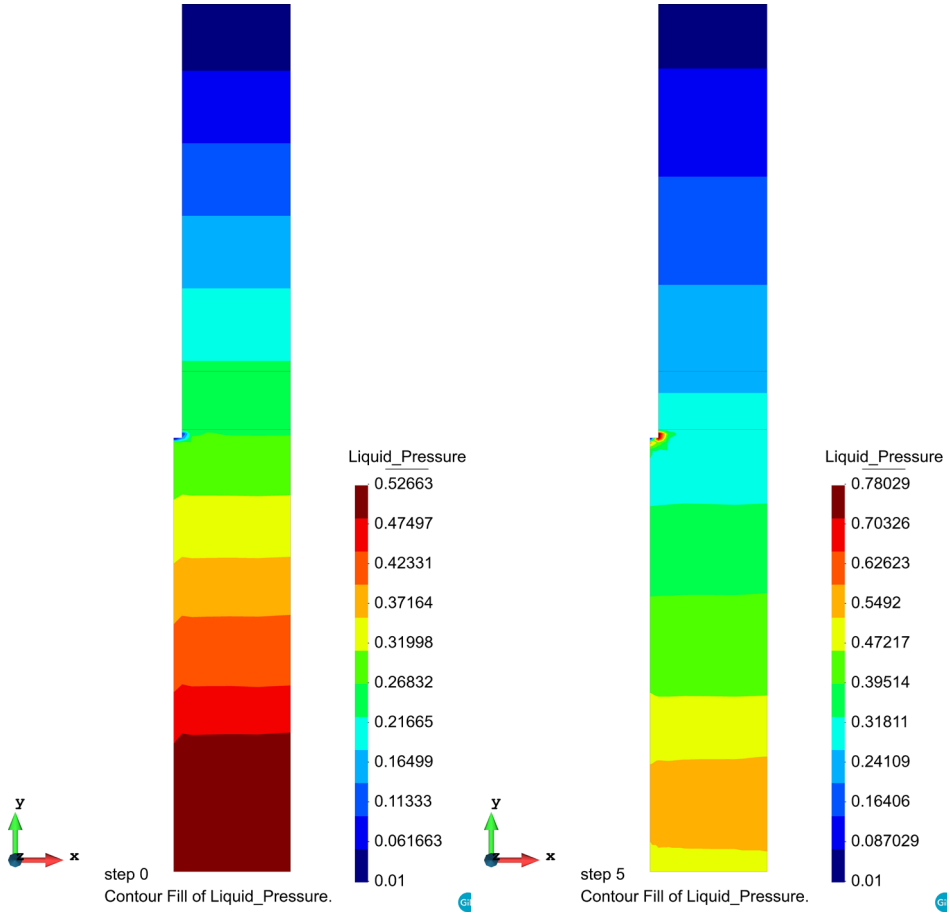

Figure C-19. Computed contours of equal pore pressure evolution for: (a) initial state (b) 5 days (computed results of Test 7).

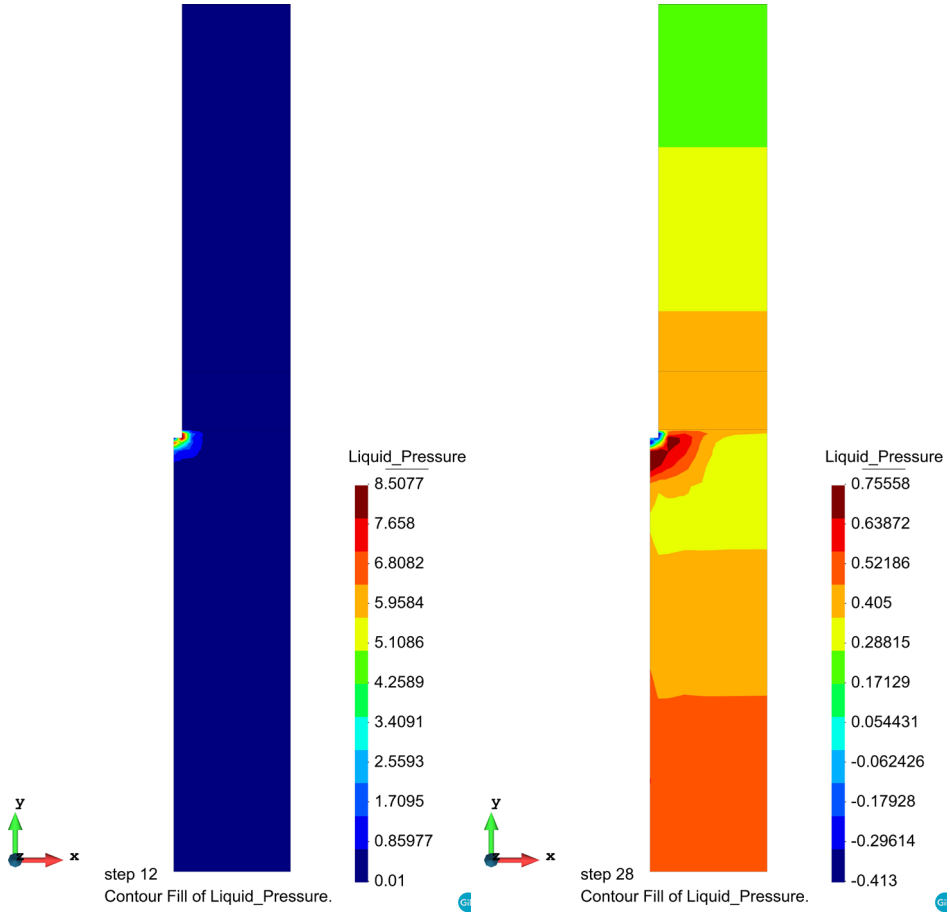

Figure C-20. Computed contours of equal pore pressure evolution for: (a) 12 days (b) 28 days (computed results of Test 7).

C.7 CONCLUSIONS

Heat exchanger piles offer a good opportunity for the use of sustainable energy for building heating and cooling. In spite of the existence of several installations of this type, the understanding of the thermo-hydro-mechanical behaviour is limited at the present time.

The THM response of geothermal energy pile placed in the five soil layers was investigated in this study using a coupled finite element procedure. The stress-strain response of the piles was considered linear elastic. The stress-strain response of soil layers was reproduced by using the state parameter based a time-dependent elastoplastic model. The uplift and axial and vertical stress/strain response of the

pile under combined thermal and thermomechanical loading were studied for two different tests. Overall, the theoretical formulation adopted and the numerical analysis performed have been able to provide a satisfactory reproduction of in situ test observations.